DEVELOPMENT OF A NEW PARALLEL CODE FOR 3-D JOINT REFRACTION AND REFLECTION TRAVEL-TIME TOMOGRAPHY OF WIDE-ANGLE SEISMIC DATA

—

SYNTHETIC AND REAL DATA APPLICATIONS TO THE STUDY OF SUBDUCTION ZONES

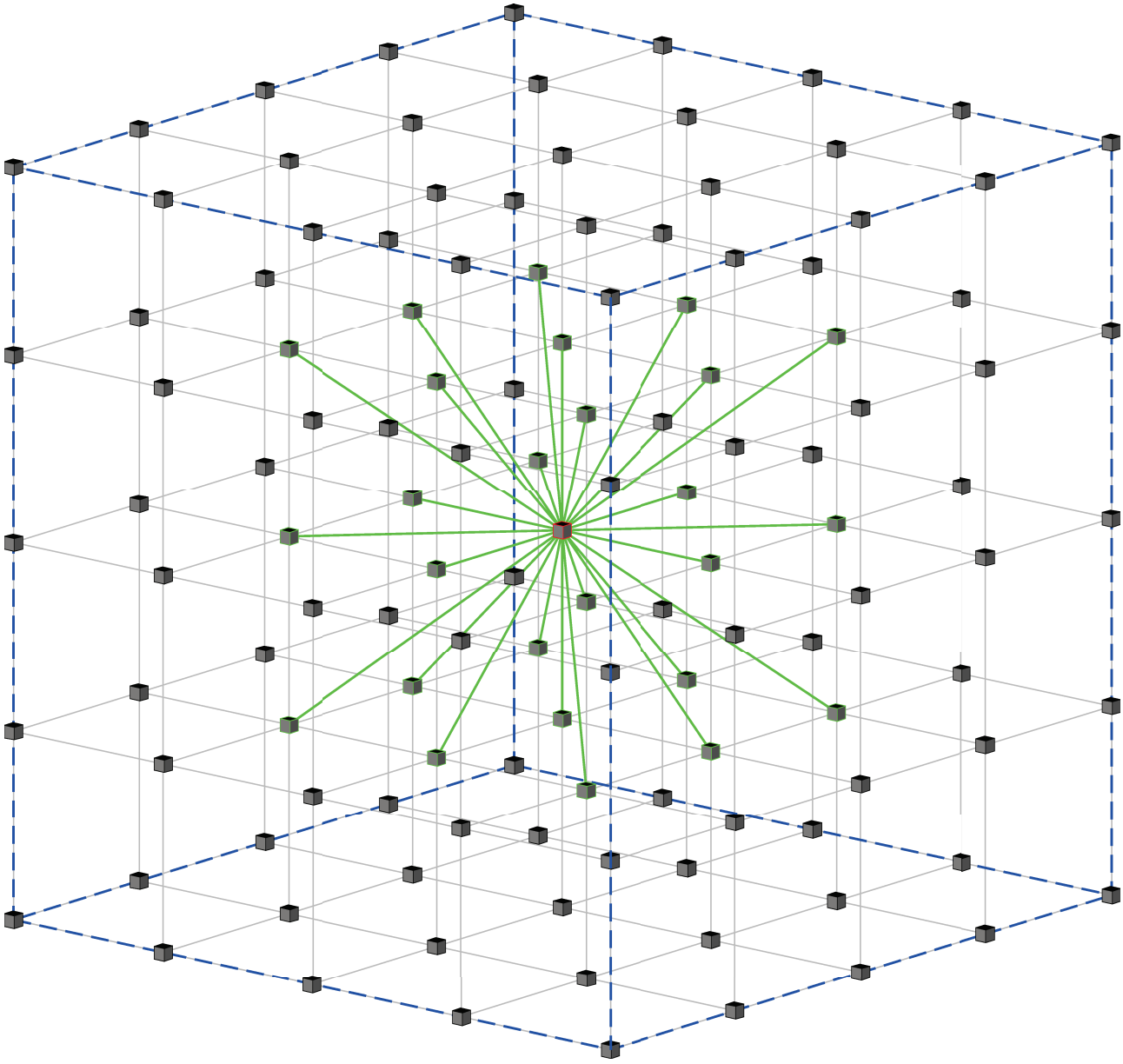

Adrià Meléndez i Catalán

Novembre de 2014

Barcelona – Center for Subsurface Imaging
Departament de Geociències Marines
Institut de Ciències del Mar (CSIC)

Programa de doctorat de Ciències de la Terra de la Universitat de Barcelona

DEVELOPMENT OF A NEW PARALLEL CODE FOR 3-D JOINT REFRACTION AND REFLECTION TRAVEL-TIME TOMOGRAPHY OF WIDE-ANGLE SEISMIC DATA

–

SYNTHETIC AND REAL DATA APPLICATIONS TO THE STUDY OF SUBDUCTION ZONES

Memòria de tesi presentada per n'Adrià Meléndez i Catalán

Directors:
Dr. Valentí Sallarès i Casas
Dr. César Rodríguez Ranero
Prof. Jun Korenaga

Tutora:
Dra. Pilar Neus Queralt i Capdevila

A les meves àvies i als meus avis, perquè cal conèixer els orígens.

A la mare, al pare i al Blai, en aquest i en qualsevol altre ordre.

A la Muntsa, tot ho farem.

“i ençà, enllà, amunt i avall,

la immensitat és oberta,

i aon tu veus lo desert

eixams de mons formiguegen.”

Jacint Verdaguer i Santaló,

Extracte del poema “Plus Ultra” a *Al cel* (1903).

AGRAÏMENTS

El projecte de tesi ha estat una part principal de la meva vida en els darrers anys i com a tal m'ha ofert la possibilitat de gaudir d'un munt d'experiències que han contribuit al meu creixement personal de manera molt significativa. Una etapa que s'acaba amb aquesta memòria on es recullen els fruits científics que ha donat. La resta de descobriments i aprenentatges els guardo en d'altres memòries tan importants com aquesta. Però és gràcies a aquest treball científic que he pogut emmagatzemar la resta de records.

Agraeixo al meu director, en Valentí, l'esforç que ha dedicat a portar a bon port el meu projecte de tesi amb la combinació adequada de supervisió de la meva feina i la capacitat d'atorgar-me responsabilitat sobre la mateixa. A en César, co-director, per ser una enorme font directa i indirecta de coneixement geològic, moltes gràcies. És en gran part per això que avui m'atreveixo a considerar-me un bon projecte de geofísic. A tots dos gràcies per la inversió que heu fet en mi en forma de viatges, visites i congressos que sempre m'han obert una nova perspectiva al món científic. To Jun, co-advisor, thanks for welcoming me so warmly to New Haven, and above all for trusting me with the task of creating TOMO3D. Half of the credit goes to you and your TOMO2D; the foundations could not have been stronger. Also, for the opportunity of sailing across the Pacific, visiting Guam and Hawai'i, and doing my particular around the world trip by plane and boat, ありがとう. Finalement, je veux aussi remercier Alain, ingénieur informatique, pour son travail sur le code. Sans ton aide, j'aurais dû attendre beaucoup plus pour obtenir mon grade de docteur.

A la meva tutora de la universitat, na Pilar Queralt, li agraeixo la seva feina durant el meu doctorat i sobretot durant la carrera de Física; gràcies per introduir-me al món de la Geofísica. Un record per en Carles, company de pràctiques de l'assignatura, i també per en Juanjo Ledo i n'Anna Martí per la meva primera sortida de camp. També voldria dedicar un agraïment al director del Programa de Doctorat, en Carles Martín Closas, i als membres de la meva Comissió de Seguiment, na Belén Alonso, en César Casquet i en Manuel Prieto, per la seva crítica que ha fet millor el resultat d'aquesta etapa.

Finalment i per damunt de tot, una abraçada ben forta a les companyes i els companys de feina, de doctorat, de campanyes, de pis, d'aventures diverses, de viatges i de lluites pel suport mutu que ens hem donat i que m'ha ajudat a acabar el doctorat i sobretot a escollir el meu camí fins avui. A la meva mare i al meu pare, al Blai i a la Muntsa, les paraules es queden curtes, el meu temps és vostre.

FUNDING

The author was funded by Repsol in the framework of the projects KALEIDOSCOPE and CO-DOS, and worked at the Grup de Recerca de la Generalitat de Catalunya 2009SGR146: Barcelona Center for Subsurface Imaging (Barcelona-CSI) of the Institut de Ciències del Mar (CSIC). Part of this work was also financed by the MICINN projects POSEIDON (CTM2010-21569), MEDOC (CTM2007–66179-C02-01/MAR, CTM2007–66179-C02-02/MAR), and HADES (CTM2011–30400-C02-01, CTM2011–30400-C02-02). The collection of the seismic data presented in chapter 2 was funded by the US National Science Foundation (NSF) and the German Science Foundation (DFG). The seismic data presented in chapter 5 were acquired in the framework of the ESMERALDAS project funded by the Institut de Recherche pour le Développement (IRD), the Institut National des Sciences de l'Univers (INSU – CNRS), and the Spanish Complementary Actions Estudio sísmico del margen activo de Ecuador (ECUASIS) and Subducción y riesgo sísmico en Ecuador y Colombia (SURSECO).

TABLE OF CONTENTS

INDEX OF EQUATIONS, FIGURES AND TABLES

Many of the figures in this work were generated with the Generic Mapping Tools (GMT) software from Wessel & Smith [1998].

RESUM

Aquesta tesi està dedicada a la tomografia sísmica de temps de trajecte. Concretament, he implementat una nova eina de modelització en 3D per a la tomografia conjunta de temps de trajecte de refraccions i reflexions de dades de sísmica de gran angle (TOMO3D). La raó darrere d'aquest objectiu central és l'evidència de que la informació basada en dades i models sísmics 2D no permet copsar ni reproduir la complexitat estructural de gran part dels cossos d'interès geològic, i en particular de la zona sismogènica en marges de subducció. En efecte, les comparacions entre models 2D de propietats elàstiques i models d'atributs sísmics de terratrèmols, que típicament presenten una gran variabilitat 3D, tot i ser valuoses, sovint són esbiaixades i/o incompletes. El raonament científic per aquesta afirmació, que justifica la part central de la meu treball de tesi, neix de l'anàlisi de models 2D obtinguts al marge convergent de Nicaragua, una àrea sísmicament activa on el 1992 va tenir lloc un exemple paradigmàtic de terratrèmol associat a un tsunami anòmal. En aquesta aplicació he modelitzat dos perfils de sísimica de gran angle per a la caracterització de la placa cavalcant i la falla d'interplaca. Per fer-ho he aplicat el TOMO2D, un codi d'avantguarda per a la tomografia conjunta de refraccions i reflexions en 2D que ha estat verificat en la modelització de numerosos experiments sísmics. Els resultats de la inversió són dos models 2D de velocitat al llarg d'ambdós perfils, i la geometria 1D del límit interplaca. En combinació amb altres dades geofísiques, en concret perfils coincidents de sísmica multicanal i dades de gravimetria, aquests models aporten nou coneixement sobre la naturalesa i l'estructura del marge, i en particular afegeixen contribueixen a la comprensió de la nucleació i la propagació de l'esmentat terratrèmol i el seu comportament tsunamigènic. En última instància, aquest estudi evidencia les limitacions prèviament mencionades de la modelització 2D en la investigació d'estructures i fenòmens geològics, i mostra la necessitat de prospeccions i eines de modelització en 3D. De resultes d'aquesta primera aplicació i amb la idea d'incrementar la quantitat de dades utilitzades en la tomografia de temps de trajecte, em vaig centrar en un fenomen a priori paradoxal relacionat amb les fases de múltiples de la capa d'aigua que, en certes circumstàncies, s'observa en els registres de sísmica de gran angle. L'interès d'aquest estudi rau en el fet que aquest fenomen pot aportar informació addicional als models de tomografia de temps de trajecte. En primer lloc, proposo i corroboro la hipòtesi que explica la paradoxa aparent, i a continuació dedueixo les condicions geològiques més favorables per a que el fenomen ocorri. Seguidament, la possibilitat de modelitzar aquesta mena de fases múltiples és introduïda al TOMO3D.

El desenvolupament i implementació del TOMO3D, que constitueix el nucli del meu treball, es basa en el TOMO2D, del qual hereda els mètodes numèrics per resoldre els problemes directe i invers.

Els arxius de codi font han estat reescrits, redefinint i introduint les variables i funcions necessàries per dur a terme la inversió de dades 3D. Els testos fets amb la versió seqüencial del codi posen de manifest la necessitat de paral·lelització per raons de viabilitat. En efecte, l'increment de la mida dels conjunts de dades així com la modelització de la dimensió espacial afegida fan que les inversions siguin computacionalment exigents. Així doncs, he paral·lelitzat la part del codi encarregada de la modelització directa, que representa fins al 90% del temps de computació, amb una combinacio d'extensions de *multiprocessing* i *message-passing interface*. Seguidament, la versió paral·lelitzada del TOMO3D ha sigut aplicada a un cas sintètic complex que simula una zona de subducció en un marge convergent oceà–continent. Aquesta primera aplicació 3D serveix per evaluar la correcció de la programació del codi, i com una descripció pas a pas del procediment de modelització, amb especial atenció a l'estratègia de *layer-stripping* utilitzada per modelitzar diversos reflectors. Els resultats demostren la capacitat del codi i de l'estratègia d'inversió emprada per recuperar acuradament la distribució de velocitat i la geometria dels dos reflectors. Val la pena destacar que, si el mostreig azimutal és suficientment dens, els resultats de la inversió poden ser satisfactoris fins i tot en àrees on la cobertura de rajos és majoritàriament o únicament donada només per fases reflectides. Finalment, com el millor dels testos possibles, el TOMO3D és aplicat a un conjunt 3D de dades de sísimica de gran angle adquirit al marge pacífic d'Equador i Colòmbia per extreure'n un model 3D de la velocitat de les plaques cavalcant i subduïda, que seguidament és comparat amb resultats previs obtinguts amb un codi 3D de tomografia de temps de trajecte de refraccions extensament testat i usat (FAST). La comparació indica que el TOMO3D és més acurat que el FAST però al mateix temps és computacionalment més exigent. Tot i així, la paral·lelització del TOMO3D permet utilitzar plataformes de supercomputació, a diferència del que passa amb el FAST i la majoria de codis existents.

ABSTRACT

This dissertation is devoted to travel-time seismic tomography. In particular, I have implemented a new modelling tool for 3-D joint refraction and reflection travel-time tomography of wide-angle seismic data (TOMO3D). The reason behind this central objective is the evidence that the information based on 2-D seismic data and models does not allow to capture and reproduce the structural complexity of many 3-D geological targets, and in particular that of the seismogenic zone in subduction margins. Indeed, comparisons between 2-D models of elastic properties and models of earthquake attributes, which typically display large 3-D variability, although valuable, are often biased and/or incomplete. The scientific rationale for this statement, which justifies the central part of my thesis work, is based on the analysis of 2-D models obtained in the convergent margin of Nicaragua, a seismically active area where a textbook example of tsunami earthquake took place in 1992. In this application I modelled two perpendicular wide-angle seismic profiles for the characterisation of the overriding plate and the interplate fault. To do this, I applied TOMO2D, a state-of-the-art joint refraction and reflection 2-D travel-time tomography code that has been verified in the modelling of numerous seismic experiments. The inversion outcomes are two 2-D velocity models along both profiles, together with the 1-D geometry of the interplate boundary. In combination with other geophysical data measurements, namely coincident multichannel seismic profiles and gravity data, these models provide new constraints on the nature and structure of the margin, and in particular add new insights on the nucleation and propagation of the said earthquake and its tsunamigenic behaviour. Ultimately, this case study evidences the aforementioned limitations of 2-D modelling in the investigation of 3-D geological structures and phenomena, thus calling for the need of 3-D prospecting and modelling tools. Following from this first application and with the idea of increasing the amount of data used in travel-time tomography, I focused on an *a priori* paradoxical phenomenon related to water-layer multiple phases, that under certain circumstances, is observed on wide-angle record sections. The interest of this study lies in the fact that this phenomenon can provide additional constraints on travel-time tomography models. First, I propose and corroborate the hypothesis explaining the apparent paradox, and then derive the most favourable geological conditions for the phenomenon to occur. Subsequently, the possibility to model this multiple-like phases is introduced in TOMO3D.

The development and implementation of TOMO3D, which constitutes the core of my work, is founded on TOMO2D, from which it inherits the numerical methods for solving the forward and inverse problems. Source files have been rewritten, redefining and introducing the necessary variables and functions to handle 3-D data inversion. The tests made with the sequential version of

the code emphasise the need of parallelisation for practicality reasons. Indeed, the increasing size of data sets along with the modelling of the additional spatial dimension results in computationally demanding inversions. Hence, I parallelised the forward modelling part of the code, which takes up to 90% of the computing time, with a combination of multiprocessing and message-passing interface extensions. Subsequently, the parallel version of TOMO3D is applied to a complex synthetic case simulating a subduction zone at an ocean–convergent margin. This first 3-D application serves to evaluate the correctness of the code's programming, and as step-by-step description of the modelling procedure, with particular attention on the layer-stripping strategy used to successively model several reflectors. The outcomes demonstrate the ability of the code and the chosen inversion strategy to accurately recover the velocity distribution and the geometry of the two reflectors. It is worth noting that, if azimuthal sampling is sufficiently dense, the inversion results can be satisfactory even in areas where ray coverage is mostly or only provided by reflected phases. Finally, as the best test possible, TOMO3D is applied to a real 3-D wide-angle seismic data set acquired at the Pacific margin of Ecuador and Colombia to extract a 3-D velocity model of the overriding and incoming plates, which is then compared to previous results obtained with an extensively tested and used 3-D refraction travel-time tomography code (FAST). The comparison indicates that TOMO3D is more accurate than FAST but at the same time it is computationally more demanding. However, the parallelisation of TOMO3D allows using high-performance computing facilities, which is not the case of FAST or most of the existing codes.

MOTIVATION

The study of 3-D geological structures using 2-D methods is always incomplete, and although often financial, logistical or computer limitations have forced collection of 2D data in grids, currently the amount of 3-D experiments is increasing. A notable example of the shortcomings arising from 2-D data sets are the studies of convergent margins, where the subduction of oceanic plates beneath continental or island arc plates causes great 3-D deformations and the Earth's largest and most destructive earthquakes and tsunamis. The study of the processes governing earthquake and tsunami generation at these regions constitutes one of the main research lines of the Barcelona-CSI research group, where I have developed my PhD.

Most geophysical past experiments in subduction zones are based on 2-D profiles acquired perpendicular to the trench. Whereas these profiles have provided valuable information on the variation of the structure and properties of the overriding and subducting plates down-dip of the subduction zone, they lack information on the variability parallel to the trench. Contrarily, seismological and tsunami observations indicate that the earthquake moment release and co-seismic slip distribution strongly vary both along and across the megathrust interplate fault. This makes 3-D experiments and modelling tools essential to capture the structural complexity of the interplate boundary zone and, in turn, to understand if and how the structural parameters exert a control on earthquake nucleation and propagation. The 3-D investigation of the Earth's interior naturally yields results that are more robust and lead to more reliable and complete geological interpretations. It should be noticed that the advantage of 3-D acquisition lies not only in the greater number of data sampling the region of interest in the subsurface but also in the multi-azimuth coverage that it provides.

Technical improvements in data acquisition experiments as well as the proliferation of research groups with a growing number of recording units, and the generalisation of international collaborative projects have favoured the collection of large seismic data sets, including 3-D experiments. Further, 3-D experiments are comparatively much more common for the industry, which systematically collects data sets that are beyond the financial and logistical capabilities of academia, but that are often available through collaboration projects. As 3-D seismic experiments become more common, so does the need for the appropriate tools to process the collected data sets. In the case of active data travel-time tomography, the availability of 3-D seismic data has stimulated the extension of travel-time tomography to 3D. Indeed, a 3-D approach overcomes the main conceptual limitations of 2-D modelling. First, during experiments it is technically not feasible to

arrange sources and receivers in an exact 2-D plane, although this can be done accurately enough so that it does not become a significant error source. More importantly though, waves propagate in a 3-D space and thus in general ray paths are not restricted to a 2-D plane. Furthermore, with 3-D modelling we account for the real 3-D structure of the medium and therefore the only errors are caused by technical limitations, that mainly include spatial sampling limitations, limitations in the illumination of subsurface regions, and numerical approximations in the method and coding.

In the case of earthquake data, almost any existing 3-D travel-time tomography code uses only first arrivals to derive coarse models of the velocity structure without sharp discontinuities. In other words, it is not possible to define the location and geometry of geological interfaces such as faults or layers. In the context of convergent margins and the investigation of subduction earthquakes, this poses a major drawback because knowing the precise location and geometry of the megathrust fault and the elastic rock properties above and below it is critical to understand earthquake rupture dynamics. This combination of a major, unresolved scientific problem, and the absence of an appropriate tool to extract part of the required information from the data, is the main motivation of this work. In this regard, TOMO2D [Korenaga et al., 2000] is a popular and well-tested 2-D travel-time tomography code that possesses some interesting characteristics which make of it a suitable basis for a modern 3-D travel-time tomography code. It is one of the few codes that models not only first arrivals, or refraction travel-times, but also travel-times from reflected phases, to invert simultaneously for the velocity distribution and the geometry of the reflecting interfaces. This combination of data uses more information from seismic records, and provides better ray coverage of the study area. In addition, it mitigates the velocity–depth ambiguity inherent to reflection data because the velocity model is also constrained by refraction data independently of depth. Moreover, TOMO2D allows for the quantification of this velocity–depth ambiguity, and it is the only open-source code to do so. Finally, the tomography algorithm of TOMO2D is a competitive state-of-the-art option.

Considering all the above, the **main purpose** of this work is the methodological development of a new 3-D seismic modelling tool to match the growing number of 3-D wide-angle seismic experiments, and in the particular case of our research group, to contribute to the investigation of convergent margins, and the earthquake and tsunami generation associated to subduction zones. For this purpose, this tool must perform 3-D joint refraction and reflection travel-time tomography to yield models of the 3-D velocity distribution of the incoming and overriding plates along with the 2-D geometry of geological discontinuities such as the interplate boundaries where megathrust earthquakes nucleate. For this new tool to be useful it is crucial that it is based on a robust 2-D code

as TOMO2D, which has been successfully applied to a 2-D study of the convergent margin of Nicaragua for the investigation of a megathrust tsunami earthquake. Apart from the scientific interest of the geological problem, an additional goal of this application is to serve as a step-by-step introduction to the modelling procedure of travel-time tomography and to TOMO2D's functioning in particular, and at the same time to highlight the shortcomings of 2-D experiments, and hence the need for 3-D prospecting and modelling. Furthermore, the new 3-D code must be parallelised to cope with the increased number of data and parameters making use of the available computing resources. Once implemented and with the objective of evaluating its performance, we will apply this 3-D code to a synthetic case simulating a subduction zone. Subsequently, as a final means of performance assessment, we will use it to model a real data set acquired at the convergent margin of Ecuador and Colombia, which also allows for the comparison with independently obtained results.

OUTLINE

The first chapter of this thesis is an introduction that sets the general framework of my work. This introduction is divided in three sections. The first section starts with a review of the basics of geophysical modelling and prospecting methods, and afterwards focuses on active-source seismic data acquisition, with special attention on wide-angle seismic data. Finally, travel-time tomography is explained in the context of the most common seismic modelling techniques. The second section of chapter one provides an overview of the theoretical basis of travel-time tomography and of the various approaches from early procedures to the present state of the art. In the third section, the introduction is closed with a summary of the main objectives that this thesis seeks to accomplish. The second chapter presents a case study corresponding to the 2-D inversion of data collected at the Pacific convergent margin of Nicaragua [Sallarès et al., 2013], and explains how to interpret record sections and the basic workflow of travel-time tomography, and discusses the limitations of 2-D modelling. This application of TOMO2D helped me familiarise myself with travel-time tomography modelling of wide-angle seismic data, as well as with the specific functioning details of TOMO2D. In the third chapter we work again with record sections to analyse a recurrent and apparently anomalous phenomenon involving water-layer multiples in marine wide-angle seismic data. We explain how multiples phases with anomalously high amplitude are created and how they can be properly modelled in travel-time tomography, hence increasing the use of information from data recordings [Meléndez et al., 2014]. The fourth chapter details the fundamental elements of the 3-D code: the parametrisation of velocity and interface depth, the ray-tracing algorithm used to solve the forward problem, and the formulation and solution of the inverse problem. At the end of the chapter, our parallelisation strategy is presented and its performance evaluated. The fifth chapter presents the results for applications of TOMO3D to both synthetic and real data. First, the synthetic inversion example simulating a subduction zone is discussed, and layer stripping is proposed as the best general strategy to deal with various reflecting interfaces. Next, the inversion results for the convergent margin of Ecuador and Colombia are shown and compared to those previously obtained using an alternative 3-D refraction travel-time tomography code. The general agreement between both velocity models as well as the recovery of expected, geologically-reasonable velocity values support the reliability of TOMO3D as a modelling tool. Finally, the sixth chapter summarises the achievements of this thesis, and outlines its prospects for the near future.

CHAPTER 1: INTRODUCTION

1. INTRODUCTION

This introduction consists of three sections. The first one is a general review on geophysical modelling, including a brief description of its fundamentals and a summary of the most relevant prospecting techniques, with special attention to seismic methods, and in particular to marine wide-angle seismic experiments. In the second section the focus is on travel-time tomographic inversion as the geophysical modelling method that is developed in this thesis. This section begins with an outline of the historical evolution, continues with a description of the theoretical basis, and ends with an overview of the current state of the art. The third section is a summary of the specific objectives of this work.

1.1. Geophysical modelling and prospecting methods

Geophysical modelling is the process of retrieving the distribution of a particular physical property in the subsurface from the data measurements of the medium response to a source that is sensitive to that physical property [Tarantola, 1987]. The subsurface distribution of physical properties can then be represented by a numerical model that reproduces the collected data based on an existing theoretical relationship. The retrieved physical property is associated to the nature of the rock and mineral bodies that constitute the Earth's interior, which are the object of interest of geological and geophysical studies.

Geophysical modelling is generally formulated as the solution to the problem $\mathbf{d}=\mathbf{A(m)}$ where $\mathbf{d}$ are the data, $\mathbf{m}$ are the parameters describing the numerical model of the physical property and $\mathbf{A}$ is an operator representing the theoretical relationship between $\mathbf{d}$ and $\mathbf{m}$ [Zhdanov, 2002]. This expression is known as the forward problem equation, and its solution provides a synthetic prediction of the data measurements expected for a given model. The inversion of this equation to infer the distribution of a physical property from real data is the so-called inverse problem. Geophysical modelling methods can thus be divided in forward and inverse techniques. The former follow a trial-and-error procedure to build a model that produces synthetic data which are close enough to real measurements. In the latter, the linearised version of the forward problem equation, $\mathbf{d}=\mathbf{Am}$, is inverted so that the model is determined as $\mathbf{m}=\mathbf{A}^{-1}\mathbf{d}$. Inversion schemes are a more robust approach to modelling because they are automated, which favours objectivity and speeds up the modelling process as opposed to the more subjective and time-consuming nature of forward

modelling. Moreover, only with an automated inversion scheme is it possible to assess the reliability of the resulting model through an uncertainty analysis. The assessment of uncertainty is a crucial aspect of the modelling problem because its solution is generally affected by non-uniqueness, i.e. the existence of various models that provide an acceptable fit for the data measurements, and instability, i.e. the data measurements are not sufficiently sensitive to distinguish between significantly different models. A third, perhaps even more basic issue is the actual existence of a solution to the problem. Of course, at least one physical, real-world model exists that can explain the data, but it may happen that the mathematical formulation of the problem is unable to provide a satisfactory numerical solution. Finally, the linearisation of a fundamentally non-linear problem automatically makes its solution dependent on the initial model selected. Indeed, only if the initial model is sufficiently close to the real one so that the linear approximation holds, the inversion will be able to converge to the true solution.

Modelling techniques use the data measurements obtained through different geophysical prospecting and exploration methods [Sharma, 1986]. These prospecting methods are classified according to their source of data measurements, that is, the physical field propagating in the subsurface that is recorded so that it can later be modelled. The most important prospecting techniques in terms of the recorded physical field are gravitational, electrical, magnetic, electromagnetic, and seismic methods. Physical fields may be either active, i.e. artificially created for the purpose of prospection, or passive, i.e. of natural origin. The latter can be specifically adapted, up to a point, to each study case, which allows for more accurate results. Some modelling methods can use a combination of active and passive data, and even of measurements of different physical fields. Typically several modelling methods are combined to gather as much evidence as possible in support of the geological interpretation. The selected methods depend on the nature and structure of the geological target that is to be investigated, as these determine the physical properties that will provide the best constraints. Moreover, physical properties can be empirically related to each other through laboratory tests. A common example are empirical equations relating the propagation velocity of seismic waves to rock density, which facilitate the combination of seismic and gravity modelling [e.g. Korenaga et al., 2001; Sallarès et al., 2013].

Among all these geophysical techniques, seismic methods provide the most detailed information on the Earth's interior [Sheriff, 1989]. Passive-source seismic methods, also known as earthquake seismology, use recordings of seismic events to model the velocity distribution and/or hypocentral locations. Active- or controlled-source seismic methods are particularly useful in the study of the

crust and upper-mantle to depths of a several tens of km, although they can be used at a wide range of scales. As opposed to earthquake seismology, the location and origin time of sources are precisely known. These exploration methods can be divided into two main families: refraction and wide-angle reflection studies, that yield petrological information, and near-vertical reflection studies, that provide insights on the structure of geological bodies. Wide-angle seismic experiments are devised to recover the wavefield travelling through the medium for long offsets and subhorizontal propagation as opposed to near-vertical seismic data (Fig. 1.1). The processing of the latter is commonly known as imaging, and is a sort of forward modelling in which a velocity model is built that explains the reflected arrivals, and is then used to generate an image of the position of the reflecting horizons in the subsurface. In this work I focus on the former as they provide the sort of data that our code is designed to model at the moment. However, future developments of TOMO3D include the extension to modelling both near-vertical reflection data and seismological data.

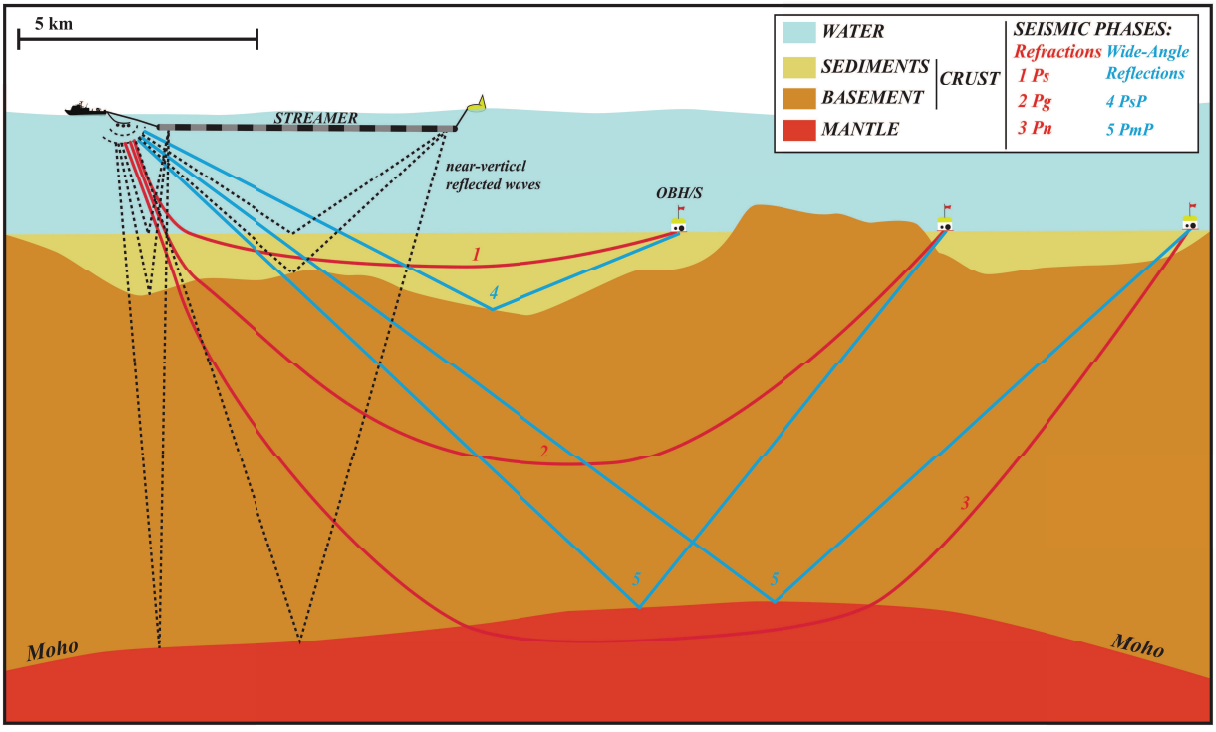

Figure 1.1. Cartoons for the acquisition configurations of the most common active-source seismic experiments. Two main types of marine surveys exists: near-vertical multichannel reflection (black dashed rays), and refraction and wide-angle reflection (red and blue rays) experiments. The former records the subvertical wavefield with a streamer cable carrying the receivers, whereas the latter collects the subhorizontal wavefield using various receivers located at the seafloor. In both cases air guns are used as source. [M. Prada, personal communication, 2014].

The origin of active-source seismic prospecting can be traced back to mid nineteenth century with the first attempt to measure the speed of sound through surface rocks by Robert Mallet in 1849 [Prodehl & Mooney, 2012]. The first seismogram dates from as early as 1908, and was recorded for the investigation of the uppermost sedimentary layers using the first portable seismograph developed only two years before. Academic research began in the 1920s-30s with the use of large explosions, also in shallow water-covered areas with underwater explosions. Nonetheless, it was not until the end of World War II that active-source scientific exploration of the Earth's interior started on the path to become what it is today. International cooperation and the generalised use of large explosions only began after 1945 in land. At sea, experiments were extended from shallow waters to deep oceanic areas with the introduction of hydrophones, and in 1950 an overall picture of the continental/oceanic crust structure was available: granitic/basaltic upper crust, gabbroic lower crust separated from the peridotitic upper mantle by the Mohorovicić discontinuity. By mid 1950s systematic seismic investigation of the detailed structure of the lithosphere started in Europe, and by the end of the decade wide-angle seismic experiments were well established with offsets reaching several hundred km. During 1960s the production of instrumentation for wide-angle seismic exploration became regular, and together with the improvement of interpretation resulting from the introduction of record sections, as well as notable advances in wave propagation theory helped pushing forward the understanding of the interaction of waves with the Earth's crustal structure. Also, by the end of this decade, the first synthetic seismograms were computed. The decade of 1970s saw a significant improvement in computer facilities that led to better modelling codes and techniques, and subsequently to the abandonment of constant-velocity layer in favour of velocity gradients to represent the subsurface seismic structure. Hundred- and thousand-km long profiles were acquired all over the northern hemisphere and Australia including the first profiles around the Mediterranean. After the development of the ray method [Červený et al., 1977] ray tracing methods became the reference tool in seismic modelling and they still are nowadays. In 1980s there was an increase in ray coverage that was necessary to match the precision of new codes and allowed studying complicated regions in more detail; large-scale international wide-angle seismic surveys were conducted, and the first digital recorder was used. The 1990s witnessed the sophistication of sources, receivers and acquisition equipment in general with the transition from analog to digital devices, and marked the start of the modern recording, modelling and interpretation techniques. Regarding projects, they have been growing more and more ambitious, and thus bigger, more expensive, and involving almost always several research institutions.

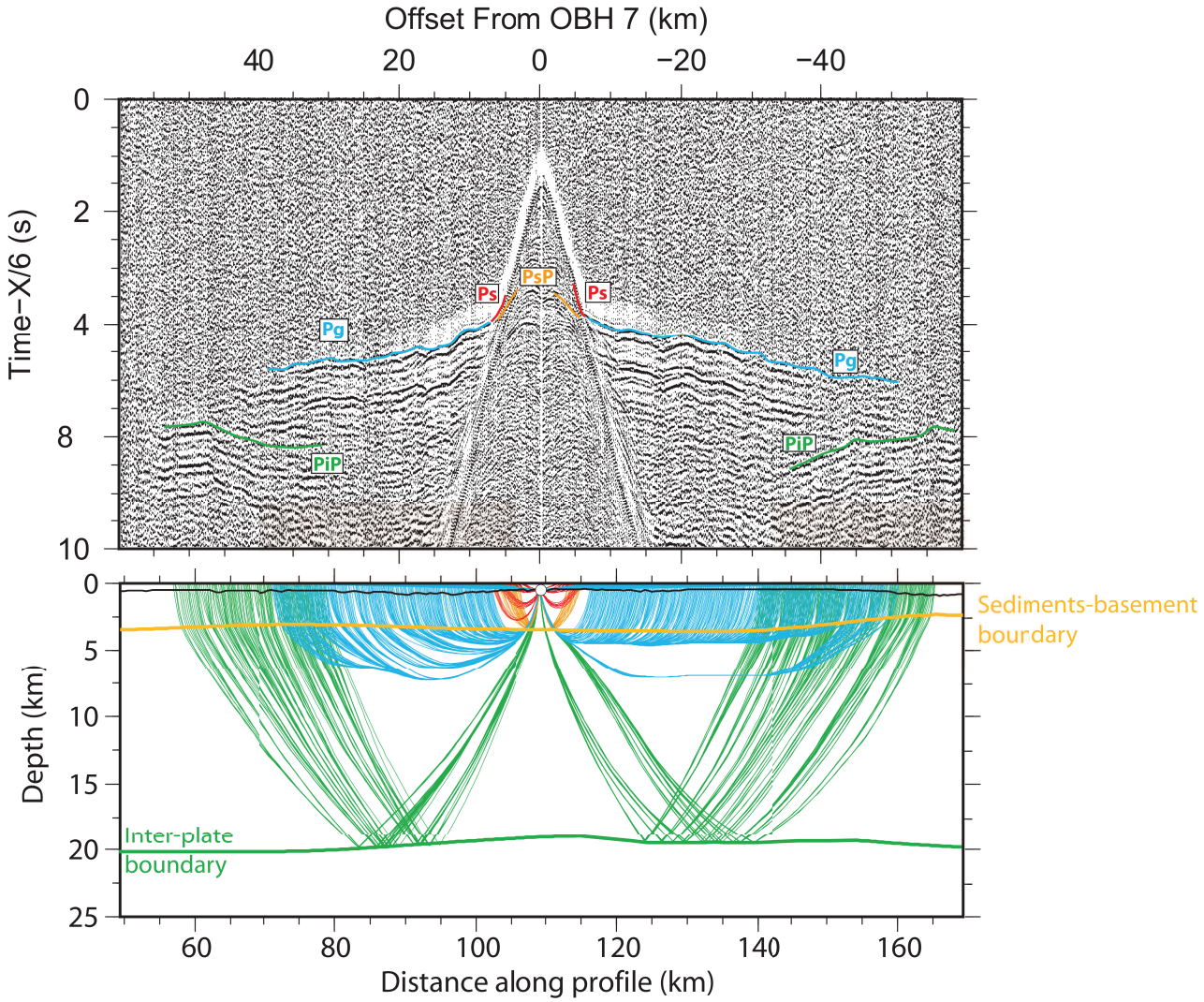

Figure 1.2. (top) Sample record section for OBH 7 from the trench-parallel profile NIC-125 acquired off-shore Nicaragua over the continental slope during R/V Maurice Ewing cruise EW00-05 in 2000 [Sallarès et al., 2013]. Colour contours mark the various seismic phases: refractions within the sedimentary layer (Ps) and the continental crust (Pg), and reflections from the top of the basement (PsP) and the interplate boundary (PiP). (bottom) 2-D section defined by profile NIC-125 displaying the ray paths associated to the travel-time picks from OBH 7. Rays were traced using TOMO2D for the final velocity and interface depth model presented in Sallarès et al. [2013]. The colour code is consistent with seismic phases indicated above. The thin black line represents the seafloor relief whereas the two reflecting interfaces are plotted as thick lines of the same colour as the corresponding reflected rays [M. Prada, personal communication, 2014].

Wide-angle data is displayed in the aforementioned record sections (Fig. 1.2). In record sections traces are plotted at their corresponding source–receiver offset so that seismic phases appear from

the lateral coherence of the same arrival recorded at consecutive offsets over many traces. Among these phases, the most important are diving waves, i.e. refractions, that are only dependent on the subsurface velocity distribution, and wide-angle reflections associated to major geological impedance contrasts, which are controlled by velocity and reflector depth. Other phases correspond to late arrivals such as multiply reflected or converted waves. In this representation, refraction's local slope is proportional to the average propagation velocity of waves travelling down to a certain depth, and reflections are seen as hyperbolas deformed by the effect of geological relief, reflector's geometry and velocity heterogeneities. Because velocity increases with depth, refracted waves are only recorded above a certain offset threshold, while below it first arrivals are direct waves [Červený, 2001]. Therefore, the selected total offset of an experiment depends on the desired target depth that it seeks to resolve and on the subsurface velocity gradient. In practice, a 1:4 relationship between depth and offset can be assumed based on general experience, and the objective is to record refracted phases at the longest offsets possible so that we can maximise depth. This maximum offset is determined by several factors such as the initial amplitude of the source, the decay by geometrical spreading and attenuation, the transfer function and seafloor coupling of the receiver, and the ambient noise. Land, marine, and combined acquisitions are possible, and wide-angle experiments commonly consist in several tens or even hundreds of thousands of shots recorded at between tens and hundreds of receivers. Offshore sources are typically produced by air-gun shots, whereas, depending on the target depth, land surveys may use human-made sources for shallow depths, usually hammering a metal plate, or use vibroseis trucks for deeper targets, among other much less frequent methods. A common land data acquisition method is the vertical seismic profile (VSP); unlike in the typical horizontal acquisition configurations, here receivers are arranged vertically within a borehole. Recording stations usually include a 3-component (3-C) seismometer and/or a geophone (Fig. 1.3a); cutting-edge landstations are 4-C meaning that they incorporate both. There are two main types of marine receivers: ocean bottom seismometers (OBS) and ocean bottom hydrophones (OBH), where the former typically carries an hydrophone along with the seismometer (Fig. 1.3b). Other more recently developed options are ocean bottom cables (OBC) and ocean bottom nodes (OBN), which also incorporate an hydrophone and a seismometer (Figs 1.3c,d). State-of-the-art OBS/H can operate at a water depth of 6-7 km, whereas OBC are limited to 2-2.5 km, and OBN to 3-3.5 km. The advantage of OBC and OBN is on the greater density of receivers that they can provide, with spacings <~100 m.

(a)

(b)

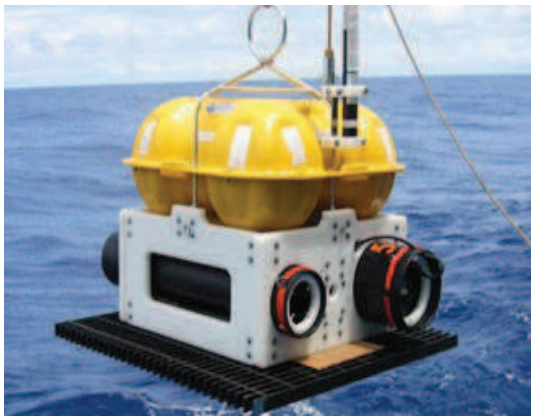

(c)

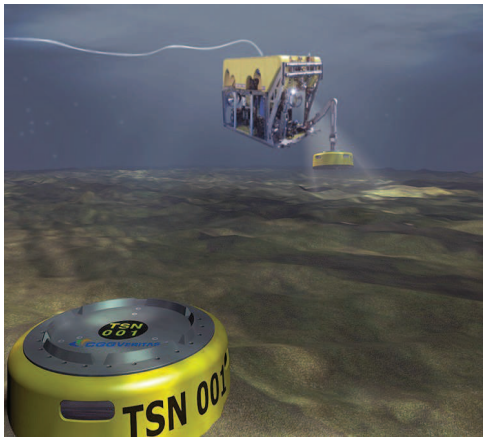

(d)

Figure 1.3. Examples of the main types of seismic receivers. (a) Geophone. For recording, the nail-like end is driven into the ground. Image from www.mitchamindustries.com. (b) OBS/H. For deployment, the device is dropped into the water and it falls to the seafloor. For recovery, it releases a weight (the metal piece attached at the bottom in the image) and it comes back up to the sea surface. Image from www.venturedeepocean.org. (c) OBN. These compact receivers are deployed and recovered using ROVs (Remotely Operated Vehicle), and are typically laid out forming a grid. Image from www.cggveritas.com. (d) OBC. In 3-D experiments cables are usually arranged parallel to each other over the target study area. Image from www.sercel.com.

1.2. Travel-time tomography

Travel-time tomography or travel-time inversion are generic names given to the inverse modelling technique that uses the arrival times of the different phases in seismic data to derive velocity models of the Earth's interior. This technique was first devised for its application to seismological data

when Aki & Lee [1976] used this method on local earthquake data to derive subsurface velocity anomalies. Codes have been developed that invert for velocity using travel time picks from either first-arrival refracted phases [e.g. Zhang & Toksöz, 1998] or reflected phases [e.g. Pullammanappallil & Louie, 1993]. Travel-time tomography has also been adapted to use reflection data to produce velocity and reflector depth models [e.g. Bishop et al., 1985; Farra & Madariaga, 1988]. First attempts to combine refraction and reflection information in a single modelling tool alternated between the inversion of refraction data to infer velocity and that of reflection data to infer interface depth [Lutter & Nowack, 1990]. Early implementations of the joint inversion used few parameters by defining velocity and depth functionals [Zelt & Smith, 1992]. The joint (i.e. simultaneous) non-linear inversion of refraction and reflection data using travel-time tomography, as we know it today, was first developed by Zhang et al. [1998]. The modelling of reflected phases caused by impedance contrasts related to geological discontinuities, such as the top of the basement, plate-boundary faults or the Moho, permits the recovery of their geometry. A fundamental advantage of the combination of both types of phases, besides the greater number of available data and the consequent enhancement of ray coverage, is the reduction of the ambiguity, inherent to reflection data, between a reflector's depth and the velocity distribution above it [e.g. McCaughey & Singh, 1997]. The proven usefulness in the study of the lithosphere at different scales of travel-time tomography modelling of refraction and wide-angle reflection data has motivated the development of numerous codes within the academic world. However, the number of 3-D codes for travel-time tomography is rather small [e.g. Kissling, 1988; Toomey & Foulger, 1989; Zelt & Barton, 1998; Koulakov, 2009], and among them only a few perform joint refraction and reflection travel-time tomography of wide-angle seismic data [Van Avendonk et al., 2001b; Hobro et al., 2003; Dunn et al., 2005; Rawlinson & Urvoy, 2006]. Van Avendonk et al.'s [2001b] is the most similar code to TOMO3D, but it doesn't allow for the systematic investigation of the velocity–depth ambiguity intrinsic to reflection data. Hobro et al.'s [2003] is not parallelised and uses an out-dated ray-tracing technique making it computationally expensive to the point of impracticality. Dunn et al.'s [2005] ray-tracing method is typically less accurate for the same computational time or slower for the same target accuracy. Rawlinson & Urvoy's [2006] uses an inversion solver that is best suited for problems with a small- to moderate-sized models, whereas wide-angle seismic data modelling typically requires large numbers of parameters.

Historically, the main alternative to travel-time tomography has been forward modelling, i.e. the manual or semi-automated update of a velocity model in a trial-and-error process, e.g. the widely used RAYINVR by Zelt & Smith [1992] (Fig. 1.4a). In addition to the time-consuming nature of

this task, the intrinsic non-uniqueness associated with non-linear problems, such as travel-time tomography, implies that the determination of a reliable model by forward modelling is virtually impossible [Zelt, 1999]. In other words, forward modelling is prone to over- or underfitting the data, and can lead to geological misinterpretations due to excess or lack of structure. Moreover, the formal assessment of the uncertainty of the resulting models is only feasible with inverse methods because they update the model automatically. Thus, this method is becoming less popular as a tool for geologically meaningful interpretations, and even less so as it does not allow for the evaluation of uncertainty. Still, it can be a useful tool in the preparation of initial models for travel-time tomography, similarly to the use of travel-time tomography as a means of generating initial models for full waveform tomography [Pratt et al., 2002; Virieux & Operto, 2009; Takam Takougang & Calvert, 2013; Dagnino et al., 2014] (Fig. 1.4b,c). Full waveform tomography maximises the use of data by trying to fit the entire seismic traces instead of just some arrival times (Fig. 1.2). In doing so this method can produce more detailed models of the subsurface physical properties. However, the improvement in model accuracy comes at the expense of much greater computational time, to the point that it forbids the performance of uncertainty analyses analogous to those used in travel-time tomography. Despite some satisfactory results, full waveform tomography is a complex, still developing method with a highly non-linear nature, which makes it strongly dependent on the initial models and frequency content of the data. In addition, it requires extremely dense and expensive data acquisition configurations that are currently only available to industry. On the contrary, travel-time tomography uses only a small portion of the information in seismic recordings, but it is a robust and well-established method that can work with the sparse data acquisitions commonly used in academic exploration projects. Travel-time tomography has multiple applications in the investigation of the Earth's interior. It has been applied to studies at a broad range of scales as well as to different data acquisition configurations and exploration methods such as refraction and wide-angle reflection, multichannel reflection, VSP, and passive seismic experiments. Apart from building initial velocity models for full waveform tomography and depth imaging, typically from near-vertical reflection data but also from wide-angle data, the contribution of travel-time tomography within the industry is also particularly relevant in the field of near-surface geophysics mainly through high-resolution surveys to derive velocity models used, for example, for reservoir monitoring or cavity and fracture detection. Such shallow-depth models are also helpful in correcting field statics produced by the weathered layer in normal-incidence land data. Joint refraction and reflection travel-time tomography, as performed with TOMO3D, is especially valuable in this regard as it allows recovering not only the velocity structure of the shallow subsurface but also the geometry of the basal reflector, thus delimiting the weathered layer.

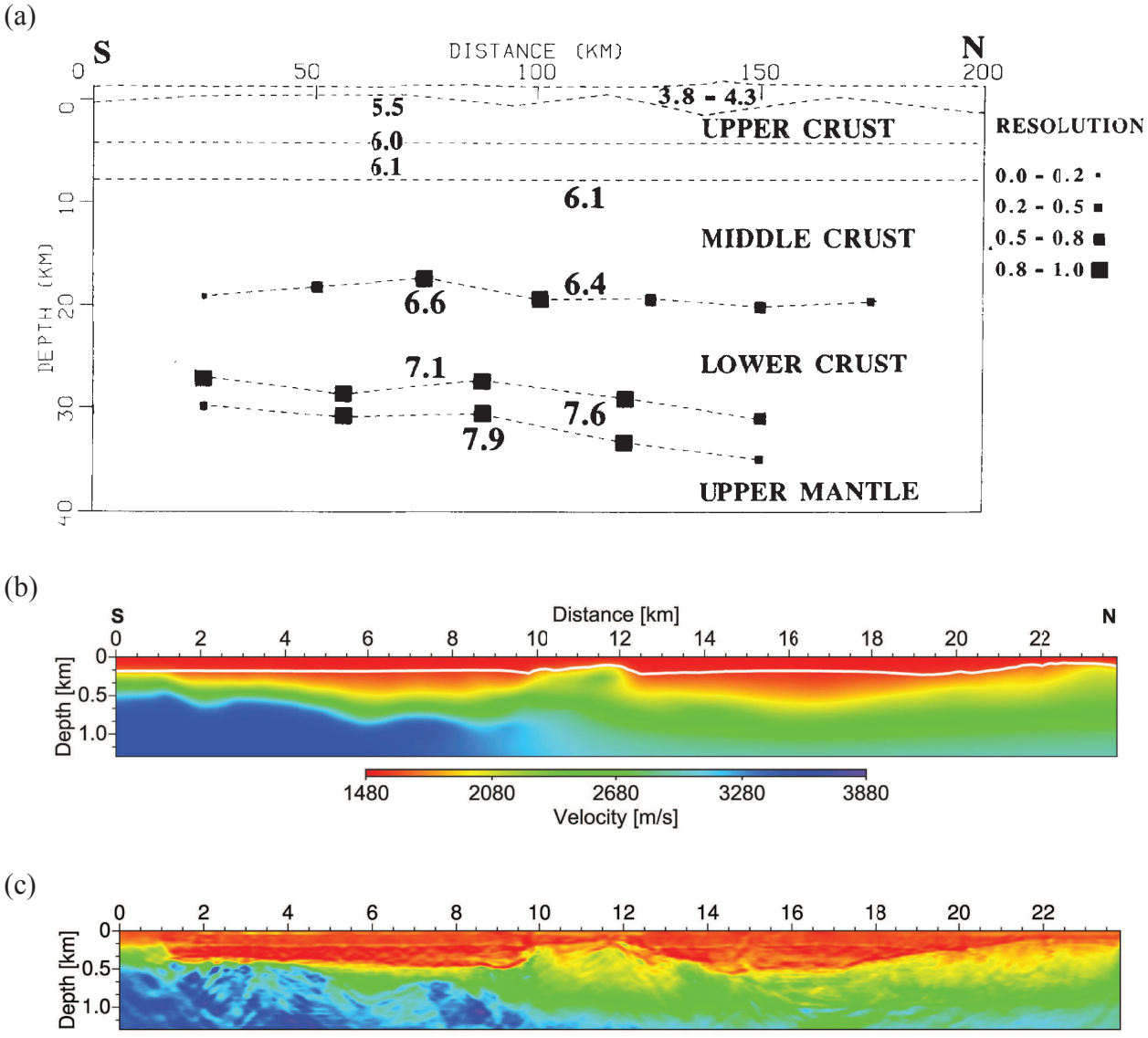

Figure 1.4. (a) Final 2-D velocity model obtained through travel-time forward modelling in Zelt & Smith [1992]. The information provided is scarce due to the limitations of the method. (b) Initial 2-D velocity model derived by travel-time tomography of first arrivals and used for full waveform inversion in Takam Takougang & Calvert [2013]. (c) Final 2-D velocity model obtained by full waveform inversion in Takam Takougang & Calvert [2013]. This detailed result is achieved thanks to the extensive use of data and a highly demanding computational performance.

The basic principle behind this technique is the ray theory, which is the high-frequency approximation of seismic wave propagation [Červený, 2001]. The travel times of wave arrivals are picked from seismic records to be used as data. Ray paths simulating the propagation of the wavefront are traced within an initial approximate model of the subsufrace. For these paths, synthetic travel times are computed and compared to their corresponding travel time data. In this

way, the subsurface model can be successively modified to gradually improve the fit between real and synthetic travel times. Thus, the fundamental elements of any travel-time tomography codes are ray tracing and synthetic travel-time calculation, and the inversion method. A basic workflow scheme of travel-time tomography is shown in Fig. 1.5.

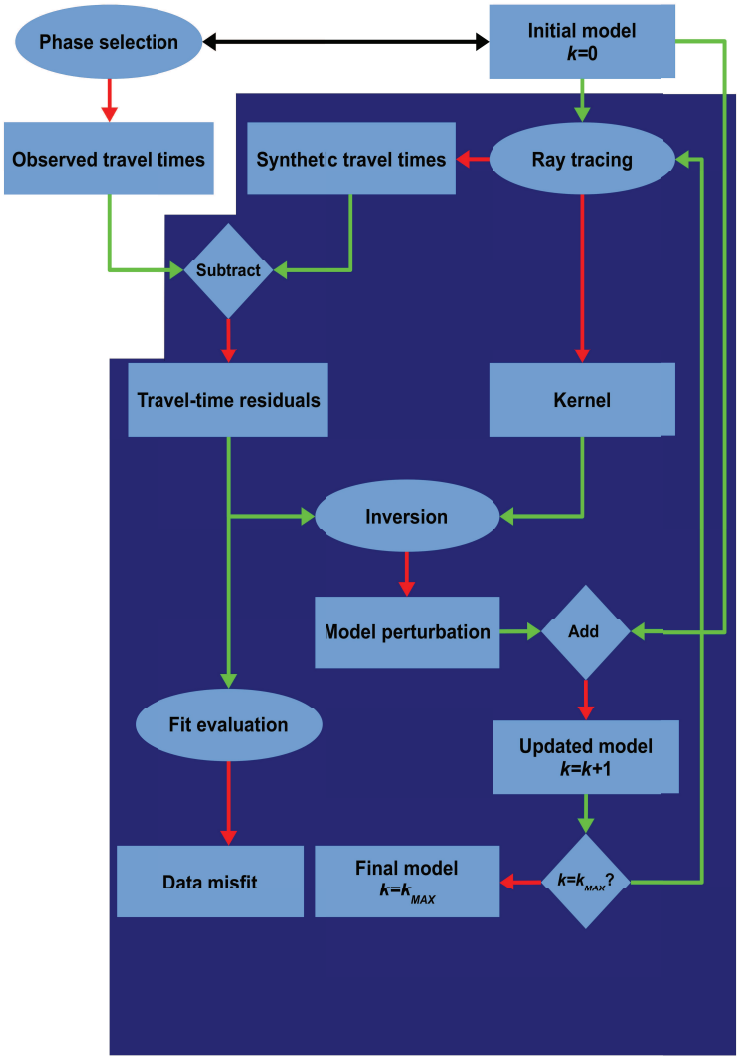

Figure 1.5. Workflow scheme for travel-time tomography with TOMO2D/3D. Rhombic and elliptical boxes represent simple and complex operations. All operations in the dark blue box are automatically performed by the code. Input and output files as well as intermediate results are represented by rectangular boxes. Arrows indicate input (green) and output (red). The relevant seismic phases for the area of interest are selected, and observed travel times are input to code. An initial model is created with as much trustworthy information as possible, which is typically limited. The black arrow expresses the link between modelled area and selected phases. Rays are traced, the associated synthetic travel times are calculated, and the kernel is built representing the relation between data and model parameters. Travel-time residuals are computed as the difference between observed and synthetic travel times. These residuals are turned into parameter perturbations through the kernels' inversion. This process is repeated for k_{MAX} iterations, and at each iteration data-misfit information is provided.

The main differences between travel-time tomography codes are found in their ray tracing algorithms. TOMO3D combines the graph method [Moser, 1991; Cheng & House, 1996] with the bending refinement method [Moser et al., 1992a] in the calculation of ray paths and synthetic travel

times [Korenaga et al., 2000; Van Avendonk et al., 2001a]. This hybrid method overcomes the major drawbacks of the two traditional ray tracing methods: shooting and bending [Julian & Gubbins, 1977]. The first ones solve the ray differential equations derived for the ray approximation. For each source–receiver pair a fan of rays is shot from the source to find the one that arrives at the receiver. These methods have convergence problems particularly in complex media and/or in 3D. Besides, ray equations cannot explain diffracted ray paths nor paths through shadow zones. The second type of methods modify a guessed reference curve to arrive at the actual ray path either iteratively fitting ray tracing equations or iteratively minimising travel time along the ray path. Because of their dependency on the initial guess, these methods also have convergence issues that grow with the complexity of the velocity structures, even more in 3D. Thus a good initial guess, such as the one provided by the graph method, is crucial to avoid local travel-time minima and converge to the global minimum. Modern ray tracing is dominated by wavefront marching methods. Two main families exist: graph solvers [Moser, 1991; Korenaga et al., 2000; Van Avendonk et al., 2001a; Bai et al, 2007] and finite-differences eikonal equation solvers [Vidale, 1988; Kim, 2002; Rawlinson & Sambridge, 2004]. The former find minimum travel time ray paths as a series of node connections following Fermat's principle, whereas the latter propagate wavefronts away from sources following the eikonal equation, and then use them to trace back rays. The graph scheme is more flexible in terms of model parameterisation. Irregular grids are straightforward to implement and geological relief is honoured. For a specific parameterisation, accuracy and efficiency are directly controlled by a simple definition of the node connections that are permitted. Moreover, it guarantees that ray paths correspond to a global travel time minimum within the chosen parameterisation. Its combination with the bending method improves accuracy with a minor loss in efficiency. In an analogy with eikonal equation solvers, ray bending would correspond to the back-tracing of rays perpendicularly to the wavefronts.

There are also several approaches to the iterative solution of the non-linear inversion problem in travel-time tomography. Two popular techniques in recent literature are the regularised inversion using gradient methods, and the backprojection of travel-time residuals (for a detailed review see Rawlinson & Sambridge [2003]). The first formulate the inversion as an optimisation problem that seeks to minimise data misfit together with some constraints in the form of penalty functions on the roughness and size of the model perturbations using a variety of classic gradient methods [e.g. Lutter & Nowack, 1990; Sambridge, 1990]. The second distributes the travel-time residual among the parameters affected by the ray path proportionally to the length of their corresponding ray path segment [e.g. Hole, 1992; Zelt & Barton, 1998]. Between the two, the former are more popular,

despite being computationally more expensive, because their convergence behaviour is faster and more stable. Another alternative are global optimisation methods such as genetic algorithms [e.g. Goldberg, 1989; Whitley, 1994] and simulated annealing [e.g. Kirkpatrick et al., 1983; Ammon & Vidale, 1993] which can find global minimum solutions even for very distant initial models but are currently rather infrequent due to their much larger computational cost for the typical number of model parameters. Another option is automatic differentation [Sambridge et al., 2007] which calculates the derivative information by applying the chain rule to the sequence of elementary mathematical assignments and operations in the code. However, this approach is not recommended if code optimisation and parallelisation are necessary [Lelièvre et al., 2011]. The gradient of the objective function can be obtained using the adjoint-state method [Sei & Symes, 1994; Leung & Qian, 2006] and then used in the minimisation by a classic gradient method. Although the computational cost is also higher because of the three propagations required, this procedure supports efficient parallelisation if an adequate forward problem solver is selected.

1.3. Specific objectives

Based on the general objectives outlined in the motivation section, the specific goals of this work can be summarised in the following bullet-point list:

1) Application of a state-of-the-art travel-time tomography code (TOMO2D) to 2-D wide-angle data collected at the convergent margin of Nicaragua in the area of a 1992 tsunami earthquake.
   1.1) Familiarisation with the interpretation of phase arrivals in wide-angle record sections and with travel-time tomography modelling process, and in particular with the usage of TOMO2D and its internal functioning.
   1.2) Determination of the structure and properties of the overriding plate and the interplate boundary at the seismogenic zone along two perpendicular wide-angle seismic profiles.
   1.3) Extraction of any existing relations of the said properties and structural features with earthquake and tsunami measurements for the better understanding of the nature, nucleation and rupture propagation of the 1992 tsunami earthquake.
   1.4) Exploration of the necessity for a new 3-D travel-time tomography tool based on the 3-D distributions of seismogenic properties that highlight the shortcomings of 2-D

modelling.

2) Further the use of information in wide-angle seismic data with the modelling of seismic phases other than first arrivals and reflections.
   2.1) Explanation of an apparent paradox related to the water-layer multiple of refracted and reflected primary phases in wide-angle seismic record sections.
   2.2) Incorporation of the water-layer multiple phases within the modelling scheme of the new travel-time tomography tool.

3) Development of a new modelling tool (TOMO3D) for 3-D seismic data that overcomes the aforementioned technical and scientific issues. To do this, I have decided to base the tool on TOMO2D. This new 3-D tool should fulfil the following requirements:
   3.1) Modelling the 3-D velocity structure of the overriding and subducting plates and the interface geometry of the megathrust fault at subduction zones.
   3.2) Use different seismic phases other than first arrivals, including reflected phases, in order to define the location and geometry of the interplate boundary or any other geological discontinuities of interest, and also water-layer multiples as mentioned in 2.2.
   3.3) Run in parallel in order to take advantage of the currently available computer facilities, and ensuring that the 3-D inversions are performed in a reasonable amount of time despite the increased number of parameters and data.

4) Application of TOMO3D to a 3-D synthetic case inspired in the geological context of a subduction zone at an ocean–continent convergent margin to demonstrate the modelling procedure.
   4.1) Assessment of the correct functioning of the program, discarding the existence of major programming errors or missing capabilities in the code.
   4.2) Description of the standard modelling procedure with TOMO3D, paying special attention to the layer-stripping strategy, which permits the sequential extension of models in depth layer by layer, hence including first-order velocity discontinuities in the velocity models.

5) Application of TOMO3D to a 3-D data set acquired at the convergent margin of Ecuador and Colombia to prove its usefulness as a modelling tool.
   5.1) Determination of a 3-D velocity model of the margin, including the overriding and

subducting plates.

5.2) Comparison with an existing 3-D velocity model based on the same data set obtained with a 3-D refraction travel-time tomography code.

CHAPTER 2: APPLICATION OF TOMO2D TO THE STUDY OF THE NICARAGUAN CONVERGENT MARGIN

2. APPLICATION OF TOMO2D TO THE STUDY OF THE NICARAGUAN CONVERGENT MARGIN

As stated in the motivation section, the study of the processes governing earthquake and tsunami generation at subduction zones is one of the main research lines of the group where I have carried out my PhD work. The first part of my PhD work was devoted to the application of TOMO2D to the study of the structure and physical properties of the Pacific convergent margin of Nicaragua (Central America). This is an active margin where a textbook example of tsunami megathrust earthquake took place in 1992. The goal of this work was two-fold. First, to use wide-angle seismic (WAS) data from two perpendicular 2-D profiles to define the structure and physical properties of the overriding plate, and the geometry of the interplate boundary containing the seismogenic zone. Second, to compare the results obtained from these 2-D profiles with independent seismological and tsunami observations and models, in order to investigate the possible existence of potential correlations between the elastic parameters derived from seismic data and the seismological observables (e.g. slip, rupture propagation velocity, and moment release), and analyse the 3-D variations of these properties in order to evaluate the actual need for 3-D inversions. Additionally, the overarching technical goal was to get acquainted with the procedure of travel-time tomography modelling, from phase picking in seismic records to the evaluation of the reliability of the final model, as well as to learn the specific use and internal functioning of TOMO2D in order to understand its advantages and drawbacks with respect to other existing software for possible future developments.

TOMO2D was used to derive 2-D seismic velocity models of the overriding plate and the interplate boundary of the Nicaraguan margin along two wide-angle seismic profiles parallel (NIC-125) and perpendicular (NIC-20) to the trench, acquired in the rupture area of the 1992 tsunami earthquake. In combination with coincident multichannel seismic (MCS) reflection images, these results provided relevant information on the structure of the overriding and subducting plates and of the interplate boundary, as well as on the nature and characteristics of this seismic event. At the same time, this application also highlighted the shortcomings of 2-D studies pointing at the necessity for 3-D surveys. This work was published in G-cubed [Sallarès et al., 2013]. I am second author of this paper, in which I carried out the technical part of the work, including WAS data processing and modelling along the two profiles, and the parameter uncertainty analysis. I also participated in the combination with other geophysical data and in the interpretation of the results.

2.1. Tectonic setting: Nicaraguan margin

At the Nicaraguan convergent margin the oceanic Cocos plate subducts under the Central America portion of the overriding Caribbean plate (Fig. 2.1). The convergence rate is 91 mm/yr [DeMets et al., 1994], and the oceanic plate subducting at the trench is ~25 My old [Barckhausen et al., 2001]. Normal faults created at the spreading axis are reactivated trenchward from the outer rise due to plate bending producing half grabens that may expose basement with escarpments of 100 to 500 m vertical offset [Ranero et al., 2003]. Based on a single MCS profile (NIC-1) acquired by the University of Texas, the margin was first interpreted to have a well-developed accretionary prism [Crowe & Buffler, 1985]. However, reprocessing of NIC-1 along with industry seismic data and drill holes at the Sandino basin, and a coincident WAS profile collected during Sonne cruise 107, proved the absence of a large accretionary prism and the resemblance of the basement to those of the limiting Guatemalan and Costa Rican margins. Furthermore, the interplate geometry was imaged down to the mantle wedge in Walther et al. [2000]. These data were also used to define the history of margin development and to propose that the Nicaraguan margin has been affected by long-term tectonic erosion [Ranero et al., 2000].

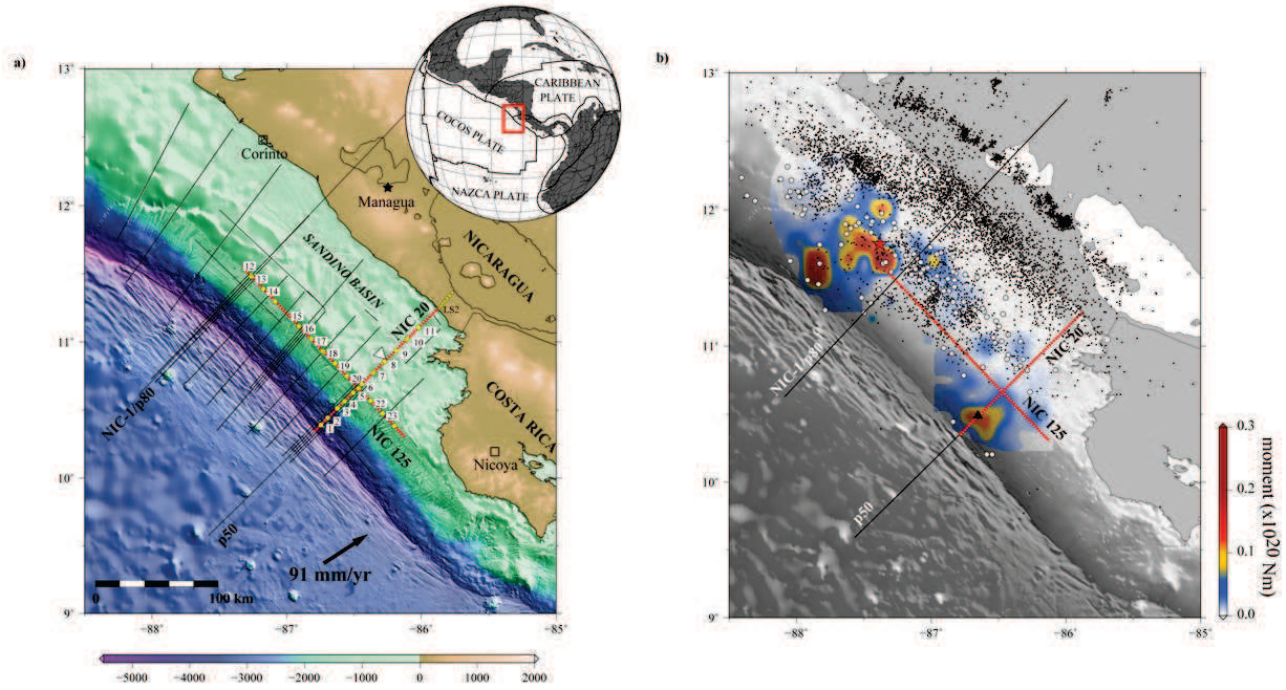

Figure 2.1. (a) Relief map of the study area off- and on-shore Nicaragua. Black lines show location of seismic profiles (MCS and WAS) acquired during R/V Maurice Ewing cruise EW00-05 in 2000. Red thick lines labelled NIC-20 and NIC-125 correspond to the WAS and MCS profiles discussed in this paper. Yellow circles and yellow triangles display OBHs and land stations deployed along these two profiles, respectively. Thick arrow correspond to the plate motion vector estimated using poles of Nuvel-1A [DeMets et al., 1994]. Inset: Regional tectonic map with tectonic plates and their boundaries. The red box encompasses the study area. Profile p50 marks the seaward extension of profile NIC-20 collected in a different cruise and presented by Ivandic et al. [2008], and p80 indicates the location of the WAS profile modelled by Walther et al. [2000], and MCS transect in Ranero et al. [2000]. (b) Shaded bathymetry map of the study region overlaid by the map of inverted moment release of the 2 September 1992, tsunami earthquake that encompasses the source region [Ihmlé, 1996b]. Red star marks the epicentral location of the 1992 event, whereas white circles correspond to aftershocks within 3 months after the main shock [Ihmlé, 1996a]. Black dots are earthquakes recorded by the Nicaraguan seismic network onshore between 1975 and 1982. Solid lines correspond to the WAS profiles in Fig. 2.1a. Black triangle indicates location of a subducted seamount imaged in MCS profiles.

2.2. Geological background: seismogenic zone and tsunami earthquakes

Subduction zones concentrate most of the world's largest earthquakes, that typically occur on the megathrust fault along the plates' interface, and much of the overall seismic activity. These seismic events take place along the interplate boundary between the underthrusting and overriding plates, in the so-called seismogenic zone [Hyndman & Wang, 1993; Hyndman et al., 1997]. The extension of the seismogenic zone is constrained by frictional variations at the contact between overriding and subducting plates. Its limits are linked to transitions from stable or aseismic to unstable or seismogenic behaviour [e.g. Marone & Saffer, 2007]. This behaviour is thought to be determined by the thermal structure [Tichelaar & Ruff, 1993; Oleskevich et al., 1999] and the local stress field [Scholz, 1998], which in turn depend on various factors including, but not limited to, the age of the subducting slab, the convergence rate, relief of the incoming plate, and the composition, structure and elastic properties of both plates [e.g., Ruff & Kanamori, 1980; Pacheco et al., 1993; Scholz & Campos, 1995]. The up-dip limit is ascribed to variations in the physical properties and in the fluid abundance at the plate interface [e.g. Moore & Vrolijk, 1992; Moore & Saffer, 2001; von Huene et al., 2004; Bangs et al., 2004; Ranero et al., 2008]. The down-dip limit is often located at the intersection of the interplate boundary with the continental Moho, and has been related to the presence of aseismic hydrous minerals of the serpentinite group [e.g. Peacock & Hyndman, 1999; Hyndman & Peacock, 2003]. In this study we assumed that the extension of the seismogenic zone is approximately delimited by the interplate seismic activity recorded in the area (Fig. 2.1b).

The 1992 seismic event offshore Nicaragua is a well documented example of a tsunami earthquake (Fig. 2.1). Tsunami earthquakes are a particular class of seismic events that propagate at abnormally slow velocities and generate anomalously large tsunamis for their surface wave magnitude [Kanamori, 1972]. It has been proposed that for such events the co-seismic rupture should involve unusually shallow and weak segments of the plate interface [e.g. Kanamori, 1972; Okal, 1988; Pelayo & Wiens, 1992; Kanamori & Kikuchi, 1993; Polet & Kanamori, 2000] and local asperities such as subducted seamounts [McIntosh et al., 2007].

2.3. Wide-angle seismic data set

The WAS data used in this experiment is an example of high quality seismic recordings in terms of both amplitude and lateral coherency of the seismic phases. They were recorded in 2000 during a

cruise with US R/V Maurice Ewing (EW00-05) with the purpose of investigating the effects of the structure of the incoming plate on the overriding plate, and their relation to interplate seismogenesis [McIntosh et al., 2007]. NIC-20 is ~160-km-long and was recorded on 11 OBHs and 7 land stations, whereas NIC-125 is ~190-km-long and was collected on 12 OBHs. These profiles cross at 52 km from the trench (Fig. 2.1). The source was an airgun array with a total volume of 136 l. The shot interval was 60 s, which resulted in a shot spacing of ~125 m. The data processing included a frequency filter (3-13 Hz), a statistical predictive deconvolution, and an automatic gain correction [Berhorst, 2006].

The data are commonly displayed in record sections, one for each receiver, in which seismic traces are plotted against source–receiver offset and/or distance along profile. The maximum distance at which the seismic signal is detected results from a combination of different factors, including the source energy, the amplitude decay by geometrical spreading and attenuation, the transfer function and seafloor coupling of the receiver, and the ambient noise level. Sample record sections for profiles NIC-20 and NIC-125 are displayed in Figs 2.2 and 2.3, respectively. The local slope of refracted phases in record sections is known as apparent velocity and it is a good approximation of their average propagation velocity in the medium. To facilitate phase picking, travel time for each trace is reduced depending on the source–receiver offset (X in Figs 2.2 and 2.3). The velocity value that divides X to compute the travel-time shift is known as reduction velocity, and in this case it was set to 6 km/s. This correction separates seismic phases in record sections depending on their respective apparent velocities; a seismic phase with apparent velocity similar to the reduction velocity will appear as approximately horizontal. Without this shift phases accumulate close to each other with steep slopes, which makes phase identification and picking virtually impossible. The selection of this value is empirical and based on the clarity of phases in the resulting record sections. This transformation in time is undone when creating the data set input file.

The observed refracted phases correspond to waves travelling through the continental sediments (P_s), and through the crust and upper mantle of the continental (P_g and P_n) and oceanic (P_{sc} and P_{mw}) plates. Reflected phases are associated to the interplate boundary (P_iP), and to the continental ($P_{mw}P$) and oceanic (P_mP) Moho boundaries. In Sallarès et al [2013] we concentrated on the structure of the continental basement and the geometry of the interplate boundary. Therefore, from the aforementioned phases only P_s, P_g, P_iP, $P_{mw}P$, and P_{mw} were used. The last two were interpreted as a refraction within the upper plate mantle wedge (P_{mw}) and a reflection at the Moho above the mantle wedge ($P_{mw}P$) because their travel times are smaller than those of the P_iP phases and the

apparent velocity of P_{mw} is greater than 7.5 km/s. As noted in previous works [e.g. Sallarès & Ranero, 2005; Lefeldt et al., 2010], typical 2-D acquisition configurations do not allow for the proper inversion of the velocity distribution of the underthrusting plate due to the limited azimuthal coverage provided by seismic phases crossing the interplate boundary. A poorly constrained incoming plate can deteriorate the velocity recovery for the overriding plate. In our case, such negative effects were confirmed by inversion tests made with and without these data.

In profile NIC-20, the P_g phase is observed in all OBHs, with offsets between <10 km for the one closest to the trench to ~70 km for the one at the upper slope (Fig. 2.2a-d), as well as at the land stations (Fig. 2.2e). P_g apparent velocities range from ~2 km/s at the seafloor to ~4 km/s at the base of the overriding plate under the lower slope, and ~2 km/s at the top and ~6 km/s at the base under the upper slope. The P_iP phase is asymptotic to the P_g phase and it is identified in all OBHs, except for OBH 6. The arrival times of P_iP increase progressively with receiver distance from the trench (Fig. 2.2a,b) as a consequence of the dip of the interplate boundary. Reflected phases P_iP and P_mP are easily distinguished in the record sections of OBHs deployed between mid slope and trench (e.g. Fig. 2.2a,b). However, for the rest of OBHs telling them apart is more complicated, in particular in the landward part of the record sections where the slab is deeper and the apparent velocity is higher. This results in P_iP and P_mP phases appearing very close to each other in record sections because the slab thickness is much smaller than the continental plate on top of it, so that the difference in travel time between both reflected phases is quite small in comparison to the total travel time. In such cases, in order to guide the identification of these phases, we searched for source–receiver pairs that are exchangeable according to the reciprocity principle, and corrected their travel times to compensate for the difference in water depth at the receiver locations. The comparison of the corrected travel times indicates whether or not both picks correspond to the same phase registered at different receivers.

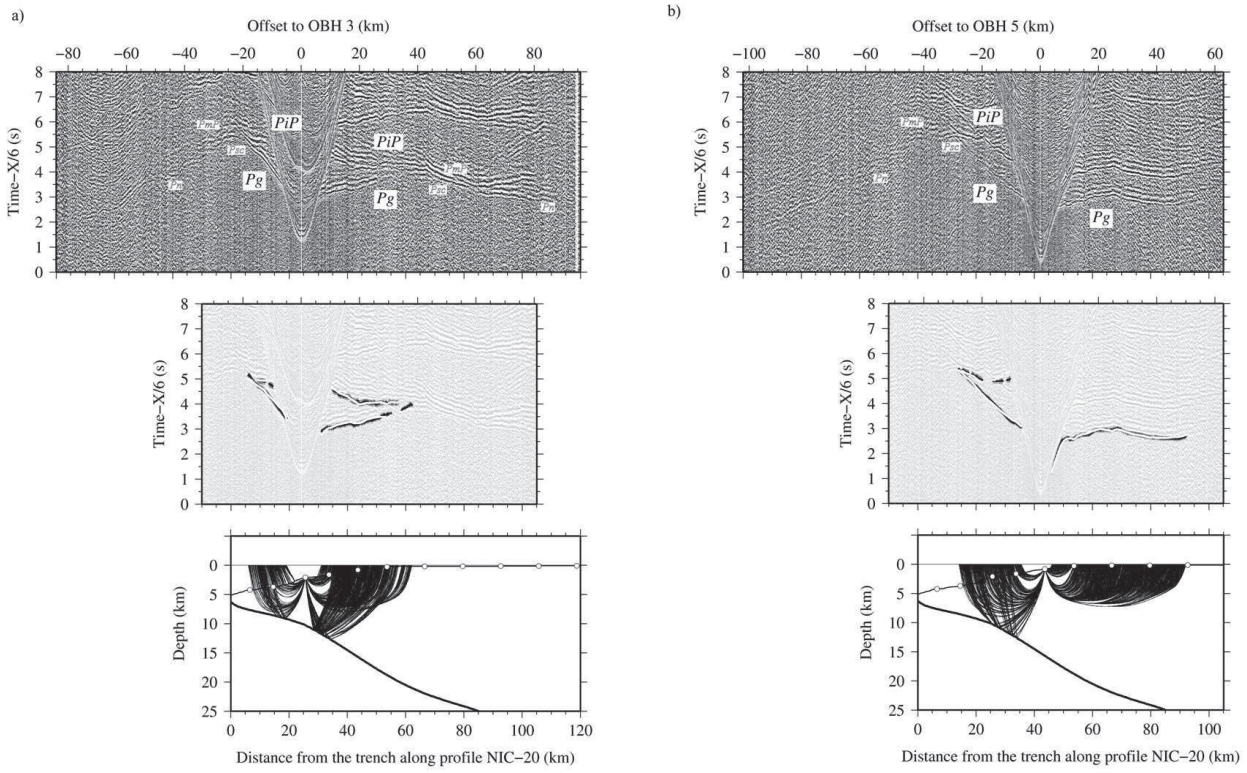

Figure 2.2. From top to bottom, record sections, travel-time fitting and ray paths corresponding to OBHs number 3 (a), 5 (b), 7 (c), and 9 (d), as well as landstation number 2 (e), along WAS profile NIC-20 (Fig. 2.1). The seismic phases of interest are the refraction through the sediments and the overriding plate crust (P_g), the reflection at the interplate boundary (P_iP), in the case of the OBH, and the reflection at the base of the crust under the Sandino basin ($P_{mw}P$) and the refraction within the top of the upper plate mantle wedge (P_{mw}), together with P_g, in the landstation. In addition, seismic phases refracted through the subducting crust (P_{sc}) and uppermost mantle (P_n), and reflected at the base of the subducting crust (P_mP) are also shown in the OBH record sections, though not included in the inverted data set. In the ray-path plots, the thick black lines show the inverted interplate and upper-plate Moho reflectors, and white circles display receiver locations.

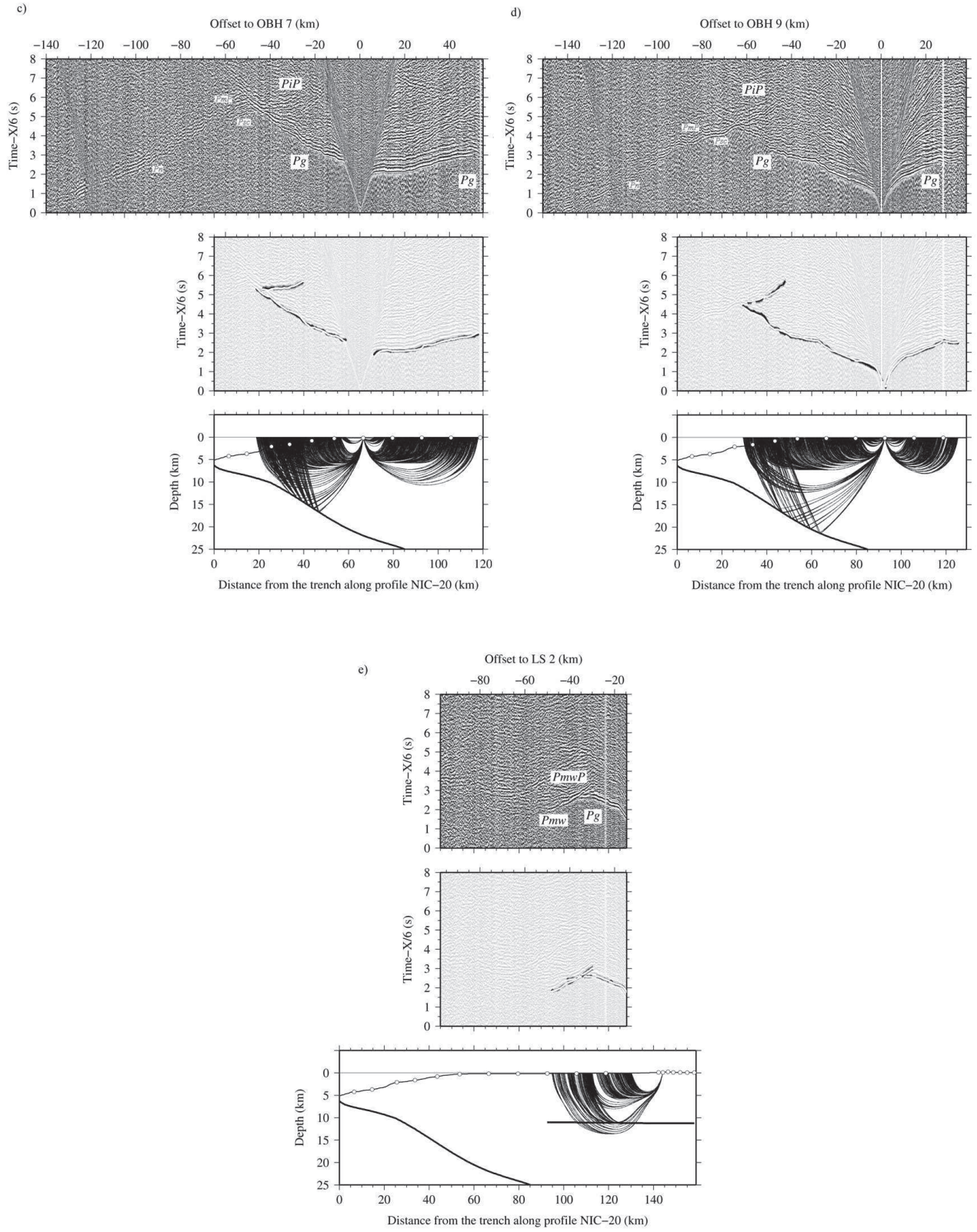

Figure 2.2. (Continued).

Record sections from NIC-125 all include very similar P_s, P_g, P_sP and P_iP phases, but none travelling deeper than the interplate boundary. P_s and P_g phases are observed to offsets of 70-80 km (Fig. 2.3). Apparent velocities for those phases are similar in all record sections, ranging from ~2 km/s at the seafloor to ~6 km/s at the bottom. Contrary to NIC-20, the travel times of P_iP do not show significant variations, suggesting that the depth of the interplate boundary does not change significantly in the trench-parallel direction (Fig. 2.3). It is worth noting the existence of a shadow zone between the P_g and P_iP phases that is particularly evident for the two record sections in Fig. 2.3. This phenomenon is typically associated to either a low velocity zone or a zone with low vertical velocity gradient, just above the plate interface [e.g. Sallarès & Ranero, 2005].

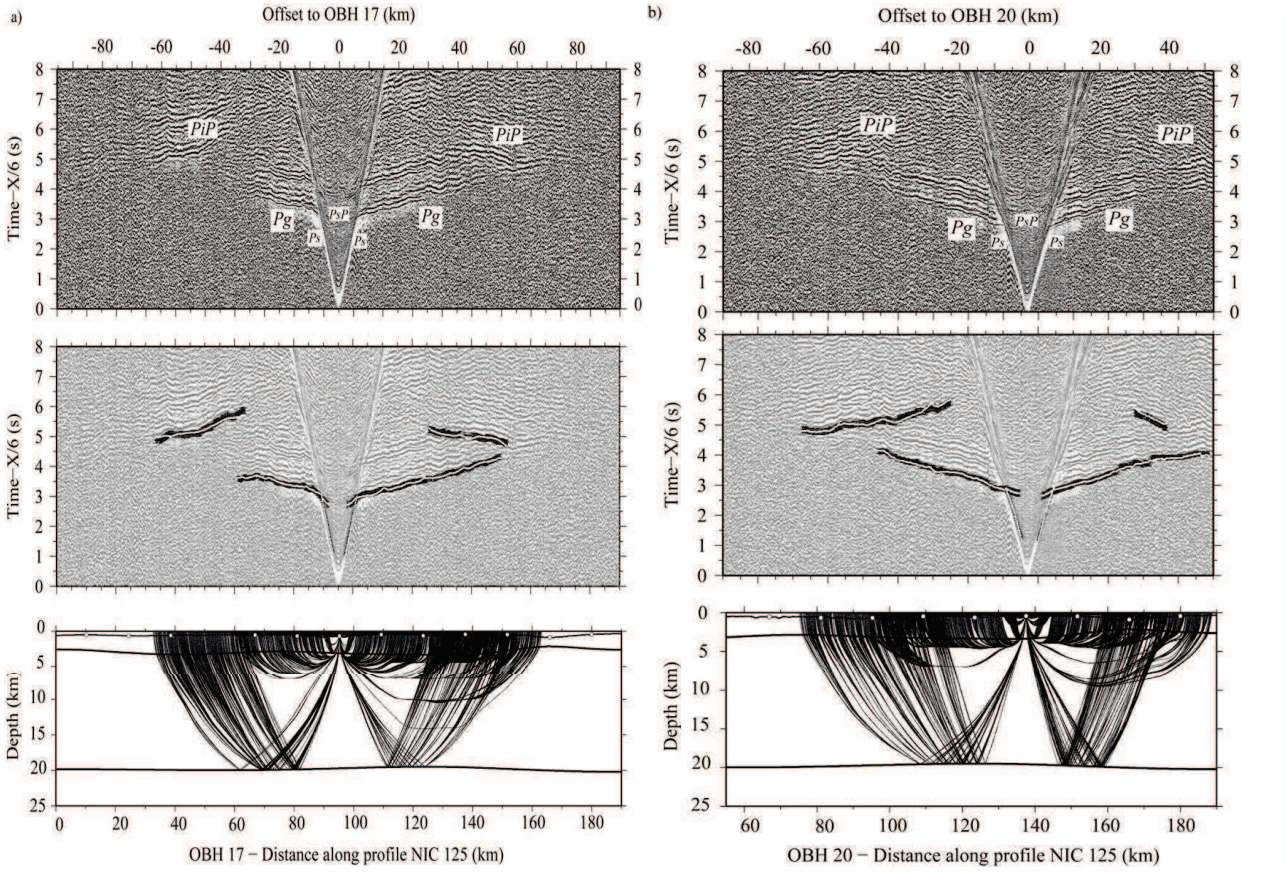

Figure 2.3. From top to bottom, record sections, data fitting and ray paths corresponding to OBHs number 17 (a) and 20 (b) along WAS profile NIC-125 (Fig. 2.1). The seismic phases of interest are the refraction through sediment (Ps) and overriding plate crust (P_g), and the reflections at the sediment-basement (PsP) and interplate (P_iP) boundaries. From top to bottom in the ray-path plots, the thick black lines show the inverted sediment-basement and interplate reflectors, white circles display receiver locations.

The travel-time data set was built by manually picking the arrival times of the different seismic phases. Each travel-time pick is associated to a location along the acquisition profile. The final data set for NIC-20 includes 7007 refraction picks (P_g and P_{mw}), and 1335 reflection picks (P_iP and $P_{mw}P$). For NIC-125, the data set is counts 6540 refraction picks (P_s and P_g), and 3748 reflection picks (P_sP and P_iP). Picking errors are chosen to be of the order of magnitude of the dominant period in WAS records (~10 Hz). The exact value is assigned depending mainly on the lateral coherency of each phase. In this case, for instance, we selected 50 ms for refractions and 75 ms for reflections.

2.4. Modelling strategy

2.4.1. Travel-time tomography and layer stripping

The 2-D models of seismic velocity distribution and reflector geometry were obtained by joint refraction and reflection travel-time tomographic inversion of the data picked along the two WAS profiles (Fig. 2.4). The inversions were performed with TOMO2D, which allowed me to familiarise myself with all the aspects of this modelling procedure before starting the development of TOMO3D. Both codes share the basic concepts and structure for the main parts of the code, which are the forward and inverse problems solving methods. The velocity models consist of a sheared mesh with variable spacing hanging from the seafloor or the land surface. The position of the floating reflector is parameterised by an independent array of nodes with the vertical degree of freedom. The forward problem is solved using a hybrid method combining the graph method [e.g. Toomey et al., 1994] and the bending method [Papazachos & Nolet, 1997; van Avendonk et al., 1998]. From the solution of the forward problem, the Fréchet derivative matrix is constructed to define a linear relation between travel-time residuals and parameter perturbations. The inversion is performed by iteratively minimising the linearised forward problem using the LSQR algorithm [Paige & Saunders, 1982]. To avoid inversion instabilities regularisation constraints are incorporated. These constraints are applied on velocity and depth parameters, and are formulated as smoothing matrices defined by correlation lengths, and as damping matrices that limit the average perturbation at each iteration. All these, together with other additional functioning details, is extensively described for the 3-D version in chapter 4 of this manuscript.

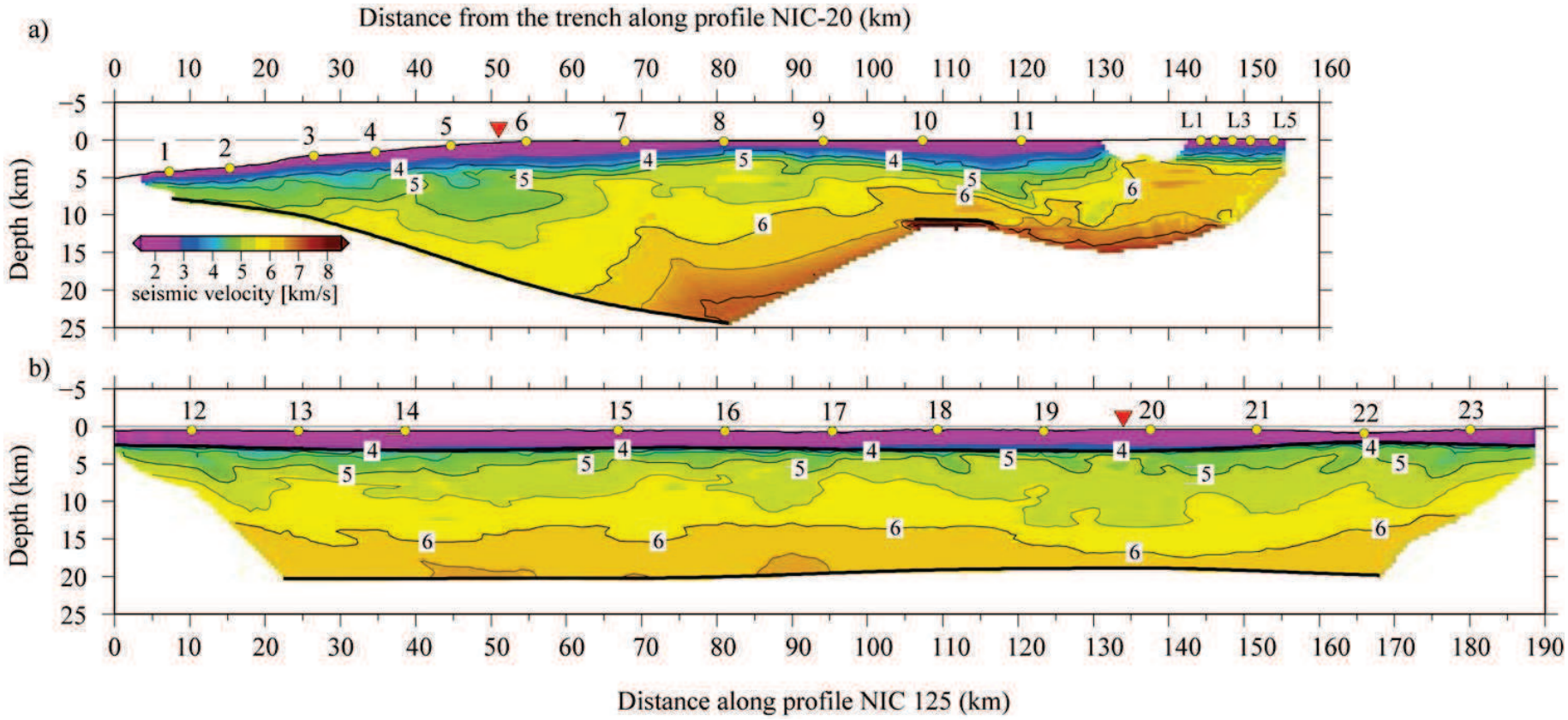

Figure 2.4. (a) P-wave velocity model of the overriding plate and geometry of the interplate boundary reflector along WAS profile NIC-20 (see Fig. 2.1 for location). The model has been obtained by joint reflection and refraction travel-time inversion using the TOMO2D code. interplate and upper plate Moho reflectors are represented by thick black lines. Yellow circles on the seafloor mark the positions of the OBH and land stations and the red triangle indicates the intersection with profile NIC-125. Iso-velocity contours in the sediments are not shown for clarity. (b) Same as (a) but for the WAS profile NIC-125 (Fig. 2.1). interplate and sediment-basement reflectors are represented by thick black lines.

One of the fundamental characteristics of our inversion strategy is dealing with a single reflecting interface per inversion. Whenever there are two or more observable seismic boundaries in a study area, they are successively modelled following a top-to-bottom layer-stripping strategy [e.g. Sallarès et al., 2011]. Layers are defined as portions of model limited by two consecutive reflectors. The seismic phases used in each inversion are the reflection from the base of the layer and all phases refracted in the newly added layer and/or in any of the previous layers. In this manner, the model is progressively extended downwards layer after layer. The main advantages of this procedure is that it reduces the trade-off between velocity and depth, and it keeps abrupt velocity contrasts between layers in successive inversions, so that resulting models are more appropriate for geological interpretation. This strategy is described and illustrated in detail in subsection 5.1.3.

Initial velocity models for the sediments and basement of the overriding plate, and depth models for the geometry of the interplate boundary were created by forward modelling of the travel times using the RAYINVR code [Zelt & Smith, 1992]. In the case of NIC-20, for the velocity model, horizontal spacing is 0.5 km, whereas the vertical one increases with depth from 0.05 km to 0.5 km. Depth nodes are 0.5-km spaced. Correlation lengths for velocity nodes increase linearly from 2 km at the top of the model to 7 km at the bottom in the horizontal direction, and from 0.6 km to 6 km in the vertical one. In the case of depth nodes, correlation length was set to 7 km. Different average perturbation limits for damping constraints were tested finally choosing 10% for both velocity and depth parameters. In NIC-125, horizontal spacing for velocity nodes is 0.5 km, and vertical spacing grows from 0.1 km to 0.5 km. Interface nodes are 0.5-km spaced. Velocity correlation lengths increase linearly with depth from 1 km to 4 km for the horizontal direction, and from 0.5 km to 2.5 km for the vertical one. Depth correlation length is 4 km. The average perturbation limits are set to 5% and 15% for velocity and depth damping respectively. The first inversion step for the velocity model of NIC-20 includes the continental crust and sediments, from the seafloor to the interplate boundary under the lower and middle slopes, and from the seafloor to the Moho under the upper slope and shelf. Therefore we used the P_s, P_g and $P_iP/P_{mw}P$ phases. In the second step, the resulting model was inserted into an extended model including the mantle wedge below the upper slope, so we added the P_{mw} phases to the data set. The inversion parameters and velocity grid spacing were the same as in the previous step, and the interplate reflector from the first step was used as starting reflector. Sedimentary reflections are clearer in NIC-125, so the first inversion step was restricted to the sedimentary layer (P_s and P_sP phases), and the second one extended the model to the basement (P_s, P_g, and P_iP phases).

2.4.2. Model validation: Data fit, ray coverage and uncertainty analysis

Unlike the methodological details of TOMO2D and TOMO3D (chapter 4) or the layer-stripping strategy, which can be detailed using a synthetic example (subsection 5.1.3), the validation of the final velocity and depth models is better illustrated with a real data example. Indeed the true model is unknown, hence comparison is not an option, and other means of evaluating the reliability of the results are needed. First of all, the final model must minimise the data misfit to a satisfactory degree. Data misfit is usually measured as the root mean square (RMS) of the travel-time residuals

$$RMS = \sqrt{\frac{\sum_{i=1}^{N} \left(t_i^{obs} - t_i^{calc} \right)^2}{N}} \qquad (2.1)$$

In Sallarès et al. [2013] the final RMS for the model along profile NIC-20 is 43 ms for refraction arrivals (P_s, P_g and P_{mw}) and 63 ms for the reflection arrivals (P_iP and $P_{mw}P$), whereas in the case of profile NIC-125, it is 48 ms for refraction arrivals (P_s and P_g) and 66 ms for the P_iP phase. These misfits are acceptable because they are smaller than the presumed picking errors. If they were much smaller though, it would mean that we had overestimated pick errors. This would also show on the average Chi squared (χ^2/N) values, where χ^2 is

$$\chi^2 = \sum_{i=1}^{N} \left(\frac{t_i^{obs} - t_i^{calc}}{\varepsilon_i} \right)^2 \qquad (2.2)$$

and t_i^{obs} is the i-th picked or observed travel time, t_i^{calc} is the corrseponding synthetic or calculated travel time, ε_i is the pick for this pick, and N is the total number of picks. In general, a final $\chi^2/N \sim 1$ indicates a final model that fits the data adequately. If the pick error estimation is correct, then greater and smaller χ^2/N values imply an underfitting and an overfitting of the data, respectively, and a $\chi^2/N \sim 1$ is considered an optimal model. The former case corresponds to a lack of structure in the final model, whereas the latter occurs when it contains unreliable, excessively fine structure. The evolution of RMS and χ^2/N over the successive iterations (Fig. 2.5) illustrates the stability of the inversion process and its convergence. Both curves should be monotonically decreasing. Any other more unstable behaviour in the convergence trend is indicative of an inadequate definition of the inversion strategy; possible causes are found in a poor initial model, erroneous ray-tracing settings or regularisation constraints, or any combination of these.

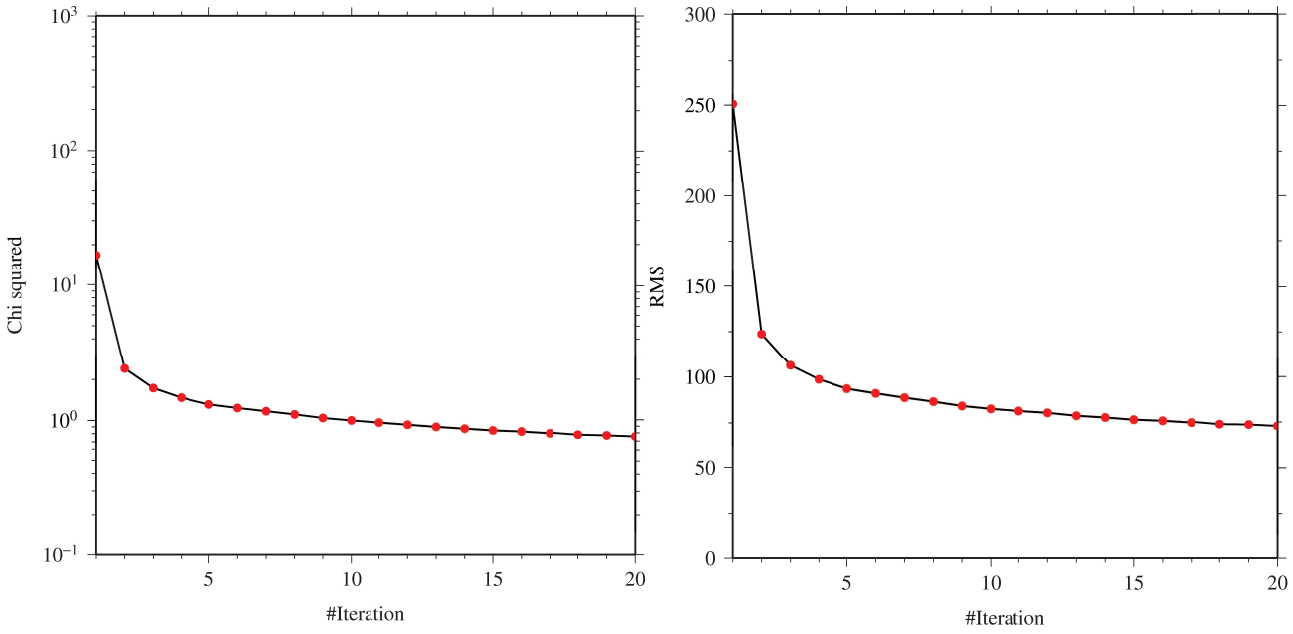

Figure 2.5. Line charts showing the evolution of (left) χ^2/N and (right) RMS throughout the iterative inversion process of data picks from profile NIC-20. Both curves show a satisfactory convergence trend. The main model improvement is achieved in the first 5 iterations. After the 10th iteration χ^2/N ~1. The improvement in successive iterations is limited, and the results can thus be considered final.

The combination of acquisition configuration and study area defines the ray coverage of the model, which is related to the linear sensitivity of the inversion. Thus a measure of the ray coverage can be used to mask the zones that are not resolved in the final model. One way to quantify ray coverage is counting, for each model parameter, the number of rays that it influences, i.e. the number of rays that cross the cells to which each node belongs. This indicates how densely the model is sampled by the recorded data, and is related to the linear sensitivity of the inversion. However, the most usual quantitative measure of ray coverage is the derivative weight sum (DWS) [Toomey & Foulger, 1989]. The DWS for each model parameter is obtained by adding up the corresponding entries in the Fréchet matrix. By construction, the values of these entries are proportional to the distance between the corresponding node and ray-path segment. Hence, the advantage of this quantitative measure of ray density is that it is sensitive to the separation of rays from the nodes. Currently, TOMO2D and TOMO3D output the velocity DWS for the last iteration, which is the most basic information necessary to mask the model. Nonetheless, further developments in this regard are being considered that will be discussed in the outlook of this thesis. The DWS for the inversions in Sallarès et al. [2013] (Fig. 2.6b,d) were used to mask the final models in Fig. 2.4.

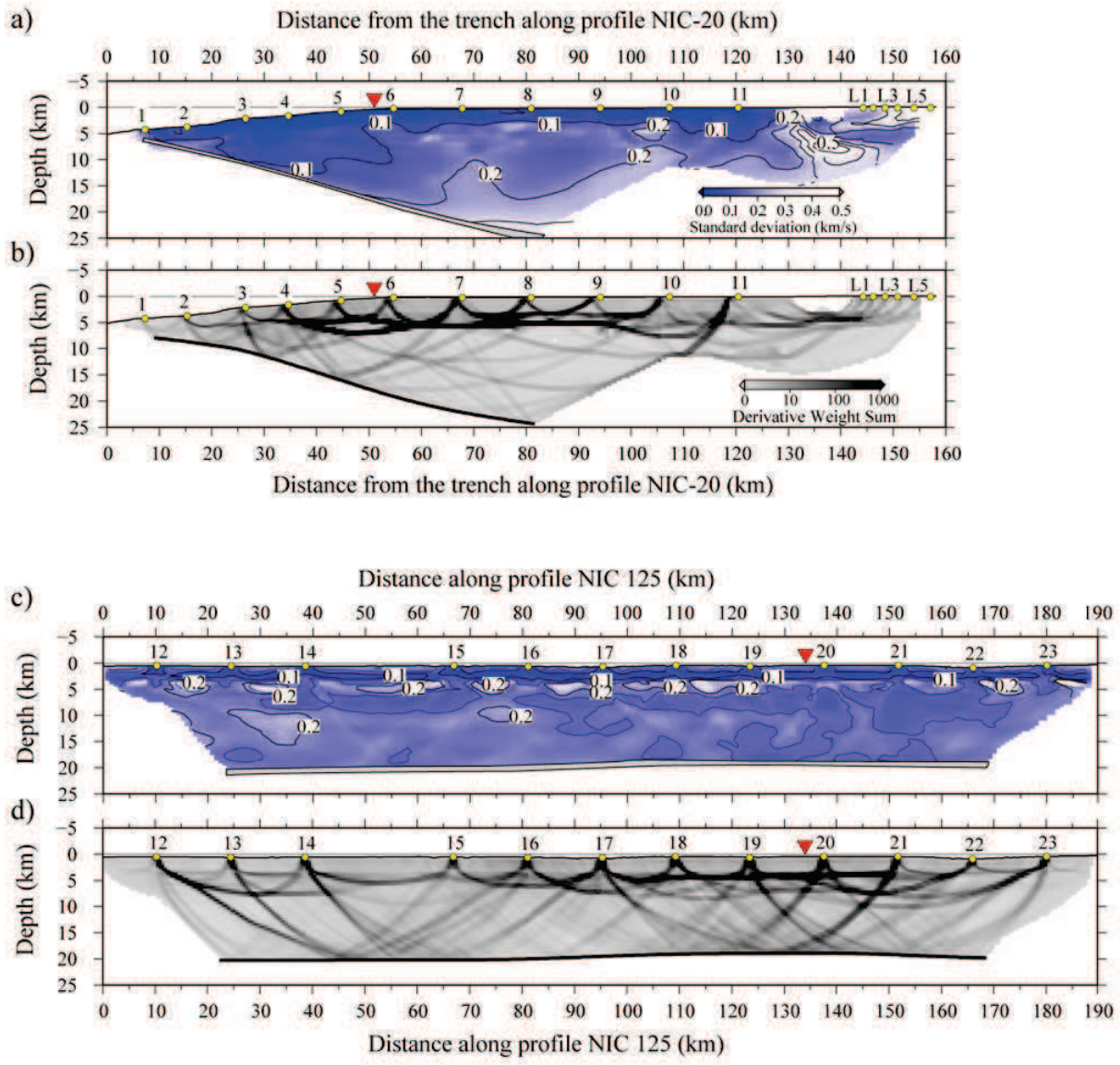

Figure 2.6. (a) Statistical uncertainty model of the P-wave velocity values and the geometry of the interplate boundary for the NIC-20 model displayed in Fig. 2.4a. Details on the calculation are given in the text. (b) Derivative weight sum (DWS) values obtained along the NIC-20 model. (c) Same as (a) but for the NIC-125 model displayed in Fig. 2.4b. (d) Same as (b) but for the NIC-125 model.

However, the DWS does not measure the accuracy and resolution nor the non-linear sensitivity of the inversion. In resolution analyses the initial model is modified with perturbations of the size and amplitude of interest, and synthetic data is generated for this perturbed model using the same acquisition configuration as in the real experiment. Random noise is then added to this synthetic data set to simulate picking errors (~100 ms), and it is inverted starting from the initial, unperturbed

model. One of the most common perturbation patterns in resolution tests is that of a checkerboard, but any sort of perturbations can be used depending on the goal of the test. Such analyses can never be comprehensive in the sense that they only estimate the quality of recovery for some specific model perturbations, but they can be useful in evaluating what areas of the model are better recovered by the data set, or whether a particular model feature is actually well resolved by the data acquisition configuration used. In our case, a resolution test was deemed unnecessary because the velocity and depth models were backed up by other experimental evidence such as MCS and gravity data.

A Monte Carlo-based uncertainty analysis was performed to estimate the accuracy of the velocity and depth parameters along the two profiles [e.g. Tarantola, 1987; Korenaga et al., 2000]. This sort of test is crucial for the validity of the geological interpretation of the inverted models. Moreover, the comparison of this analysis with the DWS provides a measure of the non-linear sensitivity of the iterative inversion of the linearised forward problem [Korenaga, 2011; Korenaga & Sager, 2012]. In this statistical method a number of randomised initial models are created together with the same number of randomly perturbed data sets, and the inversion of each initial model–data set pair is conducted. According to Tarantola [1987], if the region of non-null probability in the space of model parameters is covered by the initial models, the mean of the final models with optimal data fit (χ^2/N~1) is the most probable solution and their standard deviation is a measure of the model parameters uncertainty. A fundamental issue in the Monte Carlo analysis is thus the number of initial models necessary to fulfill this condition. To address this, Korenaga [2011] proposes creating two subsets of final models and calculating the mean and standard deviation for each of them. Comparison between the results for both subsets is a good indicator to whether the number of trials per subset samples the space of model parameters correctly. This approach to travel-time tomography was further developed in Korenaga & Sager [2012]. The authors devised a new Monte Carlo sampling scheme based on the concept of adaptive importance sampling that allows for a comprehensive exploration of the space of model parameters.

I created 500 noisy data sets for each profile by randomly perturbing the two travel-time data sets within a range of 70 ms, which corresponds to the addition of the different error sources that may affect phase picking: common phase error (30 ms), common receiver error (20 ms) and individual picking errors (20 ms). Velocity and interface depth parameters for both final models were smoothened and randomly perturbed to generate 500 different initial models for each profile. The perturbation range for the velocity was ±0.5 km/s. The interplate boundary of profile NIC-20 was perturbed by randomly varying its dip angle within a range of 8º (14º ± 4º), while that of profile

NIC-125 was modified within a ±2 km depth range. The final uncertainty distributions are displayed in Fig. 2.6a,c. Considering that the duration of a single inversion run was more than 3 hours long, it is clear that the uncertainty analysis is a time-consuming task. The 1000 inversions were performed on a cluster in groups of 24 simultaneous runs over the course of ~5 days.

2.5. Results

2.5.1. Multichannel seismic images of the convergent margin and plate boundary

The two MCS profiles coincident with the two WAS lines provide detailed images of the structure of the continental margin and plate boundary zone that complement the information in the velocity models. The images display the tectonic structure and stratigraphy of the slope sediment, the tectonic structure of the basement of the margin, the dimensions of a frontal sediment prism, and display the reflective character of the plate boundary (Fig. 2.7).

The trench-perpendicular line NIC-20 shows the structure under the continental shelf and slope. The bulk of the overriding plate is formed by a rock body that displays little internal reflectivity and is bounded at top and bottom by comparatively clear high-amplitude reflections (Fig. 2.7b). This rock body corresponds to a high velocity body in the wide-angle velocity models and is similar in character to the so-called margin wedge, described across Costa Rica [e.g. Ranero & von Huene, 2000; von Huene et al., 2000] and further NW in Nicaragua [Ranero et al., 2000; Walther et al., 2000]. The high-velocities, and drilling and dredging samples have led to the interpretation that the margin wedge is formed by igneous rock probably forming part of the Caribbean flood basalt province [Ranero et al., 2007]. The strike line NIC-125 displays well the lateral continuity of the margin wedge that show little variability in character and a fairly featureless internal reflectivity (Fig. 2.7a).

Overlying the margin wedge under the shelf region are sediments of the Sandino Basin, although the inner shelf and outer shelf are separated by an intervening basement high (Fig. 2.7b). The sediment of the Sandino basin extends under the continental slope and progressively thins downslope from ~2 s two-way time (TWT, roughly 1.8-2.2 km thickness) under the shelf edge, to a few hundreds of meter under the slope toe. Line NIC-125 shows the lateral continuity of the mid slope stratigraphy (Fig. 2.7a). The top of the margin wedge reflection can be traced from under the shelf to under the lowermost continental slope, where it extends under the slope toe to about 1-2 km

of the deformation front located at edge of the overriding plate (common mid point, CMP ~6500 in Fig. 2.7a). The 1-2 frontal km of the upper plate are formed by a sediment prism that resembles the frontal prism drilled offshore Nicoya Peninsula. There, the prism is 5-10 km wide and is made of reworked upper plate sediment because all incoming sediment in under-thrust [Kimura et al., 1997].

The plate boundary is marked by a series of reflections of variable amplitude that change in character from under the slope to under the shelf region, where they become undifferentiated at CMP 13500-14000 at about 11 s TWT (Fig. 2.7b). Under the frontal ~5 km of the lower slope, the image displays well the under-thrust sediment package (CMP ~6500-6900 in Fig. 2.7b). Further landward, lower-frequency reflections exhibiting abrupt lateral changes in amplitude characterise the plate boundary reflectivity, but there are no different reflectors at the top and bottom of the underthrust sedimentary section. A gentle shoaling and thickening of the plate boundary reflections at CMPs 8300-9000 has been interpreted as a subducted seamount [McIntosh et al., 2007] that is located just landward of a prominent landslide of slope sediment causing an abrupt change in seafloor dip (CMP 8000-8400 in Fig. 2.7b).

Line NIC-125 displays the lateral character of the plate boundary reflectivity under the middle slope. Similarly to the image of the plate boundary on the dip line NIC-20, the along strike images of the plate boundary display a fairly continuous reflectivity with abrupt changes in amplitude (Fig. 2.7a). The image on strike line NIC-125 indicates that the large-scale structure of the region is fairly 2-D.

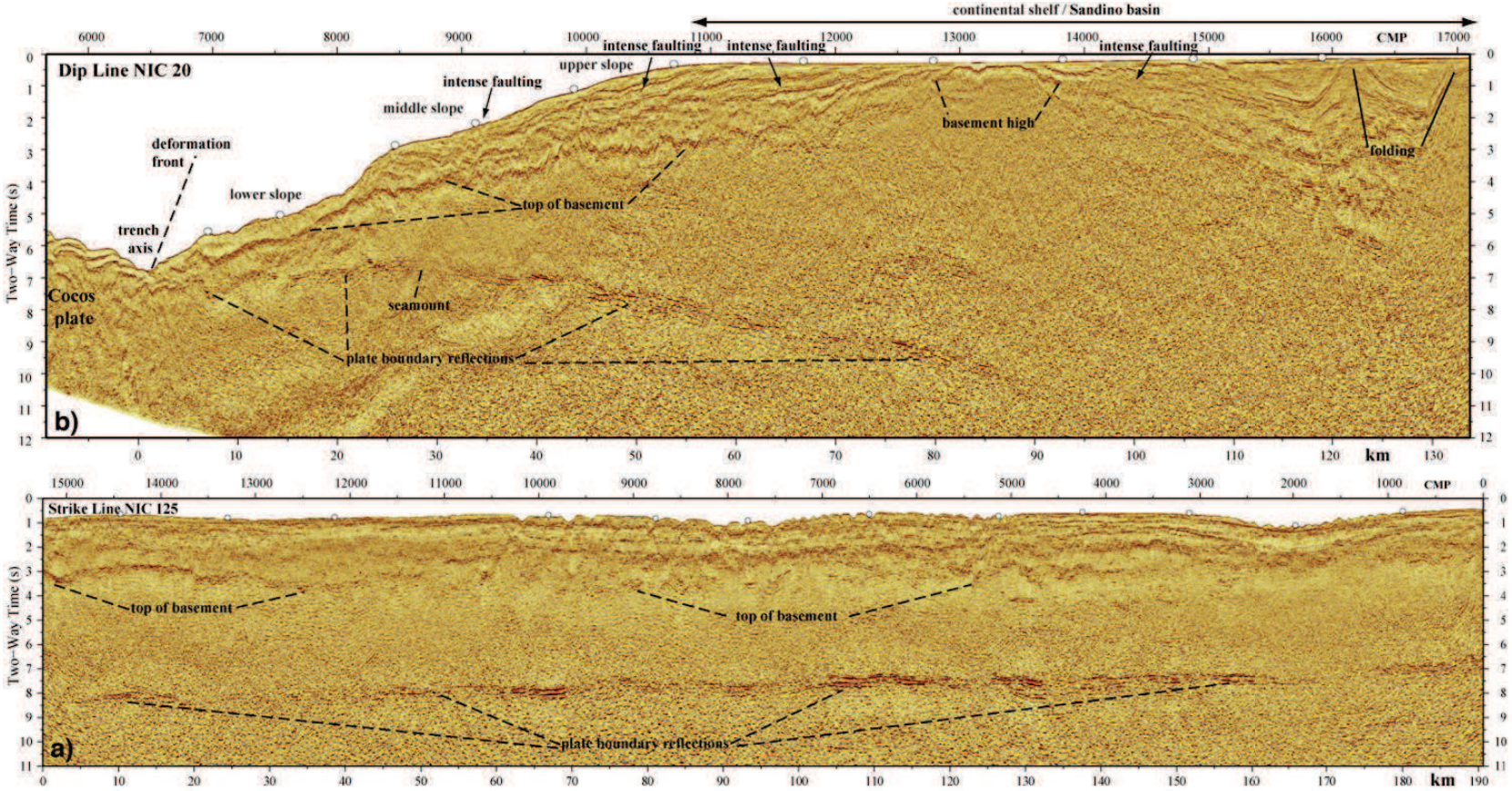

Figure 2.7. (a) Post-stack time-migrated MCS reflection strike line NIC-125 shot along the slope offshore Nicaragua. The image shows the good continuity of plate boundary zone reflection that change abruptly of amplitude along the margin. The slope sediment overlies a basement that is fairly featureless. The image shows that the regional structure is fairly 2-D. (b) Post-stack time-migrated MCS reflection dip line NIC-20, collected perpendicular to the continental margin. The image shows the continuity of the plate boundary reflective zone. The top of basement is marked by a clear reflection under the slope, showing a pronounced thinning towards the trench axis. The Sandino basin is compartmentalised in two sub-basins by an uplifted basement high. The region is cut by abundant normal faults.

2.5.2. Wide-angle seismic structure along the trench-perpendicular profile (NIC-20)

The WAS model along profile NIC-20 includes the overriding plate sediments and crust and the uppermost section of the upper-plate mantle wedge, together with the interplate and upper-plate Moho reflectors (Fig. 2.4a). The resulting velocity distribution for the continental margin shows an average vertical velocity gradient of 0.23 s^{-1} and a horizontal gradient of 0.03 s^{-1} from trench to coast along the interplate boundary. The velocity at the toe of the margin wedge varies from ~1.8 km/s at the top to ~4.7 km/s at the bottom, while velocity beneath the upper slope, at km 75-80 along profile, ranges from ~1.8 km/s at the top to ~7.1 km/s just above the interplate boundary. The uppermost part of the model represents the sedimentary blanket which overlays the igneous basement, with the top of the basement being approximately defined by the 3.8 km/s iso-velocity line. The sedimentary blanket shows two main basins: one extending from lower to middle slope, which is 3-4 km thick, and the ~5-km-thick Sandino basin in the continental shelf. The two basins are separated by a basement high at ~80 km along the profile, where the overriding plate is thickest (~20 km). If we accept that the $P_{mw}P$ phase actually corresponds to Moho reflections, then the basement thins abruptly landwards, reaching to 5-6 km thick beneath Sandino basin (see subsection 2.6.2). At this place, velocity values of ~7.5 km/s, characteristic of altered upper mantle, are found just below the interpreted Moho reflector, which is ~10 km deep. A striking feature trenchward from the basement high, is the reduced velocity zone located between km 35-55 , where velocity is 5-10% lower than in surrounding areas. The geometry of the interplate boundary is well constrained by the P_iP phases giving a dip angle of ~8º beneath the lower slope, increasing to 15º beneath the upper slope.

The plate boundary determined from the inversion of WAS data converted to TWT shows a systematic mismatch with the reflector imaged in the coincident MCS data (Fig. 2.8a). The largest misfit occurs in the segment located under the reduced velocity zone under the slope, where the inverted interplate reflector is ~1 s TWT deeper than the reflection in the MCS image. The MCS data images a reflector at CMP ~16000 at 5-6 s that matches an abrupt increase in velocity gradient (~6.5 km/s to ~7.5 km/s in ~1 km at this point) that corresponds well with the location of the modelled upper-plate Moho beneath Sandino basin (Fig. 2.8a).

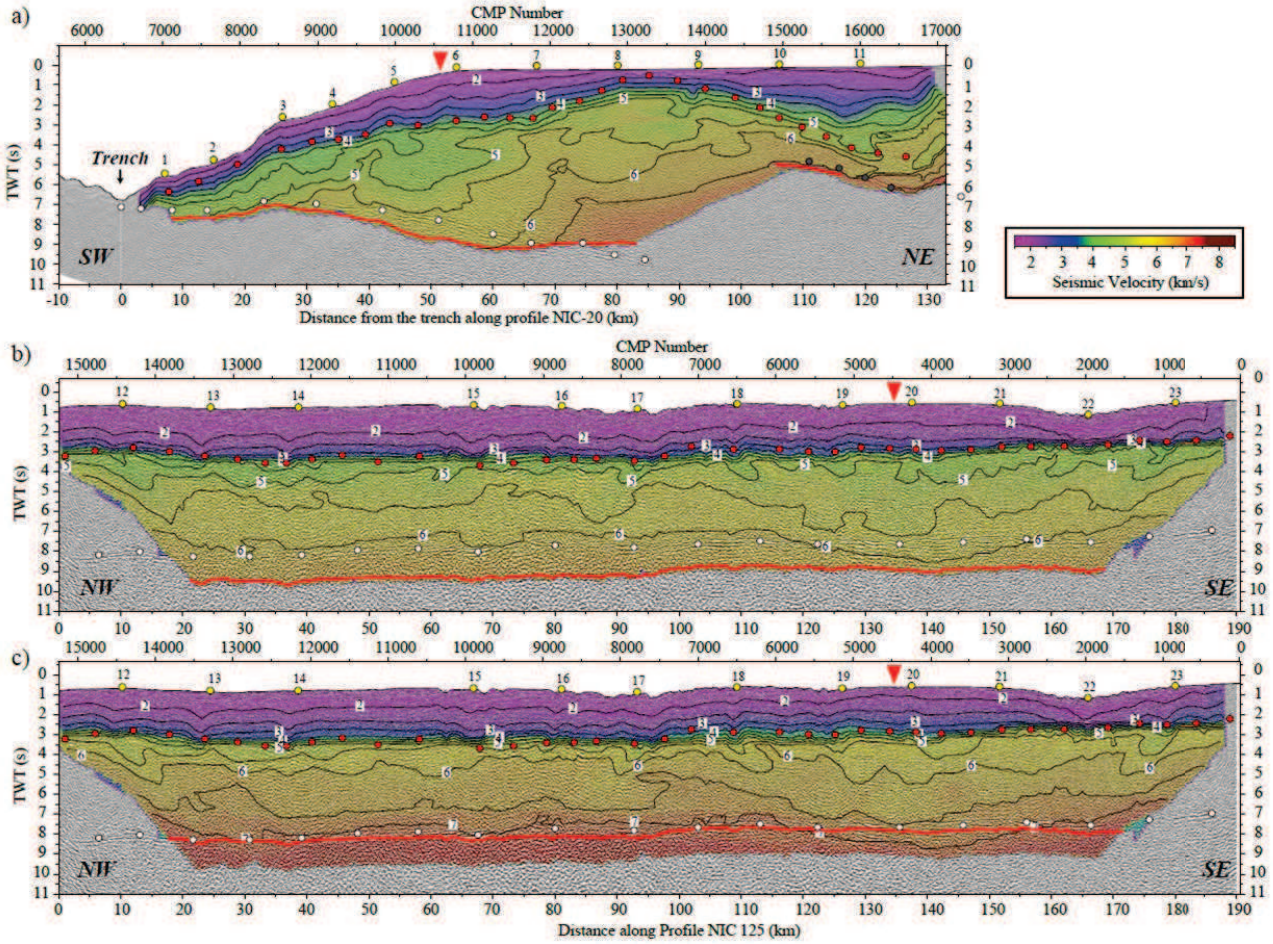

Figure 2.8. (a) MCS line coincident with the NIC-20 profile superimposed onto the TWT-converted P-wave velocity model (Figs 2.4a and 2.7a). The circles inside the model delineate the geometry of interplate (white) and upper plate Moho (gray) reflections imaged on MCS records. The thick red line corresponds to the TWT-converted interplate boundary of the WAS model. OBHs and land stations are shown as yellow circles on the seafloor and the red triangle represents the intersection point between profiles NIC-20 and NIC-125. Note the mismatch of the interplate boundary from MCS images and from WAS modelling, possibly implying seismic anisotropy. (b) Same as (a) but for the NIC-125 WAS and MCS profiles (Figs 2.4b and 2.7b). (c) Same as (b) but having increased the velocity values of the NIC-125 model (Fig. 2.4b) by 15% to account for seismic anisotropy and match the MCS image of the interplate boundary.

The velocity uncertainty throughout the western sector of the profile is smaller than 0.1 km/s in the first ~3 km beneath seafloor (Fig. 2.6a), except below the lower slope where low uncertainty reaches ~10 km under the seafloor, near the interplate boundary. Away from this region, velocity uncertainty gradually increases to ~0.2 km/s just above the interplate boundary from close to the trench to about 50 km away, where the interplate reflector is more than 15 km deep. For the rest of the western sector the uncertainty is lower than 0.3 km/s. The eastern sector, especially from km

~130 to the end of the profile, is less constrained, due to the limited azimuthal coverage (Fig. 2.6b). Here, uncertainty values are ~0.2-0.3 km/s, with local values near 0.35 km/s. However, the steep gradient, the upper mantle velocities, and geometry of the interplate reflector in this sector of the model are reasonably well constrained for their interpretation. A particularly well resolved structure is the segment below the low velocity zone, where a there is a shoaling of the interplate boundary. Thus, the results indicate that the overall velocity distribution is well constrained throughout the trench-perpendicular profile, with unconstrained regions are restricted to localised areas, particularly in the easternmost sector of the model in the offshore-onshore transition.

2.5.3. Wide-angle seismic structure along the trench-parallel profile (NIC-125)

The WAS model along the strike profile NIC-125 includes the sediments and the basement that display a laterally more uniform velocity structure and depth to the interplate boundary than NIC-20 (Fig. 2.4b). The sedimentary layer is 3-4 km thick and shows velocity varying from ~1.8 km/s at the top to ~3.8 km/s at the base. The top of the basement is characterised by a strong velocity gradient that give way to a vertical velocity gradient of 0.2 s^{-1} with an average velocity of 4.0-4.2 km/s at the top and 6.2-6.4 km/s at the bottom. The gentlest gradient is at the base of the upper plate, where it may cause the shadow zone between the P_g and P_iP phases (Fig. 2.3). The lowest basement depth-velocity relationship is at km ~135 along profile around the crossing with dip line NIC-20. The interplate boundary is subhorizontal, so that the entire overriding plate has a constant along-strike thickness of 17-18 km. The comparison between the WAS model converted to TWT and the MCS image shows a systematic ~1 s TWT mismatch at the interplate boundary interface (Fig. 2.8b), as observed on dip line NIC-20 (Fig. 2.8a). We discuss three possible explanations for this difference in travel times between the WAS and MCS reflections. A first possibility is that they represent different boundaries like interplate boundary in MCS data and oceanic Moho in WAS data. Assuming an average velocity of 6-7 km/s, the 1 s TWT misfit implies a 3.0-3.5 km thick subducting crust, which is much thinner than the ~5.5-km-thick incoming-plate crust [Ivandic et al., 2008] measured on the prolongation of NIC-20 (labelled p50 in Fig. 2.1a). Alternatively, WAS data could be mapping an intra-oceanic-crust reflector, but OBH records of the incoming plate do not show intra-crustal reflections comparable to the conspicuous PiP phase [Ivandic et al., 2008]. Additionally, it seems unlikely that the two methods image two different, comparatively high acoustic impedance reflectors at the same spatial location. Our preferred interpretation is that the velocity measured with the two methods differ due to seismic anisotropy, and that subhorizontal propagation of WAS long-offset phases occurs at lower velocities than near-vertical propagation in

smaller-offset MCS records. A 15% seismic anisotropy provides the best match between MCS and WAS reflections with a root mean square (RMS) overall difference between locations of the interplate reflections of 0.25 s TWT for NIC-20 (Fig. 2.8c).

Velocity uncertainty along NIC-125 is similar to NIC-20 (Fig. 2.6c). It is smaller than ~0.1 km/s in the sedimentary layer (upper 3-4 km) and then it increases to 0.2-0.3 km/s at the sediment-basement boundary reflecting the characteristic steep gradient of this interface. The velocity in upper third of the basement is essentially controlled by intra-crustal refractions (Fig. 2.6d), with uncertainty <0.2 km/s, increasing to 0.2-0.3 km/s towards the lower half of the basement, where both velocity and interplate geometry are resolved solely by P_iP phases (Fig. 2.6d). This means that there is a trade-off between location of the reflecting interface and velocity above, increasing uncertainty in both parameters. Nonetheless, uncertainty of interplate boundary location is <0.5 km, well below the standard deviation of the initial models considered, and together with a similar uncertainty for the velocity implies that both parameters are well resolved.

2.6. Discussion

In this section, the seismic structure and physical properties of the overriding plate are interpreted based on the models shown in Figs 2.4, 2.7 and 2.8, starting with the overriding-plate basement under the lower and mid slopes, and continuing with the basement under the upper slope and continental shelf. Gravity modelling of velocity-derived density structure is conducted to further constrain the nature of the upper plate rocks. The integration of MCS images and WAS models is used to interpret the tectonic structure and hydrogeological system of the upper plate. Subsequently, we relate the structure and physical properties of the overriding plate and the location of the mantle wedge with the interpreted location of the down-dip limit of the seismogenic zone. Finally, we discuss the potential relationship between the structure of the upper plate and relief of the interplate boundary to the anomalous tsunamigenic character of the 1992 tsunami earthquake.

2.6.1. The nature of the overriding plate basement

The velocity model of NIC-20 described in subsection 2.5.2 shows a steep velocity gradient from top to bottom and from the trench axis towards the coast (Fig. 2.4). The strong lateral and vertical gradient has been previously described in different convergent margin, and concretely in other

sectors of the MAT including Costa Rica [Ye et al., 1996; Stavenhagen et al., 1998; Christeson et al., 1999; Sallarès et al., 1999, 2000] and northern Nicaragua [Walther et al., 2000]. To interpret the meaning of these gradients it is important to know the nature of the overriding plate basement. The current interpretation of the Central America margin along the MAT in that along Costa Rica, Nicaragua and Guatemala, subduction is dominated by tectonic erosion, and the basement is made of igneous rocks [e.g. Ranero & von Huene, 2000]. Dredging of the igneous basement rock and sediment offshore Nicaragua outcropping at the middle slope [Silver et al., 2000] provide constraints on the basaltic nature of the margin wedge and the timing of first deposit of forearc sediment, during Late Cretaceous time, similar to Nicoya Complex in Costa Rica [McIntosh et al., 2007]. MCS profiles of EW00-05 survey (Fig. 2.1), indicate that the Nicaraguan margin is similar to Costa Rica [McIntosh et al., 2007], with a high-velocity margin wedge beneath the trenchward-thinning sedimentary cover. None of the MCS profiles show evidence of an accretionary wedge fronting the margin. The rough surface that characterises the top of the igneous basement typically extends to <1 km from the trench [McIntosh et al., 2007], as observed in MCS profile NIC-20 (Fig. 2.7b). A WAS profile collocated with p80 profile (Fig. 2.1a) shows a velocity structure similar to the NIC-20 model, with velocity of ~4 km/s at the top of basement, increasing with depth and distance from the trench to values of ~6.5 km/s at the base of the overriding plate under the upper slope [Walther et al., 2000]. These authors interpreted the velocity reduction towards the trench as an effect of trenchward-increasing fracturing and fluid alteration of the igneous basement.

Assuming that the basement is of igneous nature and of similar rock composition, the strong velocity gradient in NIC-20 (Fig. 2.4a) should reflect changes in the degree of rock fracturing and alteration. One can estimate the degree of rock fracturing/porosity (Φ) from P-wave velocity (α) using existing effective medium theory relationships [e.g. Mukerji et al., 1995], following the approach applied to estimate the level of structural integrity of the erosional margin offshore Antofagasta, North Chile [Sallarès & Ranero, 2005]. The parameters needed to estimate Φ as a function of α are the critical porosity (Φ_c), which represents a porosity threshold value above which the rock is fluid-supported, so it is not able to transmit loads or stresses, the velocity of the unaltered rock, α_R, and the rock velocity at Φ_c, α_c. According to experimental results, and taking the values in our model, $\alpha_R \approx 6.5$ km/s, $\alpha_c \approx 4.3$ km/s, and $\Phi_c \approx 0.15$ [Nur et al., 1998; Sallarès & Ranero, 2005]. Thus, assuming that the overriding plate basement is made of igneous rocks similar to oceanic basalt, the parts of the margin with velocities lower than ~4.3 km/s ($\Phi > 0.15$) have to be mostly disaggregated and fluid-supported. In contrast, for velocity higher than ~4.3 km/s ($\Phi < 0.15$), rock porosity can be estimated using the values of α_R, α_c, and Φ_c as referred above, so that

$\Phi=0.46-0.07\alpha$. Additional details on the calculations can be found in Sallarès & Ranero [2005].

Fig. 2.9 shows estimated upper plate porosity/fracturing along NIC-20 using the velocity model of Fig. 2.4a. Porosity uncertainty values propagated from the statistically-derived velocity uncertainty (Fig. 2.6a) are smaller than 1% within most of the upper plate, and 1-2% near the interplate boundary, being negligible for inferences of material physical properties and related tectonic processes. Porosity estimations indicate that the ~5 frontal km excluding the first ~1 km of accretionary prism of the margin correspond to highly fractured, likely partially disaggregated basement. The rest of the margin wedge is constituted by rocks where the degree of fracturing decreases progressively from ~15% to almost 0% at ~70 km from the trench axis (Fig. 2.9). Similar structure and rock properties have been observed in other erosional convergent margins such as North Chile [Sallarès & Ranero, 2005].

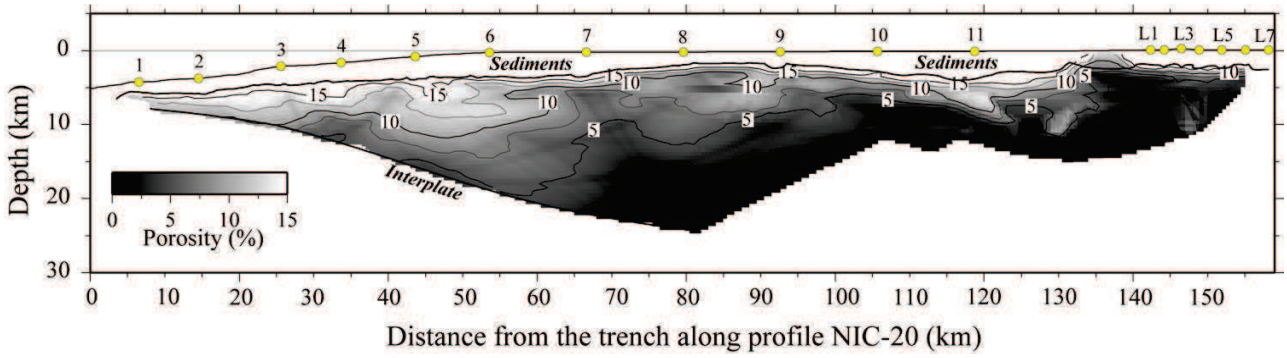

Figure 2.9. Porosity model calculated using the P-wave velocity model along the NIC-20 profile (Fig. 2.4a). To convert velocity into porosity we have assumed that the basement of the overriding plate is made of igneous rocks (basalts) and have applied an empirical relationship based on data compilation for this rock type [Nur et al., 1998]. Sediments are excluded from the calculation.

The low-velocity zone between 35-65 km along the profile (Fig. 2.4a), is associated to a porosity increase of 2-3% compared to neighbouring areas (Fig. 2.9) and is located where the WAS and MCS interplate reflections display the largest mismatch in TWT. This mismatch can be explained by an anisotropy of ~15% between subvertical and subhorizontal propagation velocity (Fig. 2.8c). Experimental evidence and numerical models indicate that P-wave velocity is more strongly decreased when elongated fractures have their long axis perpendicular to the propagation direction. Numerical tests show that, depending on the P-wave frequency, the anisotropy between perpendicular and parallel incidence may vary by as much as 30% [Carcione et al., 2012]. The slower wide-angle propagation velocity compared to near-vertical propagation (Fig. 2.8) indicates

that fractures under the slope should be elongated in a subvertical direction. These fractures may represent paths for fluids to migrate from the subducted slab towards the seafloor. Similar upper plate low-velocity anomalies have been observed in North Chile [Sallarès & Ranero, 2005] and Ecuador [Gailler et al., 2007] using WAS data. It is noteworthy that, once corrected for velocity anisotropy, the 1-D velocity profile at the intersection of profiles (Fig. 2.10) closely resembles that of aseismic volcanic ridges described in different parts of the Galápagos Volcanic Province [Sallarès et al., 2003, 2005], which can be considered the reference velocity model for non-fractured upper plate basaltic basement.

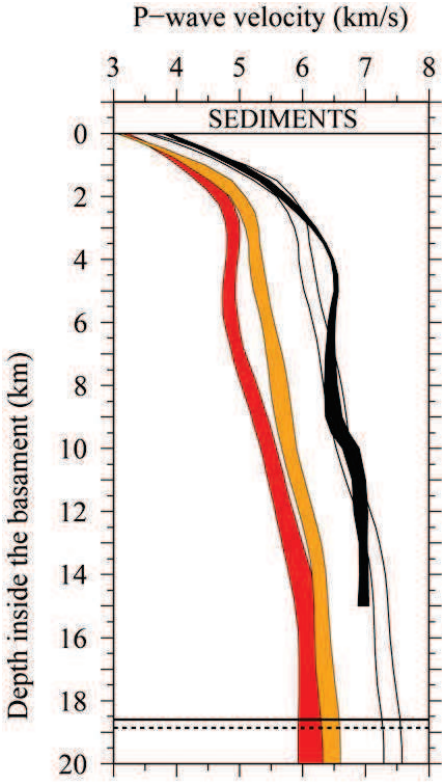

Figure 2.10. 1-D velocity profiles extracted from both velocity models (Fig. 2.4). Red and orange bands correspond to NIC-20 and NIC-125 profiles respectively at their intersection. The velocity profile represented as a white band was obtained increasing the velocities of the orange band by 15%. The black band is a reference corresponding to a 1-D velocity profile extracted from a WAS model of the thick crust of the aseismic Carnegie Ridge formed at the Galapagos Hotspot [Sallarès et al., 2005]. The horizontal lines mark the depth of the interplate reflectors for NIC-20 (solid line) and NIC-125 (dashed line) at the intersection point.

2.6.2. The Sandino fore-arc basin and the upper plate mantle wedge

The basement is covered by a 1-5-km-thick sedimentary layer that extends along the margin from the lower slope to onshore. This sediment cover is separated in two main basins. The outer basin is up to 3-4 km thick and extends across the upper slope and outer shelf to the basement high located at ~80 km from the trench, which separates the two basins. The seismic data show (Fig. 2.8a), that sediment thins rapidly from under the upper slope to the middle slope and further into the lower slope. Landward from the basement high, an inner sedimentary basin reaches 7-8 km thickness at km ~115 km from the trench. The sub-basin, are part of the fore-arc Sandino basin, that extends under the shelf from Nicaragua to Mexico. There is a good correspondence between a reflector

under the basin imaged in the MCS profile and a steep velocity gradient from ~6.5 km/s to ~7.5 km/s in less than 1 km interpreted to mark the base of the crust under Sandino basin in our model (Fig. 2.8a). Clear reflected phases are observed in the land station recordings (Fig. 2.2e). These $P_{mw}P$ phases define a reflector that separates crustal-like velocities of ~6.5 km/s above from upper mantle-like velocities of ~7.5 km/s below, suggesting the presence of thin crust (5-6 km) beneath the Sandino basin.

The low-velocity of the mantle wedge has been attributed to serpentinisation of peridotites by fluids released from the incoming plate [e.g., DeShon et al., 2006]. A similar mantle velocity body beneath Sandino basin has been modelled by Walther et al. [2000] along the p80 WAS profile offshore central Nicaragua, some 120 km NW from NIC-20 (Fig. 2.1). Two hypotheses have been suggested for the origin and evolution of the Sandino basin. One suggests that the Nicaraguan margin represents the westernmost edge of the Caribbean plate, and that the basin originated by flexure of the upper plate as a response to the initiation of subduction in the Late Cretaceous [Ranero et al., 2000]. The other hypothesis argues that the basin developed in the frontal part of a thick oceanic plateau that collided with a terrain the Nicaraguan margin in the Late Cretaceous. The basin would then represent the subduction trench previous to the collision and westward jump of the subduction zone [Walther et al., 2000], and the high velocity body would be a remaining mantle sliver of the Cretaceous subducting slab. The WAS data indicate that a similarly thin crust and shallow mantle wedge extends along Nicaragua beneath the Sandino basin.

The WAS data do not allow to map the deep structure of the mantle wedge under much of the continental shelf, because P_g and P_iP phases do not cover the deep region of the overriding plate (Fig. 2.6b). At km ~75 the overriding plate is ~20 km thick, and both the seismic velocity and velocity gradient are comparable to those of Galápagos aseismic ridges (Fig. 2.10). Here, the velocity just above the interplate boundary is ~7.2 km/s, characteristic of the lowermost Layer 3 rocks [White et al., 1992]. Therefore, assuming that the $P_{mw}P$ phase is a Moho reflection from under the Sandino basin, then the up-dip limit of the mantle wedge must be located trenchward from this point (km ~100 along profile NIC-20).

2.6.3. Gravity constraints on fracturing-related seismic anisotropy and nature of the mantle wedge

As previously discussed , two key results concerning the upper plate structure are (1) the mismatch between the MCS and WAS interplate reflections possibly due to fracture-related seismic

anisotropy, and (2) a shallow ~10-km-deep reflector separating crustal-like from mantle-like velocities beneath Sandino basin that may indicate a shallow mantle wedge. To test the interpretation of the velocity model, we performed gravity modelling of velocity-derived density models using satellite-based free-air gravity anomaly data [Sandwell & Smith, 2009] along profile NIC-20 (Fig. 2.11).

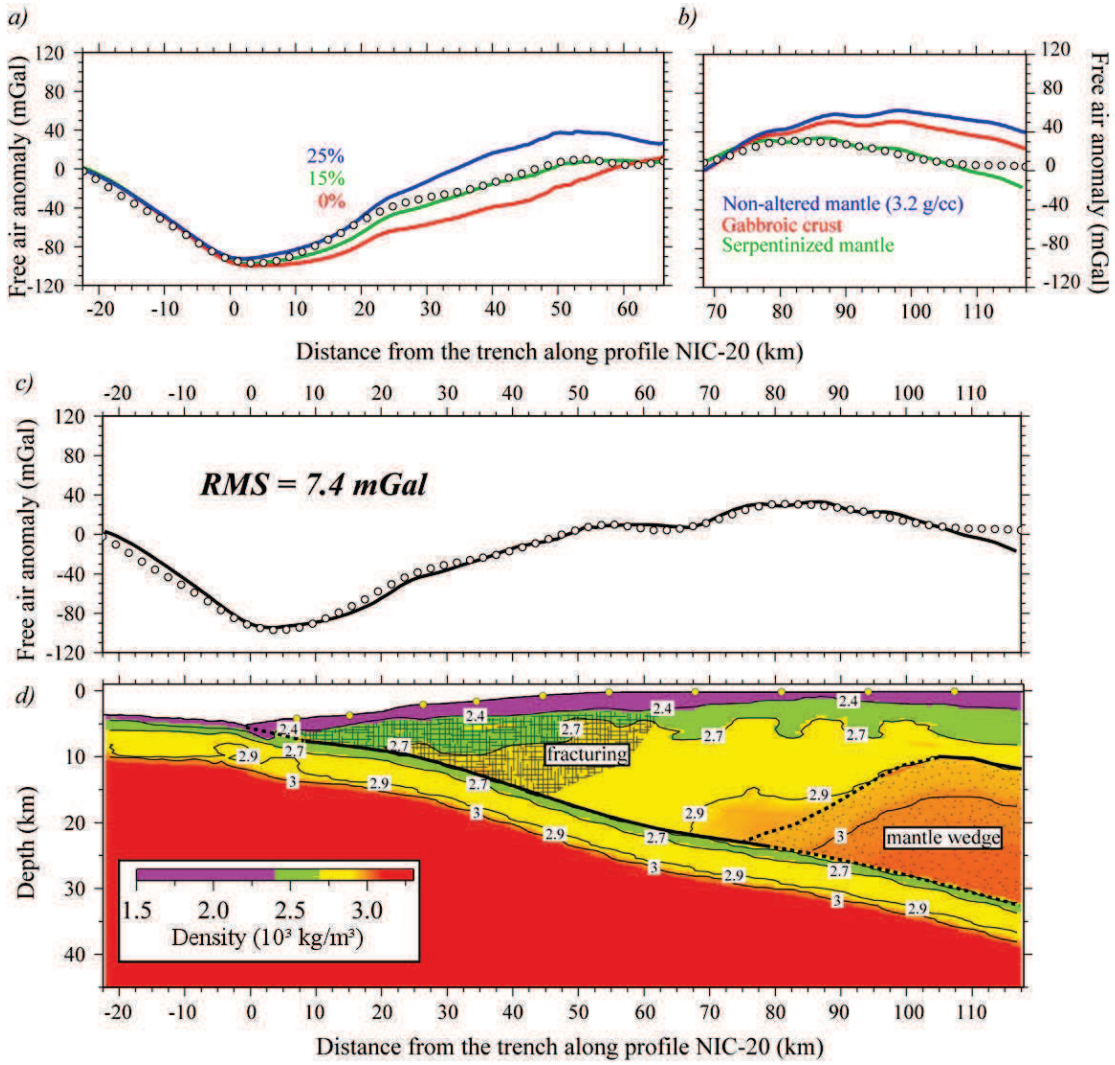

Figure 2.11. (a) Observed free-air gravity anomaly (white circles) and calculated gravity anomaly for three velocity-derived density models using Hamilton's [1978] relationship for shale for the sediment, Carlson & Herrick's [1990] for oceanic crust for the overriding and subducting plates, and Carlson & Miller's [2003] for partially-serpentinised peridotites in the zone labelled as mantle wedge. The red line is obtained transforming the velocity model shown in Fig. 2.4a, the green line increasing the velocity in the zone labelled as fracturing by 15% to account for seismic anisotropy (as in Fig. 2.8c), and the blue line increasing the velocity in the same area by 25 %. (b) Same as (a) but in this case density in the mantle wedge is varied assuming a vertical velocity gradient of 0.03 s^{-1} below the crust-mantle boundary and velocity-density relationships corresponding to Birch's

[1961] law for plagioclase, and diabase-gabbro-eclogite of oceanic layer 3 (red line), Carlson & Miller's [2003] relationship for partially-serpentinised peridotites (green line), and a constant density of 3200 kg/m^3 corresponding to non-altered mantle (blue line). (c) Best gravity anomaly fit corresponding to the model obtained increasing the velocity in the zone labelled as fracturing by 15% and applying Carlson & Miller's [2003] relationship for partially-serpentinised peridotites in the mantle wedge. (d) Density model corresponding to (c).

We employed a code based on Parker's [1974] spectral method as modified by Korenaga et al. [2001] to calculate the gravity anomaly produced by a laterally- and vertically-variable 2-D density model. The density model was constructed converting seismic velocity (Fig. 2.4a) to density using different empirical velocity-density relationships for sediments, basement and upper mantle. To build a density model of the subducting plate beneath the margin, we hung from the interplate boundary a laterally-extended averaged version of the crustal thickness and velocity model obtained along the seaward continuation of NIC-20 by Ivandic et al. [2008]. To calculate the density, we used Hamilton's [1978] law for shale for the sediment, and Carlson & Herrick's [1990] relationship for oceanic crust for the crust of both upper and subducting plates. For the mantle wedge we assumed a constant vertical velocity gradient below the crust-mantle boundary and three different velocity-density conversion relationships: (1) Carlson & Miller's [2003] relation for serpentinised peridotite; (2) Birch's [1961] law for plagioclase, and diabase-gabbro-eclogite of oceanic Layer 3; and (3) a constant density of 3200 kg/m^3 that is characteristic of unaltered uppermost mantle rocks. In all cases density and velocity were corrected from *in situ* to laboratory conditions and *vice-versa* using experimental estimates of pressure and temperature partial derivatives for oceanic crust [Korenaga et al., 2001] and for serpentinised peridotite [Kern & Tubia, 1993].

Fig. 2.11a shows that the velocity-derived density model underestimates the gravity anomaly under the slope, where seismic velocity supports that fracturing is important (Fig. 2.11d). However, a 15% velocity increase in this area (green line) matches well the anomaly, whereas a velocity increased of 25% overestimates the gravity anomaly (blue line). This result means that the upper plate P-wave velocity that best predicts rock density is that corresponding to near-vertical propagation (Fig. 2.8c), which is the least affected by the fractures causing seismic anisotropy in this area. This observation suggests that the elastic properties such as P-wave velocity are more sensitive to rock fracturing than volumetric properties such as bulk density. This result supports the interpretation that the TWT mismatch between the two reflections is caused by velocity anisotropy, associated to a subvertical fracture system [Carcione et al., 2012].

Tests on the density of the mantle wedge shows that serpentinised peridotite reproduces the observed gravity anomaly more accurately (green line in Fig. 2.11b). Assuming that the $P_{mw}P$ reflection is not the Moho reflection, and converting velocity to density applying Birch's [1961] law for oceanic layer 3 gabbros (red line), or using constant density of 3200 kg/m^3 of unaltered mantle rocks (blue line) overestimates the gravity anomaly. Thus, gravity modelling supports a velocity-density conversion using a velocity increase of 15% with respect to the WAS velocity (Fig. 2.4a) in the "fractured" area, and densities corresponding to serpentinised peridotite in the upper plate "mantle wedge". The need for the presence of a shallow mantle wedge was also proposed based on gravity modelling along p80 profile [Walther et al., 2000]. The density model including the subducting plate is shown in Fig. 2.11d, with the "fractured" area extending to km ~60 from the trench axis, and the intersection of the interplate boundary and the tip of the "mantle wedge" at km ~80 from the trenchaxis. The gravity anomaly misfit for this model is 7.4 mGal (Fig. 2.11c).

2.6.4. Multichannel seismic constraints on the tectonic structure and the hydrogeological system

The MCS images display structures that, together with the information on the nature and fracturing of the upper plate described above, help to interpret the dominant tectonic processes and hydrogeological system of the convergent margin. The images show a deep ~8 km basin under the inner shelf underlain by a basement that does not show any evidence of significant faulting. The deep basin sediment is tilted and folded at several-km-long wavelength in a manner described for the region in other profiles located to the north [Ranero et al., 2000], caused by early Miocene shortening. The deep sediment basin is separated by a ~20 km wide regional basement high from the outer shelf and slope sediment.

The sediment overlying the flanks of the basement high show short-scale tilting indicating normal faulting with opposed vergence on either side of the high (Fig. 2.7a). The outer shelf strata and top of the basement reflection are offset and tilted in numerous places indicating important landward-dipping normal faulting activity. The faults change dip polarity across the shelf edge and faulting dips seaward across the upper-middle slope. This abrupt change in fault dip polarity is accompanied by an increase in fault heave. Fault heave is difficult to calculate due to a fairly monotonous slope strata but the top of the basement reflection displays abrupt offsets of up to ~0.5 s TWT (roughly 0.5 km). Fault offsets at the seafloor are much smaller which may indicate that they are growth faults, although mass-wasting processes have clearly truncated strata at the seafloor (Fig. 2.7a).

We interpreted that upper plate extension by normal faulting is a response to tectonic erosion along the underside of the overriding plate as it has been observed elsewhere [Ranero & von Huene, 2000; von Huene & Ranero, 2003; Ranero et al., 2006]. The seaward dipping dominant fabric of the normal faults is probably a gravitational response of the overriding plate to a low-coupling environment along the plate boundary. The plate boundary is characterised under the slope and outer shelf by high-amplitude reflections that have been shown regionally to be commonly of reverse polarity, and that are indicative of the presence of abundant fluid at the fault zone [Ranero et al., 2008]. Open fractures along the plate boundary with fluids, as indicated by the lateral continuity of the plate boundary reflections in the dip and strike MCS lines, possibly require regionally widespread high pore pressures.

Faulting across the slope of the region has been described from multibeam bathymetry maps and deep-towed side scan sonar data [Ranero et al., 2008; Sahling et al., 2008] and has been linked to seepage of deep sourced fluids arising from the dehydration of clays along the plate boundary [Hensen et al., 2004]. The model proposes that deep reaching normal faults provide fluid-flow paths for the water to raise from the plate boundary to the seafloor [Ranero et al., 2008]. The 15% basement-velocity anisotropy between subhorizontal (WAS data) and near-vertical (MCS reflection data) ray paths (Fig. 2.8c), indicates the presence along the entire region of subvertical open fractures, located dominantly under the middle slope that probably correspond with fluid-filled normal faults feeding the seafloor seepage sites. This is the region where focused seepage at the seafloor has been more commonly observed [Shaling et al., 2008].

The lateral coherency of slope strata and top of the basement reflection abruptly degrades from the middle to the lower slope (CMP 8300-8000) where individual strata are difficult to discern. The basement-velocity anisotropy of the middle slope has not been detected under the lower slope. We interpret that the abrupt decrease in strata coherency and rapid thinning of the overriding plate indicate that the amount of deformation increases rapidly from the upper-middle to the lower slope, perhaps related to the subduction of the seamount imaged in the MCS data (Fig. 2.7). Further, we interpret that the absence of velocity anisotropy under the lower slope supports that the increased deformation has destroyed any preferred fracture orientation.

Thus the tectonic structure inferred from the seismic images supports a model of increased upper plate deformation towards the front of the margin that does not occur linearly but presents abrupt changes due to the effect of seamount subduction and tectonic erosion (Fig. 2.12).

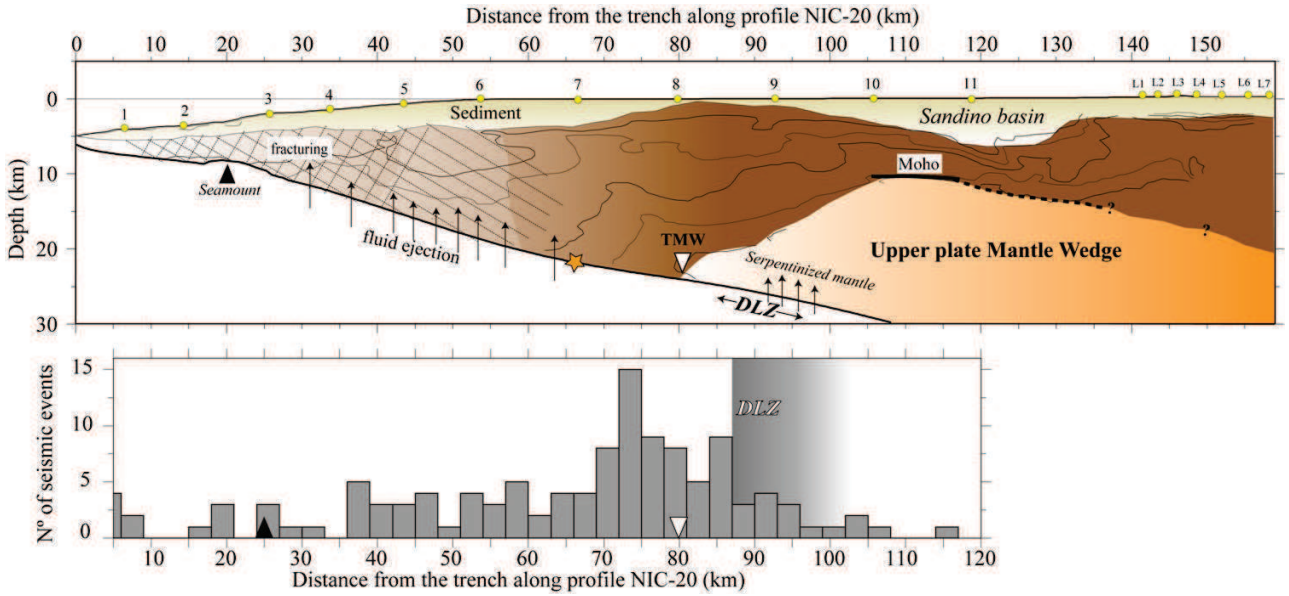

Figure 2.12. (a) Interpretative schematic cartoon of the tectonic structure and relationship to the seismogenic characteristics of the Nicaraguan convergent margin. Orange star marks the projected hypocentral location of the 2nd September, 1992, tsunami earthquake. Abbreviations are EMW for Edge of the Mantle Wedge, and DLSZ for down-dip Limit of the Seismogenic Zone. (b) Histogram for the number of aftershocks of the 1992 earthquake as a function of the distance from the trench. Counts for 3-km-wide boxes starting at the trench were computed. Aftershocks were projected to profile NIC-20. The epicentral locations corresponding to these events are shown in Fig. 2.1b.

2.6.5. The down-dip limit of the interplate seismogenic zone

The down-dip limit of the interplate seismogenic zone (DLSZ) plays an important role as it determines the landward extension of the co-seismic rupture in megathrust earthquakes. Its location is controlled by the frictional properties at the fault gouge, which are in turn modulated by a combination of thermal, structural and compositional factors. Although it is not entirely clear which rock type is related to this limit, laboratory measurements show that most crustal rocks with composition similar to subducted sediments display a critical temperature of around 325-350º C that marks the transition from velocity-weakening to velocity-strengthening behavior [e.g. Tse & Rice, 1986; Blanpied et al., 1995]. These models were originally conceived for continental faulting, but they are also applied to oceanic subduction zones, so the 350-450º C isotherms have been commonly taken as a proxy to define the DLSZ [Tichelaar & Ruff, 1993; Oleskevich et al., 1999]. In warm subduction zones, such as Cascadia or SW Japan, the DLSZ is shallow (10-20 km). Its location coincides with that of the 350-450º C isotherms, so in these cases the DLSZ is believed to be, at least partially, thermally controlled [Hyndman & Wang, 1993; Hyndman et al., 1997].

However, in other cases, particularly in colder subduction zones such as Chile or Alaska, the DLSZ appears to coincide with the location of the upper plate Moho, and not with the inferred location of the 350-450º C isotherms [e.g. Oleskevich, 1999]. This observation is surprising if we consider that dry mantle rocks are stronger than crustal compositions so faults cutting these rocks should in principle be seismogenic and display a velocity-weakening behavior at temperatures of up to 700-800º C [e.g. Kirby, 1983]. A proposed explanation for this limit is the hydration of the mantle wedge rocks by fluids expelled from the subducting slab [Hyndman et al., 1997; Peacock & Hyndman, 1999; Schmidt & Poli, 1998], transforming mantle peridotite into hydrated rocks such as serpentine and brucite. When present at the fault interface, the corresponding hydrous minerals exhibit a velocity-strengthening frictional behavior at the temperatures characteristic of the mantle wedge [e.g., Peacock, 1990; Peacock & Hyndman, 1999].

P-wave seismic velocity is sensitive to the presence of serpentinite, and laboratory experiments show that velocity decreases linearly by as much as 3.0-3.5 km/s between unaltered and 100% serpentinised peridotite for both high-T (containing antigorite) and low-T (containing lizardite and/or chrysotile) types [e.g. Christensen, 1966; Watanabe et al., 2007]. This is the reason why α is often taken as a proxy for the degree of mantle serpentinisation, and it has been a primary evidence to propose mantle wedge serpentinisation in numerous margins, including the MAT [e.g. Walther et al., 2000; DeShon et al., 2006]. In Nicaragua, a local earthquake tomography model with data recorded at an onshore-offshore seismic network displays a low velocity anomaly interpret as serpentinised mantle wedge centered beneath Sandino basin along the entire margin [Dinc et al., 2011]. Our seismic and gravity analysis results are consistent with this interpretation, and indicate that the mantle wedge is at ~10 km depth under the shelf, and extends trenchwards up to ~80 km from the trench (Figs 2.11 and 2.12).

The number of aftershocks of the 1992 earthquake sharply decays landward from the inferred edge of the mantle wedge (Fig. 2.12b). This location marks a limit in regional seismicity between a seismically active area up-dip, and a less active area down-dip (Fig. 2.1b). A seismic gap that appears to follow the whole Sandino basin, was first noted by McIntosh et al. [2007], although they suggested that it could be an artifact due to the poor azimuthal coverage of the offshore earthquakes recorded only onshore combined with the velocity model used for event location. Nonetheless, the new results from Dinc et al. [2011] show a similar distribution of seismic events with a gap beneath Sandino basin, evidencing that it is a robust feature rather than an artifact. We propose that the gap could be due to the presence of serpentinite minerals (e.g. antigorite) at the fault gouge, so that interplate fault dynamics under the mantle wedge would be dominated by stable sliding along the

fault interface. Thus, the integration of aftershock distribution, the velocity structure, and density models (Fig. 2.12), indicate that the gradual transition from unstable to stable sliding that defines the DLSZ would occur at around 90-100 km from the trench, near the edge of the mantle wedge (Fig. 2.12).

2.6.6. The up-dip limit of the interplate seismogenic zone and tsunamigenic character of the 1992 earthquake

The September 2nd, 1992 Nicaragua earthquake is often cited as a textbook example of tsunami earthquake because it was the first one to be recorded by broadband seismic networks so that many details such as the energy released, the dimensions of the rupture area and the distribution of co-seismic slip are very well documented [e.g. Kikuchi & Kanamori, 1995; Satake, 1995; Ihmlé, 1996a,b). This event excited a tsunami that was much larger than expected for its surface wave magnitude (M_s=7.2). The aftershock activity was monitored for a period of 3 months after the main earthquake, resulting in a data set of 124 events with true moment magnitudes comprised between M_w=4.2 and 5.5 (Fig. 2.1b). According to the available locations, the aftershocks of this event are distributed almost up to the trench. The duration of the rupture was anomalously long (>100 s), as a consequence of an abnormally low rupture propagation velocity. Additionally, it is commonly accepted that the tsunamigenic character implies that the rupture of tsunami earthquakes must extend into the weak sediments of the accretionary wedge or the subduction channel [Kanamori, 1972; Fukao, 1979; Okal, 1988; Pelayo & Wiens, 1992; Polet & Kanamori, 2000].

Seismological data inversion indicates that the source moment distribution of the 1992 earthquake was heterogeneous, showing patches with large slip (3-4 m) in the NW and SE limits of the rupture area within wider regions of modest or no slip, and a rupture propagation velocity varying from ~1.0 km/s to 2.5 km/s [Ihmlé, 1996b]. A large proportion of the seismic moment was released close to the trench, as required to generate the tsunami [Satake, 1995; Ihmlé, 1996b]. This heterogeneous slip distribution is consistent with inversions of tsunami run-up data suggesting that a significant part of the energy was released near the SE limit [Piatanesi et al., 1996; Geist & Bilek, 2001]. To explain the characteristics of this earthquake, it has been proposed that it nucleated at <10 km deep [Bilek & Lay, 2002], most probably within the subducted sediments [Kanamori & Kikuchi, 1993; Satake, 1994]. Alternatively, McIntosh et al. [2007] noted that the area of maximum co-seismic slip and slowest propagation velocity inferred from statistical analysis of seismological data [Ihmlé, 1996b] spatially coincides with subducted seamounts identified in the MCS data (Fig. 2.1b). The

spatial correspondence is particularly evident between the location of a large slip patch near the SE limit of the rupture area [Ihmlé, 1996b], the zone of larger tsunami energy release [Piatanesi et al., 1996; Geist & Bilek, 2001], and the seamount subducting beneath the lower-middle slope at 20-25 km from the trench that is imaged in MCS profiles NIC-28 [McIntosh et al., 2007] and NIC-20 (Fig. 2.7a). This spatial coincidence led the authors to suggest a causal relationship between the SE sub-event defined by the large slip patch, which occurred ~70 s after the main shock [Ihmlé, 1996b], and the presence of the subducted seamount.

According to Scholz & Small [1997], a situation that could favor the occurrence of unstable sliding spots is the presence of significant topographic relief on top of the subducting plate. Subducted seamounts and tall horsts locally alter the state of stress at the plate interface by increasing normal stress and hence seismic coupling. Thus, subduction of horsts and seamounts has been proposed as an alternative mechanism to account for the occurrence of tsunami earthquakes near the trench [Tanioka et al., 1997; Polet & Kanamori, 2000]. Conversely, Wang & Bilek [2012] argue that subducted seamounts produce complex fracture networks during subduction that tend to produce numerous small earthquakes rather a single large event. Recent numerical work combining the effects of sliding along a fictional contact and the geometrical effects due to the presence of a seamount suggest that both factors play their role and the subducted seamounts can act both as barriers or asperities depending on different aspects such as the distance to the trench [Yang et al., 2012, 2013].

In Nicaragua, the frontal 35-40 km of the interplate boundary (Fig. 2.12), contains scattered but significant aftershock seismicity, indicating that the moderately fractured upper plate is able to store some elastic energy close to the trench axis and perhaps some amount of coupling along the interface. The nucleation of main shock of the 1992 event occurred at 65-70 km from the trench axis [Ihmlé, 1996a] and the seismic data indicates that initiated at 20-22 km deep. Subsequently, rupture propagated to the NW and SE and towards the trench [Satake, 1994; Ihmlé, 1996a,b]. The distribution of co-seismic slip within the rupture area was heterogeneous, with minor co-seismic slip in most of the rupture area and small areas with large so-seismic slip (Fig. 2.1b). Our interpretation is that the propagation of the main shock triggered secondary events in some specific area of locally increased normal stress that became asperities. Such location of increased normal stress and measured larger slip is the subducting seamount near the SE limit of the rupture zone. We hypothesise that co-seismic rupture of this seamount or other comparable areas with increased the normal stress close to the trench, in relatively low-rigidity material [e.g. Geist & Bilek, 2001], is a key factor to explain the seafloor deformation and, therefore, the tsunamigenic character of this

moderate-magnitude earthquake.

2.6.7. On the need of 3-D modelling

The trench-perpendicular model is more heterogeneous than the trench-parallel one. However, both of them contain velocity and depth heterogeneities that would obviously benefit from 3-D travel-time modelling. For instance, a 3-D experiment would help to determine the shape of the low velocity zone related to fluid percolation and seafloor seepage, the extension of the fore-arc Sandino basin and of the thin crustal layer beneath it, or the size and locations of the subducting seamounts across the margin. 3-D experiments would also improve the ray coverage of the incoming plate at the trench and beneath the upper plate, which is generally a poorly sampled area in 2-D experiments. Other shortcomings of the 2-D modelling appear when combined with 3-D seismological observations such as the seismic moment distribution (Fig. 2.1) or the distribution of aftershocks across the margin (Fig. 2.12). For instance, the approximate interpretation of the limits of the seismogenic zone along the 1-D interplate boundary was based on the projection of the aftershocks on profile NIC-20. A 3-D model would contribute to the delimitation of the 2-D seismogenic zone of the margin.

Furthermore, actual wave propagation occurs in 3-D space, so that ray paths in 2-D profiles are subject to the influence of out-of-plane heterogeneities, and are generally not limited to a 2-D plane. Zelt & Zelt [1998] performed a series of synthetic tests to quantitatively compare 2-D and 3-D experiments considering several 3-D acquisition configurations. Among these, the so-called fine-grid geometry is the only one to make a remarkable difference with respect to 2-D acquisition profiles. This geometry [e.g. García-Cano et al., 2014] is formed by perpendicular 2-D profiles arranged to cross each other at the locations of receivers (or sources, depending on which are fewer in the experiment) and with line spacing equal to receiver (or source) spacing. The authors conclude that out-of-plane effects will most likely be significant in heterogeneous media such as convergent and passive margins, orogenic belts, mid-ocean and continental rifts, hence justifying 3-D exploration. Robust 3-D experiments overcome the 2-D plane approximation, thereby ensuring that the only sources of parameter uncertainty are the accuracy and precision limits of experimental measurements such as source and receiver locations, seismic data recordings, travel-time picking, topography and bathymetry data, numerical and theoretical approximations in the modelling code, etc.

CHAPTER 3: MULTIPLE – SEAFLOOR REFLECTION INTERFERENCE (MSRI)

3. MULTIPLE – SEAFLOOR REFLECTION INTERFERENCE (MSRI)

As explained in the introduction and in the motivation section, one the objectives of this thesis work is to use different seismic phases, other than first arrivals, in order to model as much of the information available in record sections as possible. This goal includes reflected phases as in TOMO2D, which allow defining the location and geometry of the interplate boundary or any other geological discontinuity, but also other phases of interest that cannot be currently used in TOMO2D. In this context, the application of TOMO2D described in the previous chapter showed that there is much information available in record sections that is typically not used in travel-time tomography studies. Regarding marine record sections, an apparently paradoxical phenomenon is sometimes observed in which the water-layer multiple-like phase has greater amplitude and can be followed to greater offsets than the corresponding primary arrival (Fig. 3.1). When this happens, modelling of the multiple arrivals provides additional information not available from the corresponding primary phases. However, the origin and nature of this phase is not well understood, so it is necessary to understand how it is generated prior to implementing it in TOMO3D. In Meléndez et al. [2014] we propose an explanation for such phenomenon, and proved it with a synthetic simulation that evaluates the weight of potential key factors involved. In the first part of the simulation we generated synthetic seismograms, and in the second one we approximated the effects of geometrical spreading, wave attenuation, and ambient noise. In this way we obtained a rough measure of the possible offset gain, and inferred the most propitious geological conditions for this phenomenon to take place. This study allows for a more extensive and well-grounded use of marine wide-angle seismic (WAS) data.

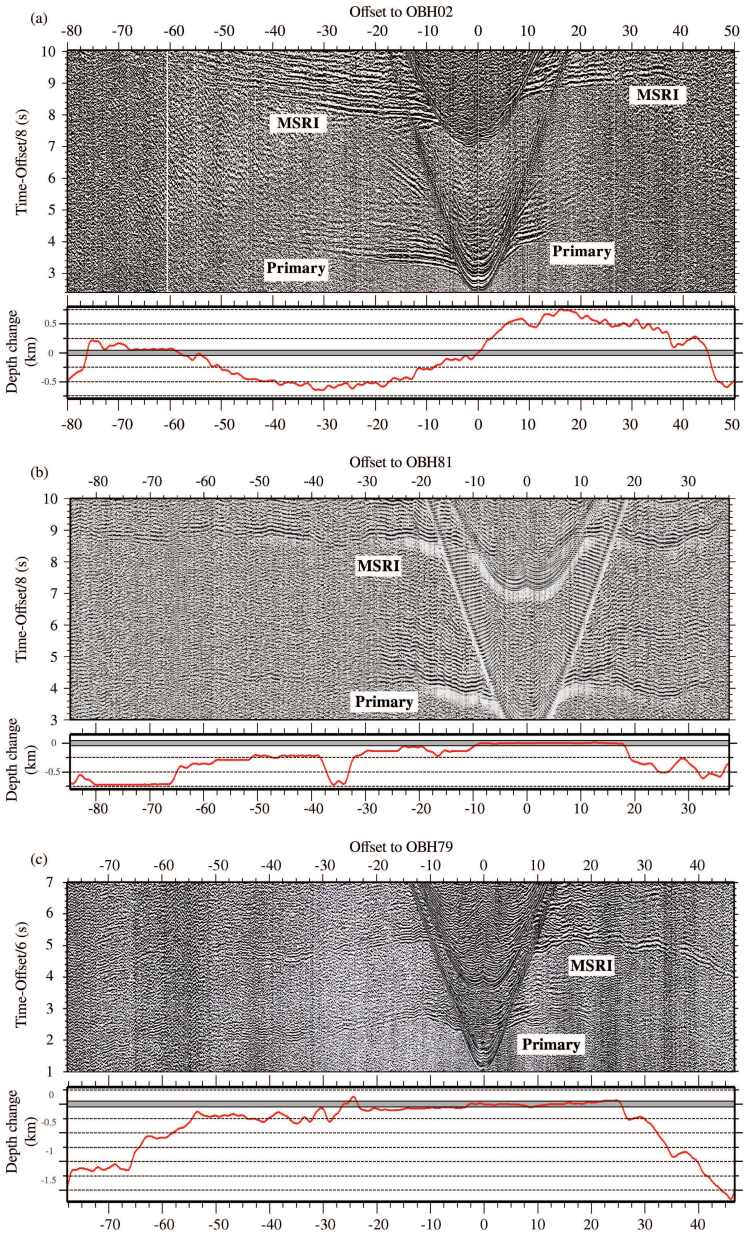

Figure 3.1. Three examples of record sections in which the water-layer multiple-like phases, which we called MSRI (multiple – sea-floor reflection interference), can be followed to longer offsets than its corresponding primary phase: (a) OBH02 from the Mid-Atlantic Expedition 2003/2004 aboard R/V Meteor (M60/2) (Dannowski et al., 2011), (b) OBH81 from the MEDOC-2010 survey (Ranero et al., 2010), and (c) OBH79 from the Paganini-1999 survey (Sallarès et al., 2003). Primary and MSRI phases are labelled. The plots below each record section show the change in bathymetry along the profile relative to the depth at the receiver location. The grey band marks the ±50 m range of depth difference for which the source – receiver multiple interference can occur.

3.1. Water-layer multiples in wide-angle seismic data

The water-layer multiple in marine seismic records results from the reflection of primary phases (both refractions and reflections) at the sea – free air interface. Given that the water layer has an approximately constant velocity, the multiple imitates the shape of the primary phases with a travel-time delay that depends on the water depth only. Backus [1959] formulated the detrimental effect of water-layer reverberations on near-vertical reflection seismic data as a linear filtering mechanism, and explored inverse filtering techniques to reduce it. However, unlike in near-vertical seismic data, in WAS experiments water-layer multiples hardly ever deteriorate the data quality and are commonly disregarded because they simply duplicate the information provided by the primary phases. Furthermore, being a secondary reflection, its amplitude should be consistently smaller than that of the corresponding primary wave. However, some recordings show multiple-like phases that can be followed to longer offsets than primary ones (Fig. 3.1), meaning that the amplitude of the primary phase is below the noise level, while the amplitude of the multiple is above it. In certain cases, the multiple is visible tens of kilometres farther than the primary waves, thus providing information on the velocity structure at deeper crustal levels that could not be retrieved from the primary phases. In terms of modelling, using these data would result in denser ray coverage and longer ray paths. In this regard, there are a few examples of the usage of multiple phases in travel-time modelling [e.g. Muller et al., 1999; Minshull et al., 2006], although they are usually discarded. Often used but typically not discussed procedures are either to convert multiple picks to the travel time expected for their corresponding primary phases or to visually inspect multiple phases to roughly guide the extrapolation of weak primary-phase picks. Nonetheless, water-layer multiples have been successfully used in other applications such as the improvement of OBS data quality with supervirtual refraction interferometry [e.g. Bharadwaj et al., 2013], the broadening of the subsurface illumination obtained by mirror imaging [e.g. Dash et al., 2009], or the determination of a 2-D velocity model of the water layer by ray-tracing forward modelling [e.g. Grad et al., 2011].

3.2. Hypothesis: constructive interference

If a multiple-like phase can be followed to longer offsets than the corresponding primary phases, its amplitude must somehow have been increased, compensating for the amplitude loss associated to longer wave propagation. Our working hypothesis is that, for sensors located close to the sea-floor, the receiver multiple and its reflection at the sea-floor interfere constructively, generating a signal

with amplitude higher than that of the primary phases (right red box in Fig. 3.2). This constructive interference is possible because the reflection of the multiple at sea-floor does not involve a phase inversion. For simplicity, from here on we term it the "multiple – sea-floor reflection interference" (MSRI) to refer to the observation on seismic data, that is the seismic phase on record sections, and limit "multiple" to indicate the reflection of primary waves at the sea – free air interface.

An alternative to our working hypothesis is that the phenomenon is caused by the constructive interference between the source multiple (reflection at the sea-floor and at the water surface before entering the subsurface) and the reflection at the sea-floor of the receiver multiple. However, it must be noted that such interference might only occur if the water depth at the source (H_{SM}) and receiver (H_{RM}) locations happens to be sufficiently similar. Indeed, for one-cycle sine waves with 10 Hz frequency, typical of WAS records, such interference would only produce an amplitude greater than the primary wave for $|H_{SM}-H_{RM}|<50$ m. Thus, the source multiple will only consistently contribute to the continuity of the multiple-like phase in the record section if the bathymetry along the profile segment corresponding to the shots that produce such phase is almost horizontal. Such a sustained coincidence in source and receiver water depth is not encountered in any of the tens of record sections from different experiments showing the anomalously-high multiple amplitude that we have inspected in the course of this work. Still, it is worth mentioning that there are certain geological contexts in which this might occur, such as oceanic abyssal plains. Fig. 3.1 displays the variation in bathymetry along the profiles with respect to the depth at the receiver location to show that the multiple-like phase with higher amplitude than the primary is almost always observed at offsets for which the depth difference is much greater than 50 m. In summary, it is clear that the MSRI, which is independent of changes in sea-floor depth, is far more general than the source – receiver multiple interference. This is the reason why we centred our numerical analysis on the MSRI.

We identified three key factors that potentially control the MSRI. Two of them are related to acquisition: the source frequency, and the sea-floor – receiver distance. The third one is the velocity field in the shallow subsurface material defining the acoustic impedance. Also, we need to account for two potential causes of amplitude loss: geometrical spreading and wave attenuation. The amplitude decay associated to the reflection at the sea – free air interface is of ~0.05% ($R_{w\text{-}a}\approx$-0.9995), so that we do not need to consider it in our modelling scheme, i.e. we assume $R_{w\text{-}a}$=-1 [Backus, 1959]. While this approximation is generally considered to be valid for typical marine seismic experiments, it does not hold for higher frequencies, and particularly under rough sea conditions [Liu & Huang, 2001].

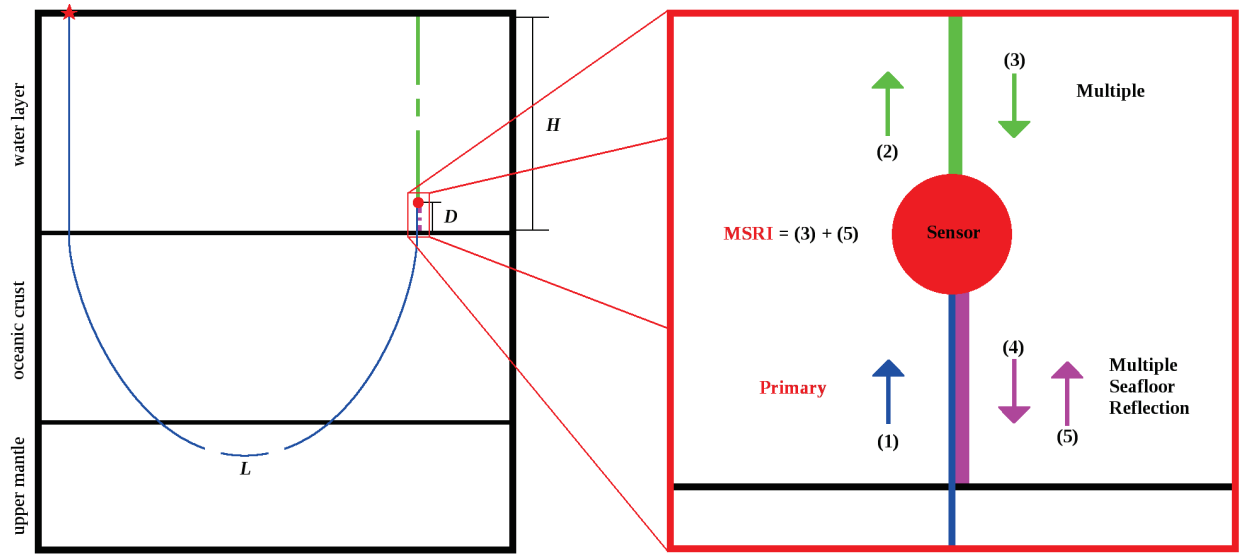

Figure 3.2. Modelling scheme for our synthetic test. The ray path is divided into three significant segments using different colours. Normal thickness and double thickness indicate one-way and two-way ray-path segments. (red box) Modelling scheme for the first part of the test in which we calculate r_o values. Arrows indicate the directions of the ray-path segments associated with the different waves, and are numbered in chronological order. The phases named in red, primary and MSRI, are those that can actually be observed in record sections. (black box) Modelling scheme for the second part of the test in which we calculate ΔL values. Source and sensor locations are marked with a star and a circle. L is the ray-path length from source to receiver, H is the water-layer thickness at the receiver location, and D is the receiver–seafloor distance. The blue segment has length L and corresponds to the primary phase ray path. The green segment has length 2·(H-D) and together with the blue one they form the multiple phase ray path (L+2H-2D). The purple segment has length 2D and with the other two segments they correspond to the ray path for the sea-floor reflection of the multiple (L+2H). All three segments include a dashed portion to signify that L, H, and D are variable parameters in our synthetic test. Note that we keep a constant water depth at the source location (L_w), so that in general it does not coincide with variable H.

One last factor to be considered is ambient noise, which limits the observable offset for primary and MSRI phases on record sections. The additional offset obtained from the MSRI phase implies an increase in the length of the ray paths used in modelling. Therefore, source-to-receiver ray-path length is a good parameter to quantitatively measure the improvement obtained by including MSRI picks in WAS data modelling.

3.3. Synthetic modelling

3.3.1. Measuring the interference

We first evaluated the ratio (r_o) between the peak amplitude of the MSRI and the reference peak amplitude of an incident multiple wave to determine the conditions that produce a constructive interference ($r_o>1$). The r_o parameter can be understood as the value that scales the peak amplitude of the multiple phase to give the MSRI peak amplitude. The factors inferred to control the interference (source frequency band, receiver – sea-floor distance, and subsurface velocity) are parameterised in our synthetic modelling scheme, and each parameter is assigned a realistic study range, defining the set of parameter combinations to be tested.

For multiple waves the propagation near the receiver is quasi-vertical and the plane-wave approximation can be assumed, so that the interference can be studied in one dimension. We used shot1D, a 1-D acoustic wave propagation code developed by Kormann et al. [2011] to generate the synthetic data needed to calculate r_o (Fig. 3.3). Synthetic traces are obtained by defining the source (a Ricker wavelet) and receiver locations. The medium is defined by the velocity values assigned to an array of depth nodes, and is assumed to be incompressible. Density effects in the water column are considered to be of second order and neglected. The propagation is modelled with a time-domain finite-difference scheme of 6th order in space and 2nd order in time defined by

$$\frac{1}{c^2(z)} \cdot \frac{\partial^2 p(z,t)}{\partial t^2} = \nabla^2 p(z,t) \quad (3.1)$$

where p is pressure, z is depth, t is time, and c is sound speed. Time increment is set to fulfil the Courant-Friedrichs-Lewy condition [Courant et al., 1967]. The upper end of the model is defined as a free-surface condition by setting $u(0,t)=0$, which implies total reflection at the top of the medium. The lower end of the model is an absorbing boundary made of complex frequency-shifted perfectly-matched layers [Kormann et al., 2009]. This simulates a half-space propagation, avoiding undesired reflection artefacts from the bottom.

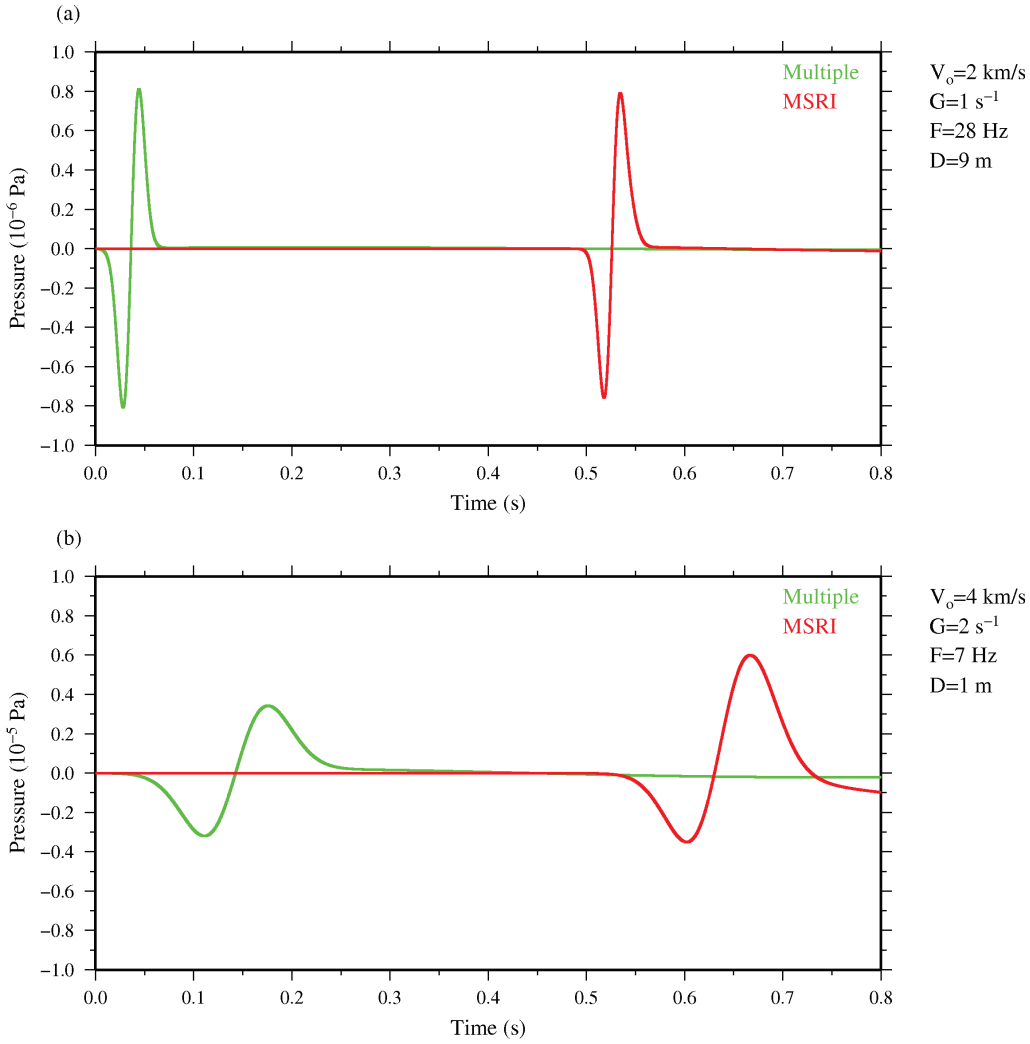

Figure 3.3. Selected examples of 1-D acoustic wave propagations performed with shot1D for (a) r_o≈0.98 with V_o=2 km/s, G=1 s^{-1}, F=28 Hz, D=9 m, and (b) r_o≈1.75 with V_o=4 km/s, G=2 s^{-1}, F=7 Hz, D=1 m (black circles in Fig. 3.4a and 3.4f, respectively). Green lines represent the traces recorded 1 m below the source from which we obtain the peak amplitudes of the incident multiple waves, whereas red lines represent the traces recorded at a distance D above the sea-floor which provide the MSRI peak amplitudes.

Within shot1D, the source frequency band is parameterised by setting the central frequency of the wavelet (*F*), while the receiver – sea-floor distance (*D*) is set by the location of the receiver with respect to the sea-floor defined in our velocity model. The dominant frequency in long-offset WAS marine experiments is typically centred around 10 Hz, with the main energy spectrum between ~5 – 15 Hz, but we considered a wider range of 4 – 30 Hz, with 0.5 Hz sampling rate, to cover a greater variety of experimental cases. The receiver – sea-floor distance (*D*) may vary from one instrument to another, and we tested the range 0 – 10 m, at 1 m interval (see Table 3.1).

Table 3.1. Ranges and sampling rates for the parameters involved in the calculation of r_o with shot1D in the first part of the test.

	F (Hz)	D (m)	V_o (km/s)	G (s^{-1})
Range	4 – 30	0 – 10	1.6 – 4	0.5 – 2.5
Sampling (unit/sample)	0.5	1	0.1	0.5

We parameterised the subsurface velocity distribution in depth (z) as a constant velocity gradient ($V(z)=V_o+G \cdot z$) described by parameters V_o, the velocity immediately below the sea-floor, and G, the velocity gradient. Above the subsurface, water velocity was fixed to 1.5 km/s. The models were extended downward to a total depth of 10 km and the maximum velocity was limited to 6.5 km/s. We used a spatial increment of 0.1 m (dx), fine enough to sample the shortest wavelength considered. For V_o, we selected values between 1.6 km/s (i.e. water-saturated sediments) and 4 km/s (i.e. basement outcrops) with a sampling rate of 0.1 km/s, and for G, 0.5 s^{-1} to 2.5 s^{-1}, and a sampling rate of 0.5 s^{-1}, a wide range that encloses most experimental samples [e.g., White et al., 1984; White et al., 1992]. See Table 3.1 for a compilation of the parameter values considered in this first part of the synthetic modelling.

The reference peak amplitude of the multiple wave was computed within the water layer avoiding any influence of the subsurface velocity field and the sea – free air interface. To do so, we located the source halfway through the water column and recorded its signal 1 m below it. The MSRI peak amplitude was measured at a distance D above the sea-floor simulating real OBS/H positions in experiments (Fig. 3.3). Note that r_o depends on F through both multiple and MSRI peak amplitudes, but on D, V_o and G only through the latter. Thus, r_o includes the effects of D, V_o, and G on the amplification of the multiple amplitude for each frequency F. Selected results for this first part of the test are shown in Fig. 3.4.

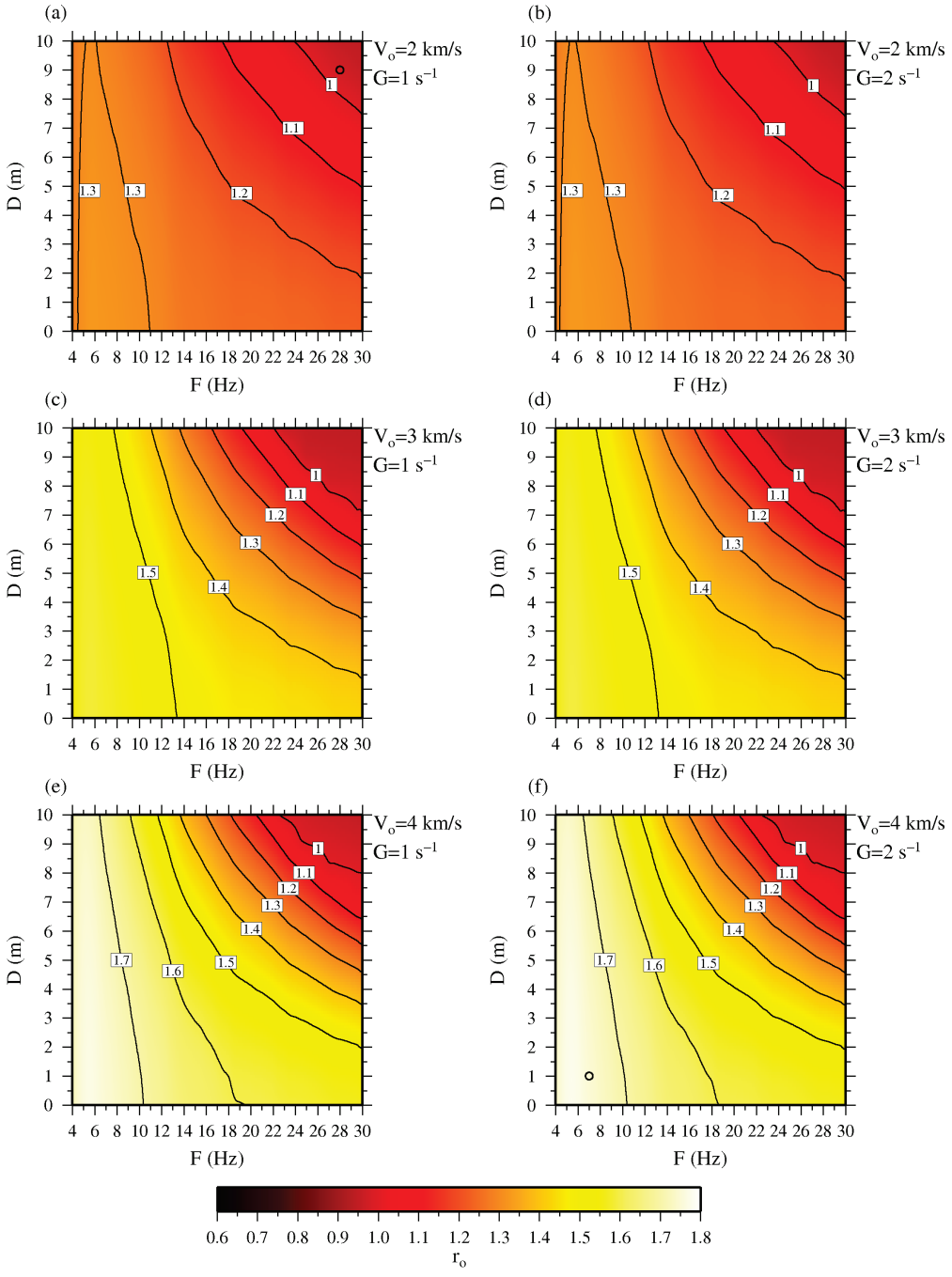

Figure 3.4. Diagrams of r_o as a function of F and D, each for a particular velocity model defined by V_o and G: (a) V_o=2 km/s, G=1 s^{-1}, (b) V_o=2 km/s, G=2 s^{-1}, (c) V_o=3 km/s, G=1 s^{-1}, (d) V_o=3 km/s, G=2 s^{-1}, (e) V_o=4 km/s, G=1 s^{-1}, and (f) V_o=4 km/s, G=2 s^{-1}. Black circles mark the examples shown in Fig. 3.3.

3.3.2. Amplitude decay

For the proper study of this phenomenon, we needed to compare the peak amplitudes of the primary and MSRI phases. To do so, we derived expressions for the peak amplitudes of these phases, using r_o and accounting for the total amplitude loss. These expressions can be compared to the ambient noise level, which allowed us to compute the ray-path length gained with the inclusion of the MSRI phase. The gain in ray-path length implies an increase in maximum recording offset, and thus provides a quantitative measure of the benefit in using these data. The ray-path length increment depends on r_o, the water-layer thickness, the attenuation coefficients, and the signal-to-noise ratio at the receiver location.

The amplitude decay by geometrical spreading in a uniform medium is inversely proportional to the distance from the source, i.e. the ray-path length L [Stein & Wysession, 2003]. The two waves interfering to create the MSRI phase have slightly different ray-path lengths (left black box in Fig. 3.2): $L+2H-2D$ for the multiple, and $L+2H$ for its reflection at the sea-floor, where L is the source-to-receiver ray-path length, i.e. the primary phase ray-path length, and H is the water-layer thickness at the location of the OBS/H receiver. However, if $H>>D$ we can approximate their ray-path lengths to being equal:

$$L+2H-2D \approx L+2H \quad (3.2)$$

which implies that both interfering waves undergo basically the same amplitude loss by geometrical spreading, and that it can be ascribed to the MSRI. To derive a relation between the peak amplitudes of the primary and MSRI arrivals using r_o, it needs to be corrected to account for the effect of geometrical spreading as follows:

$$r\left(L,H,r_o\right) = r_o \cdot \frac{\frac{1}{L+2H}}{\frac{1}{L}} = r_o \cdot \frac{L}{L+2H} \quad (3.3)$$

where $1/L$ and $1/(L+2H)$ are the correction factors for the geometrical spreading of the primary and MSRI arrivals respectively considering the source amplitude is measured at the unit distance. Assuming a source of unit amplitude, the amplitude decay by geometrical spreading of the primary and MSRI phases can be written as:

$$A_p(L)=\frac{1}{L} \qquad (3.4) \qquad\qquad A_M(L,H,r_o)=A_p\cdot r=\frac{1}{L}\cdot r_o\cdot\frac{L}{L+2H}=\frac{r_o}{L+2H} \qquad (3.5)$$

The mathematical expression for the wave attenuation in the plane-wave approximation for a source of unit amplitude is [Stein & Wysession, 2003]:

$$A(L)=e^{-\sum_i a_i\cdot L_i} \qquad (3.6)$$

where a_i is the attenuation coefficient in inverse distance units, and L_i the segment of ray path affected by this particular coefficient. The attenuation coefficient is a function of the wave frequency (F), the propagation velocity (V_i), and of the Q_i factor of the medium [Johnston & Toksoz, 1981]:

$$a_i=\frac{\pi\cdot F}{V_i\cdot Q_i} \qquad (3.7)$$

In order to model wave attenuation we assumed that the ray first travels through a water layer of L_w=4 km, an approximate average of the oceanic water depth, and then through oceanic crust and upper mantle (left black box in Fig. 3.2). Additionally, the MSRI ray travels through a water layer at the receiver location with variable thickness H. The attenuation in the water layer (a_w) for the typical frequencies of WAS experiments is ~10^{-8} m^{-1} [Urick, 1983]. The Q factor of oceanic crust and upper mantle is commonly found in a range from 10 to 1000 [e.g., Wilcock et al., 1992, 1995; White & Clowes, 1994; Goldberg & Sun, 1997; Swift et al., 1998]. For the calculation of the attenuation coefficient we also needed to select F and V. For the former we picked 10 Hz, being the central frequency of the source spectrum in WAS data, and for the latter 6 km/s, a rough average of the medium velocity. With all these considerations, the three attenuation coefficients (a_c) that we tried are ~5 10^{-4} (Q=10), ~5 10^{-5} (Q=100), and ~5·10^{-6} m^{-1} (Q=1000).

Using (3.6), expressions (3.4) and (3.5) are modified to account for attenuation as follows:

$$A_p(L)=\frac{1}{L}\cdot e^{-a_w\cdot L_w}\cdot e^{-a_c\cdot(L-L_w)} \qquad (3.8)$$

$$A_M\left(L,H,r_o\right)=\frac{r_o}{L+2H}\cdot e^{-a_w\cdot\left(L_w+2H\right)}\cdot e^{-a_c\cdot\left(L-L_w\right)} \qquad (3.9)$$

again considering the approximation in (3.2), meaning that we can also ascribe the amplitude loss by attenuation to the MSRI phase. Even though a_w is ~2.5 orders of magnitude smaller than the smallest a_c, we chose to include it in (3.8) and (3.9) because it depends on one of the parameters evaluated in this test, H.

For the evaluation of expressions (3.8) and (3.9), it is necessary to define realistic ranges for the three parameters involved (L, H, and r_o). Typical WAS profiles extend for ~100 – 300 km, so that a rough approximation of the maximum source-to-receiver ray-path length L is ~400 km. For a minimum L value we selected L_{min}=10 km, which yields 6 km of ray path through the crust ensuring that the test scanned all potentially significant L values. Regarding H, most OBS/H are limited by construction to a maximum depth of ~6 km, so we used 7 km as upper bound for this variable. For the lower bound we imposed the condition that the longest wavelength be smaller than H so we selected a minimum value of 500 m. The sampling rates were 10 m for L, and 1 m for H. The minimum H value ensures the fulfilment of (3.2). The range of r_o values was determined by the selection of 10 Hz as the frequency to obtain a_c. The maximum r_o value for F=10 Hz is >1.7, found for D=0 m (Fig. 3.4e-f). The bottom limit for r_o is 1, and the sampling rate 0.01. This information is compiled in Table 3.2.

Table 3.2. Ranges and sampling rates for the parameters in expressions (3.8) and (3.9) used in the second part of the test. For the evaluation of these expressions, we also defined a_c ($5\cdot10^{-4}$ – $5\cdot10^{-6}$) and A_n (10^{-3} – 10^{-9}) ranges and sampled them by decades. a_w was set to a constant value of $1.15\cdot10^{-8}$.

	r_o	L (km)	H (km)
Range	1 – 1.70	10 – 400	0.5 – 7
Sampling (unit/sample)	0.01	10	1

3.3.3. Ambient noise level

The ambient noise level determines the additional ray-path length (ΔL) gained from the MSRI data. For the calculation of ΔL we needed to compare expressions (3.8) and (3.9) with the noise level

normalised to the source amplitude (A_n) which is related to the signal-to-noise ratio (*SNR*). For a source of unit amplitude, the *SNR* in dB and in amplitude units are defined as follows:

$$SNR(dB) = 10 \cdot \log\left[\frac{1}{A_n}\right]^2 = 20 \cdot \log\left[\frac{1}{A_n}\right] = A_o(dB) - A_n(dB) \quad (3.10) \qquad SNR = \left[\frac{1}{A_n}\right]^2 \quad (3.11)$$

Combining (3.10) and (3.11) yields A_n as a function of the amplitudes in dB:

$$A_n = 10^{\left[\left[A_n(dB) - A_o(dB)\right]/20\right]} \quad (3.12)$$

We defined $\Delta L = L_M - L_p$, where L_p and L_M are the ray-path lengths for which A_p and A_M intersect A_n respectively. Thus $\Delta L > 0$ means that the MSRI phase is visible at greater ray-path lengths than the primary phase, that is, the phenomenon is taking place. For simplicity, all $\Delta L < 0$ were set to 0, accounting for the cases in which the phenomenon does not occur. It is worth mentioning that while ΔL values illustrate the general behaviour, they should be taken as estimates because our amplitude decay correction is an approximation, and because noise will be range-dependent if it is dominated by the previous shots.

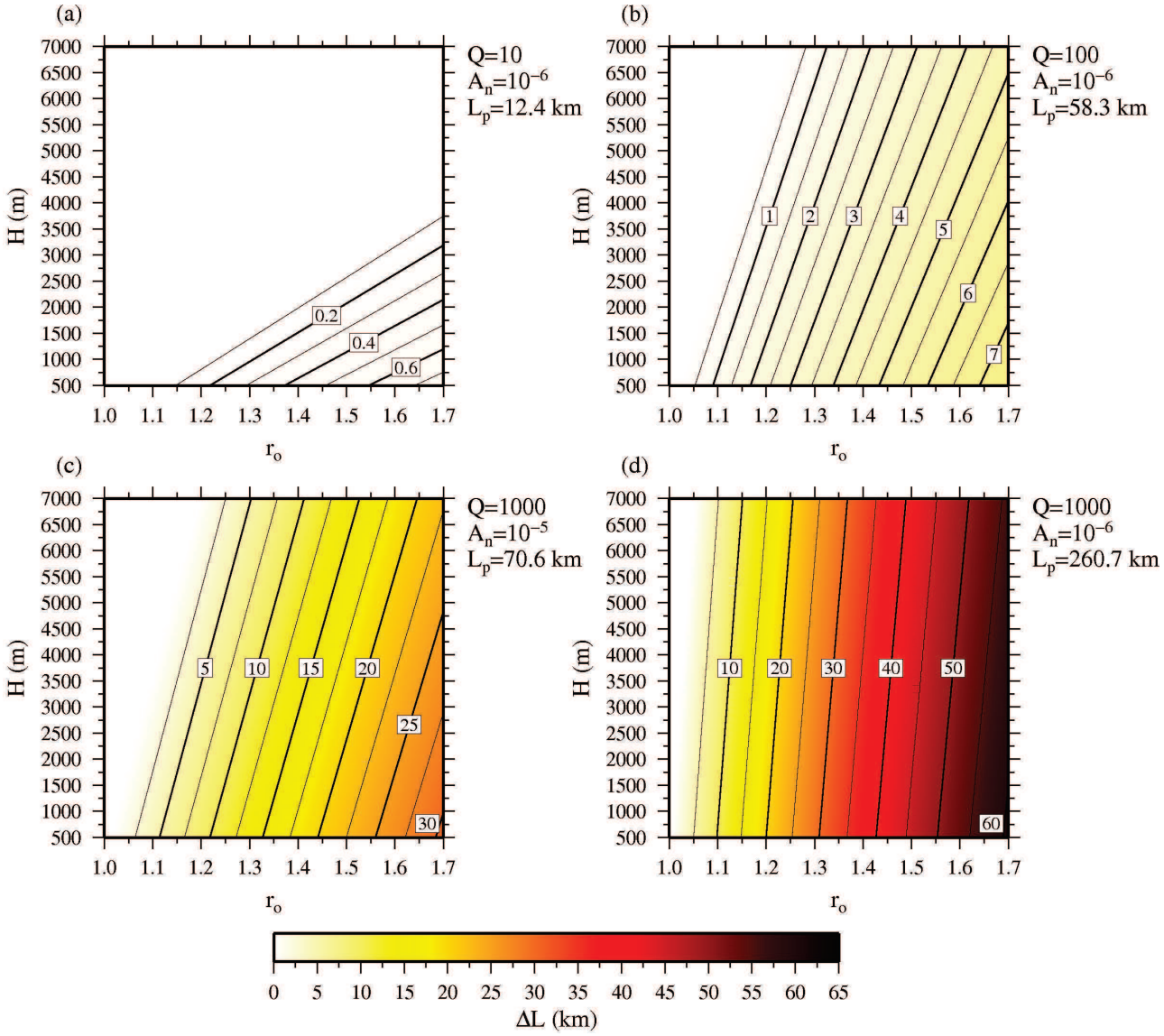

Figure 3.5. Diagrams of ΔL as a function of r_o and H, each for a particular combination of the Q factor and the ambient noise level A_n: (a) Q=10, $A_n=10^{-6}$, (b) Q=100, $A_n=10^{-6}$, (c) Q=1000, $A_n=10^{-5}$, and (d) Q=1000, $A_n=10^{-6}$.

Typical source amplitudes in WAS experiments are around 200 dB re 1 µPa at 1 m [e.g., Goold & Fish 1998; Cummings, 2004; MacGillivray & Chapman, 2005, Landrø & Amundsen, 2010], and for the dominant frequencies, the noise level is found between ~60 dB and ~110 dB [Coates, 2002]. We picked approximate end members for both the noise level (60 dB and 120 dB) and the source amplitude (180 dB re 1 µPa at 1 m and 240 dB re 1 µPa at 1 m). The end members define a range of A_n between 10^{-3} and 10^{-9} that we sampled by decades. See Table 3.2 for a compilation of the parameter values used in this second part of the synthetic modelling. A selection of the results is displayed in Fig. 3.5 and in Table 3.3.

Table 3.3. The maximum ray-path length increments (ΔL_{max}) for every combination of the Q factor and the relative ambient noise level (A_n), together with the corresponding maximum ray-path length of the primary arrival (L_p) and the percentage increment. L_p values marked with an asterisk (*) are a particular case in which the primary arrival amplitude is below the noise level from the start, that is, from the initial L_{min}=10 km, while the multiple amplitude remains above it for an $L_m=\Delta L+L_{min}$. However, the primary arrival is already below the noise level for $L_p<L_{min}$, which means that ΔL are in fact bottom limits of the actual achievable increments.

Q	A_n	L_p (km)	ΔL_{max} (km)	$\Delta L/L_p$ (%)
10	10^{-3}	-	0	0
10	10^{-4}	-	0	0
10	10^{-5}	-	0	0
10	10^{-6}	12.4	0.76	6.1
10	10^{-7}	16.3	0.81	5.0
10	10^{-8}	20.2	0.85	4.2
10	10^{-9}	24.3	0.87	3.6
100	10^{-3}	-	0	0
100	10^{-4}	10*	0.87	8.7
100	10^{-5}	28.2	5.9	20.9
100	10^{-6}	58.3	7.5	12.9
100	10^{-7}	93.3	8.3	8.9
100	10^{-8}	130.8	8.8	6.7
100	10^{-9}	169.8	9.0	5.3
1000	10^{-3}	-	0	0
1000	10^{-4}	10*	5.0	50
1000	10^{-5}	70.6	30.6	43.3
1000	10^{-6}	260.7	60.7	23.3
1000	10^{-7}	-	0	0
1000	10^{-8}	-	0	0
1000	10^{-9}	-	0	0

3.4. Results

A total of 445200 combinations of the four parameters (*F, D,* V_o and *G*) were analysed in the first

part of the synthetic test yielding the ratios r_o. The results were plotted as diagrams of r_o as a function of F and D, each for a particular velocity model defined by V_o and G. Representative examples are presented in Fig. 3.4. These diagrams show that r_o decreases with F and its highest values are systematically found for an approximate range between 4 Hz and 10 Hz, a range of frequencies that coincides well with the typical frequency spectrum of most crustal-scale WAS experiments, to the point that WAS data are usually filtered for similar frequency bands. Also, r_o decreases for increasing D, particularly for high frequencies, and the maximum value is always at D=0 m because D is proportional to the time lapse between the arrivals of the two interfering waves. Because the reflection at the sea-floor from water to crust does not involve a phase inversion, the highest two amplitudes interfering at the receiver will occur for the shortest time lapse. Concerning the velocity model, r_o increases with V_o, as should be expected on account of the increase in impedance contrast, whereas G has a small influence, and it is not possible to define a clear dependency. For F=10 Hz, the approximate central frequency of the source spectrum in WAS experiments, r_o takes a maximum value of ~1.7 for the V_o=4 km/s and D=0 m (Fig. 3.4e-f).

If r_o is smaller than 1, the phenomenon will not occur for that particular parameter combination. However, r_o being greater than 1 does not automatically imply that the phenomenon will occur, because the amplitude-decreasing effects of geometrical spreading and attenuation must be taken into account. To do so, in the second part of the test we sampled r_o, H and L to evaluate expressions (3.8) and (3.9) for the three different attenuation coefficients (a_c) and find their intersections with a series of ambient noise levels (A_n) to calculate ΔL. For a given $A_n - a_c$ combination, the maximum ray-path length for which the primary phase is visible (L_p) is constant as equation (3.8) does not depend on r_o or H. This means that only for ray-path lengths greater than L_p, the MSRI phase will provide information not available in the primary phase. The diagrams in Fig. 3.5 show ΔL as a function of r_o and H for representative $A_n - a_c$ combinations. ΔL increases with r_o, as it is proportional to the amplitude of the multiple, and decreases with H, because both the effects of attenuation and geometrical spreading grow stronger with this parameter.

For the highest attenuation coefficient (Q=10), and noise levels of 10^{-5} or higher, there is no ray-path length increment simply because amplitudes remain below the noise level. For the lower noise levels, between 10^{-6} and 10^{-9}, ΔL stays below 1 km (Fig. 3.5a). For the intermediate attenuation case (Q=100), there is a gain in ray-path length for noise levels of 10^{-4} or lower, although ΔL is still small, always below 10 km (Fig. 3.5b). As should be expected, the lowest attenuation coefficient (Q=1000) entails the most relevant ray-path length increment (Fig. 3.5c-d).

However, in terms of noise level it is the most restrictive case: only for A_n between 10^{-4} and 10^{-6} does it produce an increment in ray-path length, whereas above and below this range, both amplitudes are too low and too high respectively, and never cross the noise level for the 400 km considered. The maximum ΔL (ΔL_{max}) for A_n=10^{-5} and A_n=10^{-6} are 30.6 km and 60.7 km respectively (Table 3.3). Even though the latter case yields the overall highest ΔL_{max}, judging from their L_p values, 70.6 km and 260.7 km, the former can be considered the most profitable of the studied cases. These results are consistent with experimental evidence as for such L_p values most of the ray path is found in the upper mantle were the highest Q values occur.

3.5. Discussion

The synthetic test for our modelling scheme proves that the interference hypothesis is plausible. We have shown that under the appropriate physical conditions, the constructive interference of the multiple with its reflection at the sea-floor (MSRI) can produce an arrival with peak amplitude greater than that of the primary wave. The MSRI phase is in fact what we commonly refer to as the multiple on record sections. This mechanism explains the apparent physical paradox occurring in some record sections where multiple phases extend to longer offsets than their primary phases (Fig. 3.1).

The first part of the test (Fig. 3.4) shows that the interference systematically attains its highest r_o values within a range of dominant frequency F between 4 Hz and 10 Hz, which coincides with the typical frequency spectrum of marine WAS experiments. Logically, r_o grows for decreasing D distances (in particular for high F values) because this parameter determines the time lapse between the arrivals of the interfering waves at the receiver. Concerning the velocity model, r_o increases with the impedance contrast represented by V_o, as more energy is reflected back into the water layer at the sea-floor interface.

In the second part of the test, we calculated ΔL (Fig. 3.5) as a proxy for the potential offset increment obtained by incorporating the MSRI phase. As could be expected, ΔL increases with r_o (higher MSRI peak amplitude), decreases with H and a_c (greater amplitude decay), and with A_n (lower SNR). The results show that the phenomenon is only notable in media with a globally low attenuation (Q factor around 1000), and within a signal-to-noise ratio range from 100 dB (A_n=10^{-5}) to 120 dB (A_n=10^{-6}) which explains its relative rareness. For these relevant cases ΔL reaches

maximum values of ~30 km and ~60 km (Fig. 3.5c-d and Table 3.3). The relation between ray-path length and source – receiver offset is strongly dependent on the subsurface velocity distribution. Still, under usual circumstances, it is reasonable to assume an extension in the offset of the same order of magnitude of ΔL. This offset gain of a few tens of kilometres agrees well with experimental evidence (Fig. 3.1).

The most adequate geological conditions occur in basement outcrops, for instance in unsedimented young oceanic crust near mid-ocean ridges (Fig. 3.1a) or exhumed mantle in extensional basins (Fig. 3.1b). These geological contexts maximise the seismic impedance contrast at the sea-floor, while significantly reducing the general wave attenuation thanks to the absence of water-saturated sediments. Nonetheless, a bathymetry with the appropriate roughness to cause wave scattering in the ~5-15 Hz frequency range can diminish the effect of the seismic impedance contrast. Therefore, consolidated sedimentary sequences producing a smooth bathymetry may be a propitious setting to observe this phenomenon, as in the Tyrrhenian basin (Fig. 3.1b).

Whenever MSRI phases are longer than the corresponding primary ones, the inclusion of MSRI picks in travel-time modelling increases ray coverage, which results in tomographic models with better resolution. Also, the rays associated to these additional data will potentially have travelled deeper in the subsurface, thus extending the coverage to deeper layers. Since for oceanic crust studies, the average-quality WAS data include primary phases associated to rays travelling through the mantle, the possible supplementary MSRI picks would correspond to rays reaching further down into the mantle (see Table 3.3 for Q=1000). However, given the low velocity gradient in the mantle, this increase in penetration may be limited. Apart from the extra information, modelling the MSRI phase is useful because it allows to confidently differentiate them from other late arrivals.

Now that we understand the MSRI phenomenon, and given that it may occur in a variety of geological contexts and that it can contribute to the improvement of travel-time tomography models, it is our objective to incorporate it in TOMO3D as described in subsection 4.2.3.

CHAPTER 4: TOMO3D

4. TOMO3D

In this chapter I present all the technical details of TOMO3D, the 3-D travel-time inversion code that I have developed during the second half of my PhD. My goal within the Barcelona-CSI has been to develop a tool that could be applied to study the 3-D structure of convergent margins as well as the geometry of megathrust faults in order to overcome the issues listed at the end of chapter 2. Specifically, having information on the 3-D variations of the elastic properties and fault geometry is essential in order to understand the behaviour of earthquake rupture propagation. However, it must be noted that the interest of such a code exceeds the particular case of convergent margins and could be also applied to many geological targets that cannot be properly studied in 2-D.

TOMO3D is based on TOMO2D [Korenaga et al., 2000]. Source files have been rewritten for the 3-D version, that is, to redefine and incorporate variables and functions to account for the third dimension. The new code, as its 2-D predecessor, is written in C++ [Stroustrup, 2009], and its user manual and source files can be found in Appendix A. Once this task was completed, we had the sequential version of TOMO3D. The description of the code is divided in three main sections. The model parameterisation is the numerical formulation followed to approximate the real-world physical properties, such as wave propagation velocity, by a discrete set of nodes forming a mesh. The forward problem is the procedure to simulate the propagation of seismic waves and generate synthetic data. The solution of the inverse problem is the iterative update of the initial model to obtain a final model that minimises the misfit between synthetic and real data. The last section of this chapter details the parallelisation of the forward problem solver.

4.1. Model parameterisation

TOMO3D produces models of the subsurface P-wave velocity structure as well as of the geometry of energy reflecting boundaries (i.e. seismic reflectors). Velocity and depth models are represented by independent node meshes. These meshes are defined by the spatial coordinates of their nodes, which are each given a specific parameter value.

4.1.1. P-wave velocity

The 3-D velocity mesh (Fig. 4.1) is defined by the spatial coordinates of its nodes, and it hangs from the seafloor and the land surface. The spacing between nodes is variable, and it should be finer than the smallest spatial size of velocity changes that the model is expected to account for. For the sake of accuracy, node locations should be chosen to coincide with the locations of sources and/or receivers.

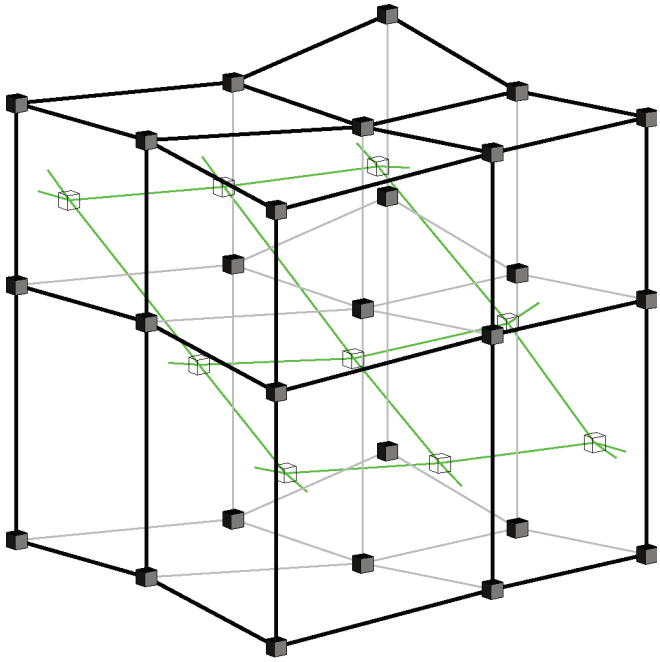

Figure 4.1. Portion of a 3-D velocity sheared mesh with variable spacing and a vertical shift corresponding to topography and/or bathymetry (black lines and filled-in nodes) combined with a portion of a 2-D depth mesh also with variable spacing (green lines and empty nodes). Velocity and depth nodes are independent from each other.

Each node in the mesh is assigned a value that corresponds to the P-wave velocity at that particular location in the subsurface. The discrete representation of the velocity distribution by explicitly defining values only at nodes was first introduced to ray tracing by Moser [1991] using a regular grid. Each set of 8 nodes defining a minimum-volume rectangular cuboid is known as a cell (Fig. 4.2a).

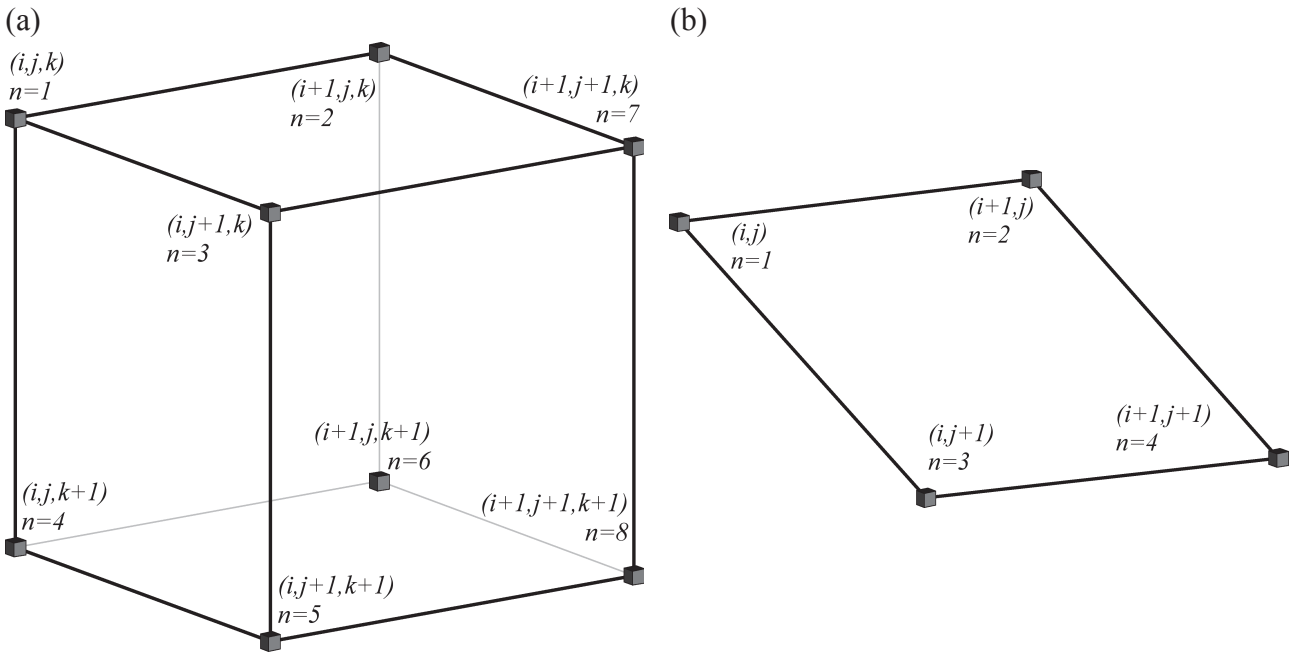

Figure 4.2. (a) 3-D velocity cell. Numbers indicate the local serial index of each node for the velocity interpolation in (4.1). Node n=1 is the origin for the local coordinates (r,s,t) which vary from 0 to 1 along the edges of the cell. (i,j,k) ordered triplets are global matrix indexes that run from 1 to the total number of nodal positions and increase in the growing direction of their corresponding spatial axes. Local and global indexes follow the same correspondence in all cells, e.g. node (i,j,k) is always node n=1. (b) 2-D depth cell. Numbers indicate the local serial index of each node for depth interpolation in (4.4). Node n=1 is the origin for the local coordinates (r,s) which vary from 0 to 1 along the edges of the cell. (i,j) ordered pairs are global matrix indexes that run from 1 to the total number of nodal positions and increase in the growing direction of their corresponding spatial axes. Local and global indexes follow the same correspondence in all cells, e.g. node (i,j) is always node n=1.

The velocity within each cell is found by trilinear interpolation of the values at each cell vertex [Thurber, 1983] so that the velocity field is continuous everywhere. For this purpose, we define local Cartesian cell coordinates *(r,s,t)*. The interpolated velocity can be expressed as

$$\begin{aligned} u(r,s,t) = {} & (1-r)\cdot(1-s)\cdot(1-t)\cdot u_1 + r\cdot(1-s)\cdot(1-t)\cdot u_2 + (1-r)\cdot s\cdot(1-t)\cdot u_3 + (1-r)\cdot(1-s)\cdot t\cdot u_4 \\ & + (1-r)\cdot s\cdot t\cdot u_5 + r\cdot(1-s)\cdot t\cdot u_6 + r\cdot s\cdot(1-t)\cdot u_7 + r\cdot s\cdot t\cdot u_8 \end{aligned} \qquad (4.1)$$

where u_n is the value of velocity at the node with local index n. The conversion between the local coordinates in (4.1) and the global coordinates (x,y,z) is given by

$$r=\frac{x-x(i)}{x(i+1)-x(i)} \qquad s=\frac{y-y(j)}{y(j+1)-y(j)} \qquad t=\frac{z-z(k)}{z(k+1)-z(k)} \quad (4.2)$$

where $x(i)$, $x(i+1)$, $y(j)$, $y(j+1)$, and $z(k)$, $z(k+1)$ are the coordinates of the nodes defining the cell that encloses (x,y,z). In order to account for geological relief, the mesh file includes a vertical shift, *b(i,j)* in (4.3), for each *(x(i),y(j))* nodal location. This sort of mesh is commonly known as sheared mesh [Toomey et al., 1994], and it is less demanding in terms of computational power than rectangular grids [White & Clowes, 1990]. Thus, in (4.2)

$$z=z'-b' \text{ with } b'=(1-r)\cdot(1-s)\cdot b(i,j)+r\cdot(1-s)\cdot b(i+1,j)+(1-r)\cdot s\cdot b(i,j+1)+r\cdot s\cdot b(i+1,j+1) \quad (4.3)$$

where z is depth in the mesh and z' is depth from the sea surface. Note that, because the mesh hangs from the bathymetry ($b'>0$) or topography ($b'<0$), the velocity model does not include neither water nor air layer, and constant velocities are assumed for both of them.

4.1.2. Reflector depth

Similarly, each node in the 2-D depth mesh is attributed the value of interface depth corresponding to its location (Fig. 4.1). This depth mesh is formulated as a floating reflector, that is, its nodes are independent from the velocity mesh, so that depth variations do not affect the velocity field. The velocity discontinuities typically associated to reflecting interfaces are modelled following the data-driven layer-stripping strategy described in subsection 5.1.3.

As the velocity field, interface geometry is defined to be continuous. Within 2-D cells (Fig. 4.2b) depth is bilinearly interpolated at any position within not coinciding with a node as expressed in (4.4)

$$d(r,s)=(1-r)\cdot(1-s)\cdot d_1+r\cdot(1-s)\cdot d_2+(1-r)\cdot s\cdot d_3+r\cdot s\cdot d_4 \quad (4.4)$$

where d_n is the depth at the node with local index n, and r and s are defined as in (4.2).

4.2. Forward problem

In TOMO3D, the forward problem is solved using a combination of two ray-tracing methods: the graph method [Moser, 1991] and the bending method [Moser et al., 1992a]. This hybrid approach to ray tracing is similar to that presented by Papazachos & Nolet [1997], Van Avendonk et al. [1998] and Korenaga et al. [2000]. It is based on Fermat's principle, that is, it does not solve the ray differential equations nor the eikonal equation. First, the graph method is applied to determine polygonal ray paths made of connected velocity mesh nodes that correspond to global minimum travel times within the chosen model parameterisation. These polygonal ray paths are subsequently used to generate good initial guesses for the bending method. In this second step the mesh nodes in each polygonal path are used as support points to represent the ray paths as Beta-splines. The interpolated ray path is then modified using the conjugate gradients method to minimise the travel time along it.

4.2.1. Graph method

The graph method is inherited from network theory [e.g. Dijkstra, 1959; Gallo & Pallottino, 1986], a field of computer and network sciences. Fig. 4.3 reproduces a scheme with the basic formulation of the graph method. In a medium represented as a mesh, this method finds the shortest route from an origin node to all other nodes in the network as a succession of node connections, sometimes referred to as polygonal path. The possible connections of each node are limited to the nodes within the selected neighbourhood, known as a forward star (FS) (Fig. 4.4). Each connection is assigned a measure of length in a predefined unit that works as a weight. For instance, in an electrical network this measure would be electrical resistance (or conductance), and on a road map it would be actual distance. Thus, if seismic travel time is chosen as nodal distance unit [Nakanishi & Yamaguchi, 1986], by Fermat's principle the graph method can be adapted to ray-tracing and used to generate approximate ray paths associated to first-arrival travel times [Moser, 1991]. Early examples of the usage of the graph method to travel-time tomography can be found in Toomey et al. [1994] and Zhang & Toksöz, [1998]. In addition to first-arrival ray paths, the calculation of ray paths of later arrivals corresponding to reflected waves can be solved by imposing a constraint defined by the reflecting surface and applying the graph method twice [Moser, 1991; Zhang et al., 1998]. More recently Bai et al. [2009] proposed a generalised strategy to trace multiply transmitted, reflected and converted arrivals.

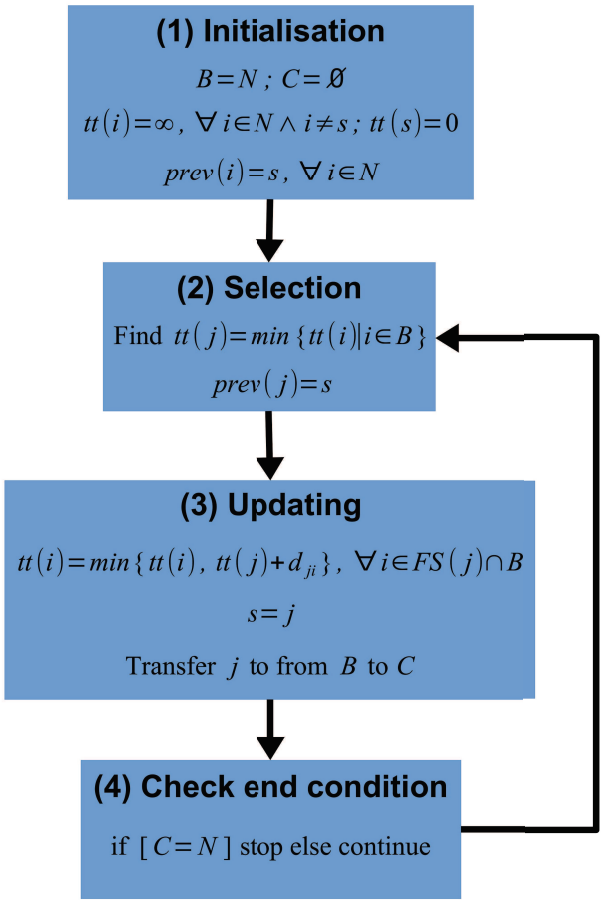

Figure 4.3. Formulation of the graph algorithm. (1) Initialisation: B and C sets are defined as equal to the set of all nodes N and the empty set, respectively. Travel times (tt) are initialised to "infinity" except for the travel time to the origin node or source (tt(s)) which is of course 0. Vector prev stores the previous node for each node and is set to the source node s for all of them including s itself. (2) Selection: The node j with the smallest travel time (tt(j)) in B is found, and prev(j) is set to s. Thus, the extraction of a ray path is completed when prev(s)=s. (3) Updating: The FS for j is built (FS(j)). Connection weights (d_{ji}) from j to the nodes in FS(j) that are still in B are calculated. For each of these nodes, the new travel time ($tt(j)+d_{ji}$) is compared to the old one (tt(i)) and the smallest of the two is kept. Finally, node j is transferred from B to C because tt(j) is the minimum travel time possible for j and it will not need further updates. (4) Check end condition: The graph solution is obtained when C=N, that is, when all nodes have been transferred from B to C. Otherwise the next iteration is started at step (2).

Nakanishi & Yamaguchi [1986] parameterised the model using constant velocity blocks each with a set of nodes distributed on its edges. This allowed Fischer & Lees [1993] to propose a local accuracy improvement imposing the fulfilment of Snell's law at the boundaries between these blocks. However, this higher accuracy is achieved at the expense of a much higher computational cost, because of the parameterisations needed to account for the complexity of real media are either a very fine grid of constant velocity blocks or the use of linear gradients within each velocity block as in Bregman et al. [1989]. Moser [1991] was the first to introduce to ray tracing the representation of the model as a discrete regular grid with velocity values explicitly defined only at its nodes. As described in the section 4.1, this is the kind of parameterisation used in TOMO3D, which actually allows for irregular discretisation, and it is nowadays the most common in applications of the graph method to travel-time tomography.

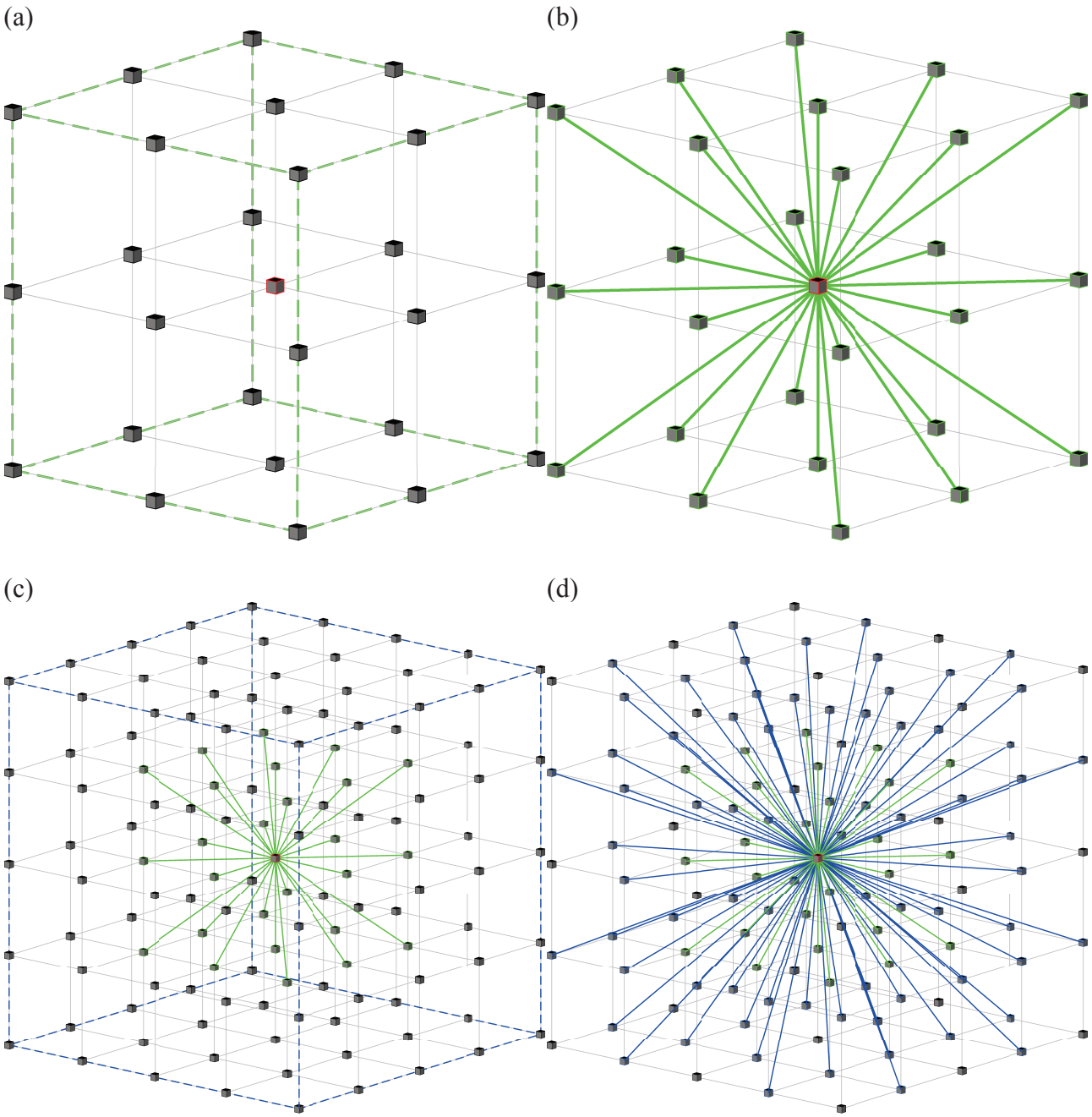

Figure 4.4. FS construction on sample portions of 3-D velocity mesh. The origin node is marked in red. (a) FS of (1,1,1). Connections are restricted to the nodes within the limits indicated by the green dashed lines. (b) Candidate path segments for (a). (c) and (d) idem as (a) and (b) for an FS of (2,2,2). This FS includes all previous connections plus those marked in blue. A higher-order FS increases the take-off angles, which increases accuracy as well as computational time. Note that the FS in (c) and (d) only considers nodes that yield candidate ray path directions not present in the FS in (a) and (b).

The sorting process of ordering the nodes in travel time to propagate the rays away from the source

is the most determinant step for the computational efficiency of graph algorithms. In Dijkstra [1959] this step takes the order of N^2 operations, N being the number of nodes in the mesh. Johnson [1977] introduced the heapsort method with computational time increasing as order $Nlog_2N$ (see also Gallo & Pallottino [1986]) that was adapted to travel-time tomography in Moser [1991]. This breakthrough is fundamental for the application of graph method to ray-tracing in 3-D media. Cheng & House [1996] showed that the quicksort method, also of order $Nlog_2N$, can be faster than heapsort. According to [Press et al., 1992] the speed is increased by a factor of 1.5 or 2. However, the worst performance for quicksort is of order N^2 and it occurs when the nodes are already ordered. In other words, the better ordered the nodes are, the worse the performance of quicksort, and given the nature of the graph algorithm –propagating the rays from a source node to the rest of the nodes in the network– it is not unlikely to have some degree of order in the node array. Also it is a moderately more complicated program than heapsort and so not that easily adapted [Press et al., 1992]. Klimeš & Kvasnička [1994] showed that replacing heapsort with what they named interval algorithm reduced the computational time of the graph-solving scheme in Moser [1991] by a factor of almost five for 3-D cases. They also proposed an optimised FS to increase travel time and ray path accuracy. Cao & Greenhalgh [1993] implemented a dynamic directed FS controlled by local velocity contrasts. Bai et al. [2010] introduced an irregular parameterisation of the velocity model that again improved efficiency while at the same time saving memory resources with respect to the strategy by Klimeš & Kvasnička [1994]. Nevertheless, all these developments focus on reducing computational time in order to achieve the necessary accuracy of ray paths required for travel-time tomography applications in a practical amount of time using the graph method alone. Since our ray-tracing strategy is to use the polygonal path to produce a good initial guess for bending refinement as in Korenaga et al., [2000], it suffices that it is a good global approximation regardless of possible local roughness. Even so, any improvement in the graph method will contribute positively to our hybrid strategy and should be considered in this thesis' outlook, although the benefits can be rather insignificant given the coarser parameterisations that our strategies permit.

The implementation of the graph method in TOMO3D follows the same scheme as in TOMO2D, except for the fact that nodes have three spatial coordinates associated, with all the technical changes that this implies in terms of defining new types of variables and rewriting all functions that involve any kind of dimensional operation. The most relevant function within the graph algorithm is the one in charge of calculating the weights of each possible two-node connection, that is, the travel time between neighbouring nodes as defined by the selected FS. In Moser et al. [1992b] this is done with Bresenham's algorithm [Newman and Sproull, 1973] but this uses the indexing of a rectangular

grid and thus can't directly work with a sheared mesh accounting for geological relief. In our case, each connection is divided into segments defined as the portions of path enclosed between consecutive parallel cell boundaries in the horizontal direction that maximises their number. Partial travel times are found as the multiplication of the explicit trilinear interpolation of slowness at the midpoint of each segment by that segment's length. The total travel time of a two-node connection is then the addition of all these partial travel times. Had we instead chosen to minimise the number of segments, the precision of travel time calculations for axis-parallel and near axis-parallel rays would be much lower than for the rest of possible rays. Our travel times are more accurate than in Moser et al. [1992b] at the expense of a slightly higher computational time, but that is particularly advantageous in the presence of strong velocity gradients.

The nature of the graph method is such that calculating one ray path is just as costly as calculating all of them. In other words, its efficiency improves with the difference in the number between sources and receivers. Indeed it is necessary to find all ray paths from the origin node to the rest of nodes in the mesh to ensure that all of them are shortest paths. Considering this and in order to improve efficiency, we apply the reciprocity principle so that the code solves the graph problem using either sources or receivers as origin nodes depending on whichever is smaller in number in each particular experiment. Thus, in marine wide-angle seismic experiments OBS/H receivers are treated as sources by the code. Henceforth, source will be used as a synonym of origin node in a graph problem. In addition, as the water layer is not part of the velocity model, the path through it is found by looking for the seafloor node that minimises the travel time to the shot location among those within a predefined radius around the projection of that location on the seafloor. Also for efficiency reasons, for each origin node the graph problem is only solved for the set of nodes within the minimum mesh volume that contains all corresponding source–receiver pairs.

Ultimately, the accuracy and the efficiency of the graph method are controlled by the chosen FS, that determines the search directions for candidate ray paths, and by the given parameterisation that affects the local coarseness of polygonal paths. Polygonal paths tend to overestimate travel times because they zigzag especially in the directions not included in the FS, even if they keep the overall azimuthal and incidence angles. The FS may limit the allowed connections to nodes in the immediate vicinity of the origin node, but for a better coverage of ray path directions it must consider connections to nodes other than the nearest neighbours [Moser et al., 1992b]. To improve the accuracy of the graph ray paths, one must refine the mesh and/or increase the order of the FS (Fig. 4.4c,d). The alternative in TOMO3D though is to use the polygonal path to interpolate an

initial guess for the bending refinement method. Polygonal paths correspond to global travel time minima for the chosen model discretisation, which makes them optimal for the bending refinement.

4.2.2. Bending method

There have been two main approaches to the bending method. The earlier variant [Julian & Gubbins, 1977; Pereyra et al., 1980; Farra, 1992] posed a linearised system of equations by discretising the ray path and using finite differences to express the derivatives in the ray tracing equations. This had to be solved iteratively due to the linear approximation. In the second formulation of the bending problem [Um & Thurber, 1987; Prothero et al., 1988, Moser et al., 1992a] rays (Γ) are derived from the minimisation of the travel time function $T(\Gamma)$. This second approach is known to be more stable than the older one [Moser et al., 1992a] and is nowadays the prevailing formulation of the bending problem. Nonetheless, the bending method alone has converging problems in complicated media, such as slow convergence or convergence to local minima, which grow even more severe in 3D. This is caused by poor initial ray path candidates. Using graph ray paths to interpolate initial guesses overcomes these limitations because such rays are very close to the exact ray paths, that is, more precisely, that each polygonal path is within one mesh spacing of the respective exact path.

Regarding the use of the graph method on its own, for the same target accuracy, the hybrid approach is generally faster than using a finer mesh and a higher-order FS, whereas for the same computational time it is more accurate. Fig. 4.5 compares graph polygonal paths with the ray paths resulting from the bending refinement. No general demonstration exists for this statement, but it could be proven for each particular case. Korenaga et al. [2000] provided a simple 2-D example, but it suffices to know that this is all the more so in 3D. Indeed, while the number of support points used to represent a ray path with a Beta-spline interpolation is of the same order of magnitude in 2D as in 3D, the number of nodes in the graph problem is increased at the very least by one order of magnitude with the new dimension. Hence, the hybrid approach is favoured because, instead of refining the entire mesh, bending only involves the refinement of a small number of nodes in the mesh, that is, those corresponding to the polygonal paths. It is worth noting that a trade-off exists between the graph and bending methods in terms of computational time: a higher-order FS increases the time spent solving the graph problem but provides a better initial guess that reduces the time spent refining it in bending. The ideal FS depends on the parameterisation and complexity

of the velocity model required for each specific study case as well as on the particular acquisition configuration and data set, so a general theory is out of the question. In the case of crustal studies, empirical evidence supports the use of a higher-order FS in the vertical direction which is consistent with the fact that the velocity gradient is much more pronounced in this direction [Van Avendonk, 1998, Korenaga, 2000].

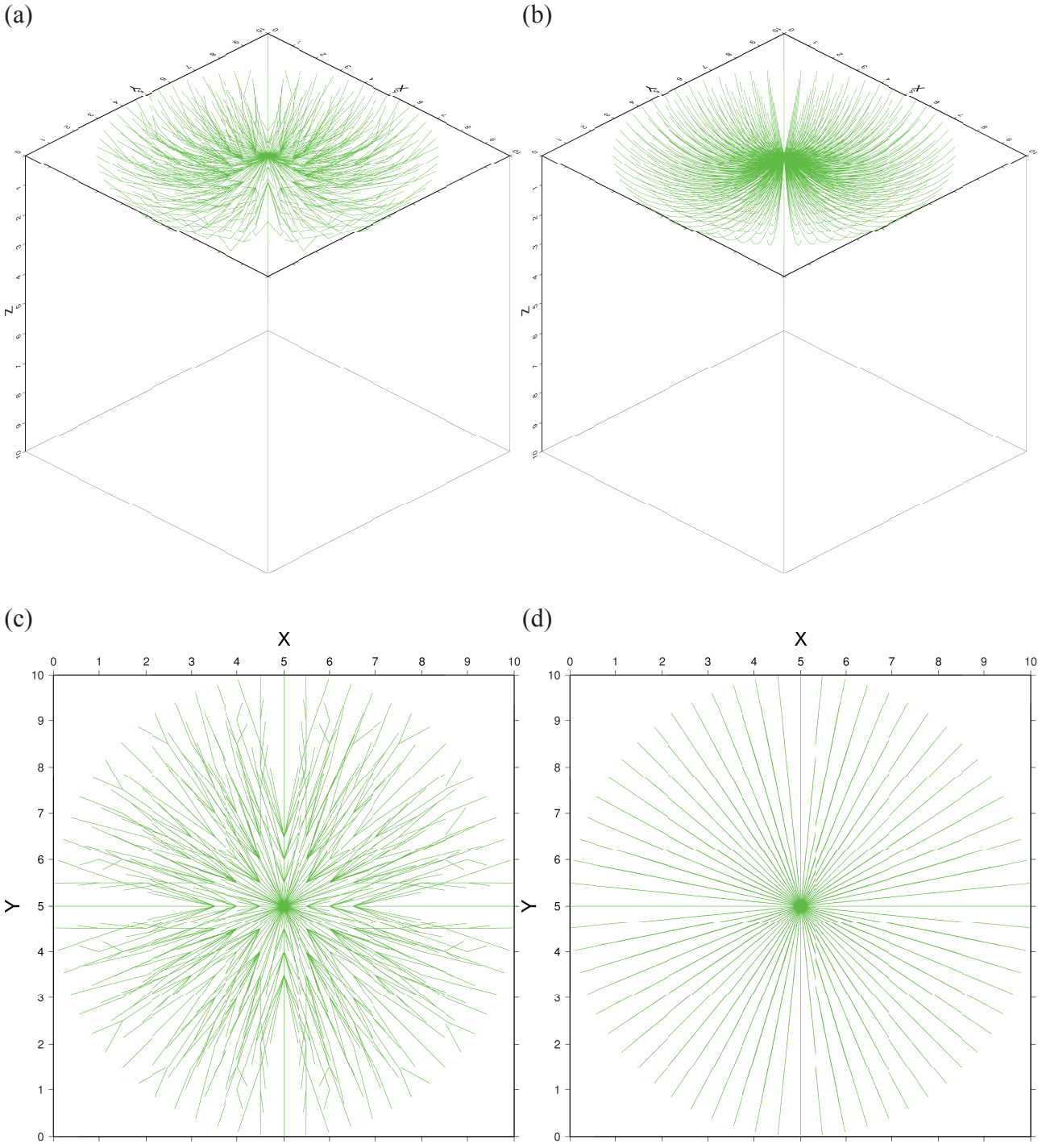

Figure 4.5. (Continues on the next page).

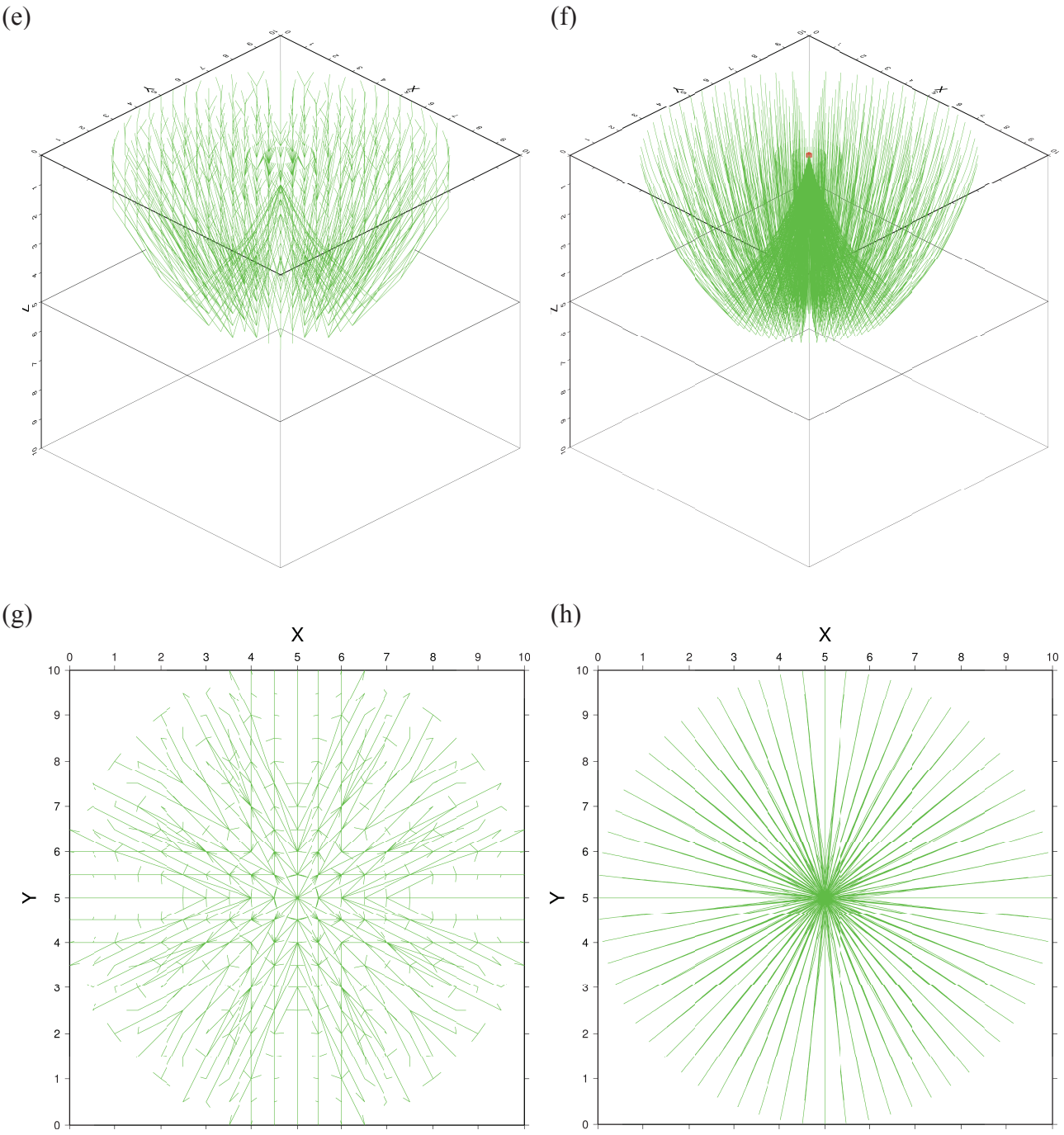

Figure 4.5. Sample polygonal paths and ray trajectories for refractions and reflections calculated with TOMO3D. Polygonal paths are obtained with the graph method and then used to build initial guess paths for the bending method, which produces the refined ray trajectories. Polygonal paths for refractions are plotted in (a) and (c), and the corresponding refracted paths after bending in (b) and (d). Analogously, polygonal paths for reflections are in (e) and (g), and the corresponding reflected paths after bending in (f) and (h). The velocity model follows a 1-D linear gradient with depth which, together with the horizontal reflector, explain the symmetry exhibited by the ray paths.

The bending refinement method as described in Moser et al. [1992a] is thus applied to the polygonal paths resulting from the graph method to produce continuous ray paths. The mesh nodes forming the polygonal paths are taken as support points to parameterise the rays as Beta-splines. A Beta-spline is a curve made of connected segments ($\mathbf{Q}_i$) each expressed on the basis of four consecutive support points

$$\mathbf{Q}_i(q) = \sum_{r=-2}^{1} b_r(\beta_1, \beta_2, q)\mathbf{V}_{i+r} \quad \text{for } 0 \leqslant q \leqslant 1 \qquad (4.5)$$

where q is the local coordinate for the i-th segment, b_r are four cubic polynomials in q whose coefficients are defined by the shape parameters β_1 and β_2, and $\mathbf{V}_{i+r}$ are the four support points that are averaged with b_r acting as weights to produce the Beta-spline segment. Successive segments share three consecutive support points, maximising overlap. These polynomial weights are built as

$$b_r(\beta_1, \beta_2, q) = \sum_{g=0}^{3} c_{gr}(\beta_1, \beta_2) q^g \quad \text{for } r = -2, -1, 0, 1 \qquad (4.6)$$

The c_{gr} coefficients are determined from the continuity conditions between consecutive segments, which depend on the shape parameters,

$$\begin{aligned} \mathbf{Q}_{i+1}(0) &= \mathbf{Q}_i(1) \\ \frac{d\mathbf{Q}_{i+1}}{dq}(0) &= \beta_1 \frac{d\mathbf{Q}_i}{dq}(1) \\ \frac{d^2\mathbf{Q}_{i+1}}{dq^2}(0) &= \beta_1^2 \frac{d^2\mathbf{Q}_i}{dq^2}(1) + \beta_2 \frac{d\mathbf{Q}_i}{dq}(1) \end{aligned} \qquad (4.7)$$

The smoothest Beta-spline curves possible are obtained for β_1=1 and β_2=0 which impose the continuity of the first and second derivatives. Beta-splines naturally do a good job mitigating the possible poor ray path approximations, particularly near the end-points, arising from the limited search of azimuthal and take-off/incidence angles in the FS. Excessively long segments produced by high-order FS are split to introduce intermediate support points.

This formulation is preferred over the finer resampling of polygonal paths [e.g. Pereyra et al., 1980; Van Avendonk et al., 2001a] for a number of reason described in Moser et al. [1992a]. For instance, interpolation saves computational time because it avoids having to increase the resampling of ray paths to make them behave correctly in the presence of strong gradients or especially in low velocity zones. Also, close ray path points are not completely independent from each other because of the basic fact that ray paths are continuous curves. In a path resampling scheme additional constraints on ray path points are needed to impose such continuous behaviour. On the contrary, Beta-spline interpolation requires only a few parameters to describe complex continuous curves that can latter be sampled as necessary. In other words, the number of points to be perturbed in the minimisation process to adequately modify the ray path is smaller than the number of points for a sufficiently accurate integration of travel time along it. This formulation intrinsically supports the dependency between nearby ray points, and it facilitates the convergence of the conjugate gradients minimisation of $T(\Gamma)$. This method is chosen over Newton's and the steepest decent methods because it is less demanding in terms of memory requirements than the first [Stoer & Bulirsch, 1980], and it converges faster than the second [Press et al., 1992]. In the Beta-spline interpolation scheme of TOMO3D, for a polygonal path with k support points, $T(\Gamma)$ is constructed following the trapezoidal rule as

$$T(\Gamma)=\sum_{i=1}^{k+1}\sum_{j=1}^{m}\frac{1}{2}\left(u\left(\mathbf{Q}_i(q_j)\right)+u\left(\mathbf{Q}_i(q_{j-1})\right)\right)\left\|\mathbf{Q}_i(q_j)-\mathbf{Q}_i(q_{j-1})\right\| \quad \text{with } q_j=j/m \tag{4.8}$$

where $\|\cdot\|$ is the Euclidian norm, k+1 is the total number of segments, and m is the number of sampling points per segment. k+1 segments are produced because two copies of the first and last support points in the polygonal path are added to the vector of support points at the beginning and at the end, respectively. In the Beta-spline parameterisation, this repetition forces the interpolated ray to pass through the repeated support point, in this case the end points which the ray must visit necessarily. These end points are the source and either the receiver or the entry point at the seafloor, and their location is known. m is currently determined empirically to provide the desired accuracy in travel time calculation (see subsection 4.2.4). In the case of resampling schemes, the number of ray points is gradually increased throughout the minimisation process, which has been claimed to accelerate convergence. However, in my opinion, the choice of the manner in which the number of points is increased can be as subjective as the empirical choice of m, and it might even result in a slower convergence if not adequate to a specific case. Nonetheless, a similar adaptive approach

could be applied to m, but it suffices to test that the selected value produces a clearly satisfactory accuracy, and as said before, resampling inevitably results in higher computational time. The gradient of $T(\Gamma)$ with respect to the support points is calculated as

$$\frac{\partial T}{\partial \mathbf{V}_i} = \sum_{j=i-1}^{i+2} \int_0^1 \left(u\left(\mathbf{Q}_j(q)\right) b'_{i-j}(q) \frac{\mathbf{Q'}_j(q)}{\|\mathbf{Q'}_j(q)\|} + \|\mathbf{Q'}_j(q)\| \nabla\left(u\left(\mathbf{Q}_j(q)\right)\right) b_{i-j}(q) \right) dq \qquad (4.9)$$

where the prime indicates the derivative with respect to q. Minimisation is stopped when the difference between successive travel times is smaller than a certain tolerance value. This threshold is set to 0.1 times the desired travel time resolution. When refining a path that interacts with the reflector, the conjugate gradients search is modified to force the ray to keep that interaction, as explained in the next subsection 4.2.3. Finally, since the locations of the end points are known, they are fixed and left out of minimisation by setting $\frac{\partial T}{\partial \mathbf{V}_i}$ to 0 at the respective support points.

4.2.3. Seismic rays: refractions, reflections and MSRI

TOMO3D forward problem solver traces rays corresponding to refracted and reflected primary waves, and to their respective water layer multiples or more precisely their MSRI (Multiple–Seafloor Reflection Interference) as interpreted by Meléndez et al. [2014]. The ray tracing of refractions consists in solving the graph problem for each source to find the ray paths to all receivers, and then refining them by the bending method. Reflection ray-tracing needs to be constrained so that rays visit the pertinent depth interface. This requires at least one and at most two more graph solutions that can be associated to the downward and upward propagations. The downward problem is identical to the refraction problem except that only nodes above and at the interface are considered. The velocity nodes at the interface are defined as those closest to the depth interface, and when extracting the polygonal ray paths their vertical coordinate is modified to the depth of the interface at their horizontal location. In the upward problem the travel times of the interface nodes from the downward solution are kept and the graph algorithm is restarted, again only for nodes above and at the interface. This constrained ray-tracing scheme provides the interface-reflected ray path with minimum travel time, and is founded on Huygens' principle as interface nodes act as sources of the upgoing wavefronts/ray paths. For a more accurate solution, the downward and upward problems must be solved. On the contrary, if efficiency is prioritised, the

refraction solution is used to approximate the downward solution, and only the upward problem is solved. Just as with refraction, the bending method is only applied once, but using an adapted version of the conjugate gradients minimisation. A Beta-spline curve passes through a point if this is included three consecutive times in the vector of support points. Upon construction initial polygonal paths include the reflection node at the subsurface interface three times. Hence, the conjugate gradients method is modified so that at each iteration these three points are equally changed, keeping them identical to each other throughout the process of minimisation. Additionally, because these points are required to stay on the interface, no variation in the vertical direction is applied to them, and their vertical coordinate is given by the depth of the reflector at their horizontal location. MSRI ray paths are identical to those of their primary counterparts except for the additional propagation within the water layer. The code assumes constant velocity for the water layer, so that MSRI travel times are computed as the addition of the primary travel times and the two-way travel time delay due to the vertical propagation through the water layer at the receiver location. The ray-tracing scheme does not need to be modified to account for the MSRI rays because the modelling is restricted to the subsurface, and therefore the portion of ray path in the water layer is not used in the inversion. The inclusion of MSRI picks would improve ray coverage, with the consequent increase model resolution and size. Moreover, the possibility to model this phase may prove useful in validating the interpretation of certain phases as late arrivals.

4.2.4. Accuracy tests: travel times and ray paths

A simple test model was created to check that our implementation of the hybrid ray tracing method was working correctly and free of any major coding issues. Additionally, the test showed that this method is sufficiently accurate for the typical data resolution, chiefly of wide-angle experiments. The velocity model was a 1-D linear velocity function of depth on a 10-km sided cube with no topography, and the reflector model was a flat surface at 5 km depth. A node spacing of 0.5 km was used for both velocity and depth models. The ray-tracing method uses a relatively low-order FS of (3,3,3), 8 sample points per Beta-spline segment (m=8), and a conjugate gradients tolerance of 0.1 ms. Ray paths calculated with TOMO3D's hybrid method are plotted in Fig. 4.5b,d,f,h. For such model, analytical solutions exist for the ray trajectories and the associated travel times [Sheriff & Geldart, 1995] so that misfits can be computed (Fig. 4.6). Despite having no 3-D structure this is an adequate test as vertical changes are dominant in the Earth's subsurface. Travel time misfit is obtained as the difference between analytical and calculated values. Ray path misfit is a weighted

average expressed as

$$\delta p = \sqrt{\sum_{i=1}^{N} p_i \cdot \left[\left(\delta r_i \right)^2 + \left(\delta z_i \right)^2 \right]} / \sum_{i=1}^{N} p_i \qquad (4.10)$$

where i indicates the i-th sampling point of the calculated ray, δr_i and δz_i are the horizontal and vertical misfits respectively, and p_i is the length of that segment. In turn, δr_i (and equivalently δz_i) is defined as the difference in length between the horizontal projections of the analytical and calculated trajectories at the i-th segment. For both refractions and reflections, the average ray path and travel time misfits are respectively ~6 m and ~1 ms. The latter is as expected for the chosen conjugate gradients tolerance. Regarding typical wide-angle experiments, these misfits are satisfactory considering that typical spatial resolution is ~1 km and thus node spacing in velocity grids is of several hundreds of meters, and the typical data sampling interval is ~10 ms. Nevertheless, if necessary, accuracy can still be improved refining the model discretisation, selecting a higher-order FS, and/or using more sampling points per Beta-spline segment.

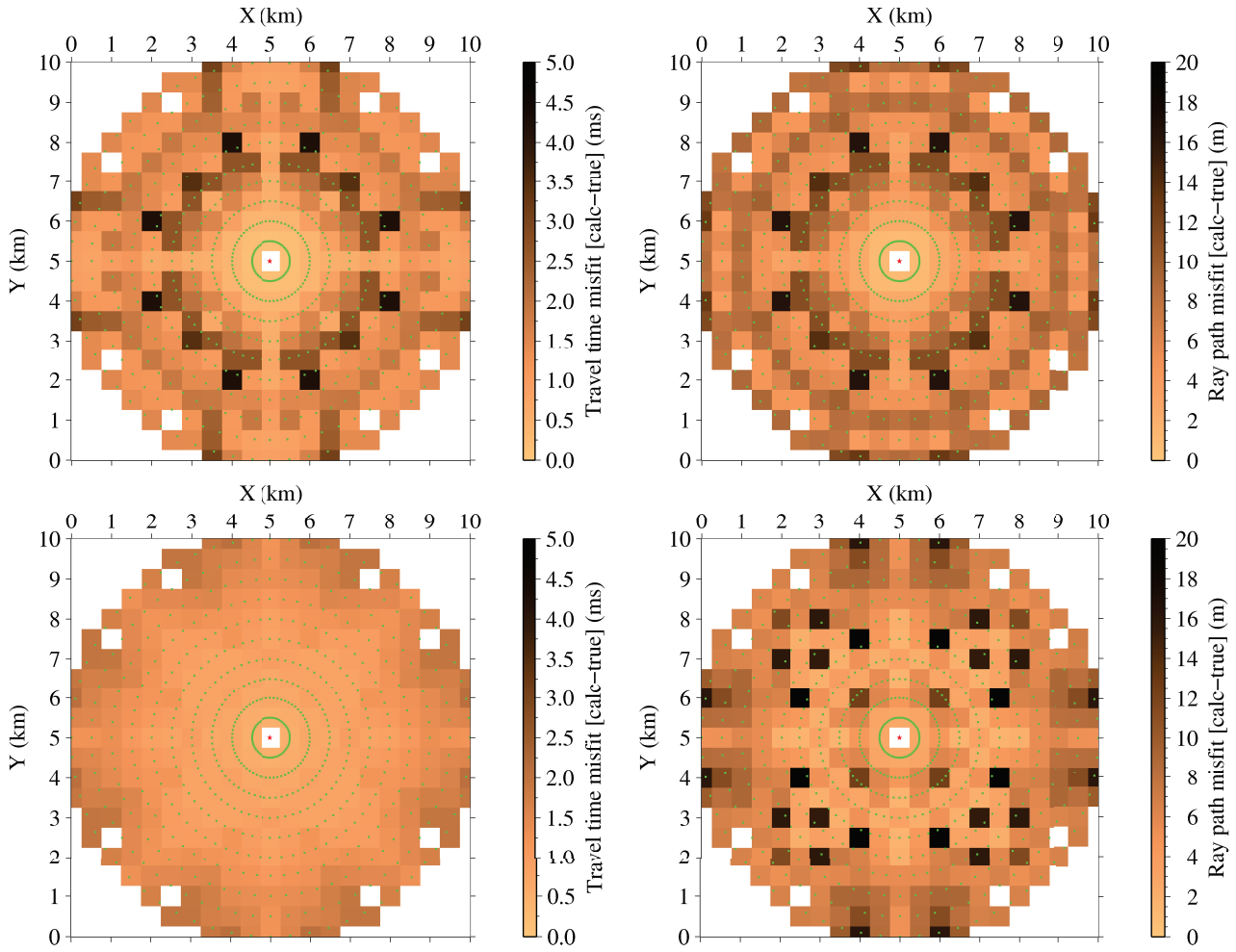

Figure 4.6. Travel-time and ray-path misfits for refracted (top) and reflected (bottom) data. A discrete plot with 2-D bins is preferred over a smoothened one because significantly different misfit values are obtained for close locations. As mentioned in the text, this depends on the selected parameterisation and FS definition that inevitably privilege certain directions over others, and is ultimately intrinsic to the use of a Cartesian coordinate system. The geometry of the acquisition configuration included 640 receivers (green dots) equally distributed in 10 concentric circles and 1 centred source (red star), all located at the upper face of the cube. Given this acquisition configuration and the velocity and depth models used in this test, the observed symmetry in the misfit distributions can be anticipated, and it means that the code does not present undesirable directional biases.

4.3. Inversion of travel-time residuals

Once the forward problem is solved, rays are fixed throughout the inversion, and the misfit between calculated and observed travel times is attributed to errors in the model parameters. In reality travel

time is a nonlinear function of slowness because the ray path depends on velocity and, in the case of reflections, also on interface depth. However, for a smoothly varying model, the dependency of travel time on ray path (Γ) is of second order. Thus, for a small parameter perturbation ($\mathbf{\delta m}$) it can be assumed that $\Gamma(\mathbf{m}+\mathbf{\delta m})\approx\Gamma(\mathbf{m})$ [Aldridge, 1992]. This approximation allows posing a linearised relation between travel time residuals and parameter perturbations which is then iteratively inverted.

4.3.1. Linearised forward problem equation

Refraction (δt_i^0) and reflection (δt_j^1) travel time residuals for a given slowness (u or velocity $v=1/u$) and depth model are turned into parameter perturbations (δu and δz, respectively) following the integral equations for refracted (Γ_i^0) and reflected (Γ_j^1) ray paths

$$\delta t_i^0 = \int_{\Gamma_i^0} \delta u \; d\Gamma \qquad (4.11)$$

$$\delta t_j^1 = \int_{\Gamma_j^1} \delta u \; d\Gamma + \left[\frac{\partial t}{\partial z}\right]_{(x,y)_j} \delta z \qquad (4.12)$$

$$\left[\frac{\partial t}{\partial z}\right]_{(x,y)_j} = \frac{2\cdot\cos\theta\cdot\cos\beta}{v\left((x,y)_j\right)} \qquad (4.13)$$

where the latter reflects at the position $(x,y)_j$ on the interface, and θ is the incidence angle, β is the local slope of the reflector, and v is the velocity at this point [Bishop et al., 1985]. Equations (4.11) and (4.12) make use of the fact that the dependency of travel time on ray path is of second order in relation to velocity [Rawlinson & Sambridge, 2003]. Then, considering the discretisation and interpolation in our parameterisation of the problem, (4.11) and (4.12) can be unified in the following linear system:

$$\begin{pmatrix} \mathbf{\delta t^0} \\ \mathbf{\delta t^1} \end{pmatrix} = \begin{pmatrix} \mathbf{G^{u0}} & \mathbf{0} \\ \mathbf{G^{u1}} & w\,\mathbf{G^{z}} \end{pmatrix} \begin{pmatrix} \mathbf{\delta u} \\ \frac{1}{w}\mathbf{\delta z} \end{pmatrix} \qquad (4.14)$$

where $\mathbf{\delta t}=(\mathbf{\delta t^0},\mathbf{\delta t^1})=\mathbf{t^{obs}}-\mathbf{t^{calc}}$ are respectively the vectors of refraction and reflection travel time residuals, $\mathbf{G^{u0}}$, $\mathbf{G^{u1}}$ and $\mathbf{G^{z}}$ are the Fréchet derivative matrices (or kernels) for velocity and depth, and $\mathbf{\delta u}$ and $\mathbf{\delta z}$ are the vectors of parameter perturbations. Kernels are built considering equations (4.11) and (4.12). As shown in (4.14), both refractions and reflections contribute to the complete velocity kernel $\mathbf{G^{u}}$, whereas only reflections contribute to $\mathbf{G^{z}}$. Each element in the velocity kernel is the length of the portion of a specific ray path partitioned to a relevant velocity parameter consistently with the adopted trilinear interpolation. Similarly, each element in the depth kernel is

the portion of (4.13) for a specific reflected ray path partitioned to a relevant depth parameter consistently with the adopted bilinear interpolation. The depth-kernel weighting parameter w is described in Korenaga et al., [2000]. It is important to mention that it is not an inversion parameter. Instead, its purpose is the empirical investigation of the inherent velocity–depth trade-off in reflection data if (4.14) is singular [Korenaga, 2011].

4.3.2. Regularisation constraints

Typically, the number of available data is smaller than the number of model parameters, which prevents the inversion of (4.14) due to singularity of the kernels. This is solved by imposing regularisation constraints to the system, usually in the form of smoothing matrices on the parameter perturbations (4.15). The program works with three velocity smoothing matrices ($\mathbf{L}^{\mathbf{u}}$), one for each direction, because it uses independent 1-D constraints [Toomey et al., 1994]. In this way we avoid dealing with a dense matrix resulting from a fully 3-D smoothing, which would also be rather demanding in terms of memory storage. Similarly, two depth smoothing matrices ($\mathbf{L}^{z}$) are used.

$$\begin{pmatrix} \boldsymbol{\delta t}^{0} \\ \boldsymbol{\delta t}^{1} \\ \mathbf{0} \\ \mathbf{0} \\ \mathbf{0} \\ \mathbf{0} \\ \mathbf{0} \end{pmatrix} = \begin{pmatrix} \mathbf{G}^{\mathbf{u0}} & \mathbf{0} \\ \mathbf{G}^{\mathbf{u1}} & w\,\mathbf{G}^{\mathbf{z}} \\ \lambda_u \mathbf{L}^{\mathbf{uX}} & \mathbf{0} \\ \lambda_u \mathbf{L}^{\mathbf{uY}} & \mathbf{0} \\ \lambda_u \mathbf{L}^{\mathbf{uZ}} & \mathbf{0} \\ \mathbf{0} & w\lambda_z \mathbf{L}^{\mathbf{zX}} \\ \mathbf{0} & w\lambda_z \mathbf{L}^{\mathbf{zY}} \end{pmatrix} \begin{pmatrix} \boldsymbol{\delta u} \\ \frac{1}{w}\boldsymbol{\delta z} \end{pmatrix} \quad (4.15)$$

Coefficients λ_u and λ_z determine the relative importance of smoothing with respect to the kernels, and are usually selected empirically. Alternatively, Korenaga [2011] defined λ_u and λ_z as functionals of misfit, so that they are adjusted throughout the inversion. These functionals still include empirical, case-dependent parameters, but their choice is less subjective. This approach permits a better exploration of the model space because it keeps the importance of smoothing proportionate with the kernels, that is, it prevents smoothing matrices from dominating the inversion.

Smoothing matrices are built considering the decay of a Gaussian function over selected correlation lengths that can be specifically set for each node. The elements of these five matrices can be

expressed as follows

$$L_{ii} = \sum_j \exp\left(-\left(x_j - x_i\right)^2 / l_i^2\right) \quad (4.16)$$

$$L_{ij} = \exp\left(-\left(x_j - x_i\right)^2 / l_i^2\right) \text{ if } |x_j - x_i| \leqslant l_i \text{ and } L_{ij} = 0 \text{ if } |x_j - x_i| > l_i \quad (4.17)$$

where x_i and x_j represent the positions of nodes i and j in one of the spatial dimensions of the velocity and depth models, and l_i is the correlation length assigned to the i-th parameter (i.e. node i) for that dimension. Thus, the smoothness equation for the i-th parameter in that model dimension can be written as

$$0 = \sum_j \left(\exp\left(-\left(x_j - x_i\right)^2 / l_i^2\right) \cdot \delta m_j\right) - \left(\sum_j \exp\left(-\left(x_j - x_i\right)^2 / l_i^2\right)\right) \cdot \delta m_i \quad (4.18)$$

Because the initial model is generally far from the true one, this system of linear equations (4.15) must be solved iteratively. However, this can lead to excessively large model perturbations producing inversion instabilities, particularly during the first iterations. In such cases, damping constraints on velocity and/or depth perturbations can be incorporated to stabilise the inversion as indicated in Van Avendonk [1998]. If the iterative inversion finds a good convergence trend, damping constraints are not necessary after the first iterations. Damping equations are derived from the integrals of the squared parameter perturbation over each model cell

$$\int_V (\delta u)^2 \, dxdydz \quad (4.19) \qquad \int_S (\delta z)^2 \, dxdy \quad (4.20)$$

where V and S are the volume and surface of velocity and depth cells, respectively. For the discrete parameterisation of the models these integrals can be expressed in matricial form as

$$\frac{V}{216}\begin{pmatrix}\delta u_1\\ \delta u_2\\ \delta u_3\\ \delta u_4\\ \delta u_5\\ \delta u_6\\ \delta u_7\\ \delta u_8\end{pmatrix}.\begin{pmatrix}24 & 4 & 4 & 2 & 4 & 2 & 2 & 1\\ 4 & 24 & 2 & 4 & 2 & 4 & 1 & 2\\ 4 & 2 & 24 & 4 & 2 & 1 & 4 & 2\\ 2 & 4 & 4 & 24 & 1 & 2 & 2 & 4\\ 4 & 2 & 2 & 1 & 24 & 4 & 4 & 2\\ 2 & 4 & 1 & 2 & 4 & 24 & 2 & 4\\ 2 & 1 & 4 & 2 & 4 & 2 & 24 & 4\\ 1 & 2 & 2 & 4 & 2 & 4 & 4 & 24\end{pmatrix}\begin{pmatrix}\delta u_1\\ \delta u_2\\ \delta u_3\\ \delta u_4\\ \delta u_5\\ \delta u_6\\ \delta u_7\\ \delta u_8\end{pmatrix} \quad (4.21)$$

$$\frac{S}{36}\begin{pmatrix}\delta z_1\\ \delta z_2\\ \delta z_3\\ \delta z_4\end{pmatrix}.\begin{pmatrix}4 & 2 & 1 & 2\\ 2 & 4 & 2 & 1\\ 1 & 2 & 4 & 2\\ 2 & 1 & 2 & 4\end{pmatrix}\begin{pmatrix}\delta z_1\\ \delta z_2\\ \delta z_3\\ \delta z_4\end{pmatrix} \quad (4.22)$$

where δu_i and δz_j are respectively the velocity and depth perturbations at the cell nodes. The Cholesky decomposition is applied to these matrices, in order to obtain an expression that is linear with parameter perturbations as are the linearised forward problem and the smoothing constraints. This procedure finds an upper triangular matrix **B** fulfiling that $\mathbf{A}=\mathbf{B}^{\mathbf{T}}\mathbf{B}$, where $\mathbf{B}^{\mathbf{T}}$ is the transpose of **B**. For instance, if **A** represents the matrix in (4.22), the right hand side of the resulting expressions (**Bδm**) is the basis for building the depth damping matrix, and its exact expression is as follows

$$\frac{\sqrt{S}}{6}\begin{pmatrix}2 & 1 & 0.5 & 1\\ 0 & \sqrt{3} & \sqrt{3}/2 & 0\\ 0 & 0 & \sqrt{3} & \sqrt{3}/2\\ 0 & 0 & 0 & 1.5\end{pmatrix}\begin{pmatrix}\delta z_1\\ \delta z_2\\ \delta z_3\\ \delta z_4\end{pmatrix} \quad (4.23)$$

The analogous exact expression for the velocity damping matrix is much more cumbersome, but it suffices to say that within the code both decompositions are performed using the same numerical recipe. Velocity nodes may belong to 1, 2, 4 or 8 different 3-D cells, and depth nodes to 1, 2 or 4 different 2-D cells. The velocity and depth damping matrices ($\mathbf{D}^{\mathbf{u}}$ and $\mathbf{D}^{\mathbf{z}}$) are constructed by adding for each node the contributions from the different cells which it belongs to. Whenever the average perturbation for velocity and/or depth is greater than the user-defined limits, the corresponding damping matrix is added to (4.15) yielding (4.24). In this automatic damping strategy, the code automatically finds the appropriate weights, α_u and α_z by the secant and bisection method so that the inversion keeps the average perturbation below this limit.

$$\begin{pmatrix} \delta t^0 \\ \delta t^1 \\ 0 \\ 0 \\ 0 \\ 0 \\ 0 \\ 0 \\ 0 \end{pmatrix} = \begin{pmatrix} \mathbf{G}^{u0} & \mathbf{0} \\ \mathbf{G}^{u1} & w\,\mathbf{G}^{z} \\ \lambda_u \mathbf{L}^{uX} & \mathbf{0} \\ \lambda_u \mathbf{L}^{uY} & \mathbf{0} \\ \lambda_u \mathbf{L}^{uZ} & \mathbf{0} \\ \mathbf{0} & w\lambda_z \mathbf{L}^{zX} \\ \mathbf{0} & w\lambda_z \mathbf{L}^{zY} \\ \alpha_u \mathbf{D}^{u} & \mathbf{0} \\ \mathbf{0} & w\alpha_z \mathbf{D}^{z} \end{pmatrix} \begin{pmatrix} \delta \mathbf{u} \\ \frac{1}{w} \delta \mathbf{z} \end{pmatrix} \quad (4.24)$$

Alternatively, a fixed damping strategy can be applied that fixes damping weights and permanently imposes damping constraints throughout the entire inversion process regardless of average perturbations. However, this should only be used if an adequate convergence trend cannot be achieved following the automatic damping strategy. In this modality specific damping weights can be assigned to particular nodes. This can be useful when there is external reason to believe that part of the model is trustworthy but the data set is not robust enough to maintain it.

Finally, the code incorporates the option to check for data outliers, i.e. data picks with residuals considered too large, at each iteration and repeat the inversion without them. The discarded picks are always included in the next iteration, and a successful iterative convergence should gradually reduce the number of outliers to almost none, that is, the final model should explain all reliable data. This option also facilitates the detection of persistent outliers which may indicate either a model or part of a model that is too far away from the true one for the linearisation to be valid, or an erroneous interpretation of seismic phases in the record sections yielding mistaken travel time picks.

4.3.3. Least squares system

As in the former 2-D version of the code, all entries in (4.24) are normalised to avoid any biases in the final model deriving from the particular magnitude of either travel times or initial model parameters [Korenaga et al., 2000]. Each component of $\boldsymbol{\delta t}=(\boldsymbol{\delta t}^0,\boldsymbol{\delta t}^1)$ is divided by its corresponding travel time pick ($\mathbf{t}^{obs}$). Each element in $\mathbf{G}$ is also divided by its corresponding component of $\mathbf{t}^{obs}$ and multiplied by the value of its corresponding parameter in the initial model ($\mathbf{m}^0$). Each element in the

regularisation matrices (**L** and **D**) is multiplied by its corresponding initial model parameter. In this way, each component of the vector of parameter perturbations (**δm**) obtained from the inversion of (4.24) must be rescaled by multiplying it by its corresponding element in $\mathbf{m^0}$. Thus, the only dependency of (4.24) on the initial model is given by this normalisation.

The actual inversion of the matrix in (4.24) is impractical because of the huge memory requirements needed for the typical number of model parameters and data picks. Instead, this system of equations is posed as a linear least squares problem which is solved using the LSQR algorithm of Paige & Saunders [1982], a numerically more stable variant of the conjugate gradients method for the solution of sparse linear systems of equations. In the case of TOMO3D, this method minimises the following objective function (*OF*)

$$OF=\sum_{i=1}^{D^0}\left|\delta t_i^0-\sum_{j=1}^{N^U}G_{ij}^{u0}\,\delta u_j\right|^2+\sum_{i=1}^{D^1}\left|\delta t_i^1-\sum_{j=1}^{N^U}G_{ij}^{u1}\,\delta u_j-\sum_{j=1}^{N^Z}G_{ij}^{z}\,\delta z_j\right|^2$$
$$+\lambda_u^2\left(\sum_{k=1}^{N^U}\left|\sum_{j=1}^{N^U}L_{kj}^{uX}\,\delta u_j\right|^2+\sum_{k=1}^{N^U}\left|\sum_{j=1}^{N^U}L_{kj}^{uY}\,\delta u_j\right|^2+\sum_{k=1}^{N^U}\left|\sum_{j=1}^{N^U}L_{kj}^{uZ}\,\delta u_j\right|^2\right)+\lambda_z^2\left(\sum_{k=1}^{N^Z}\left|\sum_{j=1}^{N^Z}L_{kj}^{zX}\,\delta z_j\right|^2+\sum_{k=1}^{N^Z}\left|\sum_{j=1}^{N^Z}L_{kj}^{zY}\,\delta z_j\right|^2\right)$$
$$+\alpha_u^2\sum_{k=1}^{N^U}\left|\sum_{j=1}^{N^U}D_{kj}^{u}\,\delta u_j\right|^2+\alpha_z^2\sum_{k=1}^{N^Z}\left|\sum_{j=1}^{N^Z}D_{kj}^{z}\,\delta z_j\right|^2$$

(4.25)

to obtain **δm**, that is, the update to the *k*-th model to create the (*k*+1)-th model as $\mathbf{m^{k+1}=m^k+\delta m}$. Indexes in (4.25) are relative to the submatrices, not to the global matrix. If a reliable initial model is accessible by other geophysical means, the jumping strategy can be selected for the regularisation of the system instead of the default creeping strategy [Backus & Gilbert, 1967; Shaw & Orcutt, 1985]. The latter finds an acceptable-fit model while imposing constraints on the norm of perturbations that update the current model. The former assumes that the initial model is a rather good approximation to the solution and therefore minimises data misfit while imposing constraints on the norm of perturbations with respect to this initial model. This change consists in modifying (4.24) to

$$\begin{pmatrix} \boldsymbol{\delta t}^{\mathbf{0}} \\ \boldsymbol{\delta t}^{\mathbf{1}} \\ -\lambda_u \mathbf{L}^{\mathbf{uX}} \boldsymbol{\delta u}^{\mathbf{S}} \\ -\lambda_u \mathbf{L}^{\mathbf{uY}} \boldsymbol{\delta u}^{\mathbf{S}} \\ -\lambda_u \mathbf{L}^{\mathbf{uZ}} \boldsymbol{\delta u}^{\mathbf{S}} \\ -\lambda_z \mathbf{L}^{\mathbf{zX}} \boldsymbol{\delta z}^{\mathbf{S}} \\ -\lambda_z \mathbf{L}^{\mathbf{zY}} \boldsymbol{\delta z}^{\mathbf{S}} \\ -\alpha_u \mathbf{D}^{\mathbf{u}} \boldsymbol{\delta u}^{\mathbf{S}} \\ -\alpha_z \mathbf{D}^{\mathbf{z}} \boldsymbol{\delta z}^{\mathbf{S}} \end{pmatrix} = \begin{pmatrix} \mathbf{G}^{\mathbf{u0}} & \mathbf{0} \\ \mathbf{G}^{\mathbf{u1}} & w\mathbf{G}^{\mathbf{z}} \\ \lambda_u \mathbf{L}^{\mathbf{uX}} & \mathbf{0} \\ \lambda_u \mathbf{L}^{\mathbf{uY}} & \mathbf{0} \\ \lambda_u \mathbf{L}^{\mathbf{uZ}} & \mathbf{0} \\ \mathbf{0} & w\lambda_z \mathbf{L}^{\mathbf{zX}} \\ \mathbf{0} & w\lambda_z \mathbf{L}^{\mathbf{zY}} \\ \alpha_u \mathbf{D}^{\mathbf{u}} & \mathbf{0} \\ \mathbf{0} & w\alpha_z \mathbf{D}^{\mathbf{z}} \end{pmatrix} \begin{pmatrix} \boldsymbol{\delta u} \\ \frac{1}{w}\boldsymbol{\delta z} \end{pmatrix} \qquad (4.26)$$

where $\boldsymbol{\delta m}^{\mathbf{S}}=\mathbf{m}^{\mathbf{k}}-\mathbf{m}^{\mathbf{0}}$ is the accumulated parameter perturbation up to the *k*-th iteration. This modified system of equations poses a different least squares problem that is written as

$$\begin{aligned} OF=&\sum_{i=1}^{D^0}\left|\delta t_i^0-\sum_{j=1}^{N^U} G_{ij}^{u0}\,\delta u_j\right|^2+\sum_{i=1}^{D^1}\left|\delta t_i^1-\sum_{j=1}^{N^U} G_{ij}^{u1}\,\delta u_j-\sum_{j=1}^{N^Z} G_{ij}^{z}\,\delta z_j\right|^2 \\ &+\lambda_u^2\left(\sum_{k=1}^{N^U}\left|\sum_{j=1}^{N^U} L_{kj}^{uX}\,\delta u_j+\sum_{j=1}^{N^U} L_{kj}^{uX}\,\delta u_j^S\right|^2+\sum_{k=1}^{N^U}\left|\sum_{j=1}^{N^U} L_{kj}^{uY}\,\delta u_j+\sum_{j=1}^{N^U} L_{kj}^{uY}\,\delta u_j^S\right|^2+\sum_{k=1}^{N^U}\left|\sum_{j=1}^{N^U} L_{kj}^{uZ}\,\delta u_j+\sum_{j=1}^{N^U} L_{kj}^{uZ}\,\delta u_j^S\right|^2\right) \\ &+\lambda_z^2\left(\sum_{k=1}^{N^Z}\left|\sum_{j=1}^{N^Z} L_{kj}^{zX}\,\delta z_j+\sum_{j=1}^{N^Z} L_{kj}^{zX}\,\delta z_j^S\right|^2+\sum_{k=1}^{N^Z}\left|\sum_{j=1}^{N^Z} L_{kj}^{zY}\,\delta z_j+\sum_{j=1}^{N^Z} L_{kj}^{zY}\,\delta z_j^S\right|^2\right) \\ &+\alpha_u^2\left(\sum_{k=1}^{N^U}\left|\sum_{j=1}^{N^U} D_{kj}^{u}\,\delta u_j+\sum_{j=1}^{N^U} D_{kj}^{u}\,\delta u_j^S\right|^2\right)+\alpha_z^2\left(\sum_{k=1}^{N^Z}\left|\sum_{j=1}^{N^Z} D_{kj}^{z}\,\delta z_j+\sum_{j=1}^{N^Z} D_{kj}^{z}\,\delta z_j^S\right|^2\right) \end{aligned} \qquad (4.27)$$

Extracting the common factors (L_{kj} and D_{kj}) in the regularisation terms shows that now smoothing and damping constraints are defined as the minimisation of $\boldsymbol{\delta m}+\boldsymbol{\delta m}^{\mathbf{S}}=\mathbf{m}^{\mathbf{k+1}}-\mathbf{m}^{\mathbf{0}}$, that is, the parameter perturbation measured with respect to the initial model. Finally, post-inversion smoothing after each iteration [Deal & Nolet, 1996] remains an available option inherited from TOMO2D but is not recommended. The statistical approach of Korenaga & Sager [2012] to handle model roughness appears more appropriate because it is a more general means of dealing not only with model smoothness, but with the entire inversion problem. Instead of ensuring that a particular *a priori* selected smoothing constraint is conserved, this approach systematically scans a range of reasonable smoothing parameters.

4.4. Parallelisation

As for most travel-time tomography software, in our code most of the computational time is spent in solving the forward problem in order to calculate the travel time residuals and the kernels. For instance, in the 2-D real data case in chapter 2, and in the 3-D synthetic case in section 5.1 this part takes ~90% out of the total run time per iteration using the sequential code. Therefore we prioritise the parallelisation of the forward problem over the inverse problem. This implementation was conducted in collaboration with Alain Minuissi, a computer engineer at the CNRS-Observatoire de la Côte d'Azur (Nice, France). After I had explained the functioning of the code in detail, we decided on a parallelisation scheme. The code was stored on a Subversion® repository in order to keep track of the successive modifications. Each significant modification was followed by a quick regression test to prevent the introduction of bugs in the code.

The code is parallelised with a combination of multi-processing (MP) and message passing interface (MPI) extensions. Taillandier et al. [2009] presented an MPI parallel 3-D refraction travel-time tomography program that used an eikonal-based forward problem solver and the adjoint-state method in combination with the steepest-decent minimisation for inversion. The parallelisation strategy for TOMO3D (Fig. 4.7) is rather intuitive and is conceptually identical to theirs as the hybrid ray tracing method also deals with each source independently. The graph problem is solved simultaneously for as many sources as the available computational resources allow: each CPU takes care of at least one source, and at most of the number resulting from distributing all the sources in the experiment among the available CPUs. Sources and receivers can be exchanged in the input data file to minimise computational time depending on the available computational resources in each specific computing facility and on the ratio between the average computational times spent in solving one graph and one bending problems for each particular data set; test iterations can be performed to chose between the two configurations. These assignments are done in the form of MPI processes. Then bending refinement is performed simultaneously for as many rays as possible: each core traces its share of rays associated to the source(s) assigned to their CPU. These assignments are controlled by MP threads. This avoids the need for communication between nodes that would generally result in higher computational time. Once all rays for the current source have been traced, a new source is passed to the CPU so that it is kept permanently busy while there are sources left to compute. The only significant communication between CPUs happens when all rays have been traced and partial kernels for all sources can be added to obtain the total velocity and depth kernels. The parallel speedup of this parallel implementation for the

synthetic example in section 5.1 is discussed in subsection 5.1.4 and it indicates a remarkable reduction in computational time.

The computation of the graph problem for each particular source can also be parallelised. However, this second level of parallelism generally requires rather large computational facilities and careful consideration of the computational time overhead needed to accommodate communication between processes in order to ensure efficiency. Monsegny & Agudelo [2013] proposed a parallel graph algorithm on GPUs. The possibility of running the code on GPUs may make the implementation of this second-level parallelism worthwhile. As far as I could investigate, currently no parallelised version of the bending method exists.

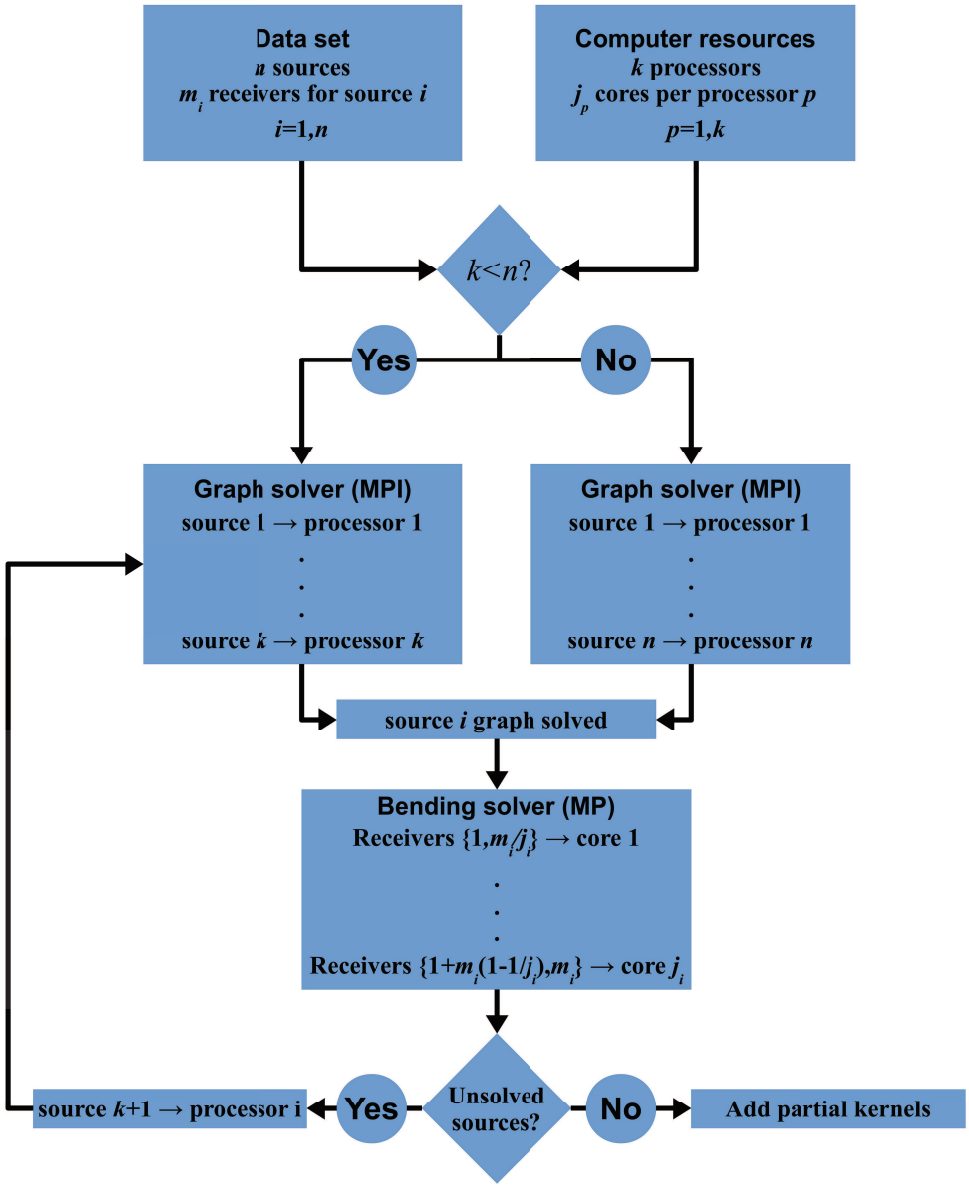

Figure 4.7. Forward problem parallelisation scheme. The number of sources (n) is compared to the number of available processors (k). If k≥n all sources are processed simultaneously. When that is not the case, the k processors start by taking care of the first k sources. When processor i has solved the graph problem for its current source i, it moves on to bend the rays of the corresponding m_i receivers equidistributing them among its j_i cores. Immediately after this task is completed, a new unsolved source k+1 is assigned to processor i and so on so forth. This is repeated until the forward problem is solved for the n sources. Finally, the partial kernels for the n sources are added to calculate the total kernel.

CHAPTER 5: SYNTHETIC AND REAL DATA INVERSION TESTS WITH TOMO3D

5. SYNTHETIC AND REAL DATA INVERSION TESTS WITH TOMO3D

5.1. 3-D synthetic inversion test

This test was designed to evaluate the resolving potential of TOMO3D under realistic but optimal conditions in terms of data acquisition configuration. The complexity of the target model was progressively increased to approximate a subduction zone setting at an ocean–continent convergent margin, but only the final, most complex test is presented here. The possibility of performing more intermediate tests was prioritised over working with larger model sizes that would substantially increase computational time. However, it must be noted that both the model and the obtained results are scalable assuming that the data coverage is comparable. The subsequent application of the code to a crustal-scale real data set in section 5.2 provides an example with typical model dimensions. Besides, the reduced size of this synthetic case allows the comparison of paralelised and sequential code performance. All of them include refraction and reflection data and thus inverted for both velocity and depth parameters. The number of iterations needed to converge to a final result was ~10. Regarding depth, notation in equation (4.3) is observed: z means vertical position within the velocity mesh, whereas z' refers to depth including geological relief $b'(x,y)$, as well as to reflector depth.

5.1.1. Velocity and depth parameterisation and target model

The 3-D volume is a prism with squared upper and lower faces of 5 km by 5 km and a depth of 3 km. Velocity nodes are equi-spaced 0.125 km in all three spatial dimensions for a total of 42025 nodes. Relief was added to the velocity models with a geometry created by applying a sinusoidal perturbation to an inclined plane (Fig. 5.1a,b). Concerning reflectors, nodal spacing is 0.5 km resulting in 121 depth nodes. It is worth noting that these synthetic experiments are straightforward to rescale, and thus the results are independent of the specific dimensions of the model. Indeed, if the distance unit of the parameterisation is multiplied by any factor and velocity values are kept the same, then new travel times are simply the old ones scaled by that factor.

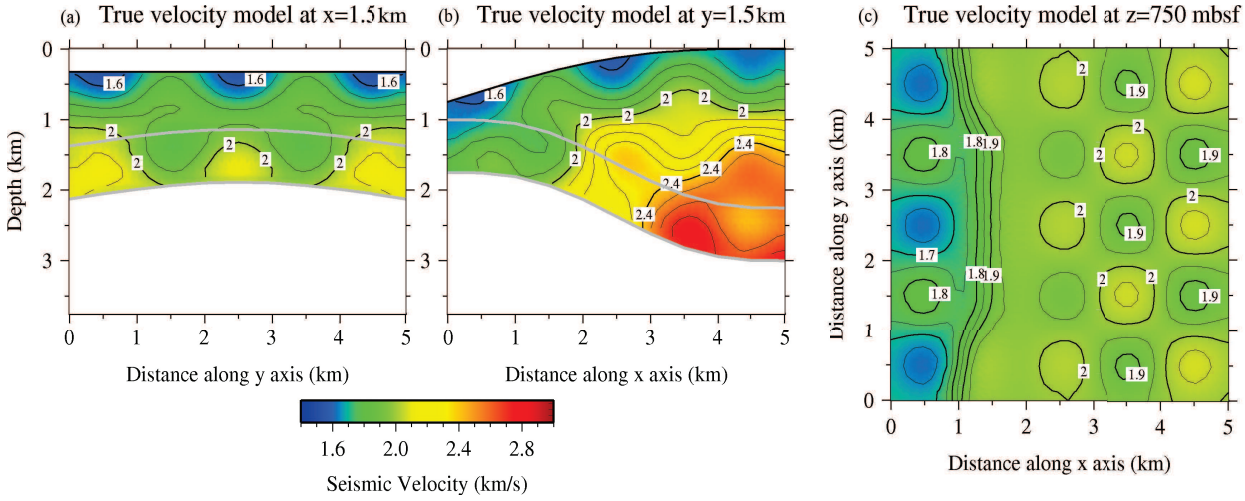

Figure 5.1. 2-D cuts of the true velocity model at (a) x=1.5 km, (b) y=1.5 km, and (c) z=750 mbsf with the corresponding 1-D cuts of both true reflectors (grey lines).

The target velocity model is built starting from the linear velocity function of depth $v(z)=1.6+0.5\cdot z$. The geometry of the first target depth model, that is, the shallowest target reflector is given by

$$z'_{T1}(x,y) = z'(x) - A\cdot\sin\left(2\pi\cdot\sqrt{(x-x_0)^2+(z'-z'_0)^2}\,/\left(c_1\cdot\sqrt{(\Delta x)^2+(\Delta z')^2}\right)\right) \cdot\sin\left(2\pi\cdot(y-y_0)/(c_2\cdot\Delta y)\right) \quad (5.1)$$

where $z'(x)=z'_0+s\cdot x$ with s=0.25 (slope) and z'_0=1 km (depth at origin), A=0.25 km (amplitude of the perturbation), $x_0=y_0$=0 km (origin coordinates), c_1=1, c_2=0.5 (number of sinus cycles), and Δx=5 km, Δy=5 km, $\Delta z'$=3 km (model dimensions). The second or deepest target reflector (z'_{T2}) follows the same expression but for z'_0=1.75 km (Fig. 5.1a,b). With these two reflectors, the previous velocity model is modified by applying a velocity shift of -0.25 km/s just beneath each reflector, which can be expressed as

$$v'(x,y,z) = \begin{cases} v(z), & z'<z'_{T1} \\ v(z)-0.25, & z'_{T1}<z'<z'_{T2} \\ v(z)-0.5, & z'>z'_{T2} \end{cases} \quad (5.2)$$

The target velocity model is completed after $v'(x,y,z)$ is perturbed with a checkerboard pattern described by

$$v_T(x,y,z)=v'(x,y,z)\cdot\left(1+0.01\cdot A\cdot\sin\left(\frac{2\pi\cdot x}{l_x}\right)\cdot\sin\left(\frac{2\pi\cdot y}{l_y}\right)\cdot\sin\left(\frac{2\pi\cdot z}{l_z}\right)\right) \qquad (5.3)$$

where l_x=l_y=l_z=2 km, and A=10% (Fig. 5.1).

5.1.2. Acquisition configuration and data set

The acquisition configuration consists of 36 receivers distributed in a squared grid of 6 by 6 receivers with 1-km spacing (Fig. 5.2a) and located at the seafloor. A total of 441 sources located 10 mbsl are spaced 0.25 km, so that the number of available data is 31752. Half of the data correspond to refraction first arrival/refraction picks and the other half to reflection picks. As occurs in this case, typical active-source real data experiments provide less data than the number of modelling parameters. This data set in combination with the total number of model parameters reproduces a rather optimal experimental situation in which the number of travel time picks is almost as big as the number of parameters to be inverted.

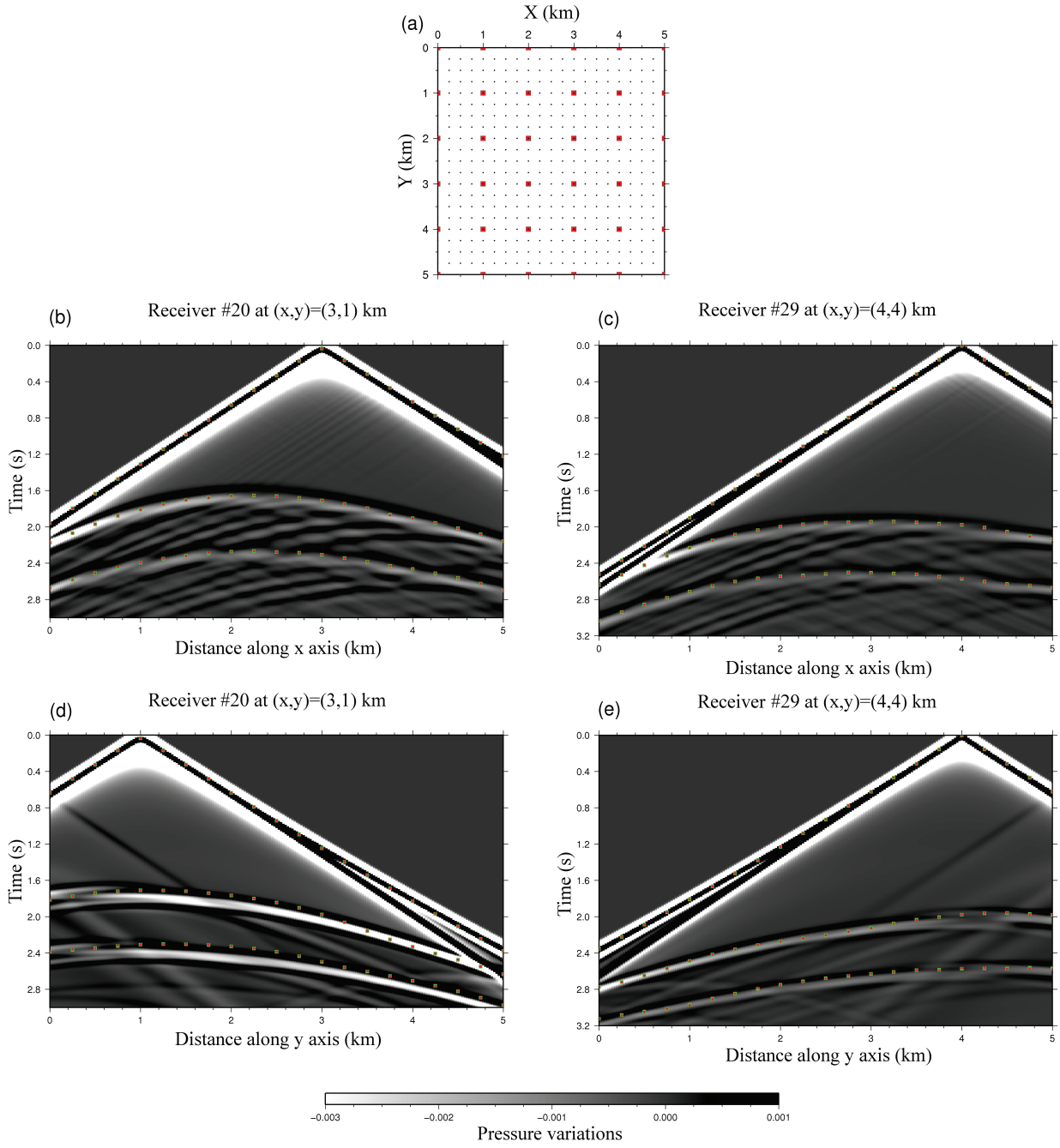

Figure 5.2. (a) Acquisition geometry with 36 receivers and 441 sources. Black dots and red squares indicate source and receiver locations. (b-e) Synthetic record sections for four sample profiles. True (green squares) and calculated (red dots) picks in the final model are plotted to show their fit as well as the correspondence with seismic phases.

The true picks were obtained with the same forward problem solver in TOMO3D and plotted on top of synthetic record sections generated with the acoustic version of the 2-D finite-differences elastic wave solver by Dagnino et al. [2014] (Fig. 5.2b-e). The fit between the picks and the seismic phases

is satisfactory and illustrates the robustness of our 3-D ray tracing and travel time calculation method. Minor mismatches most likely arise from the difference between 3-D ray tracing and 2-D wave propagation, and they point to the necessity of using 3-D codes for more accurate and reliable model estimation.

5.1.3. Layer-stripping strategy and test results

The purpose of the layer-stripping strategy [e.g. Sallarès et al., 2013, Martínez-Loriente et al., 2014] is twofold: (1) to help minimising the ambiguity that arises from the trade-off between the velocity distribution and the layer thickness, and (2) to recover sharp geological discontinuities that might otherwise appear as smooth velocity gradients. This strategy proceeds by extending the model downwards layer by layer. The first inversion is devised to recover the velocity within the first, shallowest layer and the depth of the corresponding reflector. Subsequently the area of the inverted velocity model limited by the geological relief at the top and the geometry of the inverted reflector at the bottom is inserted in a new starting model that extends down to include the next reflector. Because only one reflector is inverted at a time, at each step the reflection picks in the data set are replaced by those associated to the new reflector. If the combination of the selected inversion parameters and the data set provides a robust constraint on the model parameters of the previous inversion result, they should not be significantly altered by the next inversion step. If that is not the case but there is reason to believe that the result is correct (e.g. in the form of geophysical information that is external to the inversion process), one may choose to apply the node-specific damping to the previously inverted velocity parameters with respect to those in the new area of the extended model so that the inversion tends to modify the latter rather than the former in order to fit the new picks. Giving the layer-stripping strategy a certain degree of automation could be a future development for TOMO3D although it will generally be necessary to allow for user verification of the results after each step. This sort of improvement is intimately related to the implementation of a graphic user interface that would provide a simpler handling of input and output files.

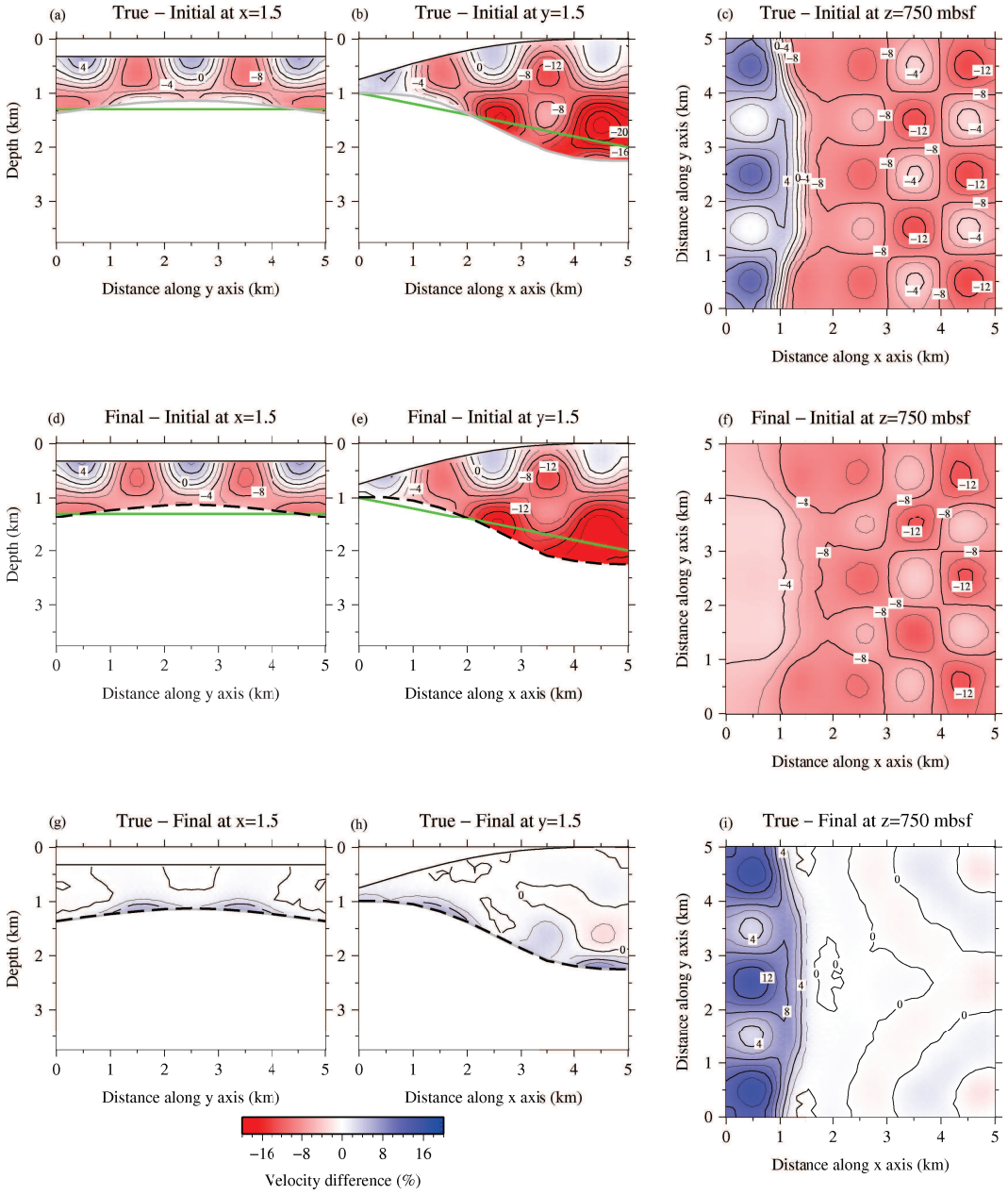

Figure 5.3. Velocity recovery after LSS step 1 illustrated as the percentage differences between 2-D cuts of the initial, final and true models. On the vertical cuts the corresponding 1-D cuts of the initial (green lines), final (black dashed lines) and true (grey lines) reflectors are also plotted.

In the first step of the layer stripping, the starting velocity model follows the function $v(z)=1.6+0.3\cdot z$, whereas the starting depth model is represented by $z'(x)=1+0.2\cdot x$. The uppermost velocity is set to the correct value considering that in a real case a very good estimate of that value could be obtained for instance by means of core drilling and testing or simply from well-established

geological knowledge. Likewise, the shallowest reflecting boundary, i.e. the seafloor in a real experiment, can be very well determined from bathymetry data or from other exploration techniques such as MCS data experiments, so that it is correctly set as well. As shown in Fig. 5.3, the velocity and depth recoveries are excellent, especially in the central area of the model where the data set offers the best ray coverage by both refractions and reflections. The velocity fit is shown via 2-D cuts. The percentage differences between initial, final and target velocity models shows the correctness of the inverted velocity distribution. The poor recovery area observed in Fig. 5.3i, which stands out against the rest of the horizontal cut, corresponds to the portion of plane that is below the first reflector, so is not mapped by the data used in this first inversion step. Outside this particular area, the highest misfit (Fig. 5.3g-i) values are around 6% and are limited to very small and localised zones at the bottom and lateral boundaries of the model. For the rest of the volume velocity misfit is always close to 0%.

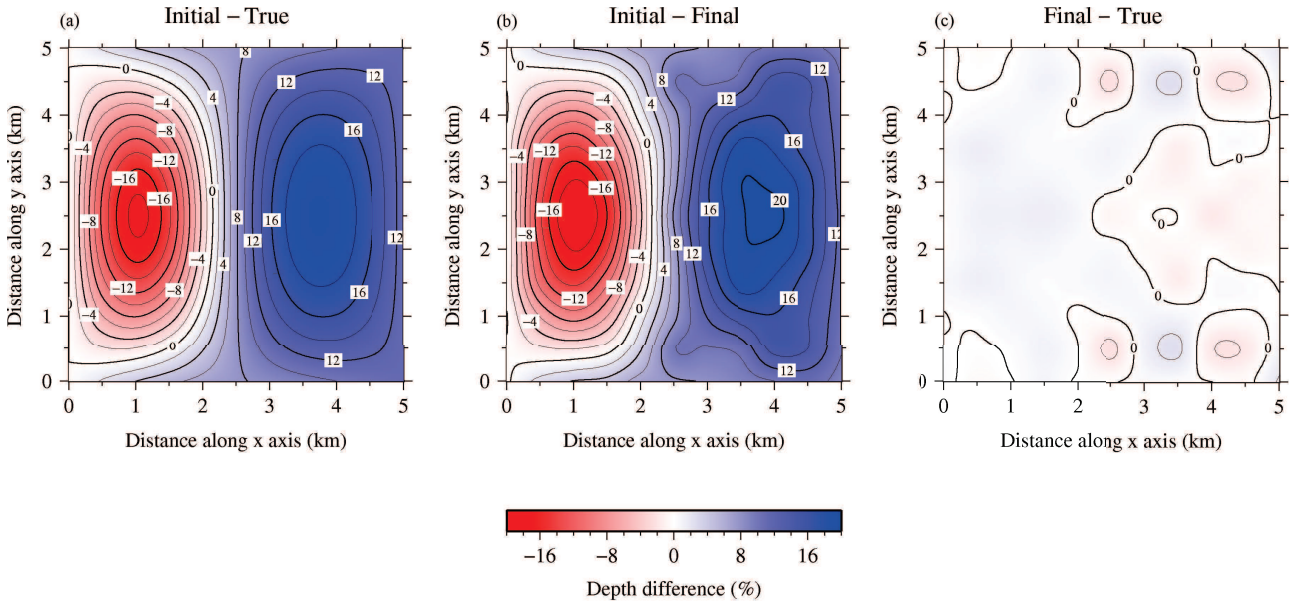

Figure 5.4. Recovery of interface geometry after LSS step 1, illustrated as the percentage differences in depth between (a) initial - true reflectors, (b) initial - final reflectors, and (c) final - true reflectors.

The fit between target and final depth model is displayed in Fig. 5.4a-c and just as for the velocity model the agreement is satisfactory, in particular for the central and shallow areas of the reflector, with misfit values between 0% and 1% (Fig. 5.4c). The highest misfit values are around 2% and again are found in very small and concentrated areas at the lateral boundaries of the deepest part of the reflector. The symmetry of the depth misfit is to be expected given the symmetries defined by

the acquisition configuration and the target velocity and depth models. Moreover, this suggests that the final velocity model and its misfit also follow an analogous symmetry that can be checked by plotting 2-D cuts at the appropriate x and y positions. Histograms in Fig. 5.5a,b show the distribution of refraction and reflection travel-time residuals before and after inversion proving that the iterative inversion produces velocity and depth models that explain the data remarkably well. The combined RMS for this first step is 1.78 ms, with 1.34 ms and 2.14 ms for refraction and reflection picks respectively.

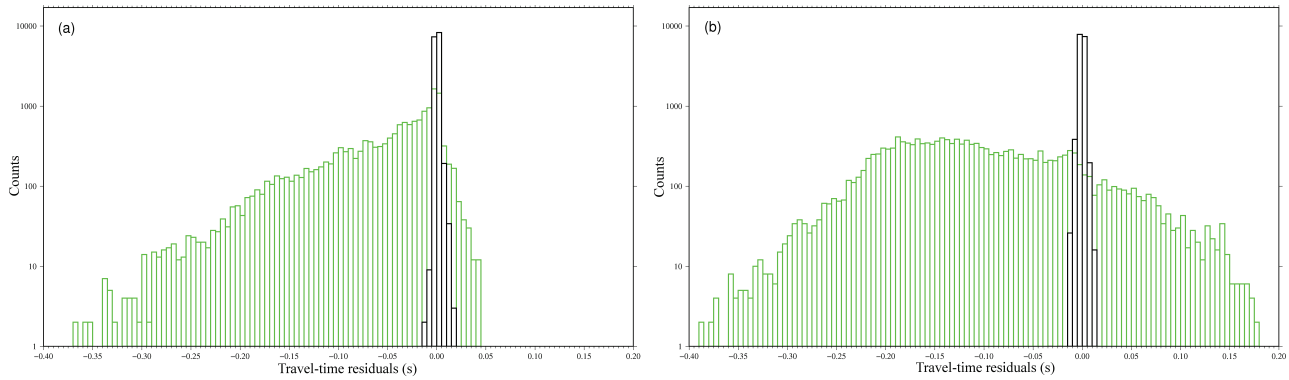

Figure 5.5. Histograms of initial (green) and final (black) travel time residuals for (a) refractions and (b) reflections after LSS step 1.

In the second step the reflection picks associated to the first reflector are replaced by those associated to the second reflector. Regarding the starting velocity model, the parameters above the first reflector are set to the result of the first inversion step, while the parameters beneath it are set to follow $v(z)=1.25+0.5 \cdot z$ so as to mark a velocity contrast matching this reflector. The starting reflector is represented by $z'(x)=1.75+0.22 \cdot x$. As in the first step certain assumptions have been made. Here we considered that some additional knowledge on the nature of this body is available that allows us to roughly guess its velocity value immediately below the boundary. As mentioned before, in a real experiment this information might be given by some supplementary geophysical exploration or data processing method such as an amplitude analysis of the reflection event in the seismic traces or by well-established geological knowledge on the nature of a particular sort of structure such as the velocity distribution of the average oceanic plate. Similarly, the shallowest position of this second starting reflector could be approximated from other geophysical techniques or from well-established knowledge about its thickness, as again would be the case for the average oceanic plate. Moreover, based on the observation of the geometry of the first boundary, one could decide to slightly increase the slope of the plane defining the starting depth model for this second

boundary. However, even if the aforementioned assumptions are reasonable, ideally in a real experiment one would like to use an adaptive importance sampling scheme as described in Korenaga & Sager [2012], which statistically evaluates pre-defined ranges of geologically reasonable model parameters. Parallelisation and optimisation of the code is critical to make these computationally-expensive analyses feasible in 3D.

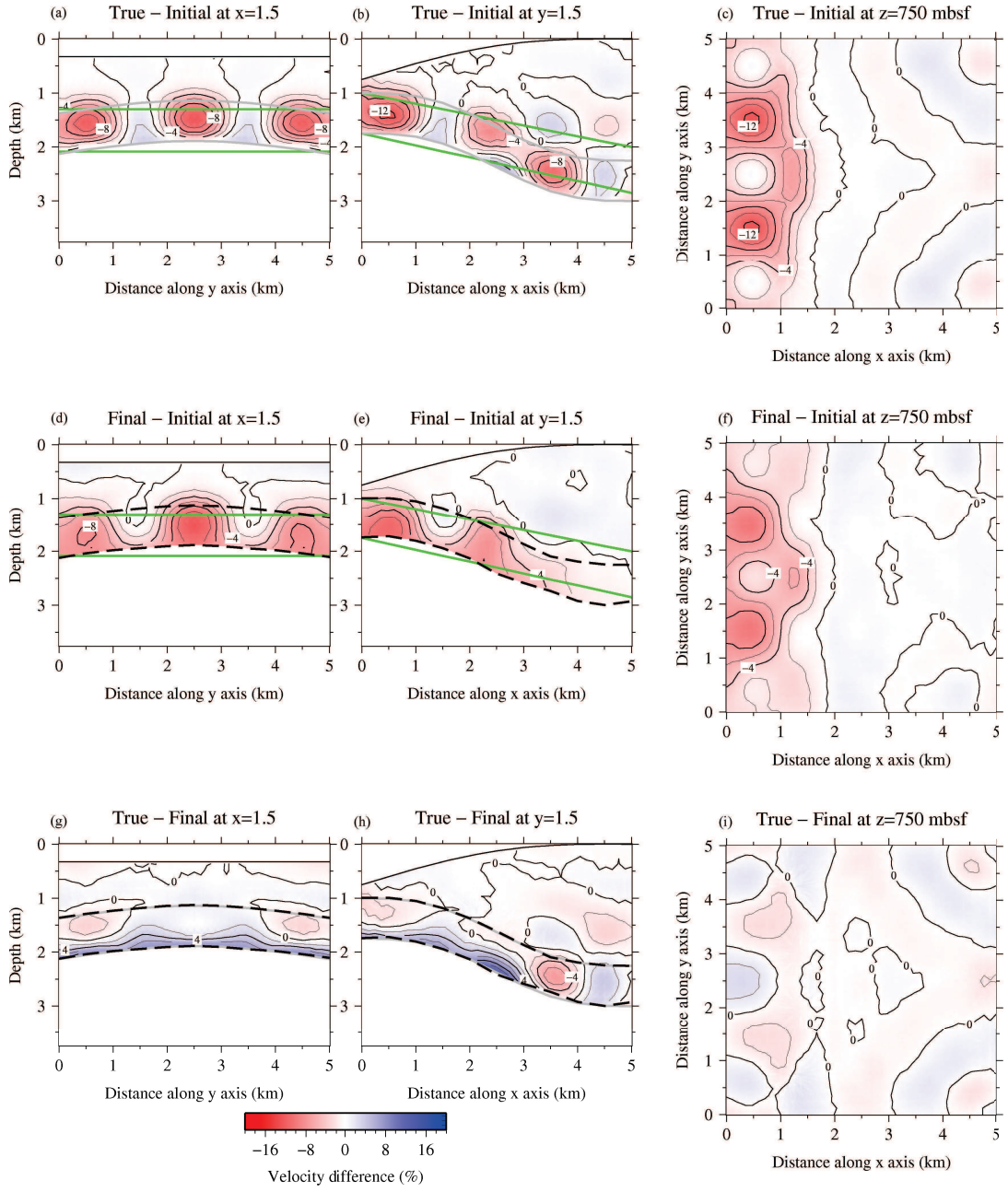

Figure 5.6. Velocity recovery after LSS step 2 illustrated as the percentage differences between 2-D cuts of the initial, final and true models. On the vertical cuts the corresponding 1-D cuts of the initial (green lines), final (black dashed lines) and true (grey lines) reflectors are also plotted.

Fig. 5.6 displays the result after the second and in this case final step of layer stripping. It was not necessary to damp the velocity parameters inverted in the first step in relation to those in the new area of the model because our data set proved sufficiently dense so as to keep the former unchanged while iteratively improving the latter to fit the newly included reflection data. The recovery of both velocity and depth parameters is not as good as for the previous layer. This could be anticipated simply because recovery generally deteriorates with depth, but also because the new layer is almost only mapped by reflections (Fig. 5.2), which, in contrast to refractions, are intrinsically subject to velocity–depth ambiguity. Satisfactory misfit values between 0% and 2% are found for the upper half and central areas of the layer above 2 km depth (Fig. 5.6g-i). At the deeper part of the layer, velocity is not retrieved correctly although misfit is mostly between 4% and 6% with very localised areas of around 8-10% at most. The accumulation of higher velocity errors just above the reflector is characteristic of velocity–depth trade-off. Still, this effect is somewhat mitigated by the fact that we are using wide-angle, instead of near-vertical reflections, so that there is an acceptable azimuthal coverage even in this second layer, especially in its upper part. However it is worth noting that the velocity fit for the previous layer is visibly improved, especially in the central part and around its bottom reflector, where misfit is between 0% and 1%, and the maximum misfit after the first step (Fig. 5.3g,h) decreases to between 0% and 2% (Fig. 5.6g,h). More importantly, the area beneath the first reflector in Fig. 5.3i is well recovered after this second step (Fig. 5.6i) proving that the layer-stripping strategy manages to retrieve sharp velocity contrasts. Consistently with the overall velocity recovery, the checkerboard pattern is well recovered for the first layer and partially recovered for the second one (Fig. 5.7).

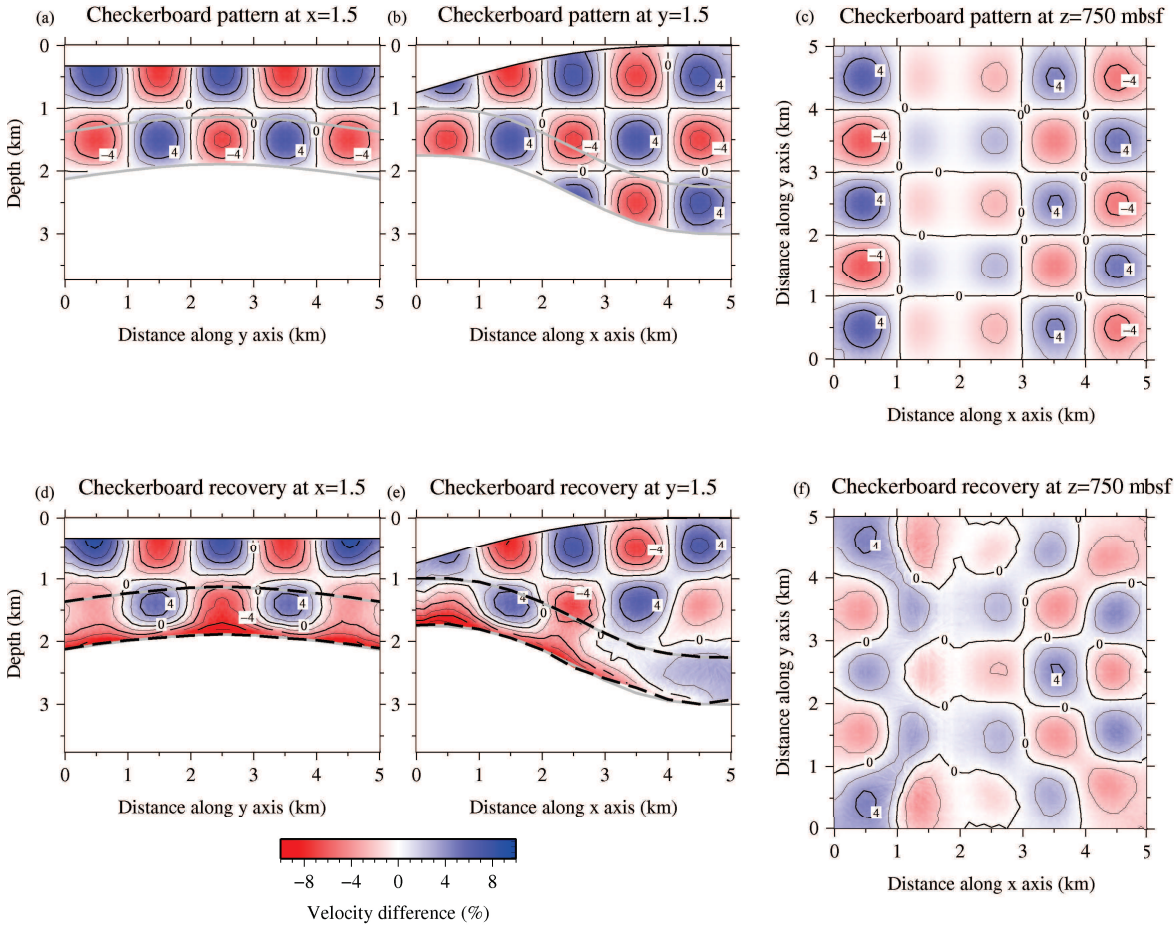

Figure 5.7. 2-D cuts of the checkerboard pattern (a) at x=1.5 km, (b) y=1.5 km, and (c) z=750 mbsf with the corresponding 1-D cuts of both true reflectors (grey lines). (d-f) Checkerboard pattern recovery after LSS step 2 for the same 2-D cuts including the corresponding 1-D cuts of both final reflectors (black dashed lines).

The geometry of the reflector is adequately retrieved, particularly at the shallow central region of the interface where misfit is between 0% and 1% (Fig. 5.8a-c). The highest misfit values are around 2% and concentrate in little pseudo-circular areas along the limits of the model as well as at the deeper region of the reflector (Fig. 5.8c). The same considerations regarding symmetrical features as for the first step results are valid here.

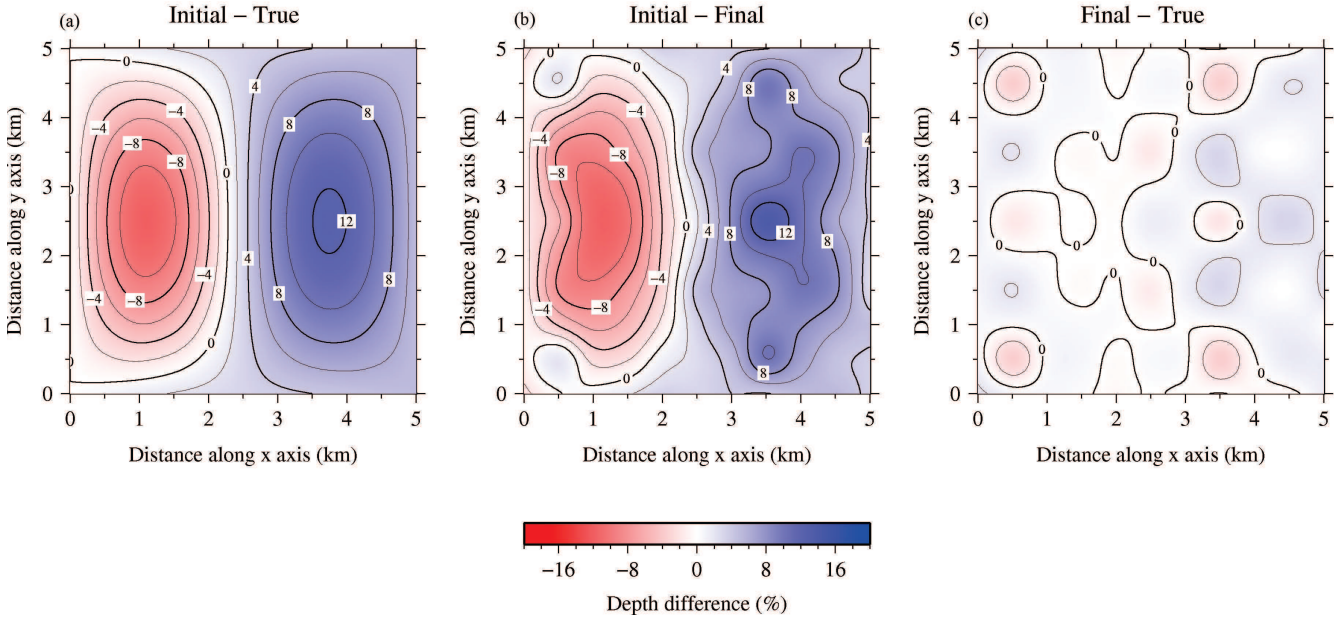

Figure 5.8. Recovery of interface geometry after LSS step 2, illustrated as the percentage differences in depth between (a) initial and true reflectors, (b) initial and final reflectors, and (c) final and true reflectors.

Also as in the first step, histograms in Fig. 5.9a,b show the distribution of refraction and reflection residuals before and after inversion. In this second step we observed how, as expected for a robust inversion solution, refraction residuals remain virtually invariable with respect to the first step. Reflection residuals for the second reflector, however satisfactory, are not as good as for the first one, in accordance with the quality of their respective depth recoveries, and due to the velocity–depth trade-off. The combined RMS for this second step is 3.44 ms, 1.35 ms and 4.67 ms for refraction and reflection picks respectively, and the overall combined RMS is 2.38 ms. Examples of the good agreement between true and calculated picks can be seen in Fig. 5.2b-e. The inversion parameters used in the two inversion steps are presented in Table 5.1.

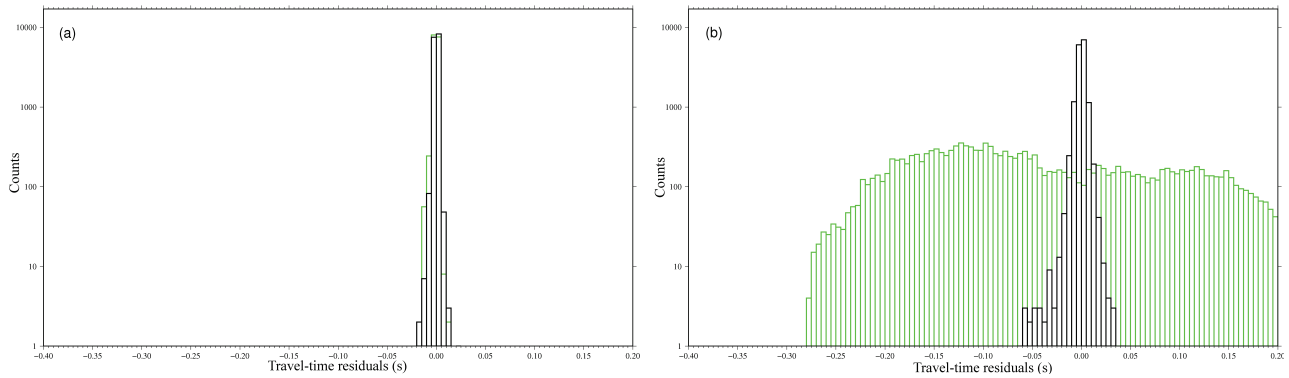

Figure 5.9. Histograms of initial (green) and final (black) travel time residuals for (a) refractions and (b) reflections after LSS step 2.

Table 5.1: Relevant inversion parameters used in the synthetic test. Correlation lengths for the velocity model are set at the top and bottom nodes of the velocity grid and interpolated for the rest of the nodes in between. The increase with depth follows from the typical decrease in resolving power. The second step needed longer correlation lengths for the depth model because of the poorer ray coverage, particularly due to the lack of refractions travelling through the deeper parts of the model.

Inversion parameters	Values for LSS step 1	Values for LSS step 2
Forward star order (x,y,z) (number of nodes)	(4,4,4)	(4,4,4)
λ_u	10	10
λ_z	1	1
Average velocity perturbation limit (%)	10	10
Average depth perturbation limit (%)	10	10
Top velocity correlation lengths (x,y,z) (km)	(0.5,0.5,0.5)	(0.5,0.5,0.5)
Bottom velocity correlation lengths (x,y,z) (km)	(1,1,1)	(1,1,1)
Depth correlation lengths (x,y) (km)	(0.5,0.5)	(1,1)

5.1.4. Parallelisation perfomance

As an idea of the improvement achieved by parallelising the code, the inversion of the first layer took 34 hours with the sequential code on an Intel® Xeon® Processor E5640 (12M Cache, 2.66 GHz, 5.86 GT/s Intel® QPI), and only 65 minutes with the parallel version using 2 MPI processes per node and 6 MP threads per CPU on 5 nodes each with 2 CPUs Intel® Xeon® Processor E5-2670 v2 (25M Cache, 2.50 GHz) with 8 cores each. Considering that the inversion takes ~10%

of the total time (~3.4 hours) and that this part of the code has not yet been parallelised, the computational time decrease might indicate that the code has also benefited from some programming optimisation during the parallelisation process. However, differences in the performance of the two CPU models may have also played a role in the time reduction. This can be corroborated by looking at the code speedup. The actual speedup is calculated as the ratio between the durations of the sequential and parallel executions of the code. In this particular case, speedup is ~31. By Amdahl's law [Amdahl, 1967] the theoretical or ideal speedup (*S(n)*) is defined as

$$S(n)=\frac{T(1)}{T(n)}=\frac{T(1)}{T(1)\cdot\left(B+\frac{1}{n}\cdot(1-B)\right)}=\frac{1}{B+\frac{1}{n}\cdot(1-B)} \qquad (5.4)$$

where *T(*1*)* and *T(n)* are the sequential and parallel durations, respectively, *B* is the fraction of the code that is not parallelised, and *n* is the number of parallel processes. Here *B*=0.1, and ideally *n*=6·2·5=60, hence ideal speedup is ~9.

5.1.5. Discussion

TOMO3D is a fully functional, state-of-the-art, parallel code for the inversion of refraction and reflection seismic data that produces 3-D velocity models of the subsurface and 2-D depth models representing the geometry of reflecting interfaces. Founded on TOMO2D, TOMO3D incorporates analogous forward and inversion methods that are modified and extended to work in 3D. Parallelisation of the forward part was critical to the practicality of the program as the additional third dimension resulted in a substantial increase of computational time, due to the greater number of data and model parameters. The forward problem solver is by far the most time consuming part of the code and thus the one that has been parallelised for the moment. The parallelisation scheme is implemented in a combination of MPI and MP languages, and it distributes the processing of sources among cluster nodes and their CPU sockets, and for each source, the processing of its receivers among the cores of their corresponding CPU. The reciprocity principle of wave propagation allows for the exchange of sources by receivers and thus for the minimisation of the number of graph problems to be solved. The speedup achieved in the synthetic test shows that the implementation of a parallel scheme has also contributed the optimisation of the code's performance.

The quality of the synthetic data set as well as of the inversion results was illustrated by plotting the picks on top of the synthetic record sections generated with a 2-D acoustic wave propagator showing the satisfactory agreement between inverted and true picks, and with their corresponding seismic phases (Fig. 5.2). These synthetic record sections also showed how the layer-stripping strategy is mostly an objective modelling process when the different reflected phases can be identified. From a technical point of view inverting for more than one reflector simultaneously is only a matter of making minor modifications to the code. The choice of a single reflector inversion and of a layer-stripping approach is thus conceptual and seeks to simplify the inverse problem that is posed, which ultimately facilitates its solution and, in my opinion, makes it a better general option, especially for the sake of the geological interpretation.

The usefulness of TOMO3D has been tested in a complex synthetic case simulating a subduction zone scenario, in which it managed to successfully resolve the velocity field of the upper and lower layers as well as the geometry of the boundary and bottom interfaces. This is exemplified by the velocity and depth misfits (Figs 5.3, 5.4, 5.6, 5.7, and 5.8), and the travel time residuals values (Figs 5.5 and 5.9). Additionally, we show our proposed strategy to model impedance contrasts that may appear at the boundaries between geological structures. Travel-time tomography velocity models are smooth gradients as opposed to constant velocity layered models obtained from MCS data processing or from forward modelling of wide-angle data. Layer stripping is devised to introduce and/or keep such sharp velocity contrasts throughout the entire inversion process, which results in more realistic geological models. Moreover, applying this strategy, together with the joint inversion of refracted and reflected data, mitigates the ambiguity between the interface depth and the velocity distribution above it that is intrinsic to reflection-based inversions. The depth-independent constraint on the velocity model from refraction data restricts the range of velocity values to fit reflection data, and consequently of depth values as well. Nevertheless, trade-off effects can still be present in the joint inversion of refraction and reflection data, and its quantification is essential in real cases as demonstrated in Korenaga [2011]. As with TOMO2D, the degree of velocity–depth trade-off can be evaluated exploring a range *w* values.

5.2. 3-D real data inversion: Esmeraldas survey

As a further realistic means of evaluating the reliability of TOMO3D, the code has been used to model a sub-set of a wide-angle seismic data set acquired across the ocean–continent convergent

margin of Ecuador and Colombia. These data were acquired in 2005, in the framework the ESMERALDAS project. The offshore data were acquired with the oceanographic R/V L'Atalante in a cruise leaded by IRD-Géosciences Azur and funded by French agencies. These data were complemented by onshore recordings of the air-gun shots in a network of landstations deployed by a French–Spanish team that was funded by a Spanish Complementary Action. Refraction travel time picks from this data set had been previously modelled by García-Cano [2009] and García-Cano et al. [2014] using the FAST 3-D refraction travel-time tomography code. Comparison between the resulting 3-D models indicates that TOMO3D is capable of producing sound results for the velocity distributions of the overriding and underthrusting plates, and thus that it is a valuable tool for crustal-scale investigation. More specifically, these results should prove useful for the on-going study of this subduction zone, the characterisation of the North Andean margin, and the associated seismicity.

5.2.1. Tectonic setting and previous results

The subduction of the Nazca plate beneath the South American plate at the North Andean margin creates notable volcanic and seismic activity, including four great megathrust earthquakes during the past century in the region of interest [Kanamori & McNally, 1982; Kelleher, 1972; Mendoza & Dewey, 1984]. The purpose of the Esmeraldas survey was to gather 3-D information on the nature and structure of the margin at the rupture area of the 1958 seismic event, to further the geological knowledge derived from existing 2-D experiments, and to extract possible seismological implications. García-Cano et al. [2014] related the trenchward limit of the rupture area and the tsunami excitation to the weak, highly fractured outer margin wedge observed as a low-velocity gradient in their 3-D velocity model. This model also delimited the spatial extension of a low-velocity zone in the overriding plate just above the interplate boundary that had been previously observed in a 2-D velocity model by Gailler et al. [2007]; similar observations have also been described for other convergent settings such as the Nicaragua margin, as described in chapter 2 of this thesis.

The ESMERALDAS seismic network was constituted by 23 OBSs and 31 land stations (Fig. 5.10a). The OBSs were deployed at some of the intersections between perpendicular shot profiles forming the acquisition grid. All land stations were in located on mainland Ecuador. García-Cano [2009] first modelled the OBS data alone on a box of 332 km × 254 km × 30 km, and afterwards

added up to 14 land stations that had recorded marine shots to extend the model depth to 65 km. The geological interpretation and implications of this second final model were later summarised in García-Cano et al. [2014]. The total number of travel time picks is ~190000, all corresponding to refracted phases. Reflected phases corresponding to the interplate boundary are also present on record sections but have yet to be picked. The selected pick errors are between 20 ms at near offset and 100 ms at far offset. These 3-D refraction travel-time tomographic inversions were performed using FAST [Zelt & Barton, 1998]. The velocity model is parameterised as a regular grid whose spacing may be different for the forward and inverse problems. Ray paths and travel times are calculated with a finite-difference eikonal solver algorithm [Vidale, 1990; Hole & Zelt, 1995]. The iterative regularised inversion is conducted with the LSQR algorithm by Paige & Saunders [1982] as in TOMO3D, and following a jumping strategy [Shaw & Orcutt, 1985]. Regularisation, in the form of smoothness constraints, is thus posed on parameter perturbation with respect to the initial model.

(a)

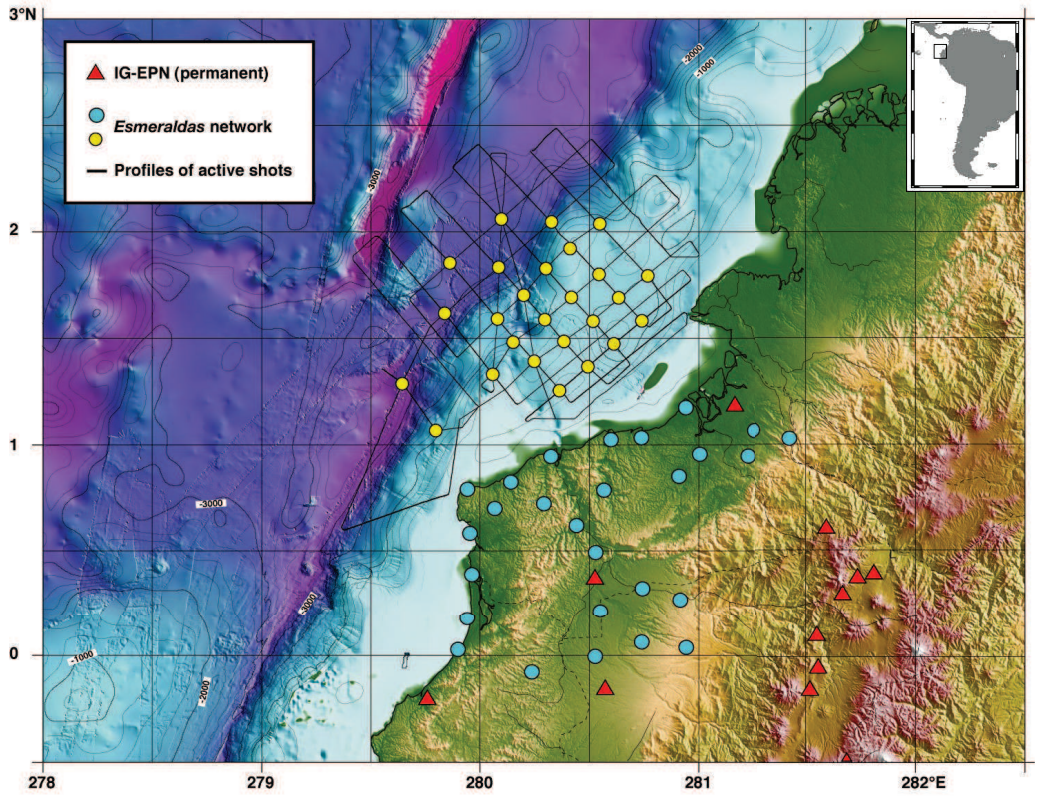

Figure 5.10. (a) Study area and acquisition geometry of the Esmeraldas experiment. Marine (yellow) and land (blue) stations are plotted along with the shot profiles (black lines). Red triangles correspond to the permanent IG-EPN seismic recording network. Inset: location of the study area on a regional map of South America, from García-Cano, [2009].

(b)

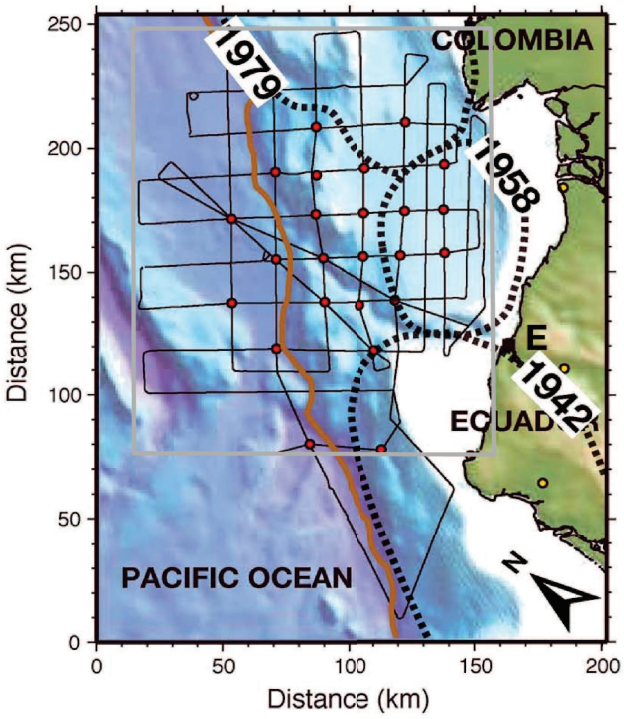

Figure 5.10. (Continued) (b) Area of the modelling box used in García-Cano et al. [2014]. The grey rectangle marks the area of the modelling box used here. Dashed lines delimit the rupture areas of three interplate seismic episodes in the region. The black square labelled E indicates the location of the city of Esmeraldas.

In García-Cano et al. [2014] the forward problem was solved on a grid of 0.5-km spacing in all three directions, whereas for the inversion horizontal spacings were 2 km and vertical spacing was 0.5 km. Two different 1-D vertical velocity profiles were extrapolated to build initial 3-D models; one approximated the velocity structure of oceanic crust and the other that of a continental margin. The best results in terms of data fit were obtained for the latter. For the inversion of OBS data, the RMS of travel time residuals was 193 ms, whereas the combined inversion of marine and land data yielded an RMS of 217 ms (Fig. 5.11). García-Cano et al. [2014] calculated an excessively high Chi² of 10.2, and in both cases the comparison of RMS values with the selected range of pick errors implies that in general either the inverted models do not fit the observed data satisfactorily or the assigned picking uncertainties are too small. According to García-Cano [2009] the 20 iterations of the inversion of the entire data set took around 48 hours on a SUN™ workstation with an Opteron 880 Dual Core Processor of 2.4 GHz and 32 Gb of RAM.

(a)

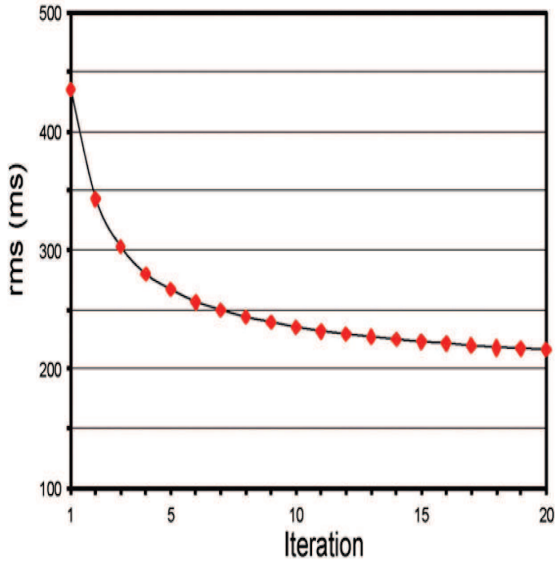

Figure 5.11. Line charts showing the evolution of (a) RMS for the iterative inversion process using FAST [Garcia-Cano et al., 2014], and (b) RMS and (c) χ^2/N for the iterative inversion process using TOMO3D. Both curves show a satisfactory convergence trend. In contrast to the inversion using FAST, the main model improvement with TOMO3D is achieved in the first 5 iterations. Afterwards, improvement is negligible, and no significant modification of the model is taking place.

(b)

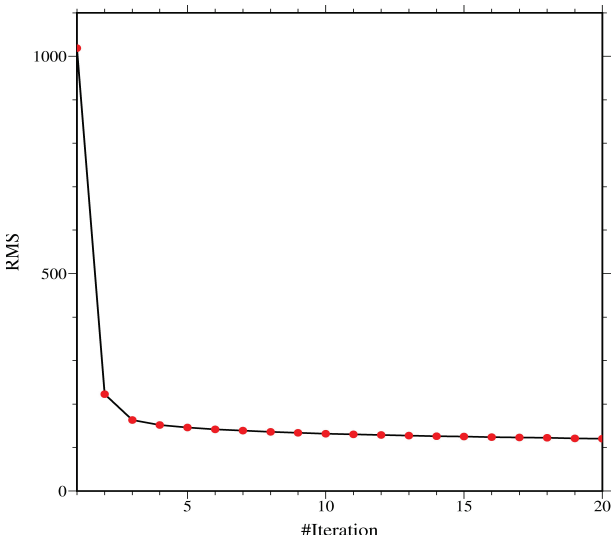

(c)

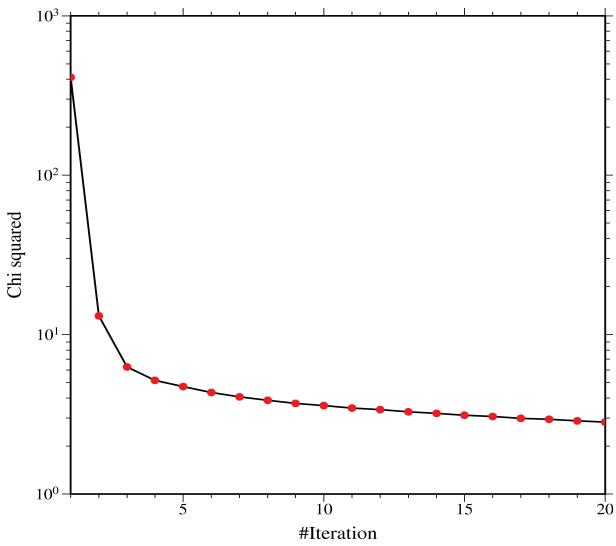

5.2.2. TOMO3D preliminary results and comparison

Similarly to the first invesion step in García-Cano [2009], TOMO3D was applied to model the marine data. However, model dimensions were reduced to include only the shot lines forming the acquisition grid (grey rectangle in Fig. 5.10b). The model includes all OBSs, and extends from km 15 to 156 in the x axis and from km 75 to 250 in the y axis. This is the area with the best ray coverage and resolution of the experiment [García-Cano et al., 2009]. Note that this choice leaves the southernmost shot line out of the data set. In addition, the rest of the picks are decimated to 1 out of 10. The velocity mesh extends to 30 km in depth, although actual model depth is greater

because the mesh hangs from the seafloor. Horizontal node spacing is 1.25 km in both dimensions, except where nodes are included to coincide with OBS locations. Vertical node spacing increases from 0.15 km at the top to 1 km at the bottom. The initial velocity model is created using the same 1-D profile that produced the results in García-Cano et al. [2014] (Fig. 5.12), which is made of four constant velocity gradients with the Moho discontinuity situated at ~18 km. The inversion parameters are summarised in Table 5.2.

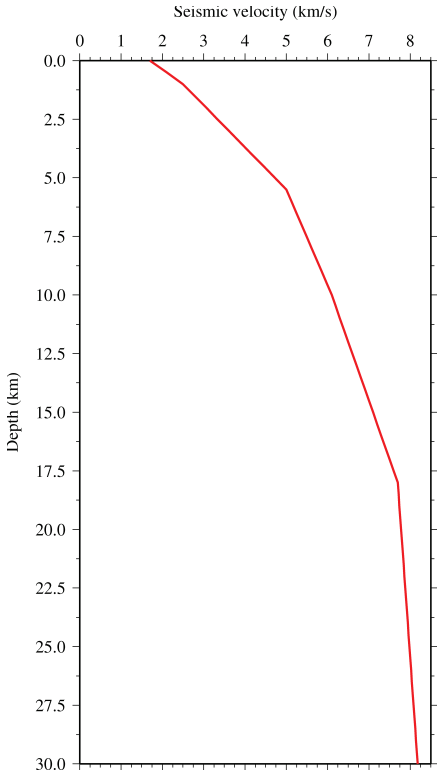

Figure 5.12. 1-D velocity–depth profile used to built the initial model. García-Cano [2009] proposes this model as an approximation to a continental margin velocity distribution. The deepest change in slope marks the location of the Moho.

Table 5.2. Relevant inversion parameters used for Esmeraldas experiment. Correlation lengths for the velocity model are set at the top and bottom nodes of the velocity grid and interpolated for the rest of the nodes in between. The increase with depth follows from the typical decrease in resolving power.

Inversion parameters	Values
Forward star order (x,y,z) (number of nodes)	(4,4,4)
λ_u	100
Average velocity perturbation limit (%)	10
Top velocity correlation lengths (x,y,z) (km)	(2.5,2.5,0.5)
Bottom velocity correlation lengths (x,y,z) (km)	(6,6,4)

Sample 2-D cuts of the velocity models for both inversion codes after 20 iterations are displayed in Figs 5.13 and 5.14 for comparison. The TOMO3D model is masked with the average DWS as described in subsection 2.4.2. The general structures defined by the isovelocity contours are rather similar. The main geological features described in García-Cano et al. [2014] are a low vertical velocity gradient that characterises the outer margin wedge (Fig. 5.13a-d), and the low-velocity zone in the overriding plate just above the interplate boundary and below the continental slope (Figs 5.13e-h and 5.14a,b). The two are also clearly identified in the model obtained with TOMO3D, and in good concordance with the FAST model.

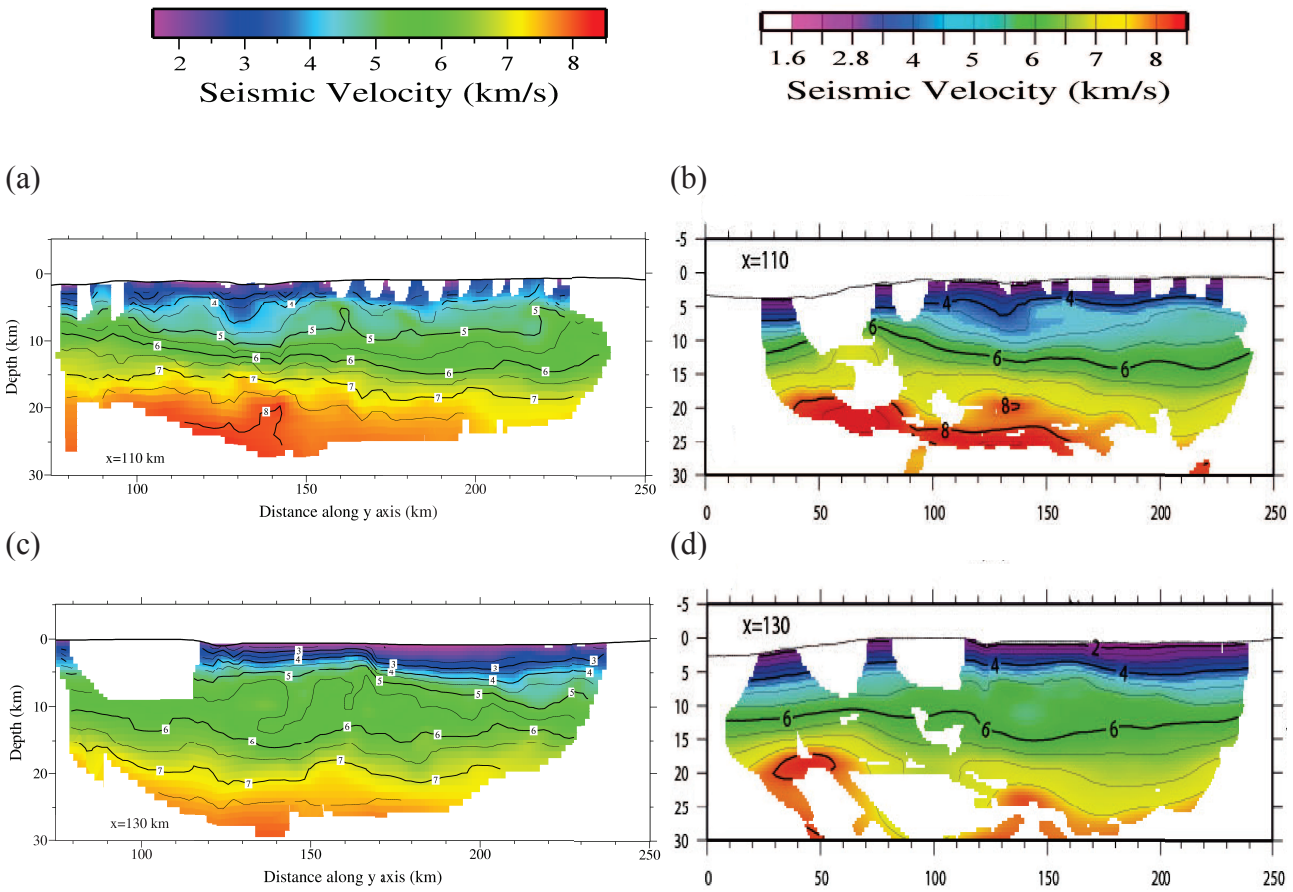

Figure 5.13. (a) and (b) vertical cuts at x=110 km. (c) and (d) vertical cuts at x=130 km. (e) and (f) vertical cuts at y=140 km. The small black arrow marks the position of the trench, whereas the big grey arrow indicates the inner limit of the low vertical velocity gradient outer wedge. The thick black line marks the rupture area of 1958 earthquake, while the dashed red line outlines the top of the low-velocity zone. (g) and (h) vertical cuts at y=160 km.

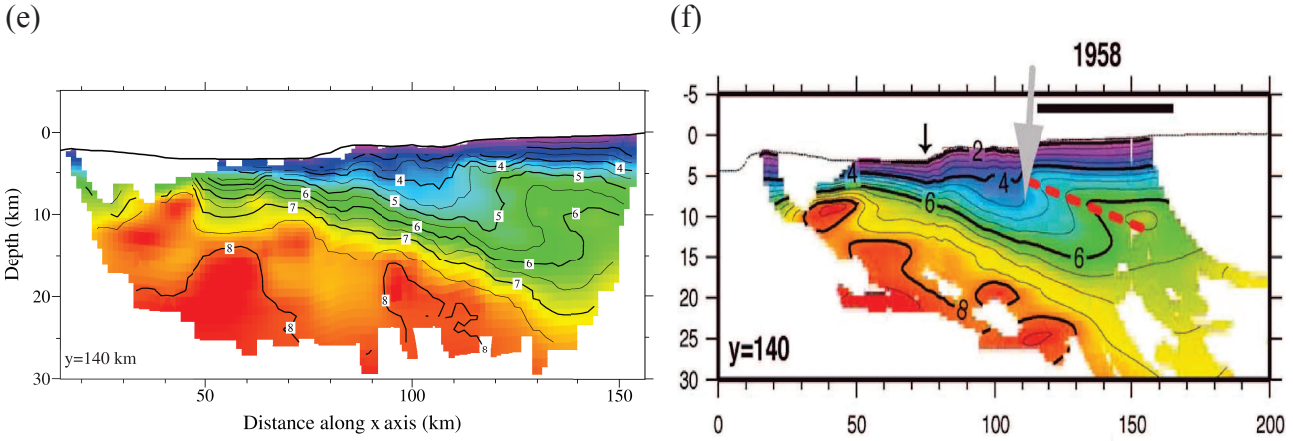

(g) (h)

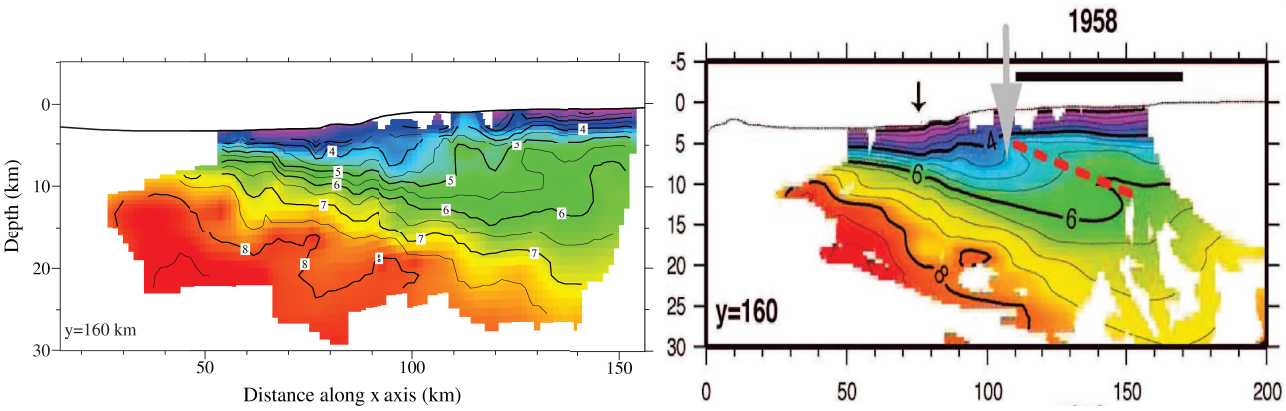

Figure 5.13. (Continued).

The sedimentary thicknesses both on the oceanic crust and on the continental shelf are also in good agreement (Figs 5.13e-h and 5.14a-d). The results also share the high velocity anomaly in the subducting plate observed in Fig. 5.13a,b, which seems to indicate a thin oceanic crust and a Moho uplift. However, the specific velocities are higher in the TOMO3D model, and the size and shape of the anomaly also differ. Another high velocity anomaly is identified in the continental crust. In this case, there is a better accord between both models in velocity values as well as in the extension and dimensions of the anomaly. García-Cano et al. [2014] discuss the thickness of the oceanic crust and its dip angle assuming that it is limited between the 4 km/s and 7.5 km/s isovelocity contours, and the agreement with TOMO3D results is satisfactory. Still, the future inversion of reflected data associated to the interplate boundary should be key in this regard. Reflections from the Moho would also contribute to the delimitation of the oceanic crust but according to García-Cano et al. [2014] they could not be identified on record sections.

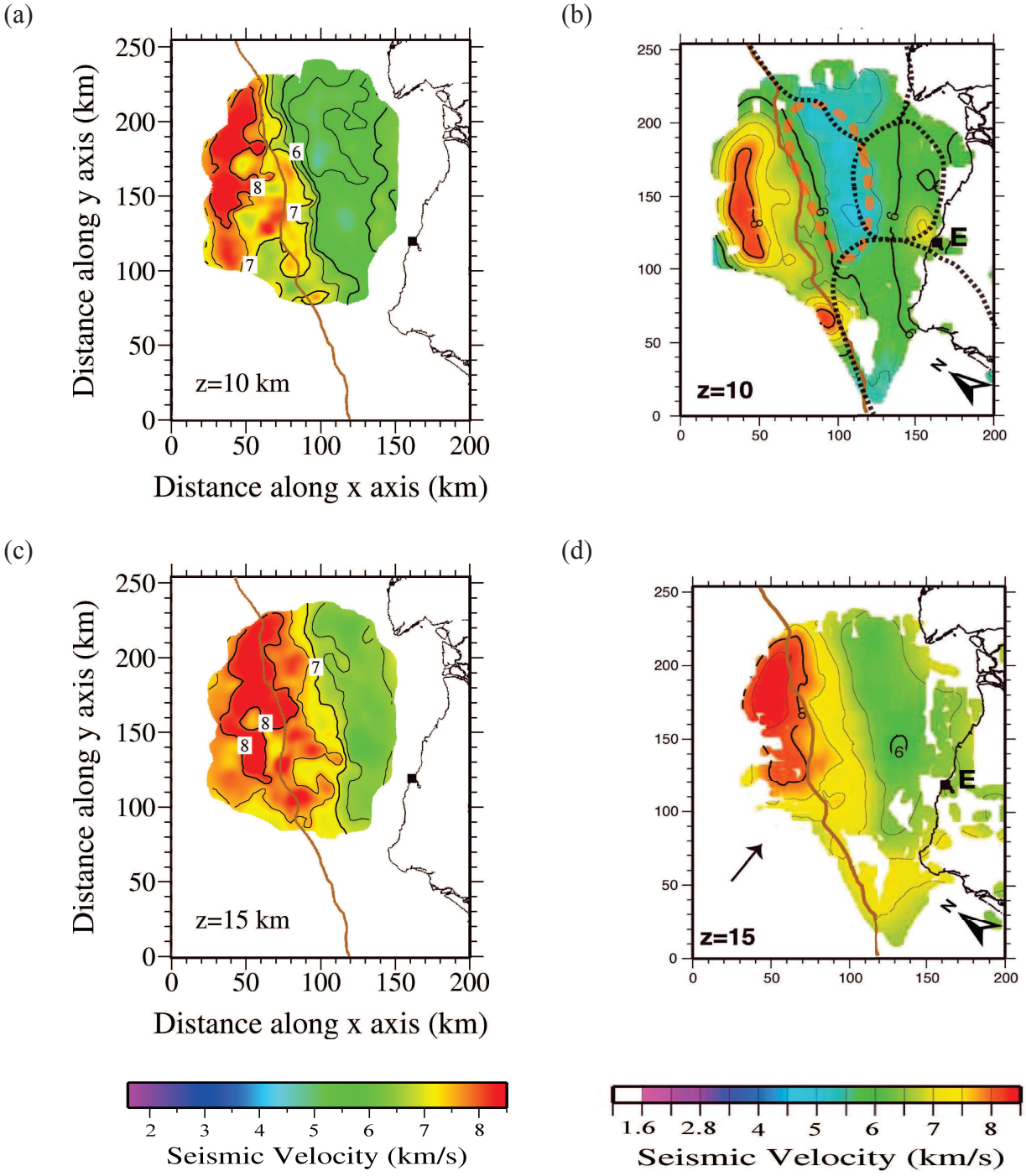

Figure 5.14. Horizontal cuts for TOMO3D (left) and FAST (right) models. Depth (z) is in kmbsf. The dashed orange line marks the low vertical gradient outer wedge. The brown line is the trench. The black square (E) marks the city of Esmeraldas. The black arrow point in the convergence direction.

5.2.3. Discussion

Fig. 5.11 displays the RMS evolution for the inversions with TOMO3D and FAST [García-Cano et al., 2014] as well as the χ^2 evolution with the former, all of them showing steady convergence trends. The RMS after the 20th iteration is ~120 ms and the corresponding χ^2 ~2.8. This data misfit is notably smaller than the one achieved in García-Cano et al. [2014]. After 5 more iterations the fit was improved to ~117 ms and χ^2 2.6. This means that the data fit is virtually not improving anymore, and although it is close to satisfactory, it may be worth trying to slightly tune the selected inversion parameters. In any case, results clearly improve the data fit achieved with FAST. Part of the explanation for the better fit with TOMO3D is the fact that the finite-difference scheme used in FAST includes homogeneous grid spacing in the three dimensions and the grid includes the water layer. This means that the error in the bathymetry will be, on average, as high as 50% of the grid spacing, so that the associated error can be considerable. In contrast, in the case of TOMO3D the grid of nodes hangs from the seafloor so that the bathymetry is fully honoured. The higher accuracy of TOMO3D is achieved at the expense of notably longer computational time, single iterations took ~15 hours, even though the number of data was one order of magnitude smaller than in García-Cano [2009]. Parameterisations are not straightforward to compare since inversions with FAST used a finer grid for ray tracing and travel time calculation than for the iterative inversion. Considering the dimensions of the new model, García-Cano et al. [2014] discretised the same volume with 281 × 351 × 61 nodes in the forward computation, and with 71 × 88 × 61 nodes in the inversion part, whereas in my inversion with TOMO3D the model consists of 153 × 177 × 42 nodes. TOMO3D updated the model on a finer mesh than FAST (~3 times more nodes), and doing so it found a final model that reproduces the observed travel times more accurately than FAST with a coarser forward discretisation (~5 times fewer nodes). In Fig. 5.11 after the first iteration the RMS for TOMO3D is greater than for FAST because the ray paths from the former are poorer approximations of the true ones due to the coarser parameterisation. However, after the second iteration the RMS for TOMO3D is now smaller because the finer inversion grid provides a better update of the initial model and the new synthetic travel times produce a better data fit even though forward parameterisation is not as fine. Moreover, after the fifth iteration inversion with TOMO3D does not make significant modifications to the model as shown by the stabilisation of the RMS and curves in Fig. 5.11, and at that point the RMS for TOMO3D is significantly smaller than the final RMS for FAST. In terms of computational time, TOMO3D achieves a notably better data fit in ~75 hours, a ~56% increment with respect to the time it takes for FAST to complete the 20 iterations. TOMO3D results were obtained using 2 MPI processes per node and 10 MP threads per CPU on 12

nodes each with 2 CPUs Intel® Xeon® Processor E5-2670 v2 (25M Cache, 2.50 GHz) of 8 cores each with the option to run up to 16 threads simultaneously. This means that in the current parallelisation scheme the bending solution could still be accelerated by launching up to 16 MP threads in each CPU.

The results obtained from the inversions with FAST in terms of data fit, indicate the need for a finer inversion grid. Moreover, FAST uses a jumping strategy for the regularisation constraints, which requires a reliable initial model that is particularly close to the true one. Using such strategy on an initial model, which is built as the extrapolation of a 1-D vertical velocity profile is not in favour of a satisfactory result. Typically, the initial model is not that reliable and is far from the true one, which is why the creeping strategy is a more general approach and is the default in TOMO3D. Indeed this strategy does not impose regularisation constraints with respect to the initial model ($\boldsymbol{\delta m+\delta m^S=m^{k+1}-m^0}$) but on the model perturbation to update from $\mathbf{m^k}$ to $\mathbf{m^{k+1}}$ ($\boldsymbol{\delta m=m^{k+1}-m^k}$). In any case, the refinement of the inversion grid would of course reduce the difference in computational time with respect to TOMO3D.

Nonetheless, the results obtained with TOMO3D are only preliminary. First, it is necessary to gradually include all refraction data in the inversion, giving special attention to land data, and the assessment and possible re-evaluation of pick errors. In second place, the record sections will need to be carefully examined to pick reflected phases, and determine the associated reflecting interface, ensuring their consistency among all the record sections involved. If the reflected data is sufficiently robust, the joint inversion should allow retrieving not only the velocity field but also the geometry of the corresponding reflector, most likely representing the interplate boundary or megathrust fault. Defining its location and geometry, as well as the properties just above and below it, would significantly contribute to the general understanding of the margin, for instance regarding its seismological behaviour, as explained in chapter 2 of this thesis. García-Cano [2009] presented a checkerboard test, which offers an idea of the resolution of the data set. However, it is even more important to perform at least a statistical uncertainty analysis that provides an error range for the inverted parameters, which is a quantitative measure of the reliability of the different areas and features in the model. An analysis as the one presented in Korenaga & Sager [2012] is an even more robust approach to travel-time tomography. Both procedures require intensive computation, possibly including high-performance computing in supercomputers with hundreds or thousands of CPUs, and consequently the optimisation of TOMO3D and its parallelisation is vital for their feasibility at present day. Indeed, these first real data inversion results indicate that model

discretisation as well as ray tracing and inversion parameters should be adjusted to slightly improve the data fit while at the same time trying to reduce computational time. Further optimisation and parallelisation of the code, for example in the inversion part [Lee et al., 2013] or the single-ray graph solution [e.g. Monsegny & Agudelo, 2013] or the bending calculations, should also be considered but it was out from the scope of my PhD work.

CHAPTER 6: CONCLUSIONS

6. CONCLUSIONS

In the following, first the key points for the results of this thesis are summarised. Next, the future work in relation to this summary is described as an outlook for the work presented here.

6.1. Summary

In this work I have implemented and satisfactorily applied TOMO3D, a new 3-D seismic tool for the modelling of the increasing quantity of 3-D wide-angle seismic data. TOMO3D is based on TOMO2D and performs parallel 3-D joint refraction and reflection travel-time tomography to yield models of the 3-D velocity distribution and the 2-D geometry of geological discontinuities. As a topic of interest in our research group, TOMO3D has been succesfully tested on its application to the investigation of the subduction zone at convergent margins. Results are encouraging and should prove useful in the study of the seismic and tsunami activity associated to this geological context where devastating megathrust earthquakes occur. The following summarises the main achievements of this thesis work:

6.1.1. TOMO2D, the Nicaraguan convergent margin and the 1992 tsunami earthquake

The application of TOMO2D to the study of the Nicaraguan margin shown in chapter 2 is a classic example of a robust 2-D travel-time tomography modelling. The seismic phases in record sections from the two wide-angle seismic profiles were carefully interpreted and correlated, with special attention on the identification of reflected phases and the associated interfaces. Picked refraction and reflection data were successfully explained by the final velocity and depth models, that display a good agreement at the intersection of profiles on both velocity and interplate reflector depth. The uncertainty for these models was quantified through a Monte Carlo-based analysis, showing that both the velocity field and the location of the interplate boundary are well recovered along most of the profiles. These models were subsequently interpreted to characterise the structure of the margin in combination with multi-channel seismic data. A misfit between wide-angle and multi-channel data interplate reflectors revealed a velocity anisotropy between near-vertical and sub-horizontal propagation. This anisotropy was attributed to the presence of a low-velocity zone caused by hydrofracturing of the overriding plate by overpressured water escaping from the subduction

channel. A subducted seamount was observed in both seismic data sets coinciding with an area of high seismic moment release, which is in accord with the suggestion that such geological features may create seismic asperities. The increase in normal stress at the interplate boundary may have contributed to the propagation of seismic energy to shallow depth, and thus to the consequent tsunami excitation that characterises the 1992 Nicaragua seismic event as a tsunami earthquake. Furthermore, empirical relations were employed to derive density and fracturing from the velocity distribution of the trench-perpendicular profile. The fracturing model served as a proxy of rock disaggregation in the margin, indicating that upper-plate rigidity is a key factor to account for the rupture characteristics (i.e. rupture propagation velocity, co-seismic slip, etc.) of this, and probably other, megathrust earthquakes. Additionally, the large slip that results from the low rigidity is key to explain its tsunamigenic character. The density distribution was used in the modelling of gravitational data, which confirmed the presence of a shallow, low-velocity continental mantle wedge, and together with the distribution of seismic events across the margin, contributed to the approximate determination of the down-dip limit of the seismological zone.

Through this case study, I have been able to learn the fundamentals of seismic phase interpretation and travel-time tomography modelling, and in particular of the usage of TOMO2D and its methodological and technical specificities. Also, the limitations of 2-D experimental approaches and the necessity for 3-D travel-time tomography modelling has become evident in the light of the instrinsic 3-D nature of seismic events.

6.1.2. MSRI

In travel-time tomography, much information is typically left unused in record sections. As a first attempt to increase data exploitation, in chapter 3 I focused on the water-layer multiples. The observation of water-layer multiple-like phases at longer offsets than their corresponding primary phases, a recurrent paradoxical phenomenon in wide-angle seismic record section, is described in chapter 3 as the constructive interference between the water-layer multiple and its reflection at the seafloor (MSRI). As explained in subsection 4.2.3., the possibility of inverting MSRI phases was included in TOMO3D so that it is possible to directly pick and use these data as it appears in record sections, without previoulsy having to convert MSRI picks to the travel times expected for the corresponding primary phases or having to use MSRI phases to roughly guide the extrapolation of primary picks. Whenever the said phenomenon takes place, including MSRI information on the

inversion increases ray coverage and potentially extends the model in depth.

6.1.3. TOMO3D: development and synthetic inversion test

TOMO3D, described in chapter 4, is a functional 3-D travel-time tomography code based on the former 2-D version TOMO2D, which overcomes the shortcomings of 2-D modelling. The joint inversion of refraction and reflection data can satisfactorily recover both velocity structure and reflector depth in complex synthetic cases. The hybrid ray tracing strategy combining the graph and bending methods provides adequate travel time and ray path accuracy as proven by comparison with analytical solutions and synthetic seismograms. Parallelisation of the forward problem is crucial for the practicality of the program as over 90% of the run time is typically spent in this part of the code, and adapts the code so that it can benefit from the currently available supercomputer facilities ensuring that the 3-D inversions are performed in a reasonable amount of time despite the increased number of parameters and data. The speedup achieved in the synthetic case is greater than the theoretically-calculated ideal speedup by a factor of ~3, showing that the parallelisation process also helped in the optimisation of the code.

As illustrated in section 5.1, TOMO3D succesfully retrieves the 3-D velocity structure and the geometry of two reflectors in a complex synthetic case that approximates a subduction setting. The layer-stripping strategy is proposed for the sequential extension of models in depth layer by layer, which poses simpler inversion problems. In combination with our joint refraction and reflection inversion scheme, this strategy allows for the inclusion of sharp contrasts to the otherwise smoother velocity distributions produced by classic refraction travel-time tomography. Moreover, the negative impact of the velocity–depth ambiguity is reduced, although it can still be present, and in real data experiments it should be estimated [Korenaga, 2011].

6.1.4. TOMO3D and the convergent margin of Ecuador and Colombia

The results from the first real data application of TOMO3D to the convergent margin of Ecuador and Colombia demonstrate that the code is a valid tool for crustal-scale studies. Just as TOMO2D, its 3-D version provides meaningful information for the investigation of the ocean–continent convergent margins, in this case in the form of the 3-D velocity distribution of the overriding and

underthrusting plates. Convergent margins are relevant geological settings because oceanic plate subduction generates most part of the Earth's seismic and volcanic activity, particularly at the Pacific Ring of Fire. The resulting 3-D velocity model is comparable to that obtained with FAST, another state-of-the-art 3-D travel-time tomography code, in that their respective velocity fields share the same major features, and so they support a common geological interpretation. The data fit achieved with TOMO3D is significantly better than that for the model in García-Cano et al. [2014], and it is achieved in only 5 iterations in contrast with the 20 iterations of FAST. Regarding computational time though, TOMO3D was slower than FAST. However, using a finer model parametrisation with FAST may have improved the data fit at the expense of an increase in computational time, whereas TOMO3D can take advantage of high-performance computing resources thanks to its parallelisation.

6.2. Outlook

The application to the Nicaraguan margin presented in chapter 2 shows the potential of seismic tomography and, at the same time, exemplifies the limitations of 2-D experiments, and evidences the need of 3-D surveys. The trench-parallel profile shows that even if this direction is more homogeneous than its perpendicular, there are observable lateral changes in the velocity distribution and in the interface geometry. A 3-D velocity and depth modelling would also facilitate measuring, for instance, the dimensions of the subducted seamount or the extension of the low velocity zone. More so, in the delimitation of the seismological zone, the 3-D distribution of seismic events had to be projected on the 2-D plane defined by the trench-perpendicular wide-angle profile. These events, and especially the greatest and most dangerous ones, mostly nucleate along the interplate boundary, which is a 2-D surface whose geometry can only be retrieved with a 3-D travel-time tomography code. The interplate coupling, seismic moment distribution and co-seismic slip distribution are also fundamentally 3-D and rather heterogeneously distributed across the margin, as it is the rupture propagation speed. This is the case for almost any earthquake, including the largest, tsunamigenic and most destructive ones (Fig. 6.1). All these parameters depend on the distribution of the elastic properties (e.g. rigidity) in a volume around the interplate boundary, which can be retrieved with the appropriate resolution from 3-D active seismic data.

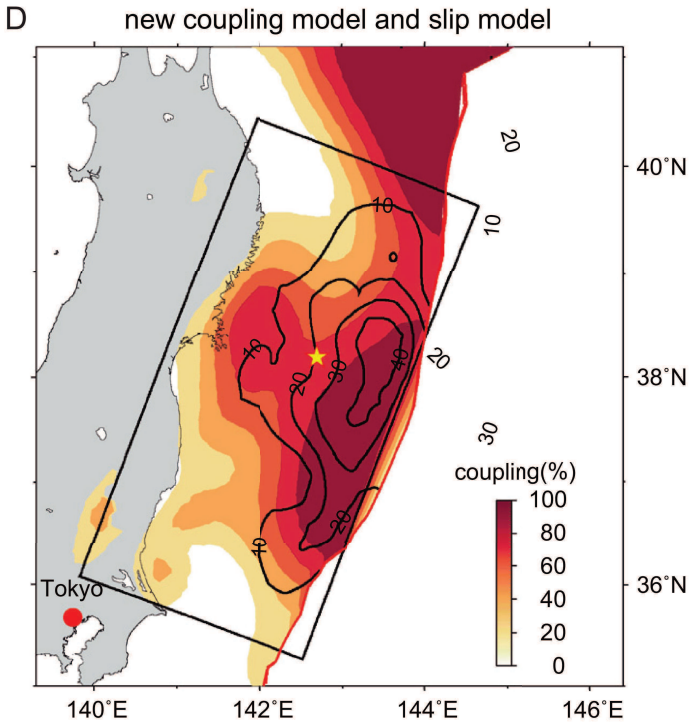

Figure 6.1. Co-seismic slip (black lines) and coupling distributions of the same event [Wei et al., 2012].

To properly address these issues I would propose to perform dedicated 3-D seismic surveys in areas of interest such as those displaying a high seismic risk, where previous knowledge is important. A few examples could be the Tohoku region in Japan, probably the subduction zone with more extensive and detailed geophysical, seismological and tsunami information; Cascadia in the US Western margin, where there is one of the most prominent seismic gaps and a history of destructive earthquakes and tsunamis; or Costa Rica in Central America, which has been studied in detail in the framework of the US Margins project and will be the site of a deep drilling within the i-ODP programme targeting the interplate seismogenic zone. Further, all these studies would surely benefit from the combination with passive seismic data as I explain below.

From a technical point of view, TOMO3D is currently being adapted to treat 2-D experiments as well, just as TOMO2D but with the advantage of parallelisation. For instance, the performance of uncertainty analyses is a time-consuming task, even in 2D and all the more so in 3D, which can clearly benefit from parallelisation and optimisation. Moreover, the ultimate goal is to implement statistical inversions as described in Korenaga & Sager [2012], which are posed as an iterative uncertainty analysis from which the final model is obtained as the mean of all acceptable-fit models, with a parameter error distribution given by their standard deviation.

The ray tracing method can be adapted to include phases other than primaries and their MSRI with a generalised scheme to find multiply transmitted, reflected and converted ray paths [Bai et al., 2009]. Another methodological development would be the possibility to incorporate near-vertical reflection seismic data, which would require allowing the graph origin nodes to be located in the water layer [e.g. Wang & Braile, 1996], and would increase the control on the shallowest parts of the models. The generalised ray-tracing scheme should prove useful in making the most of near-vertical data. As evidenced in the application to the Nicaraguan data set, if the code is to use both near-vertical and wide-angle data at the same time, it will also be necessary to incorporate velocity anisotropy in our code [e.g. Chapman & Pratt, 1992; Pratt & Chapman, 1992; Dunn et al., 2005; Zhou & Greenhalgh, 2005]. Moreover, the tomography scheme can also be adapted to model other physical properties such as attenuation [e.g. Evans & Zucca, 1988; Myers et al., 1998].

As stated above, a major goal would be to combine the inversion of active and passive seismic data. This would allow defining not only the velocity distribution and the reflector's geometry but also the hypocentral location of local earthquakes, which would significantly contribute to the investigation of the existing relationships between structural characteristics and earthquake nucleation. Earthquake data would of course add constraints on the velocity model, particularly for the deeper areas thanks to the privileged locations of natural seismic sources. As it is now, passive seismic data can be used straightaway in TOMO3D provided that we know the hypocentral location, but an earthquake relocation scheme should be integrated in the code to make the most of the combination with active data. For instance, Rawlinson & Urvoy [2006] simultaneously invert for earthquake location, velocity and depth, whereas Wagner et al. [2007] alternate the inversion of velocity with the relocation of the natural sources.

The layer-stripping strategy could be given a certain degree of automation, but always allowing for user control after each step. In addition, we could provide the option of including in each new step some or all previous reflectors and their corresponding picks, if this were to contribute to a better model recovery. In this regard, a node-specific damping overweight for depth models could be implemented, as it is now available for the velocity model. We may also add a DWS output file for depth models. Furthermore, outputting the average DWS over the number of iterations, instead of or apart from the DWS for the last iteration, would account for the non-linearity that is expressed in the need for the iterative solution of the linearised inverse problem. Other possible technical improvements of TOMO3D include inverse problem parallelisation [Lee et al., 2013] or the implementation of a GUI.

Finally, note that the first real data application is not complete, only preliminary results using first arrivals have been obtained. First, the model must be extended including the rest of the available refraction travel times. In this regard, inversion using different data subsets could be conducted to illustrate the robustness of the results in the different parts of the model. Next, record sections will be inspected to identify and pick reflected phases associated to the interplate boundary or the Moho discontinuity, although according to García-Cano et al. [2014] the latter have not been observed. The top of the basement may also produce observable reflections that will be searched in the record sections. If two or more reflecting interfaces are detected, the inversion will follow the layer-stripping strategy. Methodological improvements in phase picking could prove useful in this case and in general, for instance automatic or semi-automatic picking of both refractions and reflections, or visualisation tools for 3-D data such as The Kingdom Suite or Opendtect. The new data set including refracted and reflected picks, will be inverted starting from two initial velocity models: the same initial model used here and the final model obtained from refractions alone. This will serve as a basic evaluation of the dependency on the initial velocity model. As for the initial depth models, they will be built to roughly follow the specific isovelocity contours typically associated to each reflecting interface. The velocity–depth ambiguity will be explored by modifying the depth-kernel weight parameter w and checking the variations in the final velocity and depth models. The assessment of parameter uncertainty will be performed as in Sallarès et al. [2013], but as mentioned above this will probably require further optimisation of the code and high-performance computing resources that can be obtained, for instance through the access programme to the Mare Nostrum Supercomputer of the Barcelona Supercomputing Center.

REFERENCES

REFERENCES

Aki, K. & Lee, W.H.K. (1976). Determination of three-dimensional velocity anomalies under a seismic array using first P arrival times from local earthquakes. 1. A homogeneous initial model, *J. Geophys. Res.*, **81**, 4381–4399.

Aldridge, D.F. (1992). Analysis and inversion of seismic refraction traveltimes, PhD thesis, University of British Columbia, Vancouver.

Amdahl, G.M. (1967). Validity of the Single Processor Approach to Achieving Large-Scale Computing Capabilities, *AFIPS Conference Proceedings*, **30**, 483–485. doi:10.1145/1465482.1465560.

Ammon, C.J. & Vidale, J.E. (1993). Tomography without rays, *Bull. Seism. Soc. Am.*, **83**, 509–528.

Backus, M.M. (1959). Water reverberations – their nature and elimination, *Geophysics*, **24**, 233–261.

Backus, G. & Gilbert, F. (1967). Numerical applications of a formalism for geophysical inverse problems, *Geophys. J. Roy. Astr. Soc.*, **13**, 247–276.

Bai, C., Greenhalgh, S. & Zhou, B. (2007). 3D ray tracing using a modified shortest-path method, *Geophysics*, **72**, T27–T36.

Bai, C.-Y., Tang, X.-P. & Zhao, R. (2009). 2-D/3-D multiply transmitted, converted and reflected arrivals in complex layered media with the modified shortest path method, *Geophys. J. Int.*, **179**, 201–214.

Bai, C.-Y., Huang, G.-J. & Zhao, R. (2010). 2-D/3-D irregular shortest-path ray tracing for multiple arrivals and its applications, *Geophys. J. Int.*, **183**, 1596–1612.

Bangs, N.L., Shipley, T.H., Gulick, S.P.S, Moore, G.F., Kuromoto, S. & Nakamura, Y. (2004). Evolution of the Nankai Trough décollement from the trench into the seismogenic zone: Inferences from three-dimensional seismic reflection imaging, *Geology*, **32**, 273–276, doi:10.1130/G20211.1.

Barckhausen, U., Ranero, C.R., von Huene, R., Cande, S.C. & Roeser, H.A. (2001). Revised tectonic boundaries in the Cocos plate off Costa Rica: Implications for the segmentation of the convergent margin and for plate tectonic models, *J. Geophys. Res.*, **106**, 19207–19220.

Berhorst, A. (2006). Die Struktur des aktiven Kontinentalhangs vor Nicaragua und Costa Rica—Marin-seismische Steil- und Weitwinkelmessungen, PhD thesis, Christian-Albrechts-Univ., Kiel.

Bharadwaj, P., Wang, X., Schuster, G. & McIntosh, K. (2013). Increasing the number and signal-to-noise ratio of OBS traces with supervirtual refraction interferometry and free-surface multiples, *Geophys. J. Int.*, **192**, 1070–1084.

Bilek, S.L. & Lay, T. (2002). Tsunami earthquakes possibly widespread manifestations of frictional conditional stability, *Geophys. Res. Lett.*, **29**, doi:10.1029/2002GL015215.

Birch, F., (1961). The velocity of compressional waves in rocks to 10 kilobars, part 2, *J. Geophys. Res*., **66**, 2199-2224.

Bishop, T.N., Bube, K.P., Cutler, R.T., Langan, R.T., Love, P.L., Resnik, J.R., Shuey, R.T., Spindler, D.A. & Wyld, H.W. (1985). Tomographic determination of velocity and depth in laterally varying media, *Geophysics*, **50**, 903–923.

Blanpied, M.L., Lockner, D.A. & Byeflee, J.D. (1995). Frictional slip of granite at hydrothermal conditions, *J. Geophys. Res.*, **100**, 13045–13064.

Bregman, N.D., Bailey, R.C. & Chapman, C.H. (1989). Crosshole seismic tomography, *Geophysics*, **54**, 200–215, doi:10.1190/1.1442644.

Cao, S. & Greenhalgh, S. (1993). Calculation of the seismic first-break time field and its ray path distribution using a minimum traveltime tree, *Geophys. J. Int.*, **114**, 593–600, doi:10.1111/j.1365-246X.1993.tb06989.x.

Carcione, J.M., Picotti, S. & Santos, J.E. (2012). Numerical experiments of fracture-induced velocity and attenuation anisotropy, *Geophys. J. Int.,* **191**, 1179–1191, doi:10.1111/j.1365-246X.2012.05697.x.

Carlson, R.L. & Herrick, C.N. (1990). Densities and porosities in the oceanic crust and their variations with depth and age, *J. Geophys. Res.*, **95**, 9153–9170.

Carlson, R.L. & Miller, D.J. (2003). Mantle wedge water contents estimated from seismic velocities in partially serpentinized peridotites, *Geophys. Res. Lett.*, **30**, 1250, doi:10.1029/2002GL016600.

Červený, V., Molotkov, I. A. & Pšenčík, I. (1977). *Ray method in seismology*. Univerzita Karlova.

Červený, V. (2001). *Seismic Ray Theory*, Cambridge University Press.

Chapman, C.H. & Pratt, R.G. (1992). Traveltime tomography in anisotropic media – I. Theory, *Geophys. J. Int.*, **109**, 1–19.

Cheng, N. & House, L. (1996). Minimum traveltime calculation in 3-D graph theory, *Geophysics*, **61**, 1895–1898.

Christensen, N.I. (1966). Elasticity of ultrabasic rocks, *J. Geophys. Res.*, **71**, 5921–5931.

Christeson, G. L., McIntosh, K.D., Shipley, T.H., Flueh, E.R. & Goedde, H. (1999). Structure of the Costa Rica convergent margin, offshore Nicoya Peninsula. *J. Geophys. Res.*, **104**, 25443–25468.

Coates, R. (2002). *The Advanced SONAR Course*, Seiche, ISBN:1–904055–01-X.

Courant, R., Friedrichs, K. & Lewy, H. (1967). On the partial difference equations of mathematical physics, *IBM J. Res. Dev.*, **11**, 215–234.

Crowe, J.C. & Buffler, R.T. (1985). Multichannel seismic records across the Middle America Trench and Costa Rica- Nicaragua convergent margin, NCY-7 and NIC-1, in *Middle America Trench off Western Central America, Data Syn. Ser., Atlas 7*, edited by Ladd, J.W. & Buffler, R.T., 11 pp., Ocean Margin Drill. Prog., Woods Hole, Mass.

Cummings, J. (2004). *Seismic surveys: what we don't know may hurt*, Report of the Acoustic Ecology Institute prepared for Greenpeace USA.

Dagnino, D., Sallarès, V. & Ranero, C.R. (2014). Scale- and parameter-adaptive model-based gradient pre-conditioner for elastic full-waveform inversion, *Geophys. J. Int.*, **198**, 1130–1142.

Dannowski, A., Grevemeyer, I., Phipps Morgan, J., Ranero, C.R., Maia, M. & Klein, G. (2011). Crustal structure of the propagating TAMMAR ridge segment on the Mid-Atlantic Ridge, 21.5◦ N, *Geochem. Geophys. Geosyst.*, **12**, Q07012, doi:10.1029/2011GC003534.

Dash, R., Spence, G., Hyndman, R.D., Grion, S., Wang, Y. & Ronen, S. (2009). Wide-area imaging from OBS multiples, *Geophysics*, **74**, Q41–Q47.

Deal, M.M. & Nolet, G. (1996). Nullspace shuttles, *Geophys. J. Int.*, **124**, 372–380.

DeMets, C., Gordon, R.G., Argus, D.F. & Stein, S. (1994). Effect of recent revisions to the geomagnetic reversal time- scale, *Geophys. Res. Lett.*, **21**, 2191–2194.

DeShon, H. R., Schwartz, S.Y., Newman, A.V., González, V., Protti, M., Dorman, L.M., Dixon, T.H., Sampson, D.E. & Flueh, E.R. (2006). Seismogenic zone structure beneath the Nicoya Peninsula, Costa Rica, from three-dimensional local earthquake P- and S-wave tomography, *Geophys. J. Int.,* **164**, 109–124.

Dijkstra, E.W. (1959). A note on two problems in connection with graphs, *Numer. Math.*, **1**, 269–271.

Dinc, A.N., Rabbel, W., Flueh, E.R., & Taylor, W. (2011). Mantle wedge hydration in Nicaragua from local earthquake tomography, *Geophys. J. Int.*, **186**, 99–112. doi:10.1111/j.1365-246X.2011.05041.x.

Dunn, R.A., Lekić, V., Detrick, R.S. & Toomey, D.R. (2005).Three-dimensional seismic structure of the Mid-Atlantic Ridge (35ºN): Evidence for focused melt supply and lower crustal dike injection, *J. Geophys. Res.*, **110**, B09101, doi:10.1029/2004JB003473.

Evans, J.R. & Zucca, J.J. (1988). Active High-Resolution Seismic Tomography of Compressional Wave Velocity and Attenuation Structure at Medicine Lake Volcano, Northern California Cascade Range, *J. Geophys. Int.*, **93**, 15016–15036.

Farra, V. & Madariaga, R. (1988). Non-linear reflection tomography, *Geophys. J. Int.*, **95**, 135–147.

Farra, V. (1992). Bending method revisited: a Hamiltonian approach, *Geophys. J. Int.*, **109**, 138–150.

Fischer, R. & Lees, J.M. (1993). Shortest path ray tracing with sparse graphs, *Geophysics*, **58**, 987–996, doi:10.1190/1.1443489.

Fukao, Y. (1979). Tsunami earthquakes and subduction processes near deep-sea trenches, *J. Geophys. Res.*, **84**, 2303–2314.

Gailler, A., Charvis, P. & Flueh, E.R. (2007). Segmentation of the Nazca and South American plates along the Ecuador subduction zone from wide-angle seismic profiles, *Earth Planet. Sci. Lett.*, **260**, 444–464 doi:10.1016/j.epsl.2007.05.045.

Gallo, G. & Pallottino, S. (1986). Shortest path methods: A unifying approach, *Math. Program. Study*, **26**, 38–64.

García-Cano, L.C. (2009). Imagerie sismique 3D de la zone de subduction à la frontière Colombie-Équateur, PhD thesis, Université de Nice Sophia Antipolis, Nice.

García-Cano, L.C., Galve, A., Charvis, P. & Marcaillou, B. (2014). Three-dimensional velocity structure of the outer fore arc of the Colombia-Ecuador subduction zone and implications for the 1958 megathrust earthquake rupture zone, *J. Geophys. Res.*, **199**, doi:10.1002/2012JB009978.

Geist, E.L. & Bilek, S.L. (2001). Effect of depth-dependent shear modulus on tsunami generation along subduction zones, *Geophys. Res. Lett.*, **28**, 1315–1318.

Goldberg, D.E. (1989). *Genetic Algorithms in Search, Optimization, and Machine Learning*, Addison-Wesley, Reading.

Goldberg, D. & Sun, Y.-F. (1997). Seismic structure of the upper oceanic crust revealed by in situ Q logs, *Geophys. Res. Lett.*, **24**, 333–336.

Goold, J.C. & Fish, P.J. (1998). Broadband spectra of seismic survey air-gun emissions, with reference to dolphin auditory thresholds, *J. Acoust. Soc. Am.*, **103**, 2177–2184.

Grad, M., Mjelde, R., Czuba, W., Guterch, A. & Schweitzer, J. (2011). Modelling of seafloor-multiples observed in OBS data from the North Atlantic – new seismic tool for oceanography?, *Pol. Polar Res.*, **32**, 375–392.

Hamilton, E.L. (1978). Sound velocity-density relations in sea-floor sediments and rocks, *J. Ac. Soc. Am.*, **63**, 366–377.

Hensen, C., Wallmann, K., Schmidt, M., Ranero, C.R. & Suess, E. (2004). Fluid expulsion related to mud extrusion off Costa Rica –a window to the subducting slab. *Geology*, **32**, 201–204.

Hobro, J.W.D., Singh, S.C. & Minshull, T.A. (2003). Three-dimensional tomographic inversion of combined reflection and refraction seismic traveltime data, *Geophys. J. Int.*, **152**, 79–93.

Hole, J.A. (1992). Nonlinear high-resolution three-dimensional travel-time tomography, *J. Geophys. Res.*, **97**, 6553–6562.

Hole, J.A. & Zelt, B.C. (1995). Three-dimensional finite-difference reflection travel times, *Geophys. J. Int.*, **121**, 427–434.

Hyndman, R.D. & Wang, K. (1993). Thermal constraints on the zone of major thrust earthquake failure—The cascadia subduction zone, *J. Geopyhs. Res.*, **98**, 2039–2060.

Hyndman, R.D., Yamano, M. & Oleskevich, D.A. (1997). The seismogenic zone of subduction thrust faults, *Island Arc*, **6**, 244–260.

Hyndman, R.D. & Peacock, S.M. (2003). Serpentinization of the forearc mantle, *Earth Planet. Sci. Lett.*, **212**, 417–432, doi:10.1016/S0012–821X(03)00263-2.

Ihmlé, P.F. (1996a). Frequency-dependent relocation of the 1992 Nicaragua slow earthquake: an empirical Green's function approach, *Geophys. J. Int.*, **127**, 75–85.

Ihmlé, P.F. (1996b). Monte Carlo slip inversion in the frequency domain: Application to the 1992 Nicaragua slow earthquake, *Geophys. Res. Let.*, **23**, 913–916.

Ivandic, .M., Grevemeyer, I., Berhorst, A., Flueh, E.R. & McIntosh, K. (2008). Impact of bending related faulting on the seismic properties of the incoming oceanic plate offshore of Nicaragua, *J. Geophys. Res.*, **113**, B05410, doi:10.1029/2007JB005291.

Johnson, D.B. (1977). Efficient algorithms for shortest paths in sparse networks, *J. ACM*, **24***,* 1–23.

Johnston, D.H. & Toksoz, M.N. (1981). Definitions and terminology in *Seismic Wave Attenuation*, pp. 1–5, eds Johnston, D.H. & Toksoz, M.N., SEG Geophys., Reprint Ser. No. 2.

Julian, B.R. & Gubbins, D. (1977). Three-dimensional seismic ray tracing, *J. Geophys.*, **43**, 95–114.

Kanamori, H. (1972). Mechanism of tsunami earthquakes, *Phys. Earth Planet. Int.*, **6**, 346–359.

Kanamori, H. & McNally, K.C. (1982). Variable rupture mode of the subduction zone along the Ecuador - Colombia Coast, *Bull. Seismol. Soc. Am.*, **72**, 1241–1253.

Kanamori, H. & Kikuchi, M. (1993). The 1992 Nicaragua Earthquake: A slow tsunami earthquake associated with subducted sediments, *Nature*, **361**, 714–716.

Kelleher, J.A. (1972). Rupture zones of large South-American earthquakes and some predictions, *J. Geophys. Res.*, **77**, 2087–2103.

Kern, H. & Tubia, J.M. (1993). Pressure and temperature dependence of P- and S-wave velocities, seismic anisotropy and density of sheared rocks from the sierra alpujata massif (ronda peridotites, southern Spain), *Earth Planet. Sci. Lett.*, **119**, 191–205.

Kikuchi M. & Kanamori, H. (1995). The Shikotan earthquake of October 4, 1994: Lithospheric earthquake, *Geophys. Res. Lett.*, **22**, 1025–1028.

Kim, S. (2002). 3-D Eikonal solvers: first-arrival traveltimes, *Geophysics*, **67**, 1225–1231.

Kirby, S.H. (1983). Rheology of the lithosphere, *Rev. Geophys. Sp. Phys.*, **21**, 1458-1487.

Kirkpatrick, S., Gelatt, Jr, C.D. & Vecchi, M.P. (1983). Optimization by simulated annealing, *Science*, **220**, 671–680.

Kissling, E. (1988). Geotomography with local earthquake data, *Rev. Geophys.*, **26**, 659–698.

Klimeš, L. & Kvasnička, M. (1994). 3-D network ray tracing, *Geophys. J. Int.*, **116**, 726–738.

Korenaga, J. (2000). Magmatism and dynamics of continental breakup in the presence of mantle plume, PhD thesis, Massachusetts Institute of Technology & Woods Hole Oceanographic Institution.

Korenaga, J., Holbrook, W.S., Kent, G.M., Kelemen, P.B., Detrick, R.S., Larsen, H.-C., Hopper, J.R. & Dahl-Jensen, T. (2000). Crustal structure of the southeast Greenland margin from joint refraction and reflection seismic tomography, *J. Geophys. Res.*, **105**, 21591–21614.

Korenaga, J., Holbrook, W.S., Detrick, R.S. & Kelemen, P.B. (2001). Gravity anomalies and crustal structure at the southeast Greenland margin, *J. Geophys. Res.*, **106**, 8853–8870.

Korenaga, J. (2011). Velocity–depth ambiguity and the seismic structure of large igneous provinces: a case study from the Ontong Java Plateau, *Geophys. J. Int.*, **185**, 1022–1036.

Korenaga, J. & Sager, W.W. (2012). Seismic tomography of Shatsky Rise by adaptive importance sampling, *J. Geophys. Res.*, **117**, B08102, doi:10.1029/2012JB009248.

Kormann, J., Cobo, P., Recuero, M., Biescas, B. & Sallarès, V. (2009). Modelling seismic oceanography experiments by using first- and second-order complex frequency shifted perfectly matched layers, *Acta Acust. United Ac.*, **95**, 1104–1111.

Kormann, J., Biescas, B., Korta, N., de la Puente, J. & Sallarès, V. (2011). Application of acoustic full waveform inversion to retrieve high-resolution temperature and salinity profiles from synthetic seismic data, *J. Geophys. Res.*, **116**, C11039, doi:10.1029/2011JC007216.

Koulakov, I. (2009). LOTOS code for local earthquake tomographic inversion. Benchmarks for testing tomographic algorithms, *Bull. Seismol. Soc. Am.*, **99**, 194–214.

Landrø, M. & Amundsen, L. (2010). Marine Seismic Sources Part I, *GeoExpro*, 1, Vol. **7**.

Lee, E.-J., Huang, H., Dennis, J.M., Chen, P., Wang, L. (2013). An optimized parallel LSQR algorithm for seismic tomography, *Comput. Geosci.*, **61**, 184–197.

Lefeldt, M., Ranero, C.R. & Grevemeyer, I. (2012). Seismic evidence of tectonic control on the depth of water influx into incoming oceanic plates at subduction trenches, *Geochem. Geophys. Geosyst.*, **13**, Q05013, doi:10.1029/2012GC004043.

Lelièvre, P.G., Farquharson, C.G. & Hurich, C.A. (2011). Inversion of first-arrival seismic traveltimes without rays, implemented on unstructured grids, *Geophys. J. Int.*, doi:10.1111/j.1365-246X.2011.04964.x.

Leung, S. & Qian, J. (2006). An adjoint-state method for three-dimensional transmission traveltime tomography using first arrivals, *Commun. Math. Sci.*, **4**, 249–266.

Liu, J.-Y. & Huang, C.-F. (2001). Acoustic plane-wave reflection from rough surface over a random fluid half-space, *Ocean Eng.*, **28**, 751–762.

Lutter, W.J. & Nowack, R.L. (1990). Inversion for crustal structure using reflections from PASSCAL Ouachita experiment, *J. Geophys. Res.*, **95**, 4633–4646.

MacGillivray, A.O. & Chapman, N.R. (2005). *Results from an Acoustic Modelling Study of Seismic Airgun Survey Noise in Queen Charlotte Basin*, School of Earth and Ocean Sciences, University of Victoria.

Marone, C. & Saffer, D.M. (2007). Fault friction and the upper transition from seismic to aseismic faulting, in *The Seismogenic Zone of Subduction Thrust Faults*, edited by Dixon, T. et al., pp. 346–369, Columbia Univ. Press., New York.

Martínez-Loriente, S., Sallarès, V., Gràcia, E., Bartolome, R., Dañobeitia, J.J. & Zitellini, N. (2014). Seismic and gravity constraints on the nature of the basement in the Africa-Eurasia plate

boundary: New insights for the geodynamic evolution of the SW Iberian margin, *J. Geophys. Res.*, **119**, 127–149, doi:10.1002/2013JB010476.

McCaughney, M. & Singh, S.C. (1997). Simultaneous velocity and interface tomography of normal-incidence and wide-aperture seismic traveltime data, *Geophys. J. Int.*, **131**, 87–99.

McIntosh, K.D., Silver, E.A., Ahmed, I., Berhorst, A., Ranero, C.R., Kelly, R.K. & Flueh, E.R (2007). The Nicaragua convergent margin, in *The Seismogenic Zone of Subduction Thrust Faults, Part III*, edited by Dixon, T.H. & Moore, J.C., chap. 9, pp. 257–287, Columbia Univ. Press, New York.

Meléndez, A., Sallarès, V., Ranero, C.R. & Kormann, J. (2014). Origin of water layer multiple phases with anomalously high amplitude in near-seafloor wide-angle seismic recordings, *Geophys. J. Int.*, **196**, 243–252, doi:10.1093/gji/ggt391.

Mendoza, C. & Dewey, J.W. (1984). Seismicity associated with the great Colombia-Ecuador earthquakes of 1942, 1958, and 1979 - Implications for barrier models of earthquake rupture, *Bull. Seismol. Soc. Am.*, **74**, 577–593.

Minshull, T.A., Muller, M.R. & White, R.S. (2006). Crustal structure of the Southwest Indian Ridge at 66ºE: seismic constraints, *Geophys. J. Int.*, **166**, 135–147.

Monsegny, J. & Agudelo, W. (2013). Shortest path ray tracing on parallel GPU devices, SEG 83rd Annual International Meeting, *Expanded Abstracts*, 3470–3474, doi:10.1190/segam2013-0802.1.

Moore, J.C. & Vrolijk, P. (1992). Fluids in accretionary prisms, *Rev. Geophys.*, **30**, 113–135.

Moore, J.C. & Saffer, D. (2001). Updip limit of the seismogenic zone beneath the accretionary prism of Southwest Japan: An effect of diagenetic to lowgrade metamorphic processes and increasing effective stress, *Geology*, **29**,183–186.

Moser, T.J. (1991). Shortest path calculation of seismic rays, *Geophysics*, **56**, 59–67.

Moser, T.J., Nolet, G. & Snieder, R. (1992a). Ray bending revisited, *Bull. Seismol. Soc. Am.*, **82**, 259–288.

Moser, T.J., Van Eck, T. & Nolet, G. (1992b). Hypocenter determination in strongly heterogeneous earth models using the shortest path method, *J. Geophys. Res.*, **97**, 6563–6572.

Mukerji, T., Berryman J., Mavko, G. & Berge, P. (1995). Differential effective medium modelling of rock elastic moduli with critical porosity constraints, *Geophys. Res. Lett.*, **22**, 555–558.

Muller, M.R., Minshull, T.A. & White, R.S., 1999. Segmentation and melt supply at the Southwest Indian Ridge, *Geology*, **27**, 867–870.

Myers, S.C., Beck, S., Zandt, G. & Wallace, T. (1998). Lithospheric-scale structure across the Bolivian Andes from tomographic images of velocity and attenuation for *P* and *S* waves, *J. Geophys. Res.*, **103**, 21233–21252.

Nakanishi, I. & Yamaguchi, K. (1986). A numerical experiment on nonlinear image reconstruction from first-arrival times for two-dimensional island arc structure, *J. Phys. Earth*, **34**, 195–201.

Newman, W.M. & Sproull, R.F. (1973). *Principles of interactive computer graphics*, McGraw-Hill, New York.

Nur, A., Mavko, G. Dvorkin, J. & Galmudi, D. (1998). Critical porosity: A key relating physical properties to porosity in rocks, *Leading Edge*, **17**, 357–362.

Okal, E.A. (1988). Seismic parameters controlling far-field tsunami amplitudes: A review, *Nat. Hazards*, **1**, 67–96.

Oleskevich, D.A., Hyndman, R.D. & Wang, K. (1999). The updip and downdip limits to great subduction earthquakes: Thermal and structural models of Cascadia, South Alaska, SW Japan, and Chile, *J. Geophys. Res.*, **104**, 14965–14992.

Pacheco, J., Sykes, L.R. & Scholz, C.H. (1993). Nature of seismic coupling along simple plate boundaries of the subduction plate, *J. Geophys. Res.*, **98**, 14133–14159.

Paige, C.C. & Saunders, M.A. (1982). LSQR: An algorithm for sparse linear equations and sparse least squares, *Trans. Math. Software*, **8**, 43–71.

Papazachos, C. & Nolet, G. (1997). *P* and *S* deep velocity structure of the Hellenic area obtained by robust nonlinear inversion of travel times, *J. Geophys. Res.*, **102**, 8349–8367.

Parker, R.L. (1974). New method for modelling marine gravity and magnetic anomalies. *J. Geophys. Res.*, **79**, 2014–2016.

Peacock, S.M. (1990). Fluid processes in subduction zones, *Science*, **48**, 329–337.

Peacock, S.M. & Hyndman, R.D. (1999). Hydrous minerals in the mantle wedge and the maximum depth of subduction thrust earthquakes, *Geophys. Res. Lett.*, **26**, 2517–2520, doi:10.1029/1999GL900558.

Pelayo, A.M. & Wiens, D.A. (1992). Tsunami earthquakes: slow thrust-faulting events in the accretionary wedge, *J. Geophys. Res.*, **97**, 15321–15337.

Pereyra et al. (1980). Solving two-point seismic ray tarcingt problems in a heterogeneous medium. Part 1. A general adaptive finite difference method, *Bull. Seismol. Soc. Am.*, **70**, 79–99.

Piatanesi, A., Tinti, S. & Gavagni, I. (1996). The slip distribution of the 1992 Nicaragua earthquake from tsunami run-up data, *Geophys. Res. Lett.*, **23**, 37–40.

Polet, J. & Kanamori, H. (2000). Shallow subduction zone earthquakes and their tsunamigenic potential, *Geophys. J. Int.*, **142**, 684–702.

Prada, M., Sallarès, V, Ranero, C.R., Guzman, M., Zitellini, N., Grevemeyer, I. & de Franco, R. (2012). Tectonic Structure of the Central Tyrrhenian Sea from wide-angle and near vertical seismics and gravity modelling, *Proceedings of the AGU Fall Meeting 2012*, T23F-2738, San Francisco.

Prada, M., Sallarès, V., Ranero, C.R., Vendrell, M.G., Grevemeyer, I., Zitellini, N. & De Franco, R. (2014). Seismic structure of the Central Tyrrhenian basin: Geophysical constraints on the nature of the main crustal domains, *J. Geophys. Res.*, **119**, 52–70, doi:10.1002/2013JB010527.

Pratt, R.G. & Chapman, C.H. (1992). Traveltime tomography in anisotropic media – II. Application, *Geophys. J. Int.*, **109**, 20–37.

Pratt, R.G., Gao, F., Zelt, C. & Levander, A. (2002). The limits of complementary nature of traveltime and waveform tomography, Sub-basalt imaging, *J. Conf. Abs.*, **7**, 181.

Press, W.H., Teukolsky, S.A., Vetterling, W.T. & Flannery, B.P. (1992). *Numerical recipes in C. The Art of Scientific Computing*, 2nd edn, Cambridge University Press.

Prodehl, C. & Mooney, W.D. (2012). *Exploring the Earth's Crust: History and Results of Controlled-source Seismology*, Geological Society of America.

Prothero, W.A., Taylor, W.J. & Eickemeyer, J.A. (1988). A fast, two-point, three-dimensional raytracing algorithm using a simple step search method, *Bull. Seismol. Soc. Am.*, **78**, 1190–1198.

Pullammanappallil, S.K. & Louie, J.N. (1993). A generalized simulated-annealing optimization for inversion of first-arrival times, *Bull. Seis. Soc. Am.*, **84**, 1397–1409.

Ranero, C.R. & von Huene, R. (2000). Subduction erosion along the Middle America convergent margin, *Nature*, **404**, 748–755, doi:10.1038/35008046.

Ranero, C.R., von Huene, R., Flueh, E.R., Duarte, M., Baca, D. & McIntosh, K.D. (2000). A cross section of the convergent Pacific margin of Nicaragua, *Tectonics*, **19**, 335–357.

Ranero, C.R., Phipps Morgan, J., McIntosh, K., Reichert, C. (2003). Bending, faulting, and mantle serpentinization at the Middle America Trench, *Nature*, **425**, 367–373.

Ranero, C. R., von Huene, R., Weinrebe, W. & Barckhausen, U. (2007). Convergent margin tectonics of Middle America: A marine perspective, *Central America, Geology, Hazards and*

Resources, 239–265, Ed. Alvarado, G. & Bunschu, J., A.A. Balkema Publisher.

Ranero, C.R., Grevemeyer, I., Sahling, H., Barckhausen, U., Hensen, C., Wallmann, K., Weinrebe, W., Vannucchi, P., von Huene, R. & McIntosh, K. (2008). The hydrogeological system of erosional convergent margins and its influence on tectonics and interplate seismogenesis, *Geochem. Geophys. Geosyst.*, **9**, Q03S04, doi:10.1029/2007GC001679.

Rawlinson, N. & Sambridge, M. (2003). Seismic traveltime tomography of the crust and lithosphere, *Adv. Geophys.*, **46**, 81–197.

Rawlinson, N. & Sambridge, M. (2004). Wave front evolution in strongly heterogeneous layered media using the fast marching method, *Geophys. J. Int.*, **156**, 631–647.

Rawlinson, N. & Urvoy, M. (2006). Simultaneous inversion of active and passive source datastes for 3-D seismic structure with application to Tasmania, *Geophys. Res. Lett.*, **33**, L24313, doi:10.1029/2006GL028105.

Ruff, L.J. & Kanamori, H. (1983). Seismic coupling and uncoupling at subduction zones, *Tectonophysics*, **99**, 99–117.

Sahling, H., Masson, D.G., Ranero, C.R., Hühnerbach, V., Weinrebe, W., Klaucke, I., Bürk, D., Brückmann, W. & E. Suess (2008). Fluid seepage at the continental margin offshore Costa Rica and southern Nicaragua, *Geochem. Geophys. Geosyst.*, **9**, Q05S05, doi:10.1029/2008GC001978.

Sallarès, V., Dañobeitia, J.J., Flueh, E.R. & Leandro, G. (1999). Seismic velocity structure across the Middle American landbridge in northern Costa Rica. *J. Geodyn.,* **27**, 327–344.

Sallarès, V., Dañobeitia, J.J. & Flueh, E.R. (2000). Seismic tomography with local earthquakes in Costa Rica, *Tectonophysics,* **329**, 61–79.

Sallarès, V, Charvis, P., Flueh, E.R. & Bialas, J. (2003). Seismic structure of Cocos and Malpelo Volcanic Ridges and implications for hot spot-ridge interaction, *J. Geophys. Res.*, **108**, 2564, doi:10.1029/2003JB002431.

Sallarès, V. & Ranero, C.R. (2005). Structure and tectonics of the erosional convergent margin off Antofagasta, north Chile (23º 30'S), *J. Geophys. Res.*, **110**, B0601, doi:10.1029/2004JB003418.

Sallarès, V., Charvis, P., Flueh, E.R., Bialas, J. & the SALIERI Scientific Party (2005). Seismic structure of the Carnegie ridge and the nature of the Galápagos hotspot, *Geophys. J. Int.*, **161**, 763–788, doi:10.1111/j.1365-246X.2005.02592.x.

Sallarès, V., Gailler, A., Gutscher, M.-A., Graindorge, D., Bartolomé, R., Gràcia, E., Dañobeitia, J.J. & Zitellini, N. (2011). Seismic evidence for the presence of Jurassic oceanic crust in the central

Gulf of Cadiz (SW Iberian margin), *Earth Planet. Sci. Lett.*, **311**, 112–123, doi:10.1016/j.epsl.2011.09.00.

Sallarès, V., Meléndez, A., Prada, M., Ranero, C.R., McIntosh, K. & Grevemeyer, I. (2013). Overriding plate structure of the Nicaragua convergent margin: Relationship to the seismogenic zone of the 1992 tsunami earthquake, *Geochem. Geophys. Geosyst.*, **14**, doi:10.1002/ggge.20214.

Sambridge, M.S. (1990). Non-linear arrival time inversion: Constraining velocity anomalies by seeking smooth models in 3-D, *Geophys. J. Int.*, **102**, 653–677.

Sambridge, M., Rickwood, P., Rawlinson, N. & Sommacal, S. (2007). Automatic differentiation in geophysical inverse problems, *Geophys. J. Int.*, **170**, 1–8.

Sandwell, D.T. & Smith, W.H.F. (2009). Global marine gravity from retracked Geosat and ERS-1 altimetry: Ridge segmentation versus spreading rate, *J. Geophys. Res.*, **114**, B01411, doi:10.1029/2008JB006008.

Satake, K. (1994). Mechanism of the 1992 Nicaragua tsunami earthquake, *Geophys. Res. Let.*, **21**, 2519-2522.

Satake, K. (1995). Linear and nonlinear computations of the 1992 Nicaragua earthquake tsunami, *Pure Appl. Geophys.*, **144**, 455–470.

Schmidt, M.W. & Poli, S. (1998). Experimentally based water budgets for dehydrating slabs and consequences for arc magma generation, *Earth Planet. Sci. Lett.*, **163**, 361–379.

Scholz, C.H. & J. Campos, J. (1995). On the mechanism of seismic decoupling and back arc spreading at subduction zones, *J. Geophys. Res.*, **100**, 22103–22115.

Scholz, C.H. & Small, C. (1997). The effect of seamount subduction on seismic coupling, *Geology*, **25**, 487–490.

Scholz, C.H. (1998). Earthquakes and friction laws, *Nature*, **391**, 37–42.

Sei, A. & Symes, W.W. (1994). Gradient calculation of the traveltime cost function without ray tracing, SEG 64th Annual International Meeting, *Expanded Abstracts*, 1351–1354.

Sharma, P.V. (1986), *Geophysical methods in geology*, Elsevier.

Shaw, P.R. & Orcutt, J.A. (1985). Waveform inversion of seismic refraction data and applications to young Pacific crust, *Geophys. J. Roy. Astr. Soc.*, **82**, 375–414.

Sheriff, R.E. (1989). *Geophysical methods*, Prentice Hall, New Jersey.

Sheriff, R.E. & Geldart, L.P. (1995). *Exploration Seismology* , 2nd edn, Cambridge University

Press.

Silver, E., Fisher, A., Saffer, D., Kastner, M., Morris, J. & McIntosh, K.D. (2000). Fluid flow paths in the Middle America Trench and Costa Rica margin, *Geology*, **28**, 679–682, doi:10.1130/0091-7613.

Stavenhagen, A.U., Flueh, E. R., Ranero, C.R., McIntosh, K.D., Shipley, T., Leandro, G., Shulze, A. & Danobeitia, J.J. (1998). Seismic wide-angle investigations in Costa Rica: a crustal velocity model from the Pacific to the Caribbean coast, *Zb. Geol. Paläontol., (3–6)*, 393–408.

Stein, S. & Wysession, M. (2003). *An Introduction to Seismology, Earthquakes, and Earth Structure*, Blackwell Publishing.

Stoer, J. & Bulirsch, R. (1980). *Introduction to Numerical Analysis*, Springer, New York.

Stroustrup, B. (2009). *Programming – Principles and Practice Using C++*, Addison-Wesley.

Swift, S.A., Lizarralde, D., Stephen, R.A. & Hoskins, H. (1998). Seismic attenuation in upper ocean crust at Hole 504B, *J. Geophys. Res*., **103**, 27193–27206.

Taillandier, C., Noble, M., Charius, H. & Calandra, H. (2009). First-arrival traveltime tomography based on the adjoint-state method, *Geophysics*, **74**, doi:10.1190/1.3250266.

Takam Takougang, E.M. & Calvert, A.J. (2013). Seismic waveform tomography across the Seattle Fault Zone in Puget Sound: resolution analysis and effectiveness of visco-acoustic inversion of viscoelastic data, *Geophys. J. Int.*, **193**, 763–787.

Tanioka, Y., Ruff, L. & Satake, K. (1997). What controls the lateral variation of large earthquake occurrence along the japan trench, *Island Arc*, **6**, 261–266.

Tarantola, A. (1987). *Inverse Problem Theory: Methods for Data Fitting and Model Parameter Estimation*, Elsevier, New York.

Tarantola, A. & Valette, B. (1982). Inverse Problems = Quest for Information, *J. Geophys.*, **50**, 159–170.

Thurber, C.H. (1983). Earthquake locations and three-dimensional crustal structure in the Coyote Lake area, central California, *J. Geophys. Res.*, **88**, 8226–8236.

Tichelaar, B.W. & Ruff, L.J. (1993). Depth of seismic coupling along subduction zones, *J. Geophys. Res.*, **98**, 2017–2037.

Toomey, D.R. & Foulger, G.R. (1989). Tomographic Inversion of Local Earthquake Data From the Hengill-Grensdalur Central Volcano Complex, Iceland, *J. Geophys. Res.*, **94**, 17497–17510.

Toomey, D.R., Solomon, S.C. & Purdy, G.M. (1994). Tomographic imaging of the shallow crustal structure of the East Pacific Rise at 9º30'N, *J. Geophys. Res.*, **99**, 24135–24157.

Tse S.T. & Rice, J.R. (1986). Crustal earthquakes instabilitiy relation to the depth variation of frictional slip properties, *J. Geophys. Res.*, **91**, 9452–9472.

Um, J. & Thurber, C. (1987). A fast algorithm for two-point seismic ray tracing, *Bull. Seismol. Soc. Am.*, **77**, 972–986.

Urick, R.J., 1983. *Principles of Underwater Sound*, McGraw-Hill.

Van Avendonk, H.J.A. (1998). An investigation of the crustal structure of the Clipperton transform fault area using 3D seismic tomography, PhD thesis, University of California, San Diego.

Van Avendonk, H.J.A., Harding, A.J., Orcutt, J.A. & McClain, J.S. (1998). A two-dimensional tomographyic study of the Clipperton transform fault, *J. Geophys. Res.*, **103**, 17885–17899.

Van Avendonk, H.J.A., Harding, A.J., Orcutt, J.A. & Holbrook, W.S. (2001a). Hybrid shortest path and ray bending method for traveltime and raypath calculations, *Geophysics*, **66**, 648–653.

Van Avendonk, H.J.A., Harding, A.J., Orcutt, J.A. & McClain, J.S. (2001b). Contrast in crustal structure across the Clipperton transform fault from travel time tomography, *J. Geophys. Res*., **106**, 10961–10981.

Vidale, J.E. (1988). Finite-difference calculation of travel times, *Bull. Seismol. Soc. Am.*, **78**, 2062–2076.

Vidale, J.E. (1990). Finite-difference calculation of travel times in three dimensions, *Geophysics*, **55**, 521–526.

Virieux, J. & Operto, S. (2009). An overview of full-waveform inversion in exploration geophysics, *Geophysics*, **74**, doi:10.1190/1.3238367.

von Huene, R., Ranero, C.R., Weinrebe, W. & Hinz, K. (2000). Quaternary convergent margin tectonics of Costa Rica, segmentation of the Cocos Plate, and Central American volcanism. *Tectonics* **19**, 314–334.

von Huene, R. & Ranero, C.R. (2003). Subduction erosion and basal friction along the sediment-starved convergent margin off Antofagasta, Chile., *J. Geophys. Res.*, **108**.

von Huene, R., Ranero, C.R. &. Vannucchi, P. (2004). A model for subduction erosion, *Geology*, **32**, 913–916, doi:10.1130/G20563.1.

Wagner, D., Koulakov, I., Rabbel, W., Luehr, B.-G., Wittwer, A., Kopp, H., Bohm, M., Asch, G. &

the MERAMEX Scientists (2007). Joint inversion of active and passive seismic data in Central Java, *Geophys. J. Int.*, **170**, 923–932, doi:10.1111/j.1365-246X.2007.03435.x.

Walther, C.H.E., Flueh, E.R., Ranero, C.R., von Huene, R. & Strauch, W. (2000). Crustal structure across the Pacific margin of Nicaragua : Evidence for ophiolitic basement and a shallow mantle sliver, *Geophys. J. Int.*, **141**, 759–777.

Wang, B. & Braile, L.W. (1996). Simultaneous inversion of reflection and refraction seismic data application to field data from the northern Rio Grande rift, *Geophys. J. Int.*, **125**, 443–458.

Wang, K. & Bilek, S.L. (2011). Do subducting seamounts generate or stop large earthquakes?, *Geology*, **39**, 819–822, doi:10.1130/G31856.1.

Watanabe, T., Kasami, H. & Ohshima, S. (2007). Compressional and shear wave velocities of serpentinized peridotites up to 200 MPa, *Earth Planets Space*, **59**, 233–244.

Wessel, P., & Smith, W.H.F. (1998), New, improved version of the generic mapping tools released, *Eos Trans. AGU*, **79**, 579.

Wei, S., Graves, R., Helmberger, D., Avouac, J.-P. & Jiang, J. (2012)). Sources of shaking and flooding during the Tohoku-Oki earthquake: A mixture of rupture styles, *Earth Planet. Sci. Lett.*, **333**,91–100.

White, D.J. & Clowes, R.M. (1990). Shallow crustal structure beneath the Juan de Fuca Ridge from 2-D seismic refraction tomography, *Geophys. J. Int.*, **100**, 349–367.

White, D.J. & Clowes, R.M. (1994). Seismic attenuation structure beneath the Juan de Fuca Ridge from tomographic inversion of amplitudes, *J. Geophys. Res.*, **99**, 3043–3056.

White, R.S., Detrick, R.S., Sinha, M.C. & Cormier, M.H. (1984). Anomalous seismic crustal structure of oceanic fracture zones, *Geophys. J. R. Astr. Soc.*, **79**, 779–798.

White, R.S., McKenzie, D. & O'Nions, R.K. (1992). Oceanic crustal thickness from seismic measurements and rare earth element inversions, *J. Geophys. Res.*, **97**, 19683–19715.

Whitley, D.L. (1994). A genetic algorithm tutorial, *Stats. and Comput.*, **4**, 65–85.

Wilcock, W.S.D., Solomon, S.C., Purdy, G.M. & Toomey, D.R. (1992). The seismic attenuation structure of a fast-spreading mid-ocean ridge, *Science*, **258**, 1470–1474.

Wilcock, W.S.D., Solomon, S.C., Purdy, G.M. & Toomey, D.R. (1995). Seismic attenuation structure of the East Pacific Rise near 9o 30'N, *J. Geophys. Res.*, **100**, 24147–24165.

Yang, H., Liu, Y. & Lin, J. (2012). Effects of subducted seamounts on megathrust earthquake

nucleation and rupture propagation, *Geophys. Res. Lett.*, **39**, L24302, doi:10.1029/2012GL053892.

Yang, H., Liu, Y. & Lin, J. (2013). Geometrical effects of a subducted seamount on stopping megathrust ruptures, *Geophys. Res. Lett.*, **40**, doi:10.1002/grl.50509.

Ye, S., Bialas, J., Flueh, E.R., Stavenhagen, A. & von Huene, R. (1996). Crustal structure of the Middle American Trench off Costa Rica from wide-angle seismic data, *Tectonics*, **15**, 1006–1021.

Zelt, C. A. & Smith, R.B. (1992). Seismic traveltime inversion for 2-D crustal velocity structure, *Geophys. J. Int.*, **108**, 16-34.

Zelt, C.A. & Barton, P.J. (1998). Three-dimensional seismic refraction tomography: A comparison of two methods applied to data from the Faeroe Basin, *J. Geophys. Res.*, **103**, 7187–7210.

Zelt, C.A. & Zelt, B.C. (1998). Study of the out-of-plane effects in the inversion of refraction/wide-angle reflection traveltimes, *Tectonophysics*, **286**, 209–221, doi:10.1016/S0040-1951(97)00266-7.

Zelt, C.A. (1999). Modelling strategies and model assessment for wide-angle seismic traveltime data, *Geophys. J. Int.*, **139**, 183–204.

Zelt, C.A., Hojka, A.M., Flueh, E.R. & McIntosh, K.D. (1999). 3D simultaneous seismic refraction and reflection tomography of wide-angle data from the central Chilean margin, *Geophys. Res. Lett.*, **26**, 2577–2580.

Zhang, J. & Toksöz, N. (1998). Nonlinear refraction traveltime tomography, *Geophysics*, **63**, 1726–1737.

Zhang, J., ten Brink, U.S. & Toksöz, M.N. (1998). Nonlinear refraction and reflection travel time tomography, *J. Geophys. Res.*, **103**, 29743–29757.

Zhdanov, M.S. (2002). *Geophysical inverse theory and regularization problems*, **36**, Elsevier.

Zhou, B. & Greenhalgh, S.A. (2005). Shortest path ray tracing for the most general 2D/3D anisotropic media, *J. Geophys. Eng.*, **2**, 54–63.

APPENDIX A: USER MANUAL

APPENDIX A: USER MANUAL

A.1. Overview

TOMO3D is a package for 3-D joint refraction and reflection travel-time tomography based on TOMO2D. For a copy of the code, or if you have any suggestions, find bugs in the code or errors in this manual, please contact the author by sending an e-mail to melendez@icm.csic.es. The code is free to use for academic purposes only, and will be available for download on the Internet in the near future.

gen_smesh3d - generate a velocity mesh.
edit_smesh3d - edit a velocity mesh.
tt_forward3d - calculate travel times and ray paths for given sources and receivers.
tt_inverse3d - do travel-time inversion.
NOTE: *tt_inverse3d* is a stand-alone application, i.e., it contains the forward calculation part, which is also separately available as *tt_forward3d*.

A.2. Installation

Make sure GNU C++ compiler (with the standard template library) is installed on your platform. Currently each command has its particular Makefile to generate the executable file. Edit the corresponding Makefile to reflect your computing environment, and then type the command 'make'.

A.3. File formats

A.3.1. Velocity grid file (sheared mesh)

nx ny nz vwater vair	- number of nodes in x, y and z, velocity in water and air.
x(1) x(2) … x(nx)	- node's x-coordinates.
y(1) y(2) … y(ny)	- node's y-coordinates.
b(1,1) b(1,2) … b(1,ny)	- corresponding geological relief (bathymetry or topography).
: : :	
b(nx,1) b(nx,2) … b(nx,ny)	

z(1) z(2) … z(nz) - node's z-coordinates.

v(1,1,1) v(1,1,2) … v(1,1,nz) - velocity at each node.

v(1,2,1) v(1,2,2) … v(1,2,nz)

: : :

v(1,ny,1) v(1,ny,2) … v(1,ny,nz)

: : :

v(nx,ny,1) v(nx,ny,2) … v(nx,ny,nz)

All coordinates should be in increasing order. The z-coordinate is relative to the sea floor/land surface and increases downwards. There is no limit to the number of nodes you can put in one line, as long as it is consistent with the first line and it is within the capacity of your computer. An example is given below:

5 5 5 1.5 0.33
0 1 2 3 4
0 1 2 3 4
0 0 0 0 0
0 0 0 0 0
0 0 0 0 0
0 0 0 0 0
0 0 0 0 0
0 1 2 3 4
2 2 2 2 2
2 2 2 2 2
2 2 2 2 2
2 2 2 2 2
2 2 2 2 2
2 2 2 2 2
2 2 2 2 2
2 2 2 2 2
2 2 2 2 2
2 2 2 2 2
2 2 2 2 2

2 2 2 2 2
2 2 2 2 2
2 2 2 2 2
2 2 2 2 2
2 2 2 2 2
2 2 2 2 2
2 2 2 2 2
2 2 2 2 2
2 2 2 2 2
2 2 2 2 2
2 2 2 2 2

A.3.2. Reflector file

The reflector's depth is set with the following format:

nx ny	- number of nodes in x and y,
x(1) y(1) d(1,1)	- node's x- and y-coordinates, and depth at each node.
x(1) y(2) d(1,2)	
: : :	
x(1) y(ny) d(1,ny)	
: : :	
x(nx) y(ny) d(nx,ny)	

Example:

5 5
0 0 2.5
0 1 2.5
0 2 2.5
0 3 2.5
0 4 2.5
1 0 2.5

1 1 2.5

1 2 2.5

1 3 2.5

1 4 2.5

2 0 2.5

2 1 2.5

2 2 2.5

2 3 2.5

2 4 2.5

3 0 2.5

3 1 2.5

3 2 2.5

3 3 2.5

3 4 2.5

4 0 2.5

4 1 2.5

4 2 2.5

4 3 2.5

4 4 2.5

A.3.3. Travel-time data file

The first line contains only one number, nsrc, which is the number of sources. The rest of the file must contain nsrc packets of travel-time data, each of which has the following format:

1st line of each packet:

s x y z nrcv - flag 's', src's coordinate (x,y,z), and number of receivers.

2nd to (1+nrcv)th lines:

r x y z code time dt - flag 'r', rcv's coordinate (x,y,z), code (0:refraction, 1:reflection), traveltime in seconds, and pick error in seconds.

For example:

1

s 2.5 2.5 0 18

r 1.25 1.25 0 0 1.07313 0.01

r 1.25 2.5 0 0 0.769735 0.01

r 1.25 3.75 0 0 1.07314 0.01

r 2.5 1.25 0 0 0.769735 0.01

r 2.5 2.5 0 0 7.06542e-15 0.01

r 2.5 3.75 0 0 0.769428 0.01

r 3.75 1.25 0 0 1.07314 0.01

r 3.75 2.5 0 0 0.769428 0.01

r 3.75 3.75 0 0 1.07235 0.01

r 1.25 1.25 0 1 1.61775 0.01

r 1.25 2.5 0 1 1.51322 0.01

r 1.25 3.75 0 1 1.618 0.01

r 2.5 1.25 0 1 1.51322 0.01

r 2.5 2.5 0 1 1.39929 0.01

r 2.5 3.75 0 1 1.51312 0.01

r 3.75 1.25 0 1 1.618 0.01

r 3.75 2.5 0 1 1.51312 0.01

r 3.75 3.75 0 1 1.61787 0.01

A.3.4. Correlation length files (velocity and depth)

Correlation lengths for velocity nodes are specified in a manner very similar to the velocity grid format:

nx ny nz	- number of nodes in x, y and z, velocity in water and air.
x(1) x(2) … x(nx)	- node's x-coordinates.
y(1) y(2) … y(ny)	- node's y-coordinates.
b(1,1) b(1,2) … b(1,ny)	- corresponding geological relief (bathymetry or topography).
: : :	
b(nx,1) b(nx,2) … b(nx,ny)	
z(1) z(2) … z(nz)	- node's z-coordinates.
Lx(1,1,1) Lx(1,1,2) … Lx(1,1,nz)	- correlation length in x at each node.
Lx(1,2,1) Lx(1,2,2) … Lx(1,2,nz)	

: : :

Lx(1,ny,1) Lx(1,ny,2) … Lx(1,ny,nz)

: : :

Lx(nx,ny,1) Lx(nx,ny,2) … Lx(nx,ny,nz)

Followed by correlation lengths in y and z: Ly(i,j,k) and Lz(i,j,k).

An example is given below:

2 2 2
0. 5
0. 5.
0 0
0 0
0. 3.
1. 2.
1. 2.
1. 2.
1. 2.
1. 2.
1. 2.
1. 2.
1. 2.
1. 2.
1. 2.
1. 2.

Correlation lengths for reflector nodes can be specified in a separate file as:

nx ny
x(1) y(1) Lx(1,1) Ly(1,1) - node's x- and y-coordinates, correlation lengths in x and y.
x(1) y(2) Lx(1,2) Ly(1,2)
: : : :
x(1) y(ny) Lx(1,ny) Ly(1,ny)

: : : :

x(nx) y(ny) Lx(nx,ny) Ly(nx,ny)

An example is given below:

2 2

0. 0. 2. 2.

0. 5. 2. 2.

5 0. 2. 2.

5 5. 2. 2.

Note that if a correlation length file for reflector nodes is not provided, tt_inverse3d will sample from horizontal correlation lengths for velocity nodes.

A.3.5. Variable damping file

Spatially variable damping is implemented by tt_inverse3d -DQdamp_file, which is useful for squeezing tests. The file format is very similar to those for velocity grid and correlation lengths:

nx ny nz	- number of nodes in x, y and z, velocity in water and air.
x(1) x(2) … x(nx)	- node's x-coordinates.
y(1) y(2) … y(ny)	- node's y-coordinates.
b(1,1) b(1,2) … b(1,ny)	- corresponding geological relief (bathymetry or topography).
· :· : : ·	
b(nx,1) b(nx,2) … b(nx,ny)	
z(1) z(2) … z(nz)	- node's z-coordinates.
D(1,1,1) D(1,1,2) … D(1,1,nz)	- damping weight at each node.
D(1,2,1) D(1,2,2) … D(1,2,nz)	
: : :	
D(1,ny,1) D(1,ny,2) … D(1,ny,nz)	
: : :	
D(nx,ny,1) D(nx,ny,2) … D(nx,ny,nz)	

An example is given below:

5 5 5
0 1 2 3 4
0 1 2 3 4
0 0 0 0 0
0 0 0 0 0
0 0 0 0 0
0 0 0 0 0
0 0 0 0 0
0 1 2 3 4
1 1 1 1 1
1 1 1 1 1
1 1 1 1 1
1 1 1 1 1
1 1 1 1 1
1 1 1 1 1
1 1 1 1 1
1 1 1 1 1
1 1 1 1 1
1 1 1 1 1
1 1 1 1 1
100 100 100 100 100
100 100 100 100 100
100 100 100 100 100
100 100 100 100 100
100 100 100 100 100
100 100 100 100 100
100 100 100 100 100
100 100 100 100 100
100 100 100 100 100
100 100 100 100 100
100 100 100 100 100
100 100 100 100 100

A.4. Command description

A.4.1. Manipulating velocity grid files

NAME **gen_smesh3d** - generate a velocity mesh.
SYNOPSIS gen_smesh3d [velocity options] [grid options]
DESCRIPTION This command generates a velocity grid, which is a required input file for other programs.
OPTIONS
Velocity options
-**A**v0 -**B**gradient - specifies velocity as a function of depth, V(z) = v0 + gradient * z (km/s).
-**C**v.in/ilayer [-**F**jlayer/refl_file] - uses v.in of Zelt's RAYINVR to construct a velocity field. The seafloor layer must be given by ilayer. Use -F to extract jlayer as a reflector in refl_file. (not available yet).
Grid options
-**N**nx/ny/nz -**D**xmax/ymax/zmax - specifies a uniform spacing grid with nx, ny and nz nodes, spanning from 0 to xmax, from 0 to ymax, and from 0 to zmax (km).
-**X**xfile -**Y**yfile -**Z**zfile [-**T**tfile] - specifies a variable spacing grid, as defined by xfile, yfile and zfile. Optional tfile specifies variable bathymetry (km).
-**E**dx/dy -**Z**zfile - creates a grid based on v.in given in -C option, with a (nearly) uniform horizontal spacing of dx and dy (km), a variable vertical spacing as defined by zfile (not available yet).

NAME **edit_smesh3d** - edit a velocity mesh.
SYNOPSIS edit_smesh3d grid_file -**C**cmd [-**L**vcorr_file -**U**upper_file]
DESCRIPTION This program may be useful when performing synthetic tests, for instance to add anomalies to your background model.
OPTIONS
-**C**a - set all velocities to horizontal average.
-**C**pgrid - paste grid on the original grid.
-**C**Pprof - paste 1-D profile given by prof.
-**C**sx/y/z - apply Gaussian smoothing operator with an window of x, y, and z (km).
-**C**rmx/my/mz - refine mesh by mx for x-direction, my for y-direction, and by mz for z-direction.
-**C**cA/x/y/z - add checkerboard pattern with amplitude A (%), horizontal cycles x and y km, and

vertical cycle z km.

-**C**dA/xmin/xmax/ymin/ymax/zmin/zmax - add a rectangular anomaly with amplitude A (%).

-**C**gA/x0/y0/z0/Lx/Ly/Lz - add a Gaussian anomaly of $A \cdot \exp[-(x-x0)^2/Lx-(y-y0)^2/Ly-(z-z0)^2/Lz]$ (%).

-**C**l - remove low velocity zone.

-**CR**seed/A/nrand - randomize the velocity field.

-**CS**seedA/xmin/xmax/dx/ymin/ymax/dy/zmin/zmax/dz - another randomization.

-**CG**seed/A/N/xmin/xmax/ymin/ymax/zmin/zmax - yet another randomization.

-**Cm**v/refl_file - set velocities below refl_file to v.

-**L**vcorr_file - set correlation length file used by -**Cs**.

-**U**upper_file - set upper limit depth for edit operations.

A.4.2. Forward travel-time calculation

NAME **tt_forward3d** - forward travel-time calculation.

SYNOPSIS tt_forward3d -**M**grid_file [-**G**geom_file -**F**refl_file -**A**] [-**N**xorder/yorder/zorder/clen/nintp/tot1/tot2 -**E**elem -**g** -**T**ttime -**O**obs ttime -**r**v0 -**D**diff -**R**ray -**S**src -**I**vel -**i**w/e/s/n/u/d/dx/dy/dz -**n** -**C**used_time -**V**level]

DESCRIPTION This program uses a hybrid approach based on the graph method and the bending method.

OPTIONS

-**M**grid_file - specifies a velocity grid file.

-**G**geom_file - specifies a geometry file (with the same file format as the traveltime data file - with zeros for travel time and pick error).

-**F**refl_file - specifies a reflector file.

-**A** - takes an extra care for reflection phase (more time-consuming)

-**N**xorder/yorder/zorder/clen/nintp/tot1/tot2 - specifies a x-order, y-order and z-order forward star in the graph method, sets the maximum segment length (clen), the number of interpolation points per segment (nintp), and tolerance levels for iterations (tot1 for conjugate gradient and tot2 for Brent minimization) used in the bending method.

-**E**elem file - prints out the elements of a grid file to elem file.

-**g** - use the graph method only.

-**T**ttime_file - prints out calculated travel times to ttime file.

-**O**obs_ttime_file - prints out input observed travel times to obs ttime file.

-**r**v0 - sets reduction velocity for travel time output.

-**D**diff_file - prints out differential travel times to diff file.

-**R**ray_file - prints out ray paths to ray file.

-**S**src_file - prints out source locations to src file.

-**I**vel_file - prints out a velocity file to vel file.

-**i**w/e/s/n/u/d/dx/dy/dz - specifies nodes and region for -**I**.

-**n** - suppresses printing water and air velocity nodes for -**I**.

-**C**used_time

-**V**level - sets verbose mode (level = 0 or 1).

NOTE: If -**G** is not specified, only operations regarding a velocity grid will be done.

A.4.3. Travel-time inversion

NAME **tt_inverse3d** – travel-time inversion.

SYNOPSIS tt_inverse3d -**M**grid_file -**G**data_file [-**N**xorder/yorder/zorder/clen/nintp/tol1/tol2] [-**F**refl_file -**A** -**L**logfile -**O**out_fn_root [-**o**level -**l**] -**K**dws_file] [-**P** -**R**crit_chi -**Q**lsqr_tol -**s**bound -**W**d_weight -**V**level] [-**CV**vcorr_file -**CD**dcorr_file] [iteration options] [smoothing options] [damping options]

DESCRIPTION This command is an implementation of 3-D joint refraction and reflection travel-time tomography.

OPTIONS

-**M**grid_file - specifies a velocity grid file.

-**G**data_file - specifies a traveltime data file.

-**N**xorder/yorder/zorder/clen/nintp/tol1/tol2 (see tt forward).

-**F**refl_file (see tt forward).

-**A** (see tt forward).

-**L**logfile - sets log file, with the output format as: 1. the number of iteration, 2. the number of set, 3. the number of rejected data, 4. RMS traveltime misfit (Pg+PmP), 5. initial χ^2 (Pg+PmP), 6. the number of valid Pg data, 7. RMS traveltime misfit (Pg), 8. initial χ 2 (Pg) 9. the number of valid PmP data, 10. RMS traveltime misfit (PmP), 11. initial χ^2 (PmP), 12. CPU time used for graph solution, 13. CPU time used for bending solution, 14. smoothing weight for velocity nodes, 15. smoothing weight for depth nodes, 16. damping weight for velocity nodes, 17. damping weight for depth nodes, 18. the number of LSQR calls, 19. the total number of LSQR iteration, 20. CPU time used for LSQR, 21. predicted χ^2 based on LSQR solution (Pg+PmP), 22. average velocity

perturbation, 23. average depth perturbation, 24. roughness of velocity nodes in x direction, , 25. roughness of velocity nodes in y direction, 26. roughness of velocity nodes in z direction, 27. roughness of depth nodes in x direction, and 28. roughness of depth nodes in y direction.

-**O**out_fn_root - sets file name root for output files.

-**o** - sets output level (print out travel time residual for level >=1; print out ray paths for level >=2).

-**l** - prints out the final model only.

-**K**dws_file - prints out DWS to dws file.

-**P** - sets pure jumping strategy.

-**R**crit_chi - sets critical χ for robust inversion.

-**Q**lsqr_tol - sets tolerance for LSQR algorithm.

-**s**[bound file] - applies 3-D filter after every iteration. The upper bound for filtering can be set by bound file.

-**W**d_weight - sets depth kernel weighting factor.

-**V**[level] - sets verbose level.

-**CV**vcorr_file - sets correlation length file for velocity nodes.

-**CD**dcorr_file - sets correlation length file for reflector.

Type-1 iteration options: many iterations with a single set of parameters.

-**I**niter - sets the number of maximum iterations.

-**J**target_chi2 - sets target χ^2.

-**SV**wsv - applies velocity smoothing with weighting factor wsv.

-**SD**wsd - applies depth smoothing with weighting factor wsv.

Type-2 iteration options: single iteration with many sets of parameters.

-**SV**wsv_min/wsv_max/dw [-**XV**] - tries velocity smoothing with weighting factor varying from wsv_min to wsv_max with an increment of dw. With -**XV**, smoothing weights will be raised to the power of 10.

-**SD**wsd_min/wsd_max/dw [-**XD**] - tries depth smoothing with weighting factor varying from wsd_min to wsd_max with an increment of dw. With -**XD**, smoothing weights will be raised to the power of 10.

-**TV**max_dv - applies velocity damping with maximum velocity perturbation of max_dv (%).

-**TD**max_dd - applies depth damping with maximum velocity perturbation of max_dd (%).

-**DV**wdv - applies velocity damping with weighting factor wdv.

-**DD**wdd - applies depth damping with weighting factor wdd.

-**DQ**damp_file - applied velocity damping with spatially variable weighting factor specified by damp file (for squeezing).